TABLE OF CONTENTS

Page

LIST OF TABLES

Page

LIST OF FIGURES

LIST OF ABREVIATIONS

3TL	Three time levels
agl	Above ground level
ABL	Atmospheric Boundary Layer
AR-WRF	Advanced Research WRF Model
ARPS	Advanced Regional Prediction System
B03	Bénard (2003)
B04	Bénard et al. (2004)
B05	Bénard et al. (2005)
BTF	Basic Terrain Following coordinate
CFD	Computational Fluid Dynamics
CFL	Courant–Friedrichs–Lewy number
COAMPS	Coupled Ocean/Atmosphere Mesoscale Prediction System
CWE	Computational Wind Engineering
DES, DNS	Detached Eddy Simulation; Direct Numerical Simulation
DRM	Dynamic Reconstruction Model
EC	Environment Canada
EE	Euler Equations
EPA	Environment Protection Agency
FEM	Finite Element Method
FVM	Finite Volume Method
GEM	Global Environment Multiscale unified model
GMRES	Generalized Minimal Residual iterative solver

GW	Gigawatts
HAZ	High Accuracy Zone
HPC	High Performance Computing
IOP	Intense Observation Period
LAM	Limited Area Model
LES	Large Eddy Simulation
LIDAR	Light Detection and Ranging
MAP	Mesoscale Alpine Programme
MC2	Mesoscale Compressible Community Model
MC2-LES	MC2 model with LES capability
ML	Mixed Layer
MM5	Mesoscale Model version 5
MO	Monin-Obukhov
MW	Megawatts
NCAR	National Center for Atmospheric Research
NH	Non-Hydrostatic
NS	Navier-Stokes
N-SI	New Semi-Implicit scheme
NWP	Numerical Weather Prediction
O-SI	Original Semi-Implicit scheme
RAMS	Regional Atmospheric Modeling System
RANS	Reynolds Averaged Navier-Stokes
RA	Robert-Asselin filter

RAW	Robert-Asselin-Williams filter
RE	Renewable Energy
RMSE	Root Mean Square Error
RPN	Recherche en Prévision Numérique
RSM	Reynolds Stress Model
SBL	Stable Boundary Layer
SDD	Statistical Dynamical Downscaling
SFS	Sub-Filtered Scale
SGS	Sub-Grid Scale
SHB78	Simmons, Hoskins and Burridge (1978)
SI	Semi-Implicit
SISL	Semi-Implicit Semi-Lagrangian
SL	Semi-Lagrangian
SLEVE	Smooth Level Vertical coordinate
SODAR	Sonic Detection and Ranging
SSL	Shear Surface Layer
TKE	Turbulent Kinetic Energy
TWh	Terawatt-hour
UKMO	United Kingdom Met Office
URANS	Unsteady Reynolds Averaged Navier-Stokes
US	United States
WAsP	Wind Atlas Analysis and Application Program
WRF	Weather Research and Forecast

LIST OF SYMBOLS

Constants

c_p	Heat capacity at constant pressure (1005 J kg-1 K-1)
R	Ideal gas constant (287.06 J kg-1 K-1)
p_s	Surface reference pressure (1013.25 mbar)
g	Gravitational acceleration of a fluid particle (9.81 ms-2)
υ	Dry air kinematic viscosity (1.568×10-5 m2s-1)
κ	Von Kármán non-dimensional constant (0.41)
π	Pi number (3.14159)
π	Euler number (2.71828)
Ri_c	Critical Richardson constant (0.25)

Mathematical Operators and Notation

$\mathbf{i}, \mathbf{j}, \mathbf{k}$	Unit directional vectors in Cartesian coordinates
$\mathbf{e}_i$	Unit directional vector using Einstein's notation
$(\ )\cdot(\ )$	Dot or scalar product
$(\ )\times(\ )$	Cross or vector product
$\partial(\ )/\partial t$	Local rate of change of a fluid's quantity
$\nabla(\ )$	Gradient of a fluid's quantity
$\nabla_H(\ )$	Horizontal 2D gradient of a fluid's quantity
$\nabla\cdot(\ )$	Divergence of a fluid's quantity
$\nabla^2(\ )$	Lapacian, or gradient of the divergence, of a fluid's quantity
$\nabla\cdot\rho\mathbf{v}(\ )$	Advection of a fluid's quantity
$d(\ )/dt$	Total or material derivative of a fluid's quantity
$\overline{(\ )}$	Time average
$\langle\ \rangle$	Spatial average
$\overline{\langle\ \rangle}$	Ensemble average
$u_i' u_j'$	Sub-filter velocity covariance or momentum flux
$u_i' u_i'$	Sub-filter velocity variance
$\theta' u_j'$	Sub-filter heat flux

δ_{ij}	Kronecker delta rank-2 tensor
ε_{ijk}	Levi-Civita spatial orientation rank-3 tensor

Greek Symbols

ρ	Dry air density
ρ'	Dry air density perturbation
θ	Dry air potential temperature
θ'	Dry air potential temperature perturbation
π	Exner equation for pressure and temperature relationship
ψ	Model variables
$\overline{\psi}$	Model variable time average
ψ'	Model variable perturbation
$\overline{\psi}^t$	Model variable treated implicitly
ϕ	Model solution
λ	Solution's asymptotic growth rate
δ	Time filtering coefficient
α_{RAW}	Robert-Asselin-Williams (RAW) filter strength
ξ	Time decentering coefficient
γ_*	Reference ABL height
γ	Ekman parametric constant
Ω	Planet Earth's rotational speed
$\boldsymbol{\Omega}$	Angular velocity vector
$\boldsymbol{\sigma}$	Total stress tensor
$\boldsymbol{\tau}$	Shear stress tensor
φ	Planet Earth's latitude angle
η	Kolmogorov's length scale
τ	Kolmogorov's time scale
ν	Kolmogorov's velocity scale
ε	Rate of energy transfer
σ_U	Velocity standard deviation
$\delta_x, \delta_y, \delta_z$	SISL 3D displacements
$\chi, \chi_*, \overline{\chi}$	Generic atmospheric, reference and basic states (respectively)
Π	Original equation system

Latin Symbols

$\mathbf{v}$	Velocity field or vector
u, v, w	Velocity components in Cartesian coordinates
$\mathbf{v}_g$	Geostrophic velocity vector
u_g, v_g	Geostrophic velocity components
$\mathbf{r}$	Displacement or distance vector
x, y, z	Independent distance variables in Cartesian coordinates
u_*	Friction velocity
p	Thermodynamic pressure
P	Generalized pressure
p'	Dry air pressure perturbation
T	Absolute temperature
b	Buoyancy force (conventional)
$\hat{b}$	Redefined buoyancy force
$\mathbf{f}$	Body forces
k_M	Dry air momentum diffusivity
k_T	Dry air thermal conductivity
z_0	Aerodynamic roughness length
Q	Heat sources
T_*	Reference temperature
f	Coriolis factor
N	Brunt-Väisälä frequency
L	Length scale
H	Height scale
H_*	Reference height scale
$\overline{H}$	Basic-state height scale
l_N	Natural wavelength
l_{eff}	Effective wavelength
a	Mountain's half width
z_{hill}	Local terrain height

z_i	ABL top or capping height
Ro	Rosby non-dimensional number
Ek	Ekman non-dimensional number
Re	Reynolds non-dimensional number
Fr	Froude non-dimensional number
$Fr^{\oplus}$	Effective Froude number over an obstacle
k	Eddy size wavenumber
k_{in}	Eddy wavenumber in the inertial spectral range
k_{η}	Eddy wavenumber in the energy-dissipation spectral range
l_0	Eddy spin length scale
u_0	Eddy spin velocity scale
TI	Turbulence intensity
$D_{C,i}$	Turbulent diffusion flux rate
k_i	Turbulent diffusivity coefficients
C	Fluids quantity concentration
Pr	Prandtl non-dimensional number
Pr_t	Prandtl non-dimensional number for turbulent flow
K	Turbulent kinetic energy
P_B	Buoyancy-dependent turbulence production rate
P_S	Shear-dependent turbulence production rate
TR	Turbulence redistribution rate
Ri	Richardson non-dimensional number
Ri_f	Flux Richardson non-dimensional number
Ri_b	Bulk Richardson non-dimensional number
Ri_c	Critical Richardson non-dimensional number
L	MC2's kernel left-hand-side linear terms
R	MC2's kernel right-hand-side linear terms
F	MC2's kernel source terms
Δt	Time step or interval
A	Solution's amplification factor
ℓ_*, $\bar{\ell}$	Reference and stationary linear operators (respectively)
L_{ij}, C_{ij}, R_{ij}	Leonard, cross and Reynolds stress tensors (respectively)

INTRODUCTION

Context

Fossil fuels, such as oil, coal, and natural gas, currently provide approximately 85% of all the energy used worldwide. These natural resources are constantly depleted without any chance to be replaced in a reasonable time span, and their remaining amount is foreseen to last respectively 46 years for oil, 58 years for natural gas and 118 years for coal (British Petroleum, 2017). Although fossil-based energy consumption is growing slowly and occasionally new resource deposits are found, the rapid industrialization of countries with high population growth rates (e.g. China, India and Brasil) and the need of developed countries to sustain their economic progress will drive these resources to an inevitable end.

Aside from being finite, the combustion process of fossil fuels yields polluting by-products or emissions that affect adversely our environment due to their greenhouse effect, the main cause of the current climate change. In contrast, renewable energy (RE) resources are naturally regenerated and, thus, allow their usage with a much lower environmental impact than that of fossil-based resources. Additionally, RE can boost local energy security by reducing the strategic dependence on imported fossil fuels. These factors, along with new fiscal incentives in many countries, have turned RE in the fastest growing alternative sources of energy, at a rate of 15% per year globally (U.S. Department of Energy, 2017).

By 2017, wind and solar power provided more than 80% of the RE global growth, accumulating 131 TWh for wind and 77 TWh for solar energy, despite the share of renewable power within the world's primary energy sources has only reached 3.2% (British Petroleum, 2017). Lately, China has dominated the RE sector with approximately 40% contribution to the global RE installed capacity, in addition to its 20.5% share of the RE global consumption. North America, on the other hand, has added a 21% to the RE global installed capacity and sustained a 23% of the RE global consumption (British Petroleum 2017, U.S. Department of Energy 2017). Although the generalize objective is to reach a 100% penetration of RE sources

in the world's energy matrix by 2050, the foreseeable RE share in the next 30 to 40 years drops between 45 to 50% (World Wind Energy Association 2015, U.S. Department of Energy 2017).

By the end of 2016, wind power reported significant growth worldwide reaching 487 GW of new installed capacity, which represents a development rate of 11.8%. China has added nearly 19.3 GW of new wind power installations (i.e. an annual growth rate of 13%) to its total capacity of 149 GW, which provides about 4% of the Chinese electricity demand. On the other hand, the U.S. and Canada respectively added 8.3 GW and 0.7 GW of wind power installed capacity, amounting 82 GW and 11.9 GW for both countries. Furthermore, 6.3% of U.S. and 5.4% of Canadian electricity demand is met by wind energy, enough to power over 21.3 million homes all together (World Wind Energy Association 2016, American Wind Energy Association 2017, Canadian Wind Energy Association 2017).

Out of the estimated worldwide wind energy potential of 95 TW, the prospective exploitation growth by 2050 is a 40% (World Wind Energy Association, 2015). To achieve this goal, both onshore and offshore wind farms shall augment in number and size. Although there is an increasing interest on offshore wind farms, accessible and less expensive transportation and electric infrastructure have privileged the onshore wind farm developments to deliver electricity to the public. Offshore wind farms are considerably more expensive to build, and turbines must be able to withstand further wear and tear that comes with higher wind speeds and seawater salinity. Additionally, onshore wind energy is very competitive as its current and projected levelized cost is one of the lowest among the available alternatives in the RE market (i.e., between 0.04 and 0.1 USD/MWh) (American Wind Energy Association 2017). However, onshore projects are usually located in complex terrain sites, where wind speed and direction are changing permanently, thus, requiring a highly accurate resource estimation to predict and optimize the potential energy harvest of the wind farms. Thus, the present work aims to contribute to the improvement of wind modelling for resource assessment and RE project engineering.

Problem and Motivation

Wind resource assessment (WRA) is one of the primary and most important aspects of any wind power project. It enables wind farm developers and investors to take fundamental decisions at the initial stages (i.e., project level), in addition of its influence on decision making for operational wind farms oriented by prospective energy production assessments. WRA provides policy makers enough information on the wind energy potential that is likely to be exploited at selected sites under a regulatory framework of large scale power plants. The methodology applied for WRA at project level vary depending on the approach and detail needed regarding the wind energy potential estimation. This process finally yields the baseline data to optimize a layout of wind turbines over a land patch with diverse complexities (e.g., orographic distribution and slopes, multiple vegetation types and sizes, land use, wildlife, urban versus rural populated areas, local microclimates and others) where the power plant must perform at its maximum efficiency and lowest possible cost.

Local microscale and/or regional mesoscale wind evaluations differ significantly as the covered study area can span from hundreds of square meters to thousands of square kilometers. Both boundary-layer multiscale interactions and large mesoscale motions coexist and affect wind power generation (Landberg et al., 2003). Modern wind turbines operate within the first 100 to 200 m above ground level (a.g.l.) of the turbulent atmospheric boundary layer (ABL), where average wind speeds increase logarithmically and wind directions vary rotationally with height influenced by the momentum and energy exchange with the Earth's surface microscale features, as well as synoptic and mesoscale flow phenomena. The highly fluctuating wind speeds, wind directions and differential momentum exchange must be taken into consideration for turbine design since it generates variable thrust along the disk spanned by its rotating blades upon multiscale flow phenomena. Hence, project level WRA requires a combined multiscale approach that accounts for real physical conditions in which industrial wind turbines operate.

Complex terrain, hereon understood as irregular geographic variations, in conjunction with thermal stratification of the airflow usually induce and modify the ABL turbulent circulations.

Modern WRA in complex sites relies on numerical modelling, which becomes a difficult task as the nonlinear interactions of the thermally stratified ABL over steep slopes, hills and escarpments generally cause flow separation and recirculation. The complex character of these flow phenomena and conservation principles is expressed in a simultaneous set of nonlinear partial differential equations that are usually approximated with a numerical model. To obtain solutions for these nonlinear conservation relationships it is common to remove the nonlinearities in the equations, which allows for a general analysis based on a simpler linear formulation. Numerical wind modelling based on simplified linearized equations and low-order turbulence closures is only reliable to predict neutrally stratified flow over gentle and moderate terrain slopes (up to 0.2), due to its poor prediction capabilities of flow separation downstream in the mountain lee sides (Kim and Patel 2000, Palma et al. 2008). Thus, wind simulations carried over multiple hills and/or steep topography represent at stiffer technical challenge that requires more sophisticated solvers capable of addressing nonlinear multiscale flow phenomena.

Topographic effects on mesoscale atmospheric systems combined with highly turbulent flow structures can also affect adversely the wind farm performance if not assessed properly. Thorough field measurements are usually expensive and site dependent, with significant spatial and temporal variability. Hence, the need for models based on boundary layer theory and advanced computational fluid dynamics (CFD), which can simulate the performance of a wind farm over a prescribed time lapse. Advanced CFD models account for ground surface variations and the meandering wake effect between wind turbines in a cluster configuration (Jimenez et al. 2007, Ayotte 2008).

The computational wind engineering (CWE) community has combined mesoscale numerical weather prediction (NWP) models (e.g., WRF, ARPS, RAMS, MM5, MC2, KAMM) with other nonlinear CFD models (e.g. Meteodyn WT, WindSim, MIP, EllipSys, Pheonics) or with simplified linear microscale models (e.g., WAsP, MS-Micro, WindFarmer, OpenWind, WindPRO), to accomplish the desired and necessary multiscale wind modelling. Some of the mesoscale nonlinear CFD combinations yield relatively good results for simulations over moderately sloping and complex topography (Chen et al. 2010, Harris and Durran 2010,

Lundquist et al. 2012), despite their higher computational overhead. On the contrary, mesoscale nonlinear models coupled with linear microscale models perform well only over flat and gently sloping terrain, otherwise numerical errors can reach up to 10% revealed on the wind speed overestimation (Pinard et al. 2009, Sumner et al. 2010, Gasset et al. 2012). Apart from the round-off and truncation errors, and the possible coupling mismatch due to differences in model algorithms, the intrinsic weakness of many mesoscale models is their un-damped computational mode. This characteristic spurious signal allegedly produces a time-splitting instability, which is amplified for simulations of nonlinear systems and can enhance the numerically generated noise (Durran, 2010).

Consequently, to bridge the meso-microscale gap in order to exploit all the multiscale modelling benefits and features, CWE researchers have harnessed mesoscale models with imbedded high-resolution capabilities with techniques such as unsteady Reynolds averaged Navier-Stokes (URANS), large-eddy simulation (LES) or detached-eddy simulation (DES) (Pielke and Nicholls 1997, Cuxart et al. 2000, Chow et al. 2005, Spalart et al. 2006, Moeng et al. 2007, Shur et al. 2008, Churchfield et al. 2010, Bechmann and Sørensen 2010, Gasset et al. 2014). Independent of the model employed, the reported results demonstrate that this embedded hybrid approach accounts for the multiscale unsteady physical processes that transition effectively between different space and time scales in turbulent ABL flows, capturing correctly the thermal stratification effect on the wind and the conservation of mass, momentum and energy transport. Still, with exception of a few, most of these implementations have only been introduced and validated for flat terrain or gentle slopes, which represents an opportunity to contribute to this innovative method with further adaptations for steep terrain.

Gasset (2014) upgraded and refined the Canadian Mesoscale Compressible Community (MC2) model, subject of this particular research, not only with a LES-capable 3D turbulence modelling method with several subgrid scale (SGS) schemes but also with a new vertical discretization for the “physics” parameterization package, which corrects the errors due to model levels mismatch through the standard dynamics-physics interface. In addition, the MC2-LES model counts with a new “dynamics + physics” standalone version that allows all the 3D

turbulence diffusion terms to be calculated at the same time avoiding the fractional-step separation during the calculations. These and other complementary features for MC2-LES are thoroughly explained and validated in Gasset (2014).

Objectives, Methodology and Contributions

The main objective of the present study is to continue the enhancement and adaptation of the numerical methods of the Mesoscale Compressible Community (MC2) model, in order to obtain a robust and stable multiscale simulation tool capable of performing high-resolution turbulent ABL realizations over steep terrain.

To accomplish this continuous refinement process, the following three particular issues are addressed in this work:

1. The numerical instability and spuriously generated noise during wind simulations over steep terrain;
2. Thermal stratification disregard in the original wind-climate classification for statistical dynamic downscaling initialization scheme; and
3. The necessity to adapt the Reynolds stress tensor with appropriate metric transformations to correct terrain forcing for the 3D turbulence diffusion calculations.

Firstly, the model's semi-implicit semi-Lagrangian (SISL) discretization scheme is analysed to assess its inherent numerical instability and noise problem for wind simulations over steep terrain, detected long before the LES technique was implemented (Benoit et al. 1997, Bonaventura 2000, Benoit et al. 2002a, Bénard 2003, Girard et al. 2005, Pinard et al. 2009). After applying an eigenmode analysis to identify the root of this spurious computational instability, a proper restructuration of the nonlinear terms relating the generalized buoyancy and pressure gradient is adopted to recover and enforce the hydrostatic balance in presence of steep topographic slopes. Additionally, a new energy-conserving frequency filter (Williams, 2011) is implemented to strengthen the SISL leapfrog scheme's numerical stability for long-term simulations of thermally stratified airflow over complex terrain.

Secondly, following Pinard et al. (2009) diagnosis of MC2's performance for cold-climate high-shear ABL flow over mountainous orography in the western Canadian Yukon Territory, the original wind-climate classification is examined in combination with the recently introduced numerical enhancements to assess the influence of thermal stratification for initializing real case simulations. As a result of several simulations employing different scheme combinations (Pham, 2012), the Brunt-Väisälä buoyancy frequency is added to account effectively for the initial climatological thermal stratification along with wind speed, direction and shear. For these steep terrain tests, the SLEVE vertical coordinate (Schär et al., 2002) is also employed to ensure smoother terrain-conforming grid levels aloft so the irregular surface signal do not propagate unnecessarily into the free atmosphere.

Thirdly, a specific adaptation of the Reynolds stress tensor with the corresponding metric transformations is implemented in the 3D turbulence parameterization scheme, aimed to integrate the corrected terrain-induced forcing considering MC2-LES employs a monotonic terrain-following vertical coordinate. This adaptation requires a detailed study of the staggered Arakawa C-type grid, to ensure the 3D gradients of prognostic and diagnostic variables are correctly computed. In the end, these changes enable the model to recognize the digital terrain signal that directly interacts with the wind in the momentum and energy multiscale transport processes. This last implementation is validated and discussed thoroughly in the framework of neutrally stratified ABL flow over both flat and steep terrain.

The main contributions of this research work are, firstly, the thorough assessment of the numerical instability and spurious noise generated by MC2 in presence of steep topography, along with a detailed verification and validation of the new semi-implit scheme's performance, as the proposed solution, for wind flow over both ideal and real terrain. Secondly, the implementation assessment of the Brunt-Väisälä frequency as the fundamental parameter that accounts for the influence of the thermal stratification in the new wind-climate classification. And, lastly, the development, implementation and detailed assessment of the metric transformations needed to adapt the Reynolds stresses and heat fluxes for terrain conforming grids used over steep slopes.

Supplementary model adaptations and enhancements were put in place, although these are not discussed in this thesis report. Amongst these, the main numerical modifications are:

1. A new suite of idealized cases to run verification and validation tests with isothermal and non-isothermal initially at-rest atmospheres, for diverse terrain configurations and multi-layer thermal stratifications (i.e., NOFLOW and NOFLOW-MLAY routines);
2. A special uncoupling of the pressure and temperature for neutrally stratified ABL tests, to ensure the momentum and energy calculations are calculated independently and without influencing each other. Namely, the Exner function is disabled through the local initialization routine in both the dynamical kernel and physical parameterization package;
3. A new version of the wall stress (calculated in the physical parameterization package), now expressed as a 3D function of the tangential wind modulus that includes the three velocity components as the flow conforms to the terrain slopes, ensuring the bulk aerodynamic formulation is adequately calculated;
4. An ideal analytical test initialized with polynomial temperature, pressure and velocity fields to verify that the metric terms are correctly introduced in the LES turbulent horizontal diffusion calculation for complex terrain (i.e., modified MICRO routine);
5. An adapted data postprocessing routine for ABL simulations over 2D and 3D terrain.

Thesis Overview and Structure

Chapter 1 of this work presents a comprehensive literature review of the state-of-the-art scientific knowledge of both the atmospheric flow phenomena (boundary layer dynamics, turbulence and diffusion mechanisms), CFD modelling techniques and the advancements on the numerical methods particularly applicable to geophysical non-hydrostatic compressible flow multiscale models. Then, the detailed numerical stability and noise control analysis accomplished with a new semi-implicit time discretization is presented in Chapter 2, which constitutes the fundamental enhancement to enable an efficient performance for thermally stratified wind simulations over high-impact topography. Extensive testing of the upgraded

model, based on stringent idealized cases, is discussed to prove that the proposed combined solutions are sufficiently robust and well suited to overcome these inherent issues.

An intermediate solution for wind-climate classification and thermally stratified ABL simulation initialization is discussed in Chapter 3, as a complement to the previous solutions. A strongly stratified ABL flow over real terrain is simulated, replicating the test reported in Pinard et al. (2009), for which a broad modelling error analysis is presented. Based on multiple model combinations and scenarios, a preliminary diagnosis of the numerical upgrades is drawn, revealing a promising reduction of the long-standing wind overestimation.

Chapter 4 presents the adaptation of the embedded LES method for terrain-induced turbulent forcing and diffusion calculation. After reporting a suite of canonical tests over both flat and moderately steep terrain compared with other similar models, focused on achieving a correct model setup and transition between the former and latest model versions, the interaction and influence of the new semi-implicit scheme on the LES turbulence modelling is examined with a neutral ABL flow simulation over the steep RUSHIL H3 ridge. The results are compared against both the experimental results and the UKMO mesoscale-LES model results. Based on the on-par outcomes obtained and the overall performance assessment, we arrived to the general conclusion that the MC2-LES multiscale model is indeed capable of attaining accurate high-resolution wind simulations over steep terrain.

CHAPTER 1

ATMOSPHERIC BOUNDARY LAYER FUNDAMENTALS AND MODELLING – CONCEPTUAL FRAMEWORK AND LITERATURE REVIEW

The Earth's atmosphere is a complex fluid system in which chaotic motions and transport phenomena take place. These physical complexities of the air mass circulation (wind) are described and analysed with a subdiscipline of the classical Newtonian fluid mechanics known as dynamic meteorology. The complexity of the atmosphere results from all the interactions between diverse physical processes acting at different space and time scales.

As the Earth receives the solar radiation its irregular surface exchanges heat with the air aloft, generating temperature variations and pressure differences that drive the wind with velocities and directions directly influenced by the interaction with the underlying orography and other planetary motions. At the same time, the wind displaces moisture and other tracers causing mass, momentum and energy exchange with the surrounding air masses and natural obstacles. Such dynamic transport phenomena are nonlinear in nature and, generally, occur in a coherent and multiscale fashion, which are fundamental characteristics of turbulent flow.

The atmospheric structure can be understood as the state of the air masses at different heights, which varies constantly due to changing weather conditions and solar activity. This vertical structure is usually divided into the following four macrolayers (Haltiner and Williams 1980, Stull 2000):

- Troposphere, $0 \leq z \leq 11$ km ;
- Stratosphere, $11 < z \leq 47$ km ;
- Mesosphere, $47 < z \leq 85$ km ;
- Thermosphere, $z < 85$ km .

In general terms, the forces that influence wind flow are the pressure-gradient force due to thermodynamic variations of the air masses, the Coriolis and centripetal apparent forces due

to the Earth's rotational effect, the friction or drag force due to the constraining effect of the surface's roughness and orographic irregularities. This influence can be characterized at different spatial and temporal scales, typically classified as (Stull, 2000):

- Synoptic scale, with length and time scales of $\sim 10^6$ m and several days, respectively;
- Mesoscale, with length and time scales of $\sim 10^2 - 10^6$ m and a few hours, respectively;
- Microscale, with length and time scales of $\leq 10^4$ m and a few minutes (or less), respectively.

Since the main atmospheric phenomena that affect the wind energy industry take place close to the Earth's surface, the scope of this study concentrates in the dynamical meteorology and numerical modelling of the atmospheric boundary layer (ABL) that is generated within the first 3 km of the troposphere. Nonetheless, let us not forget that the global wind circulations are connected to the surface winds through what is known as the entrainment zone, which allows the free atmosphere aloft and boundary layer to behave as a continuous medium. Namely, the entrainment zone is a transport layer of intermittent turbulence where the free atmosphere exchanges physical quantities with the top of the atmospheric boundary layer (Stull, 1988). Consequently, this work adopts a multiscale (meso-microscale) approach that covers a large part of the spectrum of wind motions, but mostly in the ABL.

1.1 Dynamics of the Atmospheric Boundary Layer (ABL)

The ABL comprises the first portion of the troposphere, extending from the Earth's surface to a height of $1-3$ km depending on the local climate conditions. The ABL, essentially, constitutes the zone where the surface directly and strongly influences the wind patterns through molecular viscosity and turbulent transport of physical quantities with timescales near to an hour or less. The Earth's differential surface absorption of solar energy during the day causes the diurnal and nocturnal cycles that, in turn, yield a deeper or shallower ABL. These transient processes are unique characteristics of the ABL, not necessarily felt by the rest of the atmosphere (Stull, 1988).

The ABL flow generally can be studied with directional separation of the physical phenomena. It is mainly, but not exclusively, dominated in the horizontal direction by the mean wind transport and in the vertical direction by turbulent transport. Mean or bulk flow is mainly responsible for horizontal advection of physical quantities, at a speed on the order of $1-10\ \mathrm{m\,s^{-1}}$. Although vertical mean wind is usually one or two orders of magnitude smaller than horizontal mean winds, the vertical velocity component can reach similar or higher magnitudes when the air masses exchange momentum and heat with underling complex topography (Holton, 2012). However, as the ABL interacts with the Earth's rough surface, turbulence becomes its dominant characteristic, generating 3D diffusion through rotational flow structures known as eddies (or vertical structures). These irregular swirls close to the surface, superimposed on each other and characterized with different length, time and velocity scales, are responsible for transfering the frictional forcing and heat transfer to the ABL's interior flow. The complete spectrum of life span, energy contents, and momentum flux rates of these eddies give the multiscale nature to the turbulent ABL flow.

The fundamental conservation laws of momentum (Newton's second law of motion), energy (first law of thermodynamics) and mass (continuity) govern the ABL fluid system. Defined in terms of the velocity ($\mathbf{v} = u\,\mathbf{i} + v\,\mathbf{j} + w\mathbf{k}$), static pressure (p), absolute temperature (T) and dry air density (ρ) fields, the conservation laws without mass exchange are written in flux form and Cartesian coordinates as (Stull 1988, Holton 2012):

$$\frac{\partial \rho \mathbf{v}}{\partial t} + \nabla \cdot (\rho \mathbf{v}\,\mathbf{v}) = \nabla \cdot \boldsymbol{\sigma} + \rho \mathbf{f}\,, \tag{1.1a}$$

$$\frac{\partial \rho T}{\partial t} + \nabla \cdot (\rho \mathbf{v} T) = \frac{k_T}{c_p} \nabla^2 T + \frac{p}{\rho} \frac{d\rho}{dt}\,, \tag{1.1b}$$

$$\frac{\partial \rho}{\partial t} + \nabla \cdot (\rho \mathbf{v}) = 0\,, \tag{1.1c}$$

where $\partial(\ )/\partial t$ represents the quantity's local rate of change, $\nabla\cdot\left[\rho\mathbf{v}(\ )\right]$ denotes the quantity's convective flux in conservative form, $\boldsymbol{\sigma}$ the second order stress tensor, $\rho\mathbf{f}$ the body forces (e.g. buoyancy, Coriolis force, external forcing, etc.), c_p the specific heat at constant pressure and k_T the thermal conductivity of dry air. In this scenario, the surface forces $\nabla\cdot\boldsymbol{\sigma}$ include both ∇p and $\nabla\cdot\boldsymbol{\tau}$ due to normal and shear stresses, respectively. Additionally, based on the Fourier's law for heat conduction, the thermal energy term is replaced by $Q=\left(k_T/\rho\right)\nabla^2 T$ in which we include the external heat sources. As explained later on this chapter, the absolute temperature is conveniently replaced by the potential temperature [$\theta = T/\pi = T\left(p_s/p\right)^{R/c_p}$] to underline the importance of thermal stratification on the shear-driven ABL. With the application of the ideal gas law valid for dry air ($p=\rho R T$), equation system (1.1) can be alternately redrafted in the advective form as (Stull 1988, Holton 2012):

$$\frac{d\mathbf{v}}{dt}=-\frac{\nabla p}{\rho}+\frac{\nabla\cdot\boldsymbol{\tau}}{\rho}-g\,\mathbf{k}+\mathbf{f}\,, \tag{1.2a}$$

$$\frac{d\theta}{dt}=\frac{Q}{c_p\pi}\,, \tag{1.2b}$$

$$\frac{d\rho}{dt}+\rho\left(\nabla\cdot\mathbf{v}\right)=0\,, \tag{1.2c}$$

where $d(\ )/dt=\partial(\ )/\partial t+\mathbf{v}\cdot\nabla(\ )$ denotes the material derivative operator, $g\,\mathbf{k}$ the gravitational force and $\pi=\left(p/p_s\right)^{R/c_p}$ the Exner function, with R as the gas constant for dry air and p_s as a reference standard pressure (generally fixed to 10^3 hPa or mbar). Based on the previous definitions, the heat redistribution term becomes $Q=\left(k_T p_0/R\rho^2\right)\nabla^2\pi^{c_p/R}$.

The complete set of equations (1.2) describes a highly complex nonlinear and unclosed mathematical system that is very challenging to solve with any numerical model. Therefore, in order to simplify its understanding and solution, different approximations are usually

employed, such that specific terms and associated processes (e.g. sound waves) are removed from the primary set of equations. The most common are (Stull 2000):

- The hydrostatic pressure approximation, which is based on the assumption $dw/dt = g$ and reduces the vertical momentum budget to a balance between the vertical pressure-gradient and gravity terms $\partial p/\partial z = -\rho g$. Scale analysis shows that this approximation is valid for synoptic scales, but it may fail for meso- and microscales less than 10^4 m. For this reason, it is preferable to perform ABL simulations with non-hydrostatic multiscale models for high resolution terrain cases;
- The Boussinesq approximation, which allows a decoupling of the density and pressure perturbations (ρ' and p', respectively) by retaining the former only in the alternative buoyancy term of the vertical momentum budget such that $b = g\rho'/\overline{\rho}$, along with the definition of the generalized pressure $P = \gamma_* R T_* \ln p'$, where $\gamma_* = g/c_p T_*$ and T_* denotes a reference basic-state temperature sounding (Haltiner and Williams, 1980);
- Flow incompressibility assumption, which is a consequence of negligible density variations of the stratified air masses subject to hydrostatic pressure. Then, the hydrostatic balance and the Boussinesq approximation allow the mass budget to become $\nabla \cdot \mathbf{v} = 0$. This is not applicable if the density field is intensely perturbed due to non-hydrostatic effects induced by microscale terrain. Then, the mass budget should account for density variations as a compressibility condition (cf. eqn. 1.2c);
- The Newtonian fluid assumption, which implies the viscous stresses are linearly proportional to the velocity gradients. Along with flow incompressibility, the friction forces can be expressed as $\nabla \cdot \boldsymbol{\tau} = \mu \nabla^2 \mathbf{v}$, where $\mu = \rho \upsilon$ represents the air's dynamic viscosity (Stull, 2000); and
- The geostrophic balance assumption, which occurs when the relative acceleration, nonlinear advection and friction terms are negligible in the horizontal momentum budget. It requires that the inertial and vertical friction forces are at least one order of magnitude smaller than rotation-induced Coriolis force, thus, resulting in the

geostrophic wind approximation $\mathbf{v}_g = \mathbf{k}\times(1/\rho f)\nabla_H p$ (with $f \equiv 2\Omega\sin\varphi$ denoting the Coriolis parameter, based on the Earth's rotational speed Ω and latitude φ).

- The f – plane approximation, which allows the variation of the Coriolis parameter to be neglected, and to assign the same value of f at particular latitude throughout the domain. This approximation can be visualized as a tangent plane touching the surface of the sphere at this latitude. In microscale modelling of the wind over topography, the f – plane approximation can be enforced since the Coriolis effect is negligible and does not provoke the effective rotation rate as in cyclones (Warner, 2011).
- The Monin-Obukov similarity, which is a generalization of the mixing length theory for non-neutral conditions employing the universal functions of the mean velocity and temperature as function of dimensionless height. By applying the Obukov length scale, the surface layer turbulence can be non-dimensionalized as a proponality measure of the relative contributions to turbulent kinetic energy from the buoyant and shear production rates.

Whenever needed, these assumptions can be enforced on the general system (1.2) to cast a resolvable subset of the Navier-Stokes (NS) equations for the ABL. For example, by applying the Newtonian fluid and geostrophic balance assumptions the resulting system for compressible non-hydrostatic flow is (Haltiner and Williams 1980, Stull 1988):

$$\frac{d\mathbf{v}}{dt} = -\frac{\nabla p}{\rho} + \upsilon\nabla^2\mathbf{v} - g\,\mathbf{k} - f\,\mathbf{k}\times\mathbf{v} + \mathbf{f}\,, \tag{1.3a}$$

$$\frac{d\theta}{dt} = \frac{Q}{c_p\,\pi}\,, \tag{1.3b}$$

$$\frac{d\ln\rho}{dt} + \nabla\cdot\mathbf{v} = 0\,. \tag{1.3c}$$

In most turbulent flow analysis the model variables ($\psi = u, v, w, p, \theta, \rho$) are usually separated into mean and fluctuating parts based on the Reynolds decomposition ($\psi = \overline{\psi} + \psi'$), where the

overbar $\bar{\cdot}$ represents the time average and the prime $\cdot'$ represents the instantaneous variation. This procedure allows the identification of important new terms such as the turbulent momentum fluxes, velocity variances and energy fluxes ($u_i' u_j'$, $u_i' u_i'$ and $\theta' u_j'$, respectively). To this effect, the NS system (1.3) can be redrafted in its expanded form using Einstein's tensor notation (i.e., $\mathbf{v} = u_i \, \mathbf{e}_i$) and the Reynolds averaging assumptions ($\overline{\psi'} = 0$, $\overline{\psi} = \overline{\overline{\psi}}$, $\overline{\partial}/\partial t = \partial/\partial t$ and $\overline{\partial}/\partial x_i = \partial/\partial x_i$) as the Unsteady Reynolds Averaged Navier-Stokes equations:

$$\frac{d\overline{u}_i}{dt} = -\frac{1}{\overline{\rho}}\frac{\partial \overline{p}}{\partial x_i} + \frac{1}{\overline{\rho}}\frac{\partial}{\partial x_j}\left(\mu \frac{\partial \overline{u}_i}{\partial x_j} - \overline{\rho u_i' u_j'}\right) - g\,\delta_{i3} - f\,\varepsilon_{ij3}\,\overline{u}_j + \overline{\mathrm{f}}_i\,, \tag{1.4a}$$

$$\frac{d\overline{\theta}}{dt} = \frac{\overline{Q}}{c_p\,\overline{\pi}} - \frac{1}{\overline{\rho}}\frac{\partial}{\partial x_j}\left(\overline{\rho\,\theta' u_j'}\right), \tag{1.4b}$$

$$\frac{d\ln\overline{\rho}}{dt} + \frac{\partial \overline{u}_i}{\partial x_i} = 0\,. \tag{1.4c}$$

Here δ_{ij} represents the Kronecker delta tensor and ε_{ijk} the third order permutation Levi-Civita tensor (Arfken et al., 2013). With the emergence of the turbulence induced Reynolds stress tensor ($\tau_{ij}' = \overline{\rho u_i' u_j'}$) and heat fluxes ($Q_j' = \overline{\rho \theta' u_j'}$), evidently, equation system (1.4) needs to be closed considering the parameterization of the twelve new variables (one for each Reynolds stress and heat flux component). As explained later in this chapter, these turbulent diffusion terms are frequently two or more orders of magnitude stronger than the molecular diffusion terms, which can then be neglected to simplify the model's equations (Blackadar 1997, Pope 2000). These concepts will be employed in the following subsections, modifying system (1.4) according to the physical or numerical principles required for the analysis.

1.1.1 Atmospheric Thermal Stratification and the ABL Structure

The dynamic behaviour and structure of the ABL is primarily controlled by its thermal stratification or density layering, which directly affects the wind and temperature profiles. Atmospheric thermal stratification, also known as static stability, is defined as the stability of

the atmosphere in hydrostatic equilibrium with respect to unsteady vertical displacements (Peppier, 1988). In general terms, the dynamical significance of thermal stratification results from the balance of kinetic and potential energies. In case of an updraft, an air parcel that is cooler than its surroundings at the same height or pressure is said to be negatively buoyant, or stably stratified, and will sink. If the air parcel is warmer it is said to be positively buoyant, or unstably stratified, and will keep rising. In case the air parcel reaches thermal equilibrium or has the same temperature with its new surroundings, i.e. has neutral stratification, it experiences zero buoyant force and remains motionless after an initial displacement (Holton 2012, Peppier 1988). For an ABL undergoing an adiabatic process, the first law of thermodynamics, previously introduced as equation (1.1b), relates the temperature and pressure in a differential logarithmic form such that:

$$c_p \frac{d\ln\theta}{dt} = c_p \frac{d\ln T}{dt} - R\frac{d\ln p}{dt}. \tag{1.5}$$

Here θ denotes the potential temperature of an air parcel at a given pressure, which represents the temperature it will acquire if brought isentropically to a standard pressure, usually taken as $p_s = 10^3$ hPa . As a consequence of the thermodynamic relation (1.5), every air parcel has a unique potential temperature, calculated with the following Exner equation for atmospheric adiabatic motions (Holton, 2012):

$$\theta = T\left(p_s / p\right)^{R/c_p}. \tag{1.6}$$

If the air parcel displacement is adiabatic, its potential temperature can be related to the corresponding frequency of buoyant oscillations N (also known as the Brunt-Väisälä frequency) by means of:

$$N^2 = -\frac{g}{\rho}\frac{d\rho}{dz} = \frac{g}{\theta}\frac{d\theta}{dz} = g\frac{d\ln\theta}{dz}. \tag{1.7}$$

In turn, N^2 is used as a measure of atmospheric thermal stratification, based on the following criteria (Stull 1988, Holton 2012):

- absolute instability when the $\partial\theta/\partial z < 0$ or $N^2 < 0$;
- absolute stability when $\partial\theta/\partial z > 0$ or $N^2 > 0$; and
- neutral equilibrium when $\partial\theta/\partial z = 0$ or $N^2 = 0$.

The diurnal and nocturnal cycles of radiative heating and cooling cause a daily cycle of thermal stratification in the ABL. Typically, unstable wind in the surface's vicinity is linked to light airflow over a warm surface (e.g., sunny day or mildly cold air over a volcano), and it rises up to heights of 5 km in a vigorous turbulent fashion. Characteristic stable winds, on the contrary, occur with light airflow over a cool surface (e.g., mountain breezes at night with clear sky), which result in shallow layers comprised within the first 20 to 500 m above ground level (a.g.l.) with very weak turbulence. In between these conditions, the neutrally stratified ABL is characterized with moderate to strong winds, little heating or cooling close to the surface, and prone to terrain-induced turbulence in adiabatic conditions (Stull 1988, Blackadar 1997).

When surface heating is strong during daytime, turbulent mixing and diffusion leads usually to a statically unstable mixed layer (ML); and during nocturnal cooling of the surface it turns into a statically stable boundary layer (SBL). The latter coexists with a nearly neutral residual layer (RL) that may contain remnant energy and tracers from the previous ML, but it is not very turbulent in nature (Stull, 2000). The wind speed and temperature of the well-mixed nearly homogeneous ML are ideally independent of height, which allows the ML to be presumed as a slab with constant velocity and potential temperature profiles. Additionally, the underlying surface layer (SL) is the ground-adjacent region where mechanical or shear generation of turbulence exceeds buoyant generation, and is assumed to be a constant flux layer based on the Monin-Obukhov similarity theory (Stull, 1988). Namely, the SL is a thin and viscous layer, where high velocity gradients, frictional drag, heat exchange, evapotranspiration from the soil and canopy, along with other physical processes, critically alter the wind mean speed, temperature and mass transport. However, turbulent stresses are relatively uniform with height, hence, allowing the SL to be treated theoretically as a constant

flux layer (Stull 2000, Holton 2012). This postulate holds well only for neutrally stratified ABL flow over flat terrain (Chow and Street, 2009).

Starting from the top of the SL, the turbulent momentum flux should vary linearly with height, indicative that the Reynolds stresses can be approximated with the conventional linear flux-gradient model. Over flat terrain, in terms of the horizontal velocity components and mean wind $\overline{U} = \left[u^2 + v^2 \right]^{1/2}$, respectively, the turbulent stresses and surface drag are estimated as (Holton, 2012):

$$\left(\overline{u'w'}\right) = -k_M \frac{\partial u}{\partial z}, \left(\overline{v'w'}\right) = -k_M \frac{\partial v}{\partial z}, \tag{1.8a}$$

$$\left(\overline{u'w'}\right)_s = C_d \left|\overline{U}\right| u, \left(\overline{v'w'}\right)_s = C_d \left|\overline{U}\right| v, \tag{1.8b}$$

where k_M denotes the eddy viscosity (variable depending of the position in the domain) and C_d is known as the non-dimensional drag coefficient of the SL, which height ranges between the first 20 to 200 m above the ground.

In presence of complex topography, as the slope increases the vertical transport becomes significant for the surface drag calculation, which requires the inclusion of the vertical velocity component for the mean speed, such that $\overline{U} = \left[\overline{u}^2 + \overline{v}^2 + \overline{w}^2\right]^{1/2}$. A comprehensive explanation of this modification in terms of the metric tensor transformations is provided in Appendix I of this work. Although this modification was included in a subroutine of the mesoscale compressible community (MC2) model, it has not been used yet in the validation simulations presented here. However, it will be the subject of a future study on how the correction for the surface drag calculation impacts the surface layer wind approximation.

1.1.2 Rotational and Topographic Effects on Stratified ABL Flow

The Earth's rotational influence on geophysical flow analysis is of great significance. This rotation affects the dynamics of the thermally stratified ABL flow over and around geographic obstacles that force and displace the air parcels in different directions. Taking the Earth's rotational framework with a constant angular velocity ($\mathbf{\Omega}$) and observing the air parcel's motion from a point fixed to the rotating reference with a distance based on the displacement vector ($\mathbf{r}$), the corresponding Coriolis and centrifugal forcing on the flow patterns are included in the equation of "horizontal" motion (i.e., $\mathbf{v} = u\,\mathbf{i} + v\,\mathbf{j}$) such that (Haltiner and Williams, 1980):

$$\frac{d\mathbf{v}}{dt} = -\frac{\nabla_H p}{\rho} + \upsilon\nabla^2\mathbf{v} - \mathbf{\Omega}\times(\mathbf{\Omega}\times\mathbf{r}) - 2\mathbf{\Omega}\times\mathbf{v}. \tag{1.9}$$

In most ABL geophysical scale analysis, the centripetal force $\mathbf{\Omega}\times(\mathbf{\Omega}\times\mathbf{r})$ becomes nearly negligible since it is balanced by the radial pressure gradient. Hence, it can be removed in an analogous fashion to the hydrostatic pressure that cancels the effect of gravitational forces. On the contrary, the effect of the Coriolis force is large compared with both the inertia of the relative motion and viscous action (i.e., $|\mathbf{v}\cdot\nabla\mathbf{v}| << |\mathbf{\Omega}\times\mathbf{v}|$ and $|\upsilon\nabla^2\mathbf{v}| << |\mathbf{\Omega}\times\mathbf{v}|$, respectively) (Holton, 2012). Expressing these quantities in terms of the length (L) and velocity ($\overline{U}$) scales, the Rossby and Ekman non-dimensional numbers are derived respectively as:

$$Ro = \overline{U}/\Omega L,\ Ek = \upsilon/\Omega L^2. \tag{1.10}$$

When the Rossby and Ekman numbers (i.e., ratios of inertial and viscosity forces to Coriolis forces, respectively) are relatively small, $Ro << 1$ and $Ek << 1$, the equation of motion (1.9) reduces to a balance between the Coriolis and horizontal pressure gradient forces, such that:

$$2\boldsymbol{\Omega}\times\mathbf{v}=-\frac{\nabla_H p}{\rho}, \tag{1.11}$$

which is best known as the geostrophic flow balance. As a resulting property, the Coriolis force is always perpendicular to the flow direction and, thus, the pressure is constant along the flow streamlines. Employing the Coriolis parameter $f\equiv 2\Omega\sin\varphi$, with φ as the Earth's azimuthal angle, this relationship defines the horizontal geostrophic wind ($\mathbf{v}_g$) as (Holton, 2012):

$$-f\,v\approx-\frac{1}{\rho}\frac{\partial p}{\partial x},\; f\,u\approx-\frac{1}{\rho}\frac{\partial p}{\partial y}, \tag{1.12a}$$

$$\mathbf{v}_g\equiv\mathbf{k}\times\frac{1}{f}\frac{\nabla_H p}{\rho}. \tag{1.12b}$$

To a first approximation in a more general manner, the horizontal momentum balance of the Coriolis force, horizontal pressure-gradient force and the turbulent momentum flux divergence that dominate the ABL dynamics are related by means of the reduced model:

$$f\left(\bar{v}-\bar{v}_g\right)-\frac{\partial\left(\overline{u'w'}\right)}{\partial z}=0, \tag{1.13a}$$

$$-f\left(\bar{u}-\bar{u}_g\right)-\frac{\partial\left(\overline{v'w'}\right)}{\partial z}=0. \tag{1.13b}$$

After solving these differential equations assuming the horizontal velocity components tend to reach at z_∞ the respective geostrophic wind components, and taking k_M as a constant eddy viscosity for the flux-gradients and the parametric constant $\gamma=\left(f/2k_M\right)^{1/2}$, the famous Ekman spiral solution is obtained (Holton, 2012), such that:

$$u=\left|u_g\right|\left(1-e^{-\gamma z}\cos\gamma z\right), \tag{1.14a}$$

$$v=\left|u_g\right|\left(e^{-\gamma z}\sin\gamma z\right). \tag{1.14b}$$

This horizontal velocity formulation does not apply to real ABL dynamics, but helps to estimate the balance between pressure gradient, Coriolis and turbulent drag forces. Applying a linear flux-gradient approximation for the constant momentum flux surface layer, by employing the so-called friction velocity $u_*^2 = \left|\left(\overline{u'w'}\right)_s\right| = \left(\kappa z\right)\left|\partial\overline{u}/\partial z\right|$ (surface momentum flux) with the von Kármán constant ($\kappa \approx 0.4$) and the aerodynamic roughness length (z_0), yields the following logarithmic wind profile:

$$\overline{U} = \frac{u_*}{\kappa}\ln\left(\frac{z}{z_0}\right), \tag{1.15}$$

based on the Monin-Obukov similarity, that is mostly valid for neutrally stratified and horizontally homogeneous ABL flow (Stull, 1998). Even though this formulation is very popular for microscale flow analysis and simulation of the SL, it might not apply correctly for stratified rotational flow over complex terrain (Brown et al. 2001, Churchfield et al. 2014).

The buoyancy frequency (N) and height scale (H) play similar roles to those of the angular velocity (Ω) and horizontal length scale (L). For wind in the lower atmosphere flowing over a topographic obstacle (e.g., a mountain range), the air masses are displaced vertically and require a supply of gravitational energy. Then, the thermal stratification will act to enhance or minimize such vertical displacements, forcing the flow to pass over or around the obstacle, respectively. The greater the restriction imposed on the vertical displacement, the greater the importance of thermal stratification, proportionality measured by the buoyancy Froude number with the ratio of the inertial to gravitational forces (Stull, 2000):

$$Fr = \overline{U}/NH\,. \tag{1.16}$$

Namely, if $Fr \le 1$, the stratification effects are important; the smaller Fr, the more important these effects are. Just as the Froude number is a measure of the vertical velocity in a stratified fluid, the Rossby number can be understood as a measure of the vertical velocity in a rotating

fluid. According to this analogy, the ratio of vertical convergence to horizontal divergence in the rotating ABL is given by Fr^2/Ro, which implies that when (Stull, 1988):

- $Fr^2/Ro \leq Ro$ thermal stratification controls vertical motions more than rotation and is the dominant process; and
- $Fr^2/Ro > Ro$ rotation controls vertical motions more than stratification.

Typically, the Froude-Rossby ratio approximates to $Fr^2/Ro \approx 10^{-4}$ and the Rossby number to $Ro \approx 10^2$, which implies that the ABL vertical motions over complex terrain are primarily affected by the atmospheric thermal stratification (Tritton, 1988). Nontheless, even though values of Ro may be large, the Earth's rotation may cause directional shear through the boundary layer.

As the stratified air masses pass a series of obstacles, the ABL depth is modified downwind in a nonlinear fashion mainly influenced by the terrain feature length scales, the buoyant and frictional forcings, and the turbulence diffusion. As the perturbed air parcels are imbedded in a stratified air mass flowing over an obstacle at a given mean wind speed ($\overline{U}$), it traces a wave oscillating with the natural wavelength defined as $l_N = 2\pi\overline{U}/N$. Therefore, the Froude number can be expressed as the ratio of this natural wavelength to the effective wavelength (i.e., $l_{eff} = 2a$, where a is the hill half-width) of the obstacle (Stull 1988, Tritton 1988):

$$Fr^{\oplus} = \frac{l_N}{l_{eff}} = \frac{\pi\overline{U}}{N\,a}. \tag{1.17}$$

For a strongly stable ABL with $Fr^{\oplus}$ lower than a unity, the air flows around the obstacle instead of over it. Namely, for cold heavy winds, the air is usually blocked upwind of the obstacle and forced to move around this blockage. On the contrary, for a weakly stable ABL with $Fr^{\oplus}$ close or equal to a unity, the lighter but slow air parcels distribute both around and over the terrain obstacle, sometimes causing some short wavelength flow separation

downwind. As the $Fr^{\oplus}$ reaches values higher than a unity, the wind becomes stronger close to the surface and tends to separate earlier with a natural wavelength that matches the size of the obstacle. Accordingly, large-amplitude lee wave propagation and boundary layer separation combines in the lee-side, where flow reversal and recirculation takes place. The downstream flow separation creates a cavity due to flow recirculation, characterized with a natural wavenumber longer than the topographic dimensions, i.e. $l_N > l_{eff}$ (Tritton 1988, Cushman-Roisin and Beckers 2011).

The Froude number can also be formulated as function of the local terrain height z_{hill} and the thermal inversion capping layer at the ABL top (z_i), such that:

$$Fr^* = \frac{\overline{U}}{N\left(z_i - z_{hill}\right)}. \tag{1.18}$$

Yet again, for a deep ABL with a slightly stable or unstable stratification (i.e., $z_i >> z_{hill}$ and $Fr^* << 1$), the capping layer is drawn down over terrain features due to energy conservation and the wind descends the downslope lee-side of the mountains with some recirculation sprouting intermittently. If the ABL has stable stratification with a moderately deep capping inversion (i.e., $z_i > z_{hill}$ and $Fr^* \cong 1$), the air masses are displaced swiftly into the mountain's lee-side prompting a chaotic flow phenomenon known as downslope windstorm. Frequently, this airflow undergoes a hydraulic jump to compensate the abrupt potential to kinetic energy conversion. On the other hand, for a shallow boundary layer with a strongly stable stratification (i.e., $z_i \leq z_{hill}$), the air masses are constrained to flow around the terrain obstacles shedding what is commonly called lee-side von Karman vortices (Stull 1988, Cushman-Roisin and Beckers 2011). The review on the ABL modelling over complex terrain will be presented in Sections 1.2.4 and 1.2.5 of this work.

1.1.3 Turbulence and Diffusion in Stratified ABL Flow

Turbulence encompasses a large spectrum of complex, chaotic, irregular and rather unpredictable fluid motions or vortices. After several decades, the scientific community has not yet arrived to an unambiguous, consistent and universal definition of this phenomenon, given the enormous number of degrees of freedom for real-world flows. Particularly, for the ABL it is a challenging exercise to separate turbulence from other coexisting flow features, such as waves and large-scale circulations associated with weather patterns (Pope, 2000).

Although no absolute definition of turbulence is available, the following set of attributes and laws have been widely accepted to describe this phenomenon as (Tennekes and Lumley 1972, Stull 1988, Long 1997, Pope 2000, Davidson 2015):

- Highly irregular, reason why turbulence analysis is traditionally treated statistically rather than deterministically;
- Stochastic and unsteady, which implies that part of the process happens randomly and requires an analysis of a nonlinear initial state of the fluid;
- Three-dimensional and rotational, since the non-zero vorticity plays an important role in what is know as eddy stretching due to the conservation of angular momentum;
- Physically coherent and multiscale, as turbulent motions of multiple scales are substantially interrelated and interdependent in a nonlinear fashion;
- Dissipative and with high Reynolds number, as the inercia dominates viscosity; and
- Highly diffusive, since turbulence is a very effective mechanism for accelerating mixing and enhanced transport of physical quantities within the fluid.

In 1941, Andrey Kolmogorov contributed with a widely used conceptual framework to explain the turbulence phenomenon. The effectiveness of turbulence for transporting flow quantities relies on the intimate nonlinear interactions of large-scale energy containing eddies with small-scale energy dissipating eddies. The characteristic turbulent energy transfer between large to small flow structures is know as the Kolmogorov turbulent energy cascade, illustrated in Figure 1.1. The main Kolmogorov hypothesis states that the turbulent energy cascade arises from

macroscale-generated vortices that absorb a significant amount of kinetic and thermal energy from its surroundings and transfer it progressively to microscale flow structures, which dissipate or convert the mechanical energy to thermal energy through molecular friction due to viscous stresses (Tennekes and Lumley, 1972).

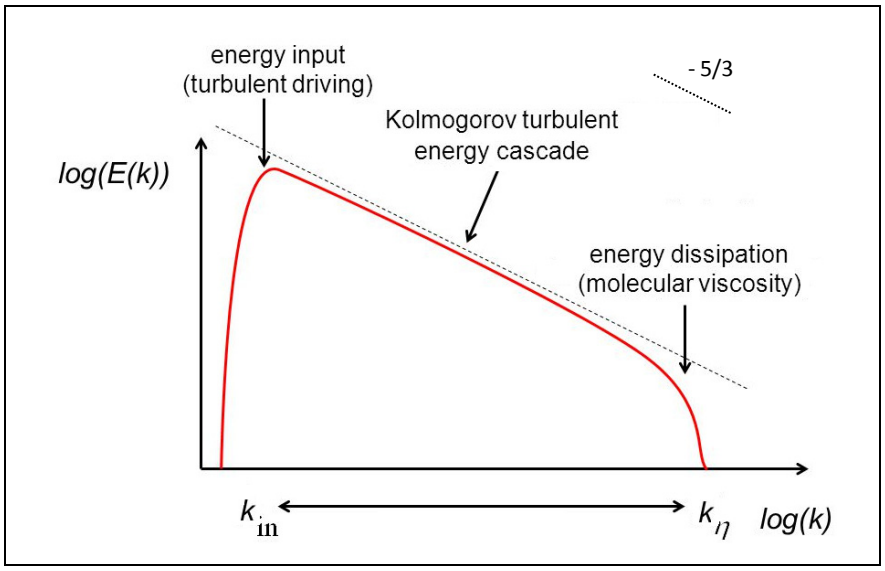

Figure 1.1 Energy spectrum of a well-developed turbulent flow

Here $E(k)$ denotes the energy spectrum (function of the wavenumber), k represents the wavenumber of a respective eddy length scale, k_{in} the low wavenumbers for large-scale inertial motions and k_{η} the high wavenumbers for fine-scale motions.

Turbulence is essentially caused by a chain of instabilities in high Reynolds number ($\mathrm{Re} = u \cdot L/\upsilon$) flows, which overcomes the damping effect of the fluid's viscosity (υ). This translates into Kolmogorov's idea that for very high Reynolds number the fine-scale turbulent motions are statistically steady, homogeneous and isotropic (i.e., that appear to be unchanging in time, uniform in space and with no preferential spatial direction) while the macroscale structures are not isotropic (i.e., anisotropic), since the latter are determined by particular geometrical features of the boundaries. All eddies of a given size characterized by a length

scale (l_0) are assumed to behave similarly and to share the same characteristic velocity scale (u_0) (Pope 2000, Davidson 2015).

The rate of energy transfer (ε) between scales must be the same for all scales, so that the energy level do not fluctuate significantly over time for a particular group of eddies sharing the same characteristic scales. In this context, flow structures of the same size are universally determined with a velocity scale mathematically dependent on the length scale and energy cascade rate as $u_0 = f(l_0, \varepsilon)$. By applying dimensional analysis, the Kolmogorov's turbulence theory also defines the smallest isotropic eddies to be uniquely determined by the kinematic viscosity (υ) and rate of energy transfer (ε), which results in what is known today as the Kolmogorov scales of length (η), time (τ) and spin velocity (ν):

$$\eta = \left(\upsilon^3/\varepsilon\right)^{1/4},\ \tau = \left(\upsilon/\varepsilon\right)^{1/2},\ \nu = \left(\upsilon\varepsilon\right)^{1/4}. \tag{1.19}$$

The unique η length scale is in the order of $10^{-4} - 10^{-3}$ m, and relates to l_0 and to a Reynolds number on the order of unity (Tennekes and Lumley 1972, Davidson 2015). Correspondingly, the lowest and highest wavenumbers are given by $k_{in} = \pi/l_0$ and $k_\eta \sim \varepsilon^{1/4}\upsilon^{-3/4}$, respectively. The energy spectrum turns to be a power law formulation such as:

$$E(k) = B\,\varepsilon^{2/3}\,k^{-5/3},\ \frac{3}{2\pi^{2/3}}B = \frac{1}{2}A^2, \tag{1.20}$$

where A and B are dimensionless constants determined experimentally that approximate respectively to $A \approx 1.45$ and $B \approx 1.5$ (Tennekes and Lumley, 1972). This $-5/3$ decay law predicted by Kolmogorov's theory is expected to apply well in the inertial range (i.e., $10^{-4} < k\,\varepsilon^{-1/4}\,\upsilon^{3/4} < 10^{-1}$), for those eddy length scales that are remote from both largest and shortest scales. The higher the Reynolds number is for the flow, the broader the span of wavenumbers over which this power law is applicable. Despite the success of the $-5/3$ power

law, with considerable experimental evidence that supports it, some have questioned its application for thermally stratified and rotating flows due to its statistical self-similarity and scale-invariant assumptions, and have proposed an alternative -2 power law instead (Pao 1967, Long 1997, Warner 2011).

Atmospheric turbulence can then be understood as a physically coherent movement of air parcels by multiscale swirls of motion (eddies or vertical structures) ranging in the order of $10^{-3} - 10^{3}$ m. Consequently, these superimposed vortices on the mean motions are responsible for transporting the excess linear and angular momentum and kinetic energy through the ABL. The flow's turbulent intensity ($TI = \sigma_U / \overline{U}$, function of the velocity standard deviation σ_U) is considered the ratio of energy associated with coherent variations of velocity and other quantities to that of quasi-steady laminar or mean motions. In other words, it measures the dominant dispersion of the fluctuations superimposed on a measured signal of flow quantities. The net effect of atmospheric turbulence is to mix air parcels from different initial locations. As turbulence tends to homogenize the ABL, potential temperature, velocity and other quantities gradually become mixed towards a uniform state. Thus, the amount of mixing varies with time and location as the turbulent intensity changes (Pope, 2000).

The process by which physical quantities in a fluid are displaced from one location to another under the action of chaotic turbulent fluctuations is known as turbulent diffusion or dispersion (Davidson, 2015). The pace at which diffusion proceeds in each spatial direction depends fundamentally on the value of the diffusion coefficients or diffusivities $\left(k_i, i = 1,2,3\right)$, which inherently results form the product of the turbulence length and velocity scales $k_i = l_0 \, u_0$; i.e. in terms of dimensions $\left[k_i\right] = L^2 \, t^{-1}$. A diffusive flux is proportional to the gradient of the quantity's concentration (C). When considering the variation of C over larger scales, those for which the eddy-size appears to be small, the 3D turbulent diffusive flux ($D_{C,i}$) of this fluid property may be approximated as (Pope 2000, Warner 2011):

$$D_{C,i} = k_i \frac{dC}{dx_i}. \tag{1.21}$$

This process depends intrinsictly on the local gradient hypothesis, since the diffusion rate is defined only at those special scales at which the concentration is quantified. Then, in the limit of an infinitesimal control volume (with $k_i = k_x$, k_y and k_z as the 3D eddy diffusivities), the transport-diffusion of the quantity's concentration can be expressed as:

$$\frac{dC}{dt} = \frac{\partial}{\partial x}\left(k_x \frac{\partial C}{\partial x}\right) + \frac{\partial}{\partial y}\left(k_y \frac{\partial C}{\partial y}\right) + \frac{\partial}{\partial z}\left(k_z \frac{\partial C}{\partial z}\right). \tag{1.22}$$

Usually, the vertical local gradient dominates the diffusion process, although horizontal local gradients can contribute directing a transport quantity in a particular direction. This is the basis of the eddy viscosity (k_M) concept, widely used in turbulence modelling. Eddy viscosity is a property of the flow state not of the fluid, and becomes greater as the flow's turbulence intensifies. This exchange coefficient is of the order of $1\,\mathrm{m^2 s^{-1}}$, at the Reynolds number of interest, or one hundred thousand times the molecular viscosity ($k_M >> \upsilon$). In an analogous way, the eddy conductivity (k_T) is a property of the flow that measures the thermal energy diffusion capacity in turbulent flows, and is generally two or three orders of magnitude higher than molecular conductivity (k). For both molecular and turbulent diffusion processes, the proportionality of their respective mechanical and thermal exchange coefficients is related with the Prandtl ($\mathrm{Pr} = c_p \mu / k$) and turbulent Prandtl ($\mathrm{Pr}_t = k_M / k_T$) numbers (Pope, 2000).

Ultimately, the source of atmospheric turbulence depends mainly on the velocity and temperature of the surface layer. For an unstable ABL, turbulence is primarily generated by natural convection or buoyancy, whereas, for a stable ABL the turbulence production is associated with shear-induced instability. Their contribution in the rate of turbulence generation can be symbolically formulated in the evolution equation of the turbulent kinetic

energy $K = \overline{u_i' u_i'}/2$ (denoted here as K, but frequently as TKE elsewhere in literature (Blackadar 1997, Cushman-Roisin and Beckers 2011, Holton 2012):

$$\frac{dK}{dt} = P_B + P_S - \varepsilon - TR\,. \tag{1.23}$$

Here P_B represents the rate of buoyant turbulence production arising from intermittent thermals and convective eddy overturning, P_S is the rate of shear turbulence production due to mechanical work of large and medium-scale flow structures, ε denotes the energy dissipation rate involving molecular friction of small-scale turbulent structures and TR represents the rate of K spatial redistribution by turbulence (which does not contribute to production or dissipation).

In general terms, for the thermally stratified turbulent ABL flow, the buoyancy and shear production terms are formulated respectively as:

$$P_B \equiv \overline{w'\theta'}\left(\frac{g}{\theta}\right), \tag{1.24a}$$

$$P_S \equiv -\overline{u'w'}\left(\frac{\partial \bar{u}}{\partial z}\right) - \overline{v'w'}\left(\frac{\partial \bar{v}}{\partial z}\right). \tag{1.24b}$$

and the proportionality of their contributions to turbulence emergence is measured with the flux Richardson number ($Ri_f \equiv -P_B/P_S$), which can be estimated either with the gradient Richardson number ($Ri = \mathrm{Pr}_t\, Ri_f$) or the bulk Richardson number (Ri_b) (Warner, 2011):

$$Ri \cong \frac{N^2}{\left(\partial \bar{u}/\partial z\right)^2}\,, \tag{1.25a}$$

$$Ri_b \approx \frac{(\rho_2 - \rho_1) g H}{\bar{\rho}(u_1 - u_2)^2}\,. \tag{1.25b}$$

If $Ri < 0$ the ABL is statically unstable and turbulence is sustained by thermal convection, on the contrary, if $Ri > 0$ the ABL is statically stable and turbulence should be generated by wind shear, as expected close to Earth's surface. If $Ri = 0$ the ABL is neutrally stratified and usually is prone to terrain-induced turbulence. Field experiments support that only if $Ri < 1/4$ the mechanical production will be strong enough to dominate the turbulence emergence for stably stratified shear flow. Thus, the condition for which the strongly stable stratification supresses turbulence sufficiently so that the flow becomes laminar is known as the critical Richardson number, i.e. $Ri_c \approx 1/4$ (Haltiner and Williams 1980, Stull 1988).

With all these concepts in mind, the importance of numerical modelling of turbulent ABL flows is highlighted to obtain an approximate realization of their physical behaviour and accurately characterize the time-evolving features of the inherent transport phenomena.

1.2 Numerical Modelling of Stratified ABL Flow over Complex Terrain

With the electronics and computer revolution experienced since the mid-twentieth century, the field of high-performance CFD has been increasingly transformed into a demanding scientific discipline, in which researchers are devoted to develop "ice-breaking" numerical methods, problem-specific codes and advanced post-processing techniques. The capabilities of each numerical solver for partial differential equations are diverse with respect to the dynamical and physical models, grid generation and post-processing of the results. However, none of these milestone novelties has fully succeeded the precise prediction or realization of turbulent flows, which is by far too complex to be completely characterized with any particular method.

Multiple spatial and time discretization, physical parameterization, numerical approximation and initialization schemes have been implemented, intensively tested, compared, enhanced and validated over the past 50 years. These efforts have paved the way to achieve a better understanding and prediction of turbulent flows, but a basic and stiff constraint persists. While the equations of motion can be applied directly to turbulent flows, the CFD models most appropriate for this application would need an exceedingly small grid spacing, and there would

still be eddies that would not be resolved on the model grid. The effects of these subgrid eddies are yet to be accounted for in some way, which usually is based upon a statistical approach to eddy effects. Namely, it is clear that for a pseudo-complete description and prediction of turbulent flow, the grid spacing (implicit filter) or explicit filter size employed should not go beyond the length scale of the smallest turbulent eddy (η). For a 3D simulation, the grid size needed to account for the smallest eddies should be on the order of $\mathrm{Re}^{9/4}$ or in the range of $10^9 - 10^{12}$ grid points (Pope 2000, Zikanov 2010).

Thus, amongst all the numerical approaches developed up to this date, the Direct Numerical Simulation (DNS) and Large-eddy Simulation (LES) techniques replicate the closest realization of turbulent flow patterns, DNS being the most precise since it solves the Navier-Stokes equations without modelling modifications or assumptions. Nonetheless, the overwhelming requirement for accurate DNS approximations of flow features with very fine grid stepping leads to large computational grids when the Reynolds number exceeds 10^4. On the contrary, the LES approach is able to represent transient flow phenomena by applying spatial filtering on the prognostic variables, yielding an accurate realization of large and medium size flow features without an unrealistic large grid. Reynolds Averaged Navier-Stokes (RANS) technique is also widely used and accepted, although it recasts the turbulence transient evolution only based on mean flow quantities, hence, corresponding to the expectations of these characteristics that could be obtained after averaging over several realizations (Moin and Mahesh 1998, Stensrud 2007, Davidson 2015). Many RANS studies can be based on steady state and/or 2D realizations, while LES is inherently time-dependent and 3D.

Although the LES does not provide a description of the full spectrum of motions that DNS permits (due to its inherent modelling error of the small scale approximation), and may demand a slightly higher computational overhead than RANS depending on the desired accuracy, it occupies an intermediate position with balanced capabilities for predicting sufficient turbulent fluctuations for practical scientific computations. Additionally, the RANS-LES hybrid approach, proposed by Spalart and other researchers (Strelets 2001, Spalart 2009, Bechmann and Sørensen 2010, Cabezón 2013), takes advantage of the time-averaged modelling for mean

statistics of the wall-bounded flow carried out with RANS and the filtered large-scale resolved flow's interior obtained with LES. The hybrid RANS-LES modelling method, also known as detached eddy simulation (DES), merges both mean statistics and low-pass-filtered large-scale resolved structures to reproduce the turbulent flows at high resolution.

These methods are applicable both separately or combined for general-purpose engineering-type flow analysis and atmospheric flow research. Particularly, for ABL turbulence parameterization, column models and RANS $K-$ models have been historically preferred (Gasset, 2014). Different first and second-order closure schemes based on turbulent kinetic energy (K), dissipation (ε), specific dissipation (ε/K), turbulent length scale (l) and time scale (τ), fluctuating transverse velocity (v'), pressure-strain correlations and other Reynolds stress relations have been implemented successfully and appear to be well-suited for mesoscale simulations (e.g. $K-\varepsilon$ SST, RNG $K-\varepsilon$, $K-\omega$ SST, $K-\omega^2$, $K-\varepsilon-\omega$, $K-l$, RSM, ASM, etc.). Nonetheless, the LES models have gained significant attention and appreciation for microscale simulations, since they are more versatile, comprehensive and just slightly more computationally demanding with parallelized codes than RANS $K-$ models (Wilcox 2006, Bechmann et al. 2011, Bengston 2015, Breton et al. 2017). Then, imbedded LES methods in mesoscale solvers seem a logical and bright combination to enable multiscale capabilities. In this scenario, a distinctive imprint of the coupled mesoscale-LES method is given by the interaction between the numerical solution method and subgrid scale (SGS) parameterization scheme (e.g. standard or dynamical eddy-viscosity models, standard or unsteady RANS models, scale-dependent or scale-invariant models, algebraic or spectral reconstruction models, etc.) (Germano et al. 1991, Lilly 1992, Mason and Thompson 1992, Porté-Agel et al. 2000, Meneveau and Katz 2000, Ding et al. 2001, Chow et al. 2005, Sumner et al. 2010, Dellwik and Arnqvist 2014, Yu et al. 2017).

1.2.1 Coupling Large-Eddy Simulation (LES) with Mesoscale Modelling

Because the LES computational domain usually spans over a limited area, it must obtain its lateral boundary conditions from observations, analyses or larger-model grids with resolutions

on the mesoscale. In this sense, a coupled mesoscale-LES model can operate with constant or variable boundary conditions, depending on large-scale flow evolution for the problem under examination. Also, initial conditions are typically prescribed from relatively smooth and horizontally uniform fields to allow microscale forcing to develop from local orography and vegetation features. In many cases distinct models simulate independently the meso- and microscale structures, thus, allowing a one-way coupling interaction. On the contrary, there is a two-way scale interaction within modern coupled mesoscale-LES methods, where the dynamical core can run as a regular mesoscale model with inner grids using LES closures and outer grids using standard mesoscale closures (Wyngaard 2004, Sumner and Masson 2010, Bechmann et al. 2011, Warner 2011).

A significant issue with the mesoscale-LES boundary conditions is that the inflow boundary is generally defined by an atmosphere for which the turbulence is parameterized, as the motions unresolved by the model are treated with a subfilter-scale (SFS) closure. If the buffer zone between nested grids is not large enough, the microscale processes will not spin-up sufficiently as the bulk airflow enters the central region of the grid (Cushman-Roisin and Beckers, 2011). Hence, no resolved microscale turbulent structures are considered to enter the LES grid, and because of the short residence time of the airflow within those grid cells there may not be sufficient time for realistic turbulence to develop before the air exits the outflow boundary. This discussion is intimately related to Wyngaard's pioneering analysis (Wyngaard, 2004), which clearly states there is still no sufficient consensus on how to apply multiscale modelling that achieves spatial-filter scales within the part of the spectrum containing the turbulent energy (i.e. the terra incognita). There is always a trade-off between the mesoscale long wavelength grid size (for which turbulence is clearly unresolved) and the required LES short wavelength spatial filter size sufficiently small to capture the flow structures exchanging turbulent kinetic energy (TKE) within the inertial range.

Another important situation-dependent aspect to consider in coupled mesoscale-LES methods is the sensitivity of the LES model solution to errors carried by lateral boundary conditions from the mesoscale results. For example, overestimated wind speeds may not impact significantly on the forecast of sensible weather, but it affects adversely the initial and

boundary conditions of the LES microscale model. Although the aim of this study is to benefit from the important advantages of mesoscale-LES coupling, it must be understood there could be negative influences on the results attributed mainly to (Durran 2010, Warner 2011, Dellwik and Arnqvist 2014, Bengtsson 2015):

- Low resolution of mesoscale data, that impacts the interpolated boundary conditions;
- Errors in the mesoscale data, arising from the quality of the data assimilation methods, poor numerical noise control, physical parameterization inconsistencies, etc.;
- Lack of interaction between small and large scales, which may occur when there is only one-way communication from mesoscale to LES nested grids, or due to limited energy backscatter;
- Subfilter scale modelling errors in partitioned models, in terms of space and time discretizations, coordinate systems or numerical solution schemes that may cause spurious gradients and feedbacks; and
- Noise generation due to nonphysical inertia-gravity modes that may mix with meteorological solutions, and grow exponentially quickly causing floating-point overflow conditions that halt the model computations.

Solutions for each of the limitations stated above, except for the last one, have been adopted to some extent in previous studies for the mesoscale-LES method used and exanimated within the present work (Girard et al. 2005, Gasset et al. 2014). Our effort will concentrate, not entirely though, on the implementation of a new semi-implicit time discretization for mesoscale modelling to remove the inherent spurious computational mode and terrain-induced noise in presence of steep slopes, ensuring the best possible quality of the imbedded large-eddy simulation method. This is performed considering the important advantages of mesoscale-LES coupled capabilities in engineering applications, such as (Warner, 2011):

- Better understanding of microscale atmospheric turbulence, that can lead to improved numerical parameterizations of the ABL physical phenomena;
- More insightful study of wind turbine siting over complex terrain to maximize the wind power harvest, as well as to minimize the turbulent loading on the generator;

- Wake turbulence analysis obtained for specific types of structures (e.g. buildings or wind turbines) that allow safe spacing to reduce turbulent loading or shadowing, as well as wind farm array interactions;
- More precise modelling of transport phenomena within urban sites, to prevent hazardous gases, aerosols or light pollutants to diffuse from a transportation or industrial accident.

In the context of turbulent ABL flow modelling over topography, the conventional requirement for a successful mesoscale-LES implementation is the appropriate realization of the neutrally stratified flow over a homogenous flat surface, achieving the constant-flux similarity within the surface layer and the equilibrium of all scales across the domain. Once this is achieved, it is necessary to replicate the expected flow features accounting for rotational, thermal stratification and terrain-induced effects over heterogeneous surfaces, which comprises complex orography as well as variable land use, surface cover, local weather, etc. This implies the use of suitable discretization and solution schemes, turbulence parameterization, boundary conditions and computational grid. Numerically reproducing the equilibrium of the TKE production and its dissipation rate for neutrally stratified flow over flat or complex terrain has proved to be a difficult task mostly near solid boundaries (Maurizi 2000, Dalpé and Masson 2008, Sumner and Masson 2010, Brasseur and Wei 2010).

1.2.2 The Mesoscale Compressible Community (MC2) Model

The present study is centered on the numerical enhancement of the Canadian mesoscale compressible community (MC2) model, which is a fully elastic non-hydrostatic flow solver employed for multiscale atmospheric research and limited-area forecasting. The MC2 numerical schemes, as for other contemporary models (e.g. WRF, COAMPS, RAMS, Meso-NH, etc.), have advanced over the past four decades based on multiple contributions of the atmospheric modelling community aiming to study meso- and microscale phenomena. As most environmental models, MC2 is divided in two modules: the dynamical kernel (needed to solve the main terms of the conservation equations) and the physical parameterization package (to

obtain modelling tendencies of turbulence, radiation, evaporation, precipitation, shallow convection, cloud cover, orographic drag and other microphysical processes).

Detailed explanations of the MC2 dynamics module are presented in Robert et al. (1985), Tanguay et al. (1990), Laprise et al. (1997), Benoit et al. (1997), Thomas et al. (1998), Benoit et al. (2002), Girard et al. (2005), Gasset et al. (2014), which describe its evolution from the earlier version of André Robert's semi-Lagrangian (SL) advection scheme implementation in a semi-implicit (SI) limited-area hydrostatic model used to solve primitive equations, to an extended and parallelized version of the SISL method in a non-hydrostatic framework to solve the fully compressible Euler equations (EE) with a terrain-conforming oblique vertical coordinate. The modern version of MC2 employs a non-symmetric generalized conjugate-residual iterative solver, known as the Generalized Minimal Residual (GMRES) algorithm, that treats the horizontal pressure gradient cross-derivative terms implicitly to control better the intrinsic instability. Despite its sophistication, the MC2 dynamical kernel still presents numerical instability that arises in presence of finescale terrain slopes (Thomas et al. 1998, Benoit et al. 2002, Girard et al. 2005).

MC2 is supplemented with the RPN (i.e., *Recherche en Prévision Numérique*) physical parameterization package, which was originally designed separately and then connected by an interpolation interface to its dynamical kernel (Benoit et al. 1997, Thomas et al. 1998, Girard et al. 2005). The RPN physics module provides the modelled tendencies for velocity, temperature, humidity, cloud water content and other fields that are added as source or sink terms in a fractional-step manner to the corresponding results of the dynamics kernel. Since this physics module was conceived for macroscale processes, a horizontal homogeneity assumption is applied on the parameterizations, thus, calculating primarily the vertical transport of these tendencies (customary of column-type models). The two numerical partitions, i.e. dynamics and physics, also have their own space and time discretization and boundary conditions, which require a careful implementation to obtain consistent horizontal and vertical terms for 3D computations (Gasset 2014, Gasset et al. 2014).

In the MC2 dynamical kernel, equation system (1.3) is simplified by eliminating density with the gas state equation such that (Thomas et al. 1998, Girard et al. 2005, Gasset 2014):

$$\frac{d\mathbf{v}}{dt} + RT\nabla q + g\mathbf{k} = -f\,\mathbf{k}\times\mathbf{v} + \upsilon\nabla^2\mathbf{v} + \mathbf{f}\,, \tag{1.26a}$$

$$\frac{dT}{dt} - \frac{RT}{c_p}\frac{dq}{dt} = \frac{Q}{c_p}\,, \tag{1.26b}$$

$$\left[1 - \frac{R}{c_p}\right]\frac{dq}{dt} + \nabla\cdot\mathbf{v} = \frac{Q}{c_p T}\,. \tag{1.26c}$$

Here $q = \ln(p/p_0)$ and p_0 is a reference pressure. Although the present work considers no external forcing or heat sources, $\mathbf{f}$ and Q are retained to provide the general formulation of the model NS equations. Neglecting the viscous effects in (1.26) yields the Euler equations (EE), which the MC2 dynamics module solves by applying the semi-implicit semi-Lagrangian (SISL) method presented in Thomas et al. (1998) and Girard et al. (2005). To achieve a proper application of the SISL scheme, the advection and linear terms are treated differently from nonlinear and source terms by linearizing the EE about a basic state (e.g., T_* that denotes a reference temperature sounding). Choosing an isothermal basic state leads to terms related with constant coefficients, contrary to a non-isothermal basic state sounding that yields variable coefficients.

The prognostic thermodynamic variables of temperature and pressure are replaced by their respective perturbations, i.e. $T' = T - T_*$ and $q' = \ln(p/p_*)$, such that the resulting equations are reformulated in terms of the buoyancy ($b = gT'/T_*$) and generalized pressure $\left(P = RT_* q'\right)$. Although the potential temperature could be used to cast MC2 kernel equations, the buoyancy allows a more consistent calculations for the semi-Lagrangian scheme (Caya and Laprise, 1999). By using $N_*^2 = g\,\partial \ln T_*/\partial z + g^2/c_p T_*$ and $c_*^2 = \left(c_p/c_v\right)RT_*$ as the square of the

reference buoyancy frequency and speed of sound, respectively, equation system (1.26) turns into (Girard et al. 2005, Gasset 2014):

$$\frac{d\mathbf{v}}{dt}+\nabla P-b\,\mathbf{k}=-f\,\mathbf{k}\times\mathbf{v}-\frac{b}{g}\nabla P+\upsilon\nabla^2\mathbf{v}+\mathbf{f}\,, \tag{1.27a}$$

$$\frac{d}{dt}\left[b-\frac{N_*^2}{g}P\right]+N_*^2\,w=-\frac{R}{c_v}b\,\nabla\cdot\mathbf{v}+\frac{N_*^2}{g}\left[\frac{c_v\,g+c_p\,b}{c_v\left(g+b\right)}\right]Q\,, \tag{1.27b}$$

$$\frac{1}{c_*^2}\frac{dP}{dt}+\nabla\cdot\mathbf{v}-\frac{g}{c_*^2}w=\frac{N_*^2}{g}\left(\frac{1}{g+b}\right)Q\,. \tag{1.27c}$$

Since heat sources are generally taken as negligible in the mass conservation equation, the energy equation is also simplified because it is originally obtained relying on the mass conservation (Thomas et al. 1998, Gasset 2014). Additionally, based on scale analysis, the contribution of molecular friction compared to turbulent diffusion is also neglected, yielding the MC2 model equations:

$$\frac{d\mathbf{v}}{dt}+\nabla P-b\,\mathbf{k}=-f\,\mathbf{k}\times\mathbf{v}-\frac{b}{g}\nabla P+\mathbf{f}\,, \tag{1.28a}$$

$$\frac{d}{dt}\left[b-\frac{N_*^2}{g}P\right]+N_*^2\,w=-\frac{R}{c_v}b\,\nabla\cdot\mathbf{v}+\frac{N_*^2}{g}Q\,, \tag{1.28b}$$

$$\frac{1}{c_*^2}\frac{dP}{dt}+\nabla\cdot\mathbf{v}-\frac{g}{c_*^2}w=0\,. \tag{1.28c}$$

Ultimately, this latter set of five equations for five prognostic variables ($\boldsymbol{\Psi}$) can be arranged in the following matrix form:

$$\frac{d\boldsymbol{\Psi}}{dt}+\mathbf{L}=\mathbf{R}+\mathbf{F}\,, \tag{1.29}$$

where the material derivatives ($d\boldsymbol{\Psi}/dt$) and left-hand-side linear terms ($\mathbf{L}$) related to acoustic and gravity waves are treated implicitly in time, and right-hand-side nonlinear terms ($\mathbf{R}$) and

source terms (**F**) are treated explicitly. Additionally, the first three terms of matrix equation (1.29) are calculated by the dynamics module for air parcel trajectories over three time-levels with the 3D SISL method, to reduce simultaneously the frequency of both gravity and sound waves that pose a severe constraint on the time step required for practical atmospheric modelling. For the last term in (1.29), its horizontal components are computed by the dynamical kernel and the vertical components with the physical parameterization module. If needed, the results obtained after each integration step are time-filtered to control remaining numerical noise or spurious instability.

The semi-Lagrangian (SL) space differencing based on the leapfrog scheme is applied for material derivatives and nonlinear terms, considering 3D displacements ($\delta_x, \delta_y, \delta_z$) implicitly calculated from the integral forms of the trajectories, that can be expressed in Cartesian coordinates with a trapezoidal integration approach as (Robert et al. 1985, Laprise et al. 1997):

$$\frac{d\psi}{dt} = \frac{\psi(x, y, z, t + \Delta t) - \psi(x - 2\delta_x, y - 2\delta_y, z - 2\delta_z, t - \Delta t)}{2\Delta t}. \qquad (1.30)$$

The SL scheme retains its simplicity and practical utility in complicated nonlinear calculations because the evolution of the flow continues to be computed following the air parcel trajectories. This spatial differencing scheme allows a completely new set of regularly spaced parcels to be chosen each time step. Namely, an initial definition of the air parcels is set at the grid points and, then, a new location is calculated for each parcel during one time interval Δt depending on the prevailing velocity field. This process is more commonly done starting with parcels at the grid points and calculating one-time-step back-trajectories using the same prevailing flow field, since it is more straightforward to interpolate (cubically) from a regular grid to irregular located points than the opposite.

André Robert and his collaborators (Robert et al. 1985, Tanguay et al. 1990, Laprise et al. 1997) combined the SL leapfrog algorithm with a semi-implicit (SI) time discretization scheme

to solve for the remaining linear terms as time averages along trajectories displaced by the decentering parameter (ξ), such that:

$$\overline{\psi}^{t} = \frac{(1+\xi)\,\psi(x,y,z,t+\Delta t)+(1-\xi)\,\psi\left(x-2\delta_x, y-2\delta_y, z-2\delta_z, t-\Delta t\right)}{2}. \qquad (1.31)$$

With the SI scheme, some terms are treated implicitly using averaging operators that smooth the fast-moving acoustic and gravity waves that normally demand the use of short time intervals. A considerable increase in efficiency and numerical stability can be realized by applying the SISL discretization scheme in combination with a frequency filter, although there is still an intrinsic stability problem related to the leapfrog's computational mode amplification due to the structure of the algebraic equations obtained from finite differences.

1.2.3 Numerical Stability of the SISL Leapfrog Method

Efficiency, accuracy and numerical stability are aspects of primary interest in multiscale modelling. Since the current atmospheric models are devised for operational weather forecasting, the finite difference method (FDM) is generally preferred with respect to finite volume (FVM) or finite element methods (FEM) since it allows a more efficient integration (Stensrud, 2007). On the other hand, although the leapfrog SISL algorithm is sufficiently stable to yield solutions that converge in the limit $\Delta t \to 0$, it may nonetheless generate a computational mode with a asymptotically growing sequence that blows up in a completely nonphysical manner when the computations are performed with finite values of the time step.

In the context of the atmospheric advection-diffusion problems, the norm of the physical solution must be bounded, decays or amplifies asymptotically with time. Defining the amplification factor as the ratio of the approximate solution of the problem (ϕ) at two adjacent time steps, i.e. $A = \phi_{n+1}/\phi_n$, it is recognized that the asymptotic growth rate (λ) is related to the time interval Δt in the sense that (Haltiner and Williams, 1980):

$$|A| \leq 1 + \lambda \Delta t \,. \tag{1.32}$$

Absolute numerical stability can be achieved if $|A| \leq 1$, or equivalently, $|\phi_n| \leq |\phi_0|$ for all n. Basically, in a nondissipative system, amplitude errors indicate spurious sinks or sources of energy, which arise from the difference between the magnitude of the approximate amplification factor $|A|$ and the correct value of unity. When $|A| = 1$ the scheme is neutral, if $|A| < 1$ the scheme is damping and if $|A| > 1$ it is amplifying (Durran 2010).

The maximum stable time step required for acoustic and gravity wave calculations is often much smaller than that required to accurately simulate the physical phenomena. Then, a significant increase in efficiency can be gained by applying SI time differencing to remove the stability constraint imposed by the rapid gravity and sound wave propagation. However, the weakness of the leapfrog SL scheme is its undamped computational mode, which slowly amplifies to produce time-stepping instability in simulations of nonlinear systems. It is a common practice, though a numerical artifice, to control this nonphysical computational mode with a second-order time filter, such as the Robert-Asselin filter (Robert 1966, Asselin 1972), related to the centered second-derivative of the solution ϕ_n by applying:

$$\underline{\varphi_n} = \varphi_n + \delta\left(\varphi_{n-1} - 2\varphi_n + \varphi_{n+1}\right). \tag{1.33}$$

Here $\underline{\varphi_n}$ denotes the filtered solution and δ is a positive real dimensionless constant that determines the strength of the filter. The last term in the latter equation is known as the displacement unit, which represents the finite difference approximation that preferentially damps the highest frequencies. This centered filter has the greatest impact on the most poorly resolved component of the solution, i.e. the $2\Delta t$ oscillation. Then, each filter application reduces the amplitude of the $2\Delta t$ wave by a factor of $1 - 4\delta$. In case δ is set to be $1/4$, each filtering operation will completely eliminate the $2\Delta t$ oscillation (Durran, 2010). The Robert-Asselin (RA) filter, with a typical damping strength of $\delta = 0.05$, controls the leapfrog

scheme's computational mode by incorporating a recursive filtering operation into the displacement unit (last term) such that for each leapfrog step (Asselin, 1972):

$$\underline{\varphi_n} = \varphi_n + \delta\left(\underline{\varphi_{n-1}} - 2\varphi_n + \varphi_{n+1}\right). \tag{1.34}$$

The main problem with the RA filter is that it degrades the global truncation error of the leapfrog scheme from a second to a first order. The use of higher order filters could be considered, although it is more costly on large computations. Namely, the unfiltered leapfrog SL scheme is second-order accurate but, after applying RA filtering, it turns into first-order accurate. To remediate this particular issue, Williams (2011) proposed an improvement to the original RA filter (which displaces ϕ_n through a unit but does not displace ϕ_{n+1}) by introducing a second filtering operation meant to displace simultaneously ϕ_n through α_{RAW} units and ϕ_n through $\alpha_{RAW} - 1$ units. Here, α_{RAW} denotes the additional dimensionless filter parameter that satisfies $0 \le \alpha_{RAW} \le 1$. Consequently, the Robert-Asselin-Williams (RAW) filter consists of the following operations:

$$\underline{\varphi_n} = \varphi_n + \alpha_{RAW}\,\delta\left(\underline{\varphi_{n-1}} - 2\varphi_n + \varphi_{n+1}\right), \tag{1.35a}$$

$$\underline{\varphi_{n+1}} = \varphi_{n+1} + \left(\alpha_{RAW} - 1\right)\delta\left(\underline{\varphi_{n-1}} - 2\varphi_n + \varphi_{n+1}\right). \tag{1.35b}$$

When $\alpha_{RAW} = 1$, the latter operation reduces to the original RA filtering. In the context of SISL method, Williams (2011) recommends the value of $\alpha_{RAW} = 1/2$ to conserve efficiently the three-time-level mean state and energy content of the solution, since it perturbs ϕ_n and ϕ_{n+1} in equal but opposite displacements. With the RAW filter, the SISL method conserves the mean of the predicted field and greatly reduces the magnitude of the first-order truncation error, reason why it will be employed in the present work as a numerical enhancement.

However, in the first part of this study, the time filter is placed aside in order to understand better the intrinsic stability issue of the SISL method and focus in finding a plausible solution

to remove its computational mode without the expense of misrepresenting or damping the transient physical mode. The original SI scheme, carefully analysed by several researchers (Simmons et al. 1978, Tanguay et al. 1990, Pinty et al. 1995, Héreil and Laprise 1996, Simmons and Temperton 1997, Bénard 2003, Bénard et al. 2004, Bénard et al. 2005), with a three time-level leapfrog discretization and height-based coordinates applied on the non-hydrostatic EE system, as done for the MC2 model, is less stable by nature when compared to the SI application on hydrostatic primitive equations (HPE). The classical SI scheme requires the selection of a reference state (χ_*) associated to a constant-in-time linear reference operator (ℓ_*), with respect to which the original system (Π) is linearized. In addition, the SI implementation enables a centered-implicit treatment on the linear terms linked to this reference state and an explicit treatment on the residual nonlinear terms. Then, the time-discretized evolution for a given atmospheric state (χ) is formulated as (Bénard, 2003):

$$\frac{\delta \chi}{\delta t} = \ell_* \cdot \overline{\chi} + \left(\Pi - \ell_*\right) \cdot \chi , \tag{1.36}$$

for which the stability of the model is conditioned by the structure of the nonlinear residual $\left(\Pi - \ell_*\right)$. When the SI scheme is applied to an atmospheric model, the equations are linearized with respect to a stationary "atmospheric basic state" ($\overline{\chi}$), associated with the corresponding linear-tangent "atmospheric" operator ($\overline{\ell}$) of Π around $\overline{\chi}$. If the flow is assumed to consist of small perturbations around a steady basic state, the full model evolution can be described by the following three time-level SI discretization in terms of $\overline{\ell}$ (Bénard et al., 2004):

$$\frac{\chi^+ - \chi^-}{2\Delta t} = \ell_* \cdot \left(\frac{\chi^+ + \chi^-}{2} \right) + \left(\overline{\ell} - \ell_*\right) \cdot \chi^0 . \tag{1.37}$$

If the reference state deviates from the basic state (i.e. $\chi_* \neq \overline{\chi}$, hence $\ell_* \neq \overline{\ell}$), nonlinear contributions arise in the SI discretization that generate potentially unstable explicitly treated residuals (Bénard, 2003). Namely, the SI-EE asymptotic instability in Δt is intimately

associated with the discrepancy between the height scales for the vertical growth of the linear reference and basic state operators, i.e. $H_* \neq \bar{H}$ (where $H_* = RT_*/g$ and $\bar{H} = R\bar{T}/g$, respectively). Consequently, the stability condition for the original SI scheme applied on EE system requires that $T_*/2 \leq \bar{T} \leq 2T_*$, which is more stringent than the stability criterion for the SI-HPE system, i.e. $0 \leq \bar{T} \leq 2T_*$ (Bénard 2003, Bénard et al. 2004). This implies that a strong thermal stratification is required for the selected reference state assigned to the MC2 model.

Bénard and other researchers (Bénard 2003, Bénard et al. 2004, Bénard et al. 2005) have proposed a careful selection of the prognostic variables to obtain a suitable reformulation of the explicitly treated thermal and baric residual terms. They remarked that the constant-coefficient SI-EE system can remain unconditionally stable with respect to Δt for an optimal choice of pressure and divergence prognostic variables, although its range of reference states is smaller than the SI-HPE system and more restrictive for simulations over complex terrain. In the next chapter, an alternative choice of generalized buoyancy and pressure prognostic variables is presented to increase the range of reference states for a stable SISL method applied on the EE system of MC2.

1.2.4 Model Equations Filtering and Turbulence Parameterization

As previously mentioned, applying the Reynolds decomposition ($\psi = \bar{\psi} + \psi'$) to time average the NS system results in the Reynolds-averaged equations (1.4), i.e. the fundamental system solved for the mean fields in the RANS models. An analogous set of equations can be obtained when applying the Favre decomposition ($\psi = \langle\psi\rangle + \psi''$) to filter the density fluctuations on the NS system, such that $\langle\psi\rangle = \overline{\rho\psi}/\bar{\rho}$ allows the separation of the mean and fluctuating parts of the velocity, temperature and non-conservative forcing and heat fluxes. As explained in section 1.2.2, although no external forcing or heating is considered in the present work, the terms related to $\vec{f}$ and Q are retained to provide a complete formulation of the model equations that are usually presented as system (1.28). Then, along with the conventional Reynolds-based

decomposition for the density and pressure fields, applying the Favre decomposition to equation system (1.28) results in (Gasset, 2014):

$$\frac{d\langle \mathbf{v} \rangle}{dt} + \nabla \overline{P} - \langle b \rangle \mathbf{k} = -f\,\mathbf{k} \times \langle \mathbf{v} \rangle - \frac{\langle b \rangle}{g} \nabla \overline{P} + \langle \boldsymbol{\mathcal{F}} \rangle, \tag{1.38a}$$

$$\frac{d}{dt}\left[\langle b \rangle - \frac{N_*^2}{g} \overline{P} \right] + N_*^2 \langle w \rangle = -\frac{R}{c_v} \langle b \rangle \nabla \cdot \langle \mathbf{v} \rangle + \frac{N_*^2}{g} \langle \Theta \rangle, \tag{1.38b}$$

$$\frac{d}{dt}\left[\frac{\overline{P}}{c_*^2} \right] + \nabla \cdot \langle \mathbf{v} \rangle - \frac{g}{c_*^2} \langle w \rangle = 0. \tag{1.38c}$$

Here $\langle \boldsymbol{\mathcal{F}} \rangle = \langle \mathbf{f} \rangle - \left(1/\overline{\rho}\right) \nabla \cdot \overline{\rho\, \mathbf{v}' \mathbf{v}'}$ and $\langle \Theta \rangle = \langle Q \rangle - \left(1/\overline{\rho}\right) \nabla \cdot \overline{\rho\, \mathbf{v}' \theta'}$. In this study no external forcing and heat sources are considered (i.e., $\mathbf{f} = 0$, $Q = 0$), thus, only the sub-filter turbulent stresses ($\tau'_{ij} = \overline{\rho u'_i u'_j}$) and heat fluxes ($Q'_j = \overline{\rho \theta' u'_j}$) remain. In the Favre-averaged equations these sub-filter quantities are clearly isolated but unresolved, thus, need to be modelled. The Favre averaging allows time and/or space filtering, with explicit or implicit numerical filters. As explained in (Léonard 1974, Murakami 1997), when an explicit filter is applied the sub-filter turbulent stress can be decomposed into three tensors $\tau'_{ij} = L_{ij} + C_{ij} + R_{ij}$, i.e., the Leonard stress $L_{ij} = \overline{\langle u_i \rangle \langle u_j \rangle}$, the cross terms stress $C_{ij} = \overline{\langle u_i \rangle} \overline{\langle u_j \rangle}$ and the Reynolds stress $R_{ij} = -2\upsilon_t S_{ij}$, expressed in terms of the strain rate tensor (S_{ij}) and turbulent viscosity (υ_t). When the computational grid is employed as an implicit filter the sub-filter turbulent stress reduces to the Reynolds stress tensor component (i.e. $\tau'_{ij} = -2\upsilon_t S_{ij}$). The latter enables the resulting equation system to be employed for both LES and RANS flow modelling (Pope 2000, Bechmann and Sørensen 2010).

Thus, in the context of the MC2 model with imbedded LES method, the matrix terms in equation (1.29) solved as the EE turn into (Gasset, 2014):

$$\boldsymbol{\Psi} = \begin{bmatrix} \mathbf{v} \\ \langle b \rangle - \left(N_*^2 / g \right) \overline{P} \\ \overline{P} / c_*^2 \end{bmatrix}, \tag{1.39a}$$

$$\mathbf{L} = \begin{bmatrix} \nabla \overline{P} - \langle b \rangle \mathbf{k} \\ N_*^2 \langle w \rangle \\ \nabla \cdot \langle \mathbf{v} \rangle - \left(g / c_*^2 \right) \langle w \rangle \end{bmatrix}, \tag{1.39b}$$

$$\mathbf{R} = \begin{bmatrix} -f \hat{k} \times \langle \mathbf{v} \rangle - \langle b \rangle \nabla \overline{P} / g \\ -\left(R / c_v \right) \langle b \rangle \nabla \cdot \langle \mathbf{v} \rangle \\ 0 \end{bmatrix}, \tag{1.39c}$$

and the turbulent forcing and source terms, added in a fractional step manner, are (Gasset, 2014):

$$\mathbf{F} = \begin{bmatrix} \langle \boldsymbol{\mathcal{F}} \rangle \\ \frac{N_*^2}{g} \langle \Theta \rangle \\ 0 \end{bmatrix} = \begin{bmatrix} -\left(1 / \overline{\rho} \right) \nabla \cdot \overline{\rho \mathbf{v}' \mathbf{v}'} \\ -\frac{g \overline{\pi}}{\overline{\rho} T_*} \nabla \cdot \overline{\rho \mathbf{v}' \theta'} \\ 0 \end{bmatrix}. \tag{1.40}$$

As explained in section 1.2.2, the horizontal components of this latter term (F_ψ^H) are computed with the dynamics module, whereas, the vertical components (F_ψ^V) are parameterized with the physics module. A thorough description of the turbulence parameterization schemes implemented in MC2-LES is provided by Gasset et al. (2014). A single 3D turbulence parameterization is certainly recommended, but the partitioned procedure is kept to ensure compatibility and consistency of MC2-LES with upgraded RPN physical packages. Gasset et al. (2014) tested multiple constant coefficient sub-grid scale turbulence models for MC2-LES, but concluded there was no significant improvement with respect to the classical Smagorinsky scheme (Smagorinksy, 1963). Testing of other parameterizations is left for future work since it is not part of this study's scope. Chapter 4 and Appendix IV of this work present more details

on the procedure followed to adapt the F_{ψ}^{H} terms of the Smagorinsky scheme (SMAG) for complex terrain calculations, employing the metric tensor transformations for the corresponding conforming grid cells.

1.2.5 Boundary Conditions and Computational Grid

Concerning the boundary conditions (BCs), the generally accepted logarithmic drag law has proven to be satisfactory, although not the only wall-layer model, to represent the roughness effects at the lower surface boundary by adding a sink term to the momentum equations. This self-similar formulation (cf. equation 1.15) is technically applicable to the mean velocity parallel to the surface within the first 20% of the ABL. On the other hand, the surface thermal boundary condition is prescribed depending on the type of simulation. Namely, for ideal test cases a constant temperature value is usually set for the whole domain surface, and for real orographic flow cases a daily cycle of temperature variations is prescribed from regional-scale data analysis or operational forecasts. An analytical temperature formulation based on local thermal stratification is employed for ideal cases based on Pinty et al. (1995), and for real cases the surface temperature is based on Wang (2017) formulation derived from weather station data of longwave radiation and sensible heat flux.

Top, lateral, inlet and outlet BCs are commonly defined for microscale CFD and engineering applications. However, for a multiscale method (e.g. LES embedded in a mesoscale model) the rotational and stratification effects must be considered for the ABL simulations, thus, demanding a stress free condition for the upper lid to damp the spurious reflection of waves and to replicate better the Ekman layer. For lateral, inlet and outlet boundaries, the periodic, slab-symmetry and perturbed velocity profile BCs are applicable for ideal-type simulations; nested BCs from a coarser domain are likely to be employed for simulations over real terrain, for which ideal homogeneous inflow conditions rarely exist (Blackadar 1997, Pope 2000, Wilcox 2006, Zikanov 2010, Dellwik and Anqvist 2014, Davidson 2015).

The computational domain or mesh is a key factor when dealing with challenges such as the spurious noise generation and/or the model's numerical stability for long-term integrations. As combined mesoscale-LES methods (e.g. WRF-LES, ARMS-LES, MC2-LES, etc.) are increasingly used for high-resolution atmospheric modeling, particularly over complex terrain, errors associated with severe deformations of terrain-following meshes degrade the accuracy of the simulations (Chow and Street 2009, Berg et al. 2011, Bechmann et al. 2011, Cavar et al. 2016). Consequently, most solvers narrow down to represent just gently sloping terrain and low hills, disregarding high-resolution steep terrain features over mountain ridges, cove-valley formations, scarp faces and cliffs. Recent reviews underline that both linear and nonlinear models become inefficient when handling slopes greater than 0.2, due to their inability to fully control ground approximations and to replicate mass conserving surface layers (Berg et al. 2011, Bechmann et al. 2011, Cavar et al. 2016).

Gal-Chen or sigma transformations (Gal-Chen and Somerville, 1975) are widely used in atmospheric models to enable a height-based terrain-following vertical coordinate simplify the lower boundary for simulations over complex terrain. Different studies point out that curvilinear conforming grids with a vertical terrain-following coordinate such as the Gal-Chen or sigma transformations pose a difficulty and are generally unsuitable for steep high-resolution topography due to errors that arise in computing the horizontal advection and pressure-gradient force (Mahrer 1984, Héreil and Laprise 1996, Bonaventura 2000, Benoit et al. 2002, Shchepetkin and Mcwilliams 2003, Klemp et al. 2003, Girard et al. 2005, Bénard et al. 2005). For both Eulerian scheme (as in WRF model) and semi-Lagrangian scheme (as in MC2 model) these errors are related to inconsistently differentiated metric terms, which introduce distortions even for small-amplitude terrain and gently sloped surfaces. If these metric terms are not numerically balanced in the semi-Lagrangian scheme, spurious contributions to gravity waves dynamics arise over fine-scale terrain with elevated orographic gradients depending on the way interpolation of variables is carried out. In the end, severe grid distortions affect adversely the hydrostatic balance consistency, believed to be related to sharp density changes between grid points of non-uniformly stretched cells that trigger interpolation errors for the hydrostatic relationship.

Nonetheless, terrain-following coordinates present certain advantages, reasons why they are preferred and widely used in numerical weather prediction models. Firstly, a terrain conforming coordinate system can map the atmospheric domain under consideration upon a rectangular computational mesh, whose data structure is well suited for implementations on digital computers. Secondly, as the transformed vertical velocity in computational space vanishes on the topographic surface, terrain-following coordinate transformations yield a simplification of the lower boundary condition. And third, as the approach allows for an unequal spacing of computational levels, it provides an easy method to couple the dynamical part of atmospheric prediction models with boundary and surface-layer parameterization schemes (Bonaventura 2000, Gallus and Klemp 2002, Steppeler et al. 2002). Thus, it is desirable to keep this curvilinear coordinate system for MC2-LES and concentrate in the solution of the deficiencies mentioned above.

To solve the inaccuracies due to grid deformations over steep complex terrain, there are some options that enable to retain the terrain-following curvilinear coordinate system and others that are designed for fixed Cartesian coordinates. In the first category, particularly for the curvilinear coordinates used in MC2, Schär et al. (2002) proposed the smooth level vertical coordinate (SLEVE), for which grid distortions resulting from small-scale terrain features decay exponentially with height, more rapidly than distortions caused by large-scale terrain features. Figure 1.2 depicts the transformation of the physical space coordinates into Gal-Chen monotonic coordinates and, then, into flat model levels for Cartesian coordinates which allows efficient calculations. They designed this SLEVE solution so the vertical coordinate flattens with height, dependent on the scale and shape of the underlying terrain. Thus, the topography is split into large- and small-scales, which decay exponentially with their respective scale-heights. Several researchers (Girard et al. 2005, Leuenberger et al. 2001, Schär et al. 2002, Leuenberger et al. 2010) have employed this vertical coordinate solution in MC2 and verified that it reduced the numerical noise due to small-scale terrain features with negligible computational cost.

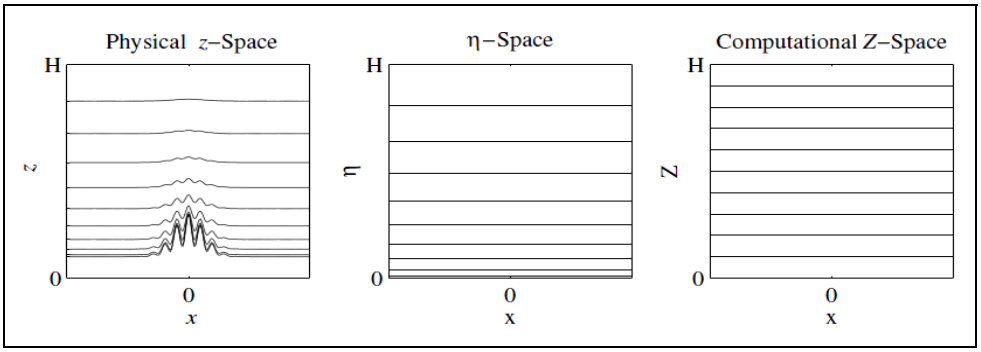

Figure 1.2 Height of the computational levels in physical z-coordinates (left), Gal-Chen η-coordinates (middle) and computational Z-coordinates (right). Leuenberger et al. (2010).

Tests by Girard et al. (2005) in MC2 with the SLEVE coordinate revealed that the physical height coordinate (z) must be transported in a Lagrangian manner to obtain a departure height consistent with departure values of the other prognostic variables. In this sense, the suggested solution by Girard et al. (2005) for the vertical displacement in oblique coordinates (W) consists in correcting the absolute vertical motion (w) by the time variation of the physical height (z) on constant-Z surfaces. Hence, the absolute vertical displacements result from evaluating the physical height advection along the Lagrangian trajectories. Even though these solutions constitute major improvements for MC2, errors due to steep terrain gradients remain an enduring constrain to compute correctly the topographic forcing. The latter aspect will be discussed thoroughly in Chapter 2 of this work.

Another alternative is a Cartesian height coordinate approach, based on the step representation, as proposed by Bonaventura (2000) and Steppeler et al. (2002). This method avoids the use of terrain-following coordinates and, therefore, abolishes the need for metric transformation coefficients that, sometimes, generate spurious flows and induce limitations for the semi-Lagrangian scheme around steep orography. Additionally, the cell-blocking procedure is introduced by setting to zero the orthogonal velocity components of the selected topographic cells combined with finite volume discretization to account for null flux contribution below the orographic surface. The surface fluxes are set to coincide with the first grid fluxes to ensure the appropriate boundary conditions.

Bonaventura (2010) derived a SISL scheme (analogous to the MC2) using this Cartesian approach with non-normalized height coordinate, from which a symmetric system of discretized equations is obtained. Then, this equation system is handled with a simple *ad hoc* preconditioner, which needs two iterations at each time-step at the most. Bonaventura (2000) and Steppeler et al. (2002) validated this Cartesian SISL scheme with 2D canonical wave studies, done previously by Pinty et al. (1995), proving that it is able to resolve flow over very steep terrain with satisfactory numerical accuracy. Even though this proposal is very similar to the MC2 curvilinear SISL scheme, its implementation requires important changes in the discretization procedures and preconditioner numerical schemes. Another shortcoming is the need for high refinement to reproduce real complex topography (due to the step-terrain representation), in order to avoid flow stagnation and inappropriate recirculation at vertical cell faces. So this new method can resolve the orographic steepness distortions but implies a significant reformulation of the MC2's kernel.

Gallus and Klemp (2000) also evaluated the viability of using a step terrain representation on the non-hydrostatic version of the NCEP regional Eta model. They performed several computational experiments of flow over an isolated mountain for small-amplitude non-hydrostatic mountain waves, and found out that the accuracy of this technique depends strongly on the horizontal scale of the terrain and the vertical resolution of the actual terrain. Their idealized 2D simulations over a Witch of Agnesi hill, represented by step-terrain coordinates, revealed a persistent tendency for the flow to separate above the lee slope of terrain features due to artificial horizontal vorticity generation at the step corners. The deviations from the classic Witch of Agnesi solution are significant, unless the vertical resolution is very small compared to the height of the mountain. In contrast, Gallus and Klemp (2000) obtained accurate results for the same cases by using terrain-following coordinates, since the vertical grid interval is small compared to the vertical wavelength of the mountain waves. In conclusion, step terrain representation helps improve the pressure-gradient forcing calculation, but its limitations show it is less reliable than terrain-following coordinates for flow simulations over complex terrain.

The immersed boundary method (IBM) is another solution envisioned for dealing with highly complex fine-scale terrain, such as shoreline cliffs and metropolitan urban obstacles. The IBM is based on the general proposal introduced by Peskins and other researchers (Mohd-Yusof 1997, Peskins 2002, Iaccarino and Versicco 2003) who first applied this method to simulate blood flow in human heart vessels and for aerodynamic design of complex geometries. In particular, this method has been successfully adapted and validated by Senocak et al. (2004) and Lundquist et al. (2010) for simulations of turbulent atmospheric boundary layer flows over flat terrain and gentle slopes, although it increased significantly the computational overhead. The IBM uses a non-conforming (i.e., fixed not terrain-following) structured grid applicable either to Cartesian or curvilinear coordinates. Basically, it allows the solid boundary that represents the terrain surface to pass through the computational cells of a structured grid, implicitly defining a body force that imposes the effects of the surface on the velocity field.

It is noteworthy that the IBM is able to coexist with curvilinear terrain-following coordinates, optimizing the combination of multiscale terrain features Lundquist et al. (2010). In other words, a hybrid terrain representation method can be implemented in mesoscale-LES models, by employing the terrain-following coordinates to resolve the gently sloping mesoscale topography and the IBM to handle fine-scale near-vertical complex terrain. Accordingly, this hybrid terrain-following with IBM system can be integrated into a downscaling procedure that, first, accounts for large-scale terrain features and, then, captures small-scales features of steep topography in a nested domain. Nonetheless, the implementation of IBM in a three-dimensional model such as the MC2-LES is not a straightforward task, and the proper coupling of the IBM and the SISL scheme must be studied in depth to set correctly the boundary conditions and direct forcing.

Evaluating these alternatives, it seems that the natural choice is the SLEVE hybrid coordinate to reduce the discretization errors produced by the terrain-following sigma vertical coordinate. As pointed out by Leuenberger et al. (2010), Klemp (2011), Zängl (2012) and Eckermann et al. (2014), the sigma coordinate simulations exhibit large divergent wind anomalies over terrain that extend from the surface to the model top and distort explicitly resolved orographic

gravity waves. Allegedly, these divergent wind errors are suppressed by an order of magnitude or more in the hybrid-coordinate analyses. Henceforth, these studies have motivated the author to adopt a SLEVE hybrid coordinate with the best error suppression characteristics for the MC2-LES multiscale modeling application.

CHAPTER 2

NUMERICAL STABILITY AND NOISE CONTROL OF A NEW SEMI-IMPLICIT SCHEME FOR MESOSCALE MODELLING OVER STEEP TERRAIN

Alex Flores-Maradiaga [1,2], Robert Benoit [2], Claude Girard [3],
Christian Masson [2] and Michel Desgagné [3]

[1] Department of Mechanical Engineering, Federico Santa María Technical University, 1680, Ave. España, Box 110-V, Office C-430, Valparaíso, Chile
[2] Département de Génie Mécanique, École de Technologie Supérieure, 1100, Notre-Dame Ouest, Montréal, Québec, Canada, H3C 1K3
[3] Recherche en Prévision Numérique, Meteorological Service of Canada, Environment Canada, 2121, Route Transcanadienne, Dorval, Québec, Canada, H9P 1J3
Article submitted in November 2017 to *Boundary Layer Meteorology*. Currently in revision.

Abstract

An eigenmode stability analysis applied on the classical three time-level semi-implicit (SI) scheme, originally coupled with the semi-Lagrangian (SL) scheme to discretize the compressible non-hydrostatic Euler equations (EE), reveals that this method is unstable and very noisy in the absence of time decentering, frequency filtering and other numerical damping mechanisms. The proposed reformulation of the SI discretization with an appropriate choice of prognostic variables yields a consistent scheme that linearizes the EE in height-based coordinates, changing the structure of their non-linear residual terms in such a way that the SISL scheme is maintained in its stable domain, thus, preventing the emergence of spurious flows. The combination of this new SI scheme with the smooth level vertical σ-coordinate and the energy conserving Robert-Asselin-Williams frequency filter ensures that the SISL algorithm meets the stability condition of the EE system for mesoscale flow simulations over steep terrain. With these modifications, the numerical instability and steep slopes limitation of the SISL method for mesoscale modelling have been overcome. The enhanced method now enables more accurate high-resolution simulations while maintaining the convenience of the terrain-following coordinate system, rather than implementing a more expensive terrain representation (e.g. immersed boundary method).

2.1 Background and Context

The Canadian Mesoscale Compressible Community model (MC2) solves the fully elastic system of non-hydrostatic Euler equations (EE) in height-based terrain-following σ-coordinates, as explained by Robert et al. (1985), Tanguay et al. (1990), Benoit et al. (1997), Thomas et al. (1998) and Girard et al. (2005). This atmospheric model has been employed for a wide range of mesoscale weather forecasts and, most recently, as core of the Wind Energy Simulation Toolkit (WEST), an open-source solver with high resolution capabilities for wind resource assessment over complex terrain (Yu et al. 2006, Gasset et al. 2012). By coupling MC2 with other micro-scale models, such as MS-Micro or WAsP, this toolkit has generated a detailed description and mapping of the North American wind resource. These results are accessible in the Canadian Wind Energy Atlas, which takes into consideration high resolution orographic and land-use configurations as well as large- and small-scale seasonal meteorological phenomena occurring over complex topography. Interesting discussions of the WEST toolkit and its multiple applications are presented in Yu et al. (2006), Pinard et al. (2009) and Gasset et al. (2012).

Until recently, the three time-level (3-TL) semi-implicit semi-Lagrangian (SISL) scheme used to discretize the model's equations was considered to be unconditionally stable, in flat-terrain case at least (Tanguay et al. 1990, Tanguay et al. 1992, Laprise et al. 1997). Nonetheless, it was demonstrated by Bénard (2003), Bénard et al. (2004) and Bénard et al. (2005) (hereafter B03, B04 and B05, respectively) that the constant coefficient semi-implicit (SI) scheme may be numerically unstable due to an inadequate choice of prognostic variables. This can generate a discrepancy of the velocity divergence with respect to the hydrostatic basic state around which the system is linearized. Then, in the asymptotic limit of large time-steps, the temperature and pressure-gradient perturbations trigger computational modes that drive the model to an inevitable crash when no explicit damping mechanisms are applied.

In presence of complex terrain, the initial imbalances of the horizontal pressure-gradient (HPG) force introduced by the deformation of constant σ-surfaces usually produce computational

modes that constraint the stability condition of the 3-TL SI scheme. To guarantee the same degree of stability for simulations over topography, which MC2 seemingly had over flat terrain, a sophisticated elliptic solver (GMRES) was adopted by Thomas et al. (1998) such that all the terrain-induced metric terms were included in the SI branch of the solver. However, the model remained subject to high-frequency noise (Bonaventura 2000, Benoit et al. 2002, Schär et al. 2002, Klemp et al. 2003, Girard et al. 2005, Pinard et al. 2009) prompted by these initial imbalances in the pressure and temperature fields, which were deemed controlled by off-centered averaging in the SISL scheme. Additionally, as described by Benoit et al. (2002), various types of frequency filtering were applied after each time-step to restrict the emergence and enhancement of terrain-induced numerical noise.

A major breakthrough in the solution of the terrain-induced noise problem came about after the demonstrative studies of Schär et al. (2002) and Klemp et al. (2003). It appears that a numerical inconsistency is introduced when a second-order accurate Eulerian diagnostic calculation of the generalized vertical velocity $W = (w - \mathrm{V} \cdot \nabla z) / \partial z / \partial Z$ is used for estimating fourth-order accurate Lagrangian vertical displacements. This inconsistency disappears if the geometric height z is horizontally advected in a Lagrangian rather than an Eulerian fashion on constant σ-surfaces (Girard et al. 2005). This is a common problem for many numerical weather prediction (NWP) models that employ the 3-TL SI scheme and height-based terrain-following coordinates, for which the smooth level vertical coordinate (SLEVE) introduced by Schär et al. (2002) became a plausible solution. The z coordinate represents the physical height above ground level, and the Z corresponds to the height of the smooth model levels following the underlining surface.

Over the last 40 years, there have been many attempts to solve this issue but no method has eliminated completely the numerical noise and instability of models that combine the constant coefficient SI scheme and height-based σ-coordinate transformation for mesoscale simulations over topography. Some of the proposed methods are reported in Kasahara (1974), Mesinger (1982), Mahrer (1984), Janic (1989), Gallus and Klemp (2000), Steppeler et al. (2002), Wedi et al. (2004) and Wong et al. (2013), which have been partly successful in reducing terrain-

induced noise sufficiently enough to ensure accurate results for atmospheric modelling. Some solutions have been proposed to smooth the steep terrain slopes to reduce the metric transformation constraint; others have applied an explicit time-splitting filter to control the model's response; others have proposed thermal diffusion schemes to damp the computational mode triggered by density fluctuations; others have rescripted the basic kernel to convert the discretization from a three time-level to a two time-level center implicit or SI scheme; or different terrain-following coordinate formulations have been applied to smooth the topographic signal on the model levels.

For example, the HPG force reconstruction method, proposed by Mahrer (1984) and implemented in the upgraded non-hydrostatic models of Klemp (2011) and Zängl (2012), allowed an efficient control of spurious flows over steep topography. Nonetheless these methods need to be coupled with other solutions, such as the SLEVE coordinate or a second-order horizontal temperature diffusion scheme, to perform better even though the cause of the problem still persists. The principal aim and contribution of the present study is precisely to unveil the origin of the computational mode for the classical three-time level SI scheme on height-based coordinates, to present a consistent solution that addresses the cause and not just the effects.

While terrain-induced noise has been a serious problem the same cannot be said of the numerical instability problem. Without time decentering in the SISL averaging operators, especially at low spatial resolution and large time-steps, the model becomes very noisy and unstable. As implemented by Héreil and Laprise (1996), these high-frequency oscillations seem to be controlled with the dynamic initialization procedure that prevents the model's blow-up. The time decentering (or off-centering, ε) can be seen as a cheap alternative to dynamic initialization, which helps prevent spurious stationary forcing known to affect adversely semi-Lagrangian (SL) schemes (Héreil and Laprise 1996). By applying an decentering value of $\varepsilon = 0.1$ MC2 has remained stable or, as recognized by B03 in the stability analysis of the SI scheme, "the practical instability becomes small under these conditions". Indeed, B04 showed that the original SISL scheme with height-based coordinates employed for MC2 is, in absence

of off-centering, absolutely unstable rather than absolutely stable.

As carefully analyzed in several studies (Simmons et al. 1978, Simmons and Temperton 1997, Caya and Laprise 1999), the original SI scheme with a 3-TL leapfrog discretization and height-based coordinates applied on the non-hydrostatic EE system, as done for the MC2 model, is less stable by nature when compared to the SI application on hydrostatic primitive equations (HPE). As in Simmons et al. (1978) (hereon referred as SHB78), B03 and B04 explained that the classical SI scheme requires the selection of a reference state (χ_*) associated to a constant-in-time linear reference operator (ℓ_*), with respect to which the original system (Π) is linearized. In addition, the SI implementation enables a centered-implicit treatment on the linear terms linked to this reference state and an explicit treatment on the residual nonlinear terms. For a given atmospheric state (χ) the stability of the model is conditioned by the structure of the nonlinear residual $(\Pi - \ell_*)$.

B04 also explain that when the SI scheme is applied to an atmospheric model, the equations are linearized with respect to a stationary "atmospheric basic state" ($\bar{\chi}$), associated with the corresponding linear-tangent "atmospheric" operator ($\bar{\ell}$) of Π around $\bar{\chi}$. If the flow is assumed to consist of small perturbations around a steady basic state, the full model evolution can be described by the three time-level SI discretization in terms of $\bar{\ell}$ such that $(\chi^+ - \chi^-)/2\Delta t = \ell_*/2 \cdot (\chi^+ + \chi^-) + (\bar{\ell} - \ell_*) \cdot \chi^0$. If the reference state deviates from the basic state (i.e. $\chi_* \neq \bar{\chi}$, hence $\ell_* \neq \bar{\ell}$), nonlinear contributions arise in the SI discretization that generate potentially unstable explicitly treated residuals. Namely, the semi-implicit discretization asymptotic instability in Δt for the EE is intimately associated with the discrepancy between the height scales for the vertical growth of the linear reference and basic state operators, i.e. $H_* \neq \bar{H}$ (where $H_* = RT_*/g$ and $\bar{H} = R\bar{T}/g$, respectively). Consequently, the stability condition in terms of reference and basic state temperature for the original SI scheme applied on EE system requires that $T_*/2 \leq \bar{T} \leq 2T_*$, which is more stringent than the stability criterion $0 \leq \bar{T} \leq 2T_*$ for the hydrostatic primitive equation system, as

detailed by SHB78, B03, and B04. This implies that a strong thermal stratification is required for the selected reference state assigned to the MC2 model.

It is Bénard's et al. insight (B03 and B04), based on a SHB78-type stability analysis, which guided our investigation towards the development of not only a more stable SI scheme but also a more accurate one, since the decentered first-order accurate averaging is no longer required for stability. Although our study of the numerical stability and noise control is limited to a residual-free linear system, it still follows the standard eigenmode analysis to explore the nature and response of the model equations. Thus, after explaining the stability problem of the original SI scheme in Section 2.2, we describe in Section 2.3 the redefinition of the buoyancy prognostic variable that satisfies the SI scheme stability criterion. In Section 2.4 we discuss the results of an extensive set of tests performed with the former and new 3-TL SISL scheme and, finally, in Section 2.5 we give the concluding remarks and some recommendations for future research on this topic.

2.2 Basic Semi-discrete Model Equations

The dynamic kernel of MC2 solves the fully compressible non-hydrostatic EE for the velocity and three thermodynamic variables (temperature T, pressure $q = \ln p$ and density ρ), supplemented with tendencies of turbulence, moisture, radiation and tracer diffusion calculated with a physics parameterization package common to other *Recherche en Prévision Numérique* (RPN) atmospheric models. This EE system involves the pressure variable as $q = \ln p$ in the three-dimensional conservation equations (Newton's second law, first law of thermodynamics and mass continuity equation, respectively) since the pressure-gradient is more consistently computed for the lagrangian advection formulation. The EE system casted for MC2 is closed with the diagnostic ideal gas equation $p = \rho R T$ (i.e., all variables are linked simultaneously and calculated at the same time level) and formulated in the following advective form:

$$\frac{d\mathbf{v}}{dt} + f\,\mathbf{k}\times\mathbf{v} + RT_*\nabla q' - g\left(\frac{T'}{T_*}\right)\mathbf{k} = \mathbf{f} - RT'\nabla q', \qquad (2.1a)$$

$$\frac{d}{dt}\left(T'-\frac{RT_*}{c_p}q'\right)+\frac{T_*}{g}N_*^2 w=\left(1+\frac{RT'}{c_vT}\right)\frac{Q}{c_p}-\frac{RT'}{c_v}\nabla\cdot\mathbf{v}\,, \tag{2.1b}$$

$$\frac{c_v}{c_p}\frac{dq'}{dt}+\nabla\cdot\mathbf{v}-\frac{g}{c_*^2}w=\frac{Q}{c_pT}\,. \tag{2.1c}$$

The variables and constants have the same meaning presented in Girard et al. (2005), where $d/dt=\partial/\partial t+\mathbf{v}\cdot\nabla$ represents the material derivative, $\mathbf{v}=(u,v,w)$ the velocity vector, f the Coriolis parameter, $\mathbf{f}=(\mathrm{f}_u,\mathrm{f}_v,\mathrm{f}_w)$ the non-conservative forcing and Q the heat sources. Additionally, the prognostic variables are complemented with the reference speed of sound $c_*^2=(c_p/c_v)(RT_*)$ and buoyancy frequency $N_*^2=g(\beta_A+\gamma_A)$, for which $\beta_A=\partial\ln T_*/\partial z$ and $\gamma_A=g/c_pT_*$. In this particular study, the reference temperature T_* is set as a constant for an isothermal atmospheric condition, which simplifies the numerical analysis by reducing the reference buoyancy frequency to $N_*^2=g^2/c_pT_*=g\gamma_*$. This EE system is not casted in terms of the potential temperature since the buoyancy resulting from temperature perturbation was selected a more consistent prognostic variable for the SISL algorithm.

To prepare the EE for the 3-TL SISL scheme, a hydrostatically-balanced isothermal reference state for temperarutre (T_*) and pressure (q_*, where $\partial q_*/\partial z=-g/RT_*$) is subtracted from the temperature and pressure prognostic variables, thus replacing T and q by their deviations $T'=T-T_*$ and $q'=q-q_*$. Then, the resulting equation system is reformulated in terms of the buoyancy $b=gT'/T_*$ and generalized pressure $P=RT_*q'$, considered the prognostic variables, to obtain:

$$\frac{d\mathbf{v}}{dt}+f\,\mathbf{k}\times\mathbf{v}+[\nabla-\gamma_*\mathbf{k}]P+\mathbf{k}(b-\gamma_AP)=\mathbf{f}-\frac{b}{g}(\nabla-\beta_A\mathbf{k})P\,, \tag{2.2a}$$

$$\frac{d}{dt}(b-\gamma_*P)+N_*^2w=\gamma_AQ-b\left[\beta_Aw+\frac{R}{c_v}\nabla\cdot\mathbf{v}\right], \tag{2.2b}$$

$$\frac{d}{dt}\left(\frac{P}{c_*^2}\right)+\nabla\cdot\mathbf{v}-\frac{g}{c_*^2}w=\frac{Q}{c_pT}. \tag{2.2c}$$

In order to ease the explanation and find a possible solution to the model's numerical instability, lets assume that the growth of the computational mode is 2D and does not depend transverse velocity component, external forcing or heat sources. Thus, it will be sufficient to consider the following simplified two-dimensional (x–z) version of the EE system in Cartesian coordinates with no Coriolis acceleration, external forcing or heat sources:

$$\frac{du}{dt}+\frac{\partial P}{\partial x}=-\frac{b}{g}\frac{\partial P}{\partial x}, \tag{2.3a}$$

$$\frac{dw}{dt}+\frac{\partial P}{\partial z}-b=-\frac{b}{g}\frac{\partial P}{\partial z}, \tag{2.3b}$$

$$\frac{d}{dt}(b-\gamma_* P)+N_*{}^2 w=-\frac{R}{c_v}bD, \tag{2.3c}$$

$$\frac{1}{c_*{}^2}\left[\frac{dP}{dt}-gw\right]+D=0, \tag{2.3d}$$

where $D=\partial u/\partial x+\partial w/\partial z$ is the two-dimensional divergence. If this system is linearized with respect to a hydrostatic resting basic state, assuming that velocity, temperature and pressure deviations are sufficiently small, the equations admit gravity and sound wave solutions in the form of $\exp(ikx+nz+i\omega t)$ with $n=i\nu+1/(2H_*)$, where k and ν are the respective wavenumbers in x and z, and $H_*=RT_*/g$. Hence, the frequencies ω are given by the dispersion relation:

$$\frac{\omega^4}{c_*{}^2}-\omega^2(k^2+nn^*)+N_*{}^2k^2=0. \tag{2.4}$$

When the 3-TL SISL discretization is applied to the linearized system (2.3), the material derivatives are replaced by second order finite differences and the remaining linear terms on the left-hand side are averaged over three time-levels, an operation denoted here by the over-bars $\overline{[\ ]}$, while non-linear terms on the right-hand side are evaluated at the central time as:

$$\frac{\delta u}{2\Delta t}+\frac{\partial \overline{P}}{\partial x}=-\frac{b}{g}\frac{\partial P}{\partial x}, \tag{2.5a}$$

$$\frac{\delta w}{2\Delta t}+\frac{\partial \overline{P}}{\partial z}-\overline{b}=-\frac{b}{g}\frac{\partial P}{\partial z}, \tag{2.5b}$$

$$\frac{\delta}{2\Delta t}(b-\gamma_* P)+N_*{}^2\overline{w}=-\frac{R}{c_v}bD, \tag{2.5c}$$

$$\frac{1}{c_*{}^2}\left[\frac{\delta P}{2\Delta t}-g\overline{w}\right]+\overline{D}=0. \tag{2.5d}$$

Here the respective meaning of the variable and SISL operators is $\psi=\psi(x,z,t)$, $\psi^{\pm}=\psi(x,z,t\pm\Delta t)$, $\delta\psi=\psi^{+}-\psi^{-}$ and $\overline{\psi}=((1+\varepsilon)\psi^{+}+(1-\varepsilon)\psi^{-})/2$. As previously mentioned, ε represents the time decentering parameter, which for the present analysis it will be fixed to $\varepsilon = 0$ in order to remove this explicit diffusion mechanism. For this discussion it is not necessary to distinguish between the various spatial positions, henceforth, a semi-discrete approach is adopted.

2.3 Stability Analysis of the Original SI (O-SI) Scheme

The stability analysis proposed by B03 is based on the classical SHB78-type eigenmode approach that considers a solution of the form $X=\exp(ikx+nz)X(t)$, for which the asymptotical growth rate λ is examined for complex values. Let us define the response factors as $\Lambda^{-}=(\lambda^2-1)/2\Delta t$ and $\Lambda^{+}=(\lambda^2+1)/2$, where $\lambda=\left(X^{+}/X^{-}\right)/2=X/X^{-}=\exp i\gamma$ is the amplification rate for which γ is a complex number with most likely a non-zero imaginary term. In the framework of this linearized system around an isothermal basic state, the right-

hand side non-linear terms in system (2.5) vanish resulting in the following:

$$\Lambda^{-}u + ik\Lambda^{+}P = 0\,, \tag{2.6a}$$

$$\Lambda^{-}w + n\Lambda^{+}P - \Lambda^{+}b = 0\,, \tag{2.6b}$$

$$\Lambda^{-}(b - \gamma_{*}P) + N_{*}^{2}w\Lambda^{+} = 0\,, \tag{2.6c}$$

$$\frac{\Lambda^{-}}{c_{*}^{2}}P - \frac{g}{c_{*}^{2}}w\Lambda^{+} + \Lambda^{+}(iku + nw) = 0\,. \tag{2.6d}$$

Solving system (2.6), after a trigonometrical simplication, leads to the dispersion relation:

$$\frac{(\Lambda^{-})^{4}}{c_{*}^{2}} + (\Lambda^{-})^{2}(\Lambda^{+})^{2}(k^{2} + nn^{*}) + N_{*}^{2}k^{2}(\Lambda^{+})^{4} = 0\,, \tag{2.7a}$$

$$\frac{\tan^{4}\gamma}{\Delta t^{4}c_{*}^{2}} - \frac{\tan^{2}\gamma}{\Delta t^{2}}\left(k^{2} + nn^{*}\right) + N_{*}^{2}k^{2} = 0\,. \tag{2.7b}$$

Relations (2.4) and (2.7b) have the same form, which by direct comparison yields $\tan\gamma = \omega\Delta t$. Thus γ is real since ω is real and $|\lambda| = 1$, leading Tanguay et al. (1990) to claim an absolute stability for the MC2 model. However, some aspects of the previous stability analysis are incomplete. It is expected, for the external mode in particular ($\nu = 0$), that temperature deviations must be contained within certain range. There will also be some damping due to interpolations associated with the semi-Lagrangian part of the SISL algorithm among other numerical damping mechanisms. Hence, the results of this classical stability analysis need to be reexamined.

By extending the stability analysis using the same SHB78-type method, it is possible to dissociate the linearization process from the basic state when considering local deviations (T'' and q'') from the mean values of temperature and pressure (T_0 and q_0), rather than deviations from arbitrary reference state variables (T_* and q_*). Namely, the mean temperature T_0 is employed to replace the instantaneous temperature T to obtain a more significant perturbation

characterization with respect to the reference temperature T_*. On the other hand, the model settings allow to prescribe the surface temperature T_{surf} as the stability control value. Namely, the model's stability is dependant on the lower thermal boundary condition (but not exclusively), such that if the surface perturbation ratio $\alpha_{surf} = \left(T_{surf} - T_*\right)\big/T_*$ is kept bounded to a small range (e.g. $-1/4 \le \alpha_{surf} \le 1/4$) the growth of computational mode can be controlled more effectively. However, the model's response is also influenced by the grid resolution, time interval, time filtering and decentering interpolation.

Linearizing system (2.3) locally around T_0 and using $\alpha = (T_0 - T_*)/T_*$, $b_1 = gT''/T_* = g\alpha$, $P_1 = RT_*q''$, $\Lambda_1^+ = (\Lambda^+ + \alpha\lambda)/(1+\alpha)$, $\Lambda_2^+ = \Lambda^+(1+\alpha) - \alpha\lambda$, $N_0^{\,2} = N_*^{\,2}/(1+\alpha)$ and $c_0^{\,2} = c_*^{\,2}(1+\alpha)$ yields the following, after the SISL discretization:

$$\frac{\delta u}{2\Delta t} + \frac{\partial \overline{P}_1}{\partial x} = -\alpha \frac{\partial P_1}{\partial x}, \tag{2.8a}$$

$$\frac{\delta w}{2\Delta t} + \frac{\partial \overline{P_1}}{\partial z} - \overline{b_1} = -\alpha \frac{\partial P_1}{\partial z} - b_1 \frac{\alpha}{1+\alpha}, \tag{2.8b}$$

$$\frac{\delta}{2\Delta t}(b_1 - \gamma_* P_1) + N_*^{\,2}\overline{w} = -\alpha g \frac{R}{c_v} D + N_*^{\,2} w \frac{\alpha}{1+\alpha}, \tag{2.8c}$$

$$\frac{1}{c_*^{\,2}}\left[\frac{\delta P_1}{2\Delta t} - g\overline{w}\right] + \overline{D} = -\frac{g}{c_*^{\,2}} w \frac{\alpha}{1+\alpha}, \tag{2.8d}$$

for which the resulting dispersion relation is (cf. Appendix II):

$$\frac{(\Lambda^-)^4}{c_0^{\,2}} + (\Lambda^-)^2 \Lambda_1^+ \left[(k^2 + nn^*)\Lambda^+ + \frac{n\alpha}{H_0}(\Lambda_2^+ - \Lambda^+) \right] + N_0^{\,2} k^2 (\Lambda_1^+)^2 (\Lambda_2^+)^2 = 0, \tag{2.9a}$$

$$\frac{\sin^4\gamma}{\Delta t^4 {c_0}^2}-\frac{\sin^2\gamma}{\Delta t^2}(\cos\gamma+\alpha)\left[(k^2+nn^*)\cos\gamma+\frac{n\alpha}{H_0}(\cos\gamma-1)\right] + {N_0}^2k^2(\cos\gamma+\alpha)^2\left[\cos\gamma+\frac{\alpha}{1+\alpha}\right]^2=0 \quad . \tag{2.9b}$$

If $T_0 = T_*$ and $\alpha = 0$, equation (2.7) is recovered from the previous relation, which means that the model is stable when the temperature perturbations are null. Considering the typical asymptotic growth when $\alpha \neq 0$, the external mode ($\nu = 0$) is stable for $-1/4 \leq \alpha \leq 1$. However, due to the complex nature of $n = i\nu + 1/(2H_*)$ the internal modes ($\nu \neq 0$) are always unstable even for $k = 0$ (i.e. one-dimensional model along the vertical). This is true whether or not the hydrostatic assumption is enforced by dropping the vertical acceleration term dw/dt from the equation system. Thus, the 3-TL SI scheme is always unstable as soon as $\alpha \neq 0$, if no other damping mechanism is employed (e.g. decentering).

To illustrate the model's response with the numerically unstable O-SI scheme, a set of experiments has been performed with the two-dimensional flat terrain model (using a grid $L_x =$ 50 km long and $L_z = 10$ km high, with horizontal and vertical resolutions of $\Delta x = 500$ m and $\Delta z = 100$ m, respectively). It is initialized with an isothermal non-rotational atmosphere at rest and a temperature basic state of $T_* = 250$ K. The model settings and test results are summarized in Table 1, where the surface temperature $T_{surf} = T_0$ for an isothermal atmosphere. The 24 hours evolution of the maximum vertical velocity $|w|_{\max}$ for two opposite cases (unstable case 1 and stable case 7) is compared in Figure 2.1. The results presented in Table 2.1 and Figure 2.1 indicate the asymptotic growth of the O-SI computational mode is affected by the variation of the surface temperature ratio $\alpha_{surf} = \left(T_{surf} - T_*\right)/T_*$, RA frequency filter ($\delta$), time decentering operator (ε) and time-step (Δt). In this context, the initially at-rest unstable cases yield mean values and standard deviation of velocities several orders of magnitude higher than stable cases.

These experiments confirm Bénard's remark in B03, outlining that instability already manifests

itself for very small temperature perturbations (e.g., case 1 with $\alpha_{surf} = 0.05$) in the absence of decentering and time-filtering. When these explicit damping mechanisms are combined (e.g., cases 4 and 7 with $\varepsilon = 0.1$ and $\delta = 0.05$), the O-SI scheme remains stable even for strong temperature perturbations associated with large negative or positive values of α. However, this is a serious limitation for low resolution mesoscale applications which require large time-steps, since the computational mode is amplified in the asymptotic limit of large time intervals ($\Delta t \to \infty$). Cases 3 and 6 in Table 2.1 are good examples of how strong temperature perturbations (either positive or negative) can trigger numerical instability when no decentering if employed for the O-SI scheme. A common characteristic of all the unstable cases is that the model yields velocity and temperature deviations of the similar order of magnitude as their respective mean values. Hence, the need of time decentering for mesoscale weather forecasts and wind simulations over complex terrain is justified. Without any explicit diffusion mechanism, the O-SI scheme is definitely unstable due to the non-linear relation of the pressure-gradient and temperature perturbations.

Table 2.1 Statistical results after 24 h for isothermal atmosphere-at-rest experiments with the O-SI scheme over flat terrain, varying the time-step (Δt), surface temperature ratio (α_{surf}), Robert-Asselin time-filter (δ) and time decentering coefficient (ε).

Case	Δt (s)	α_{surf}	δ	ε	u, mean (m/s)	u, σ (m/s)	w, mean (m/s)	w, σ (m/s)	T_{surf} (K)	T, mean (K)	T, σ (K)	Stability condition
1	120	+ 0.05	0	0	2.84351	4.10932	- 5.620 e-3	3.01096	262.5	266.639	0.68053	Unstable
2	30	+ 0.5	0.05	0	5.773 e-7	0.00252	2.947 e-5	0.00117	375	374.997	0.00144	Stable
3	60	+ 0.5	0.05	0	0.43204	2.64208	- 1.03414	0.61146	375	339.979	0.95264	Unstable
4	120	+ 0.5	0.05	0.1	- 6.401 e-7	0.00150	- 4.348 e-7	0.00112	375	374.994	0.00088	Stable
5	30	– 0.3	0.05	0	3.197 e-7	0.00185	- 1.391 e-5	0.00055	175	175.001	0.00059	Stable
6	60	– 0.3	0.05	0	- 1.52625	5.53774	- 1.38167	5.00726	175	171.351	3.29972	Unstable
7	120	– 0.3	0.05	0.1	6.306 e-7	0.00122	- 1.258 e-5	0.00103	175	175.002	0.00061	Stable

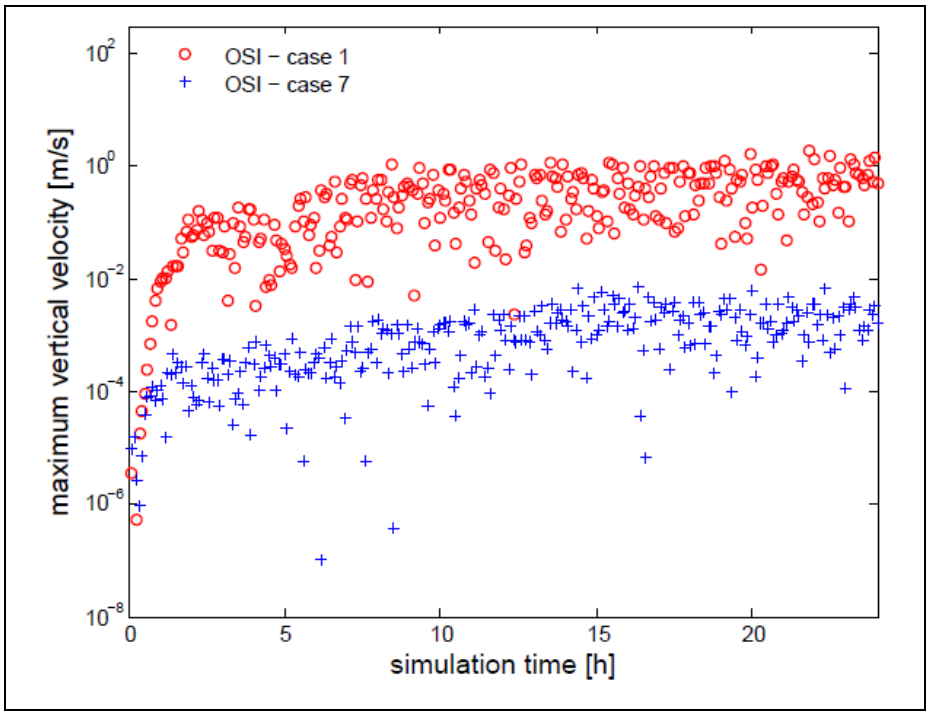

Figure 2.1 Maximum vertical velocity $|w|_{max}$ 24 h evolution for the resting-atmosphere cases 1 and 7 of Table 2.1, done with the O-SI scheme.

Despite of these results, the extended analysis might be seen as over-pessimistic since there is certain amount of damping due to interpolations associated with the semi-Lagrangian part of SISL method, which controls the computational modes that compromise the model's stability. On the other hand, the presence of the Robert-Asselin (RA) time-filter (Asselin 1972) as an integral part of the 3-TL SI scheme, helps the SISL method maintain the numerical stability during operational forecasts. However, it is vital to identify the genesis of this inherent instability to find a suitable solution without dependence of external damping subterfuges. Often, the analysis used to highlight a problem serves to find the solution. There exists at least one way to obtain a stable scheme and control numerical noise. By linearizing the EE around mean values (T_0 and q_0), certain right-hand side non-linear terms may be treated implicitly. The analytical demonstration and experimental validation of the proposed solution are presented in sections 2.3 and 2.4, respectively.

2.4 The New Semi-implicit (N-SI) Scheme

One possible solution to the inherent numerical instability and noise of the O-SI scheme consists on the implicit treatment of terms associated with the complex coefficient $n\alpha$ from equation (2.9) while keeping unchanged the other terms involving the response factor $\Lambda_1^+ = (\lambda^2 + 2\alpha\lambda + 1)/(2 + 2\alpha)$. It entails treating implicitly non-linear terms of system (2.8) that link the pressure-gradient force with the temperature perturbation ratio α. This operation was considered due to the difficulty in dealing implicitly with all right-hand side terms of system (2.8), in particular the non-linear divergence term of the thermodynamic equation. Indeed, after spatial discretization, this divergence term appears under a vertical averaging operator, which complicates the formulation of the elliptic operator in the Helmholtz problem solved for the EE system (Girard et al., 2005).

Initially, this selective implicit treatment of non-linear terms appeared to be satisfactory since the model seemed to yield a more active, less damped response. However, in the asymptotic context of large time-steps, it gradually became a noisier solution and clearly the model integrations made without off-centering were less smooth than those made with it. The model seems to have more difficulty converging when these nonlinear terms are treated implicitly. This behavior was observed with preliminary testing for an atmosphere initially at rest, which proved that the numerical instability and noise problem remained unsolved. To circumvent the implicit treatment of the non-linear divergence term in the thermodynamic equation, a redefinition of the generalized buoyancy force (b) is required implying the choice of an appropriate prognostic variable that ensures asymptotic stability, as it will be explained later in this section.

Bénard's et al. stability analysis of the 3-TL SI scheme employed for cases with both flat and complex topography (B04 and B05, respectively) highlights the importance of choosing prognostic variables that lead to a robust algorithm. Selecting the appropriate prognostic variables ensures a stable evolution of the model that entails an alternative time discretization for the EE system. However, the authors in B05 underline that the presence of terrain slopes

reduces furthermore the set of prognostic variables that can be employed in the vertical momentum equation to obtain a stable scheme, as compared to flat terrain.

The numerical noise generated from instantaneous hydrostatic imbalances related to the O-SI time-discretization could never be eliminated. Thus, a non-linear constraint can be applied on the EE if the vertical momentum equation in (2.3) is reformulated as:

$$\frac{dw}{dt}+\frac{T}{T_*}\left[\frac{\partial}{\partial z}\left(RT_*q'\right)-g\frac{T'}{T}\right]=0\,. \tag{2.10}$$

Then, using $\alpha=T'/T_*$ and $\alpha+1=T/T_*$, and redefining the buoyancy forcing with $\hat{b}=gT'/T=g\alpha/(\alpha+1)$ as opposed to $b=gT'/T_*=g\alpha$, the non-hydrostatic semi-implicit or implicit form, respectively, of the vertical momentum equation can be adopted such that:

$$\frac{\delta w}{2\Delta t}+\overline{\frac{\partial P}{\partial z}-\hat{b}}=-\alpha\left[\frac{\partial P}{\partial z}-\hat{b}\right], \tag{2.11a}$$

$$\frac{\delta w}{2\Delta t}+\overline{(\alpha+1)\left[\frac{\partial P}{\partial z}-\hat{b}\right]}=0\,. \tag{2.11b}$$

It is clear that the key factor in this new formulation is the replacement of T_* by T in the buoyancy force definition, although the generalized pressure is kept unchanged as $P=RT_*q'$. By redefining the prognostic buoyancy variable, the linearity of the perturbation relation is recovered and the hydrostatic balance is ensured for both linear and non-linear terms. Contrary to the change in two prognostic variables proposed in B04 for the EE with a mass-based coordinate system, here only one change in the buoyancy variable is required since the vertical divergence for the EE with height-based coordinates has no metric dependency on the state of the atmosphere. Namely, the mass-based coordinate system employed in B04 requires two separate reference values for temperature and pressure (T_* and π_*), whereas for the height-

based coordinate system only the reference temperature is prescribed and, consequently, the pressure is a function of T_*.

However, according to the SHB78-type numerical stability analysis, as presented in Section 2.2, both the semi-implicit (2.11a) and implicit (2.11b) formulations still lead to an unstable scheme whenever the non-linear divergence term in the thermodynamic equation remains treated explicitly (cf. Appendix III). Thus, an implicit treatment of the divergence term D is absolutely necessary to obtain a stable N-SI scheme. The remaining issue is how to modify the thermodynamic equation in order to facilitate the solution of the Helmholtz problem for the EE system. This equation already had to be modified to allow the previous redefinition of buoyancy. In fact, the thermodynamic equation has $d\hat{b}/dt$ with $\hat{b} = gT'/T$. By employing the identity $(1/T)\,dT/dt = (T/T_*)\,d(T'/T)/dt$, which is true for a constant coefficient SI scheme with an isothermal reference state ($T_* =$ constant), we obtain the following:

$$(\alpha+1)\frac{d\hat{b}}{dt} - \gamma_* \frac{dP}{dt} + N_*^2 w = 0\,. \tag{2.12}$$

In system (2.3) the divergence term D was introduced in the thermodynamic equation through a substitution of the continuity equation to linearize its left-hand side prior to applying the SISL scheme. Instead, a semi-implicit treatment is now directly applied on equation (2.12). Subsequently, the new equation system takes the final semi-discrete form:

$$\frac{\delta u}{2\Delta t} + \overline{(\alpha+1)\frac{\partial P}{\partial x}} = 0\,, \tag{2.13a}$$

$$\frac{\delta w}{2\Delta t} + \overline{(\alpha+1)\left[\frac{\partial P}{\partial z} - \hat{b}\right]} = 0\,, \tag{2.13b}$$

$$(\alpha+1)\frac{\delta \hat{b}}{2\Delta t} - \gamma_* \frac{\delta P}{2\Delta t} + \overline{N_0^2 w} = \left(N_0^2 - N_*^2\right) w\,, \tag{2.13c}$$

$$\frac{1}{c_*^2}\frac{\delta P}{2\Delta t}+\overline{D-\frac{g}{c_0^2}w}=-\left[\frac{g}{c_0^2}-\frac{g}{c_*^2}\right]w. \tag{2.13d}$$

As previously employed, $N_0{}^2=N_*{}^2/(1+\alpha)$ and $c_0{}^2=c_*{}^2(1+\alpha)$ correspond to the buoyancy frequency and speed of sound obtained from the linearization with respect to the mean values of temperature and pressure (T_0 and q_0).

Equation system (2.13) respects the hydrostatic balance no matter what initial basic state is set for the simulation. After applying the eigenmode analysis on (2.13) the resulting temperature range that meets the asymptotic stability condition is increased to $-1\le\alpha\le 1$ (cf. Appendix III), which confirms B04 conclusion regarding the optimal selection of prognostic variables for the 3-TL SI scheme in height-based σ-coordinates. Hence, the final three-dimensional semi-discrete implementation of the enhanced EE system in MC2's dynamical kernel is:

$$\frac{\delta\mathbf{v}}{2\Delta t}+f\mathbf{k}\times\mathbf{v}+\overline{(\alpha+1)(\nabla P+\mathbf{k}\hat{b})}-(\gamma_*+\gamma_A)\mathbf{k}P=\mathbf{f}+\frac{\hat{b}}{g}\beta_A\mathbf{k}P, \tag{2.14a}$$

$$\frac{\delta}{2\Delta t}\left[(\alpha+1)\hat{b}-\gamma_* P\right]+\overline{N_0^2 w}=\gamma_A Q+\left(N_0^2-N_*^2\right)w, \tag{2.14b}$$

$$\frac{\delta}{2\Delta t}\left[\frac{P}{c_*^2}\right]+\overline{\nabla\cdot\mathbf{v}-\frac{g}{c_0^2}w}=\frac{Q}{c_p T}-\left[\frac{g}{c_0^2}-\frac{g}{c_*^2}\right]w. \tag{2.14c}$$

This includes the possibility of having a variable coefficient 3-TL SI scheme through β_A.

The redefinition of the prognostic buoyancy variable for the N-SI scheme seems a minor modification with respect to the O-SI scheme, but it has an important impact in the final structure of the discretized model equations since the enforcement of the hydrostatic balance prevents that any initial pressure-gradient imbalances trigger computational modes and spurious flows. Primarily, the N-SI scheme linearizes the EE with respect to mean values that allow the implicit treatment of non-linear terms that relate the pressure-gradient and

temperature perturbations, as well as the remaining divergence term. Numerical experiments presented in the next section demonstrate that the accuracy and stability of MC2 are considerably improved with the N-SI scheme.

2.5 Validation and Discussion

In order to assess and validate the enhanced numerical stability and noise control capability of the N-SI scheme for mesoscale applications, firstly, an extensive series of tests with a two-dimensional (2D) non-rotational atmosphere initially at rest is carried out using different parametric combinations and terrain geometries. Then, a multi-layer strongly stratified atmosphere experiment over 2D parallel ridges with different heights and slopes is performed to examine the N-SI scheme response in a mountainous context. These tests showcase the computational mode that develops into high-speed spurious flows enhanced by steep terrain slopes.

The physical parameterization of moisture, precipitation, radiation, tracers and turbulence, as well as horizontal numerical diffusion and time decentering operators, are turned off to isolate the SI scheme without any explicit damping mechanisms. The scope of this study and main purpose of this section is to examine the propagation of computational modes under complex idealized conditions to validate the capabilities of the pure N-SI scheme before considering any application over fine-scale terrain.

We encourage the reader to consult Flores-Maradiaga et al. (2016), that provides a comprehensive discussion of additional validation tests of the neutrally stratified atmospheric boundary layer flow over classical terrain features using the enhanced MC2 model with imbedded large-eddy simulation method. Furthermore, in the second part of this study, presented here as Chapter 3, the model's response is examined with stratified orographic flow simulations over real high-impact topography in the Canadian Rocky Mountains, also using a modified statistical dynamical downscaling method.

2.5.1 Atmosphere-at-rest Simulations with Different Terrain Slopes

In general, an atmosphere-at-rest simulation for these 2D cases requires an initialization with a hydrostatically balanced non-rotational atmosphere with zero horizontal velocity input, zero horizontal pressure gradient and a horizontally homogenous thermodynamic sounding. For these simulations, a free-slip condition and constant temperature are imposed on the surface. At the top of the domain a numerical sponge layer, based on Shuman's boundary condition (Shuman 1957, eq. 5, pg. 358), is set to restrict the spurious reflection of acoustic and gravity waves. Following Pinty et al. (1995) and Schär et al. (2002), the initial temperature field is generally defined with a quasi-linear function of the surface temperature (T_{surf}), the local thermal stratification (N) and the physical height above the ground (z), obtained from the solution of the atmospheric lapse rate differential equation. Considering an isothermal height scale based on the initial surface temperature ($H_T = RT_{surf}/g$), it results in:

$$T(z) = T_{surf}\left[\exp\left(\frac{N^2 z}{g}\right) + \left(\frac{g^2}{c_p N^2 T_{surf}}\right)\left(1 - \exp\left(\frac{N^2 z}{g}\right)\right)\right]. \qquad (2.15)$$

However, these cases are initialized with an isothermal atmosphere, an ideal condition that simplifies the analysis of the temperature perturbation influence on the model's stability. The surface and isothermal reference temperatures are set to 250 K, which is a reasonable choice for mesoscale experiments (Girard et al., 2005).

The model grid has zonal (*x*-axis) periodicity and span-wise (*y*-axis) translational slab symmetry, which implies spatial invariance and momentum conservation of the flow field along the transverse direction of a semi-infinite grid (Goldstein and Poole, 2001). The basic terrain-following (BTF) σ-coordinate (Gal-Chen and Somerville, 1975) as well as the SLEVE coordinate (Schär et al., 2002) are employed in combination with the Arakawa C-type staggered grid. Specific model settings for each test are stated in the following sub-sections and more details on the numerical aspects of the MC2 model are available in Thomas et al. (1998), Girard et al. (2005) and Gasset et al. (2014). A 2D smooth Gaussian hill is selected for

the first suite of experiments (cf. Fig.2-b) with the analytical form:

$$h(x) = h_m \exp\left[-\left(\frac{x}{a}\right)^2\right]. \tag{2.16}$$

Here h_m is the maximum terrain height and a is the mountain half-width. The domain is $L_x =$ 10 km long and $L_z = 5$ km high, with horizontal and vertical resolutions of $\Delta x = 100$ m and $\Delta z = 50$ m, respectively. The best choice of time interval to ensure a stable SISL solver will be discussed latter, but preliminary testing revealed that $\Delta t = 10$ s is a good compromise for this grid resolution. To assess the benefits of the N-SI scheme as compared to the O-SI scheme, two isothermal atmosphere-at-rest simulations using flat terrain and a steep ridge (with a maximum slope of $\vartheta = 45°$) are carried out for 72 hours, enough integration time to observe the computational mode's asymptotic growth. With numerical instability there is no guarantee that the model would converge to the correct solution, because the floating-point round-off or truncation errors can be magnified, instead of damped, causing the deviation from the exact solution to grow exponentially in an asymptotical fashion (Burden and Faires, 2011).

The O-SI and N-SI comparison is presented in Figure 2.2, where the horizontal velocity cross-sections are taken at 42 hours of integration. The choice of this specific time for comparisons is due to the incapacity of the model to complete the full simulation with the O-SI scheme, which generates strong computational modes and causes the solver to crash shortly after 42 hours (as illustrated in Fig. 2.2-e). MC2 however is capable of successfully completing the simulation with N-SI scheme. The first two panels, Figures 2.2a and 2.2b, correspond to O-SI simulations and Figures 2.2c and 2.2d to the N-SI results with flat terrain and the Gaussian hill, respectively. It is noteworthy that the velocity scale of the O-SI results is three orders of magnitude larger than those of the N-SI scheme, indicating the former generates stronger numerical noise.

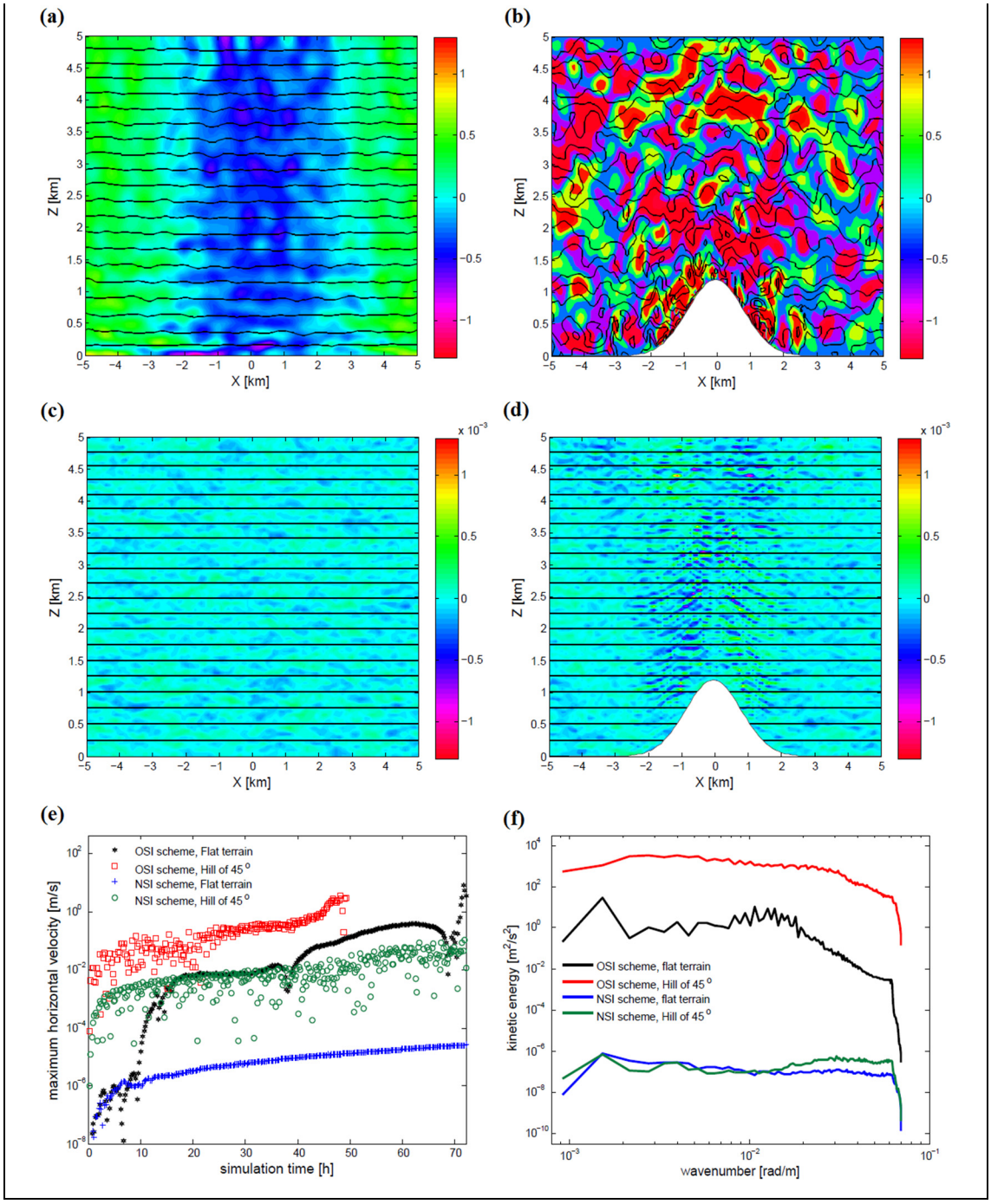

Figure 2.2 Horizontal velocity field cross-sections at 42 h, for an isothermal atmosphere initially at rest over flat terrain and a steep mountain, employing the O-SI scheme in panels (a) and (b) and the N-SI scheme in panels (c) and (d). Solid lines denote potential temperature isentropes (interval of 2.5 K) and color shading the horizontal velocity (m s-1). Panels (e) and (f) respectively illustrate the evolution of the absolute maximum horizontal velocity $|u|_{\max}$ and the 2D kinetic energy spectra of noise.

The time evolution of the maximum vertical velocity $|w|_{\max}$ for each test is presented in Figure 2.2e. Additionally, the two-dimensional kinetic energy spectra presented in Figure 2.2f is calculated with a Fast Fourier Transform (FFT) using both the horizontal and vertical velocity components. These spectra illustrate the modal decomposition of the velocity field into large- and small-scale components dependent of the grid cut-off wavenumber $k_g = 2\Delta x$ (corresponding to the minimum resolvable wavelength), which helps to assess the numerical noise kinetic energy accumulation.

In Figure 2.2a, 2.2b and 2.2e it is evident that the O-SI scheme generates an asymptotically growing computational mode over both flat and complex terrain, which inevitably yields an extremely noisy and unstable model. The horizontal inhomogeneity exhibited by the O-SI scheme over flat terrain is mainly due to the spurious flow generation that derive from initial imbalances in the pressure field. Complex terrain amplifies the high-frequency noise at least one order of magnitude and leads to an early blow-up of the unstable model. Steep hill slopes magnify spurious flows, which could erroneously be considered as mountain top speed-up or lee-side wind storms, leading to wind speed overestimation in real mesoscale applications.

On the contrary, the N-SI scheme yields very weak motions nearly three orders of magnitude lower (10^{-3} m s^{-1}) than the O-SI results for both flat and steep mountain cases (Figures 2.2c and 2.2d, respectively). The spectra comparison of both SI schemes in Figure 2.2f reveals a significant reduction of the noise kinetic energy accumulation for the full range of wavenumbers when using the N-SI scheme. Furthermore, we distinguish an extended dissipation range ($k > 10^{-2}$ m^{-1}) in the O-SI noise spectrum, which resembles the physical turbulence dissipation range. Thus the O-SI spurious circulations behave as numerically generated turbulence that can contaminate atmospheric boundary layer simulations. The O-SI scheme alone is notoriously unable to perform accurately and cannot yield reliable results due to its inherent instability and strong numerical noise generation.

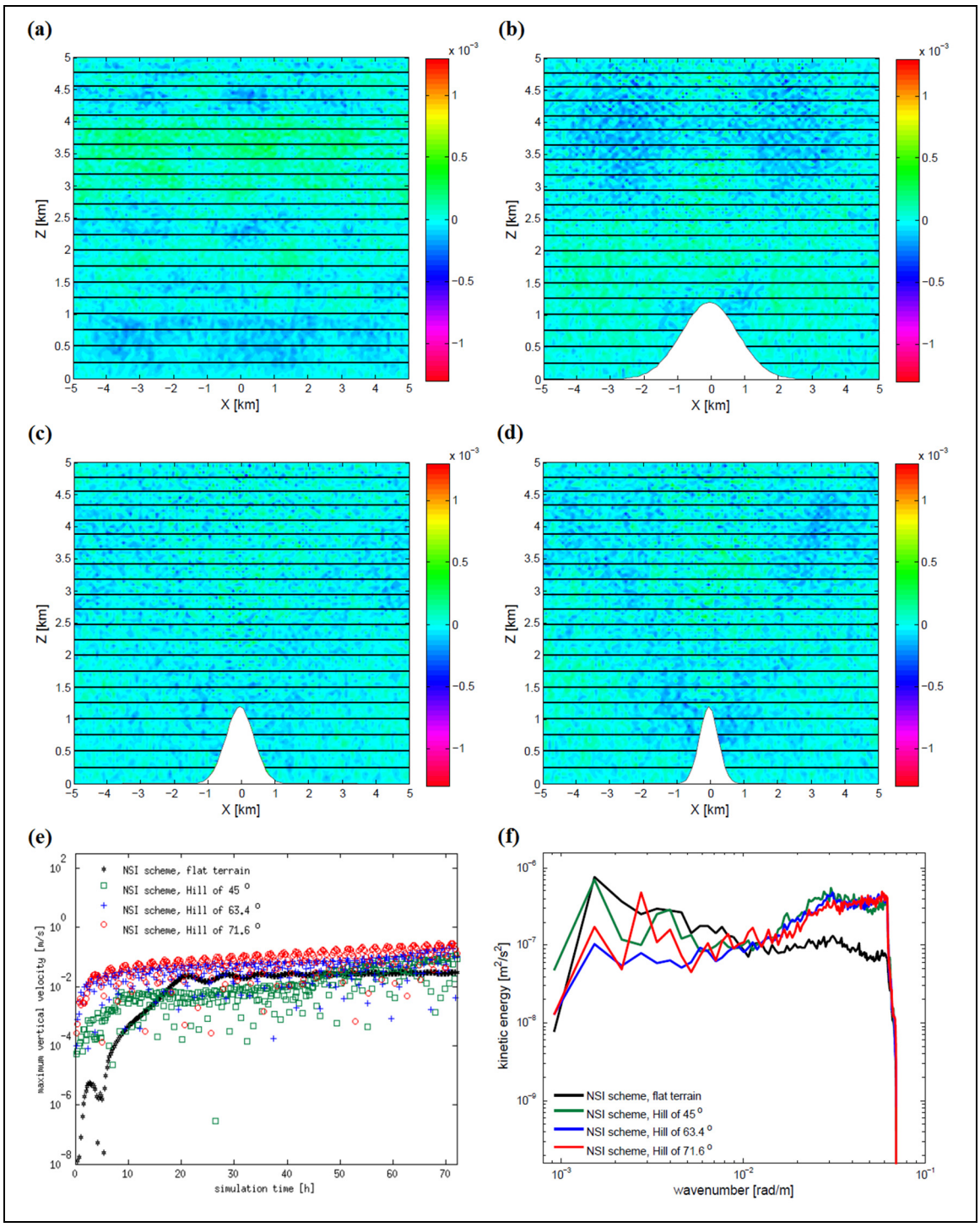

Figure 2.3 As in Figure 2.2, but comparing the vertical velocity cross-sections, $|w|_{\max}$ evolution and kinetic energy spectra of an isothermal atmosphere initially at rest using the N-SI scheme over (a) flat terrain and a Gaussian hill with maximum slope of (b) 45 °, (c) 63.4 ° and (d) 71.6 °, respectively.

Keeping the same grid ($\Delta x = 100$ m, $\Delta z = 50$ m, $L_x = 10$ km, $L_z = 5$ km, 100×100 points) and model settings ($\Delta t = 10$ s and $T_* = 250$ K), the terrain slope is increased to test the N-SI scheme in more stringent conditions. The assessment of the model's response to the grid resolution sensitivity is presented in Section 2.5.2. The 42 hours instantaneous cross-sections of the vertical velocity fields with four terrain slopes are illustrated in Figure 2.3a through Figure 2.3d. A noticeable characteristic of these results is the weak numerical noise obtained with the N-SI scheme, regardless of the terrain slope. Under the imposed conditions the computational modes and associated numerical noise are effectively controlled by the N-SI scheme, and the spurious flows close to steep slopes are inexistent. This behaviour is confirmed in Figs. 3e and 3f, which show how the time evolution of $|w|_{\max}$ and noise kinetic energy accumulation of the whole set arrive to the same orders of magnitude. Also, the spectra of the N-SI results reveal a bimodal behaviour, where numerical noise at wavenumbers higher than the cut-off $k_g = 2\Delta x$ becomes slightly stronger as the terrain slope increases.

We observe in Figure 2.3e a clear convergence of the maximum vertical velocity $|w|_{\max}$ for the flat terrain case, and slowly growing small amplitude oscillations for the three subsequent terrain slopes. This incremental response in presence of steeper terrain is caused by a remnant computational mode inherently generated by the unfiltered leapfrog solution of the EE system. Even though this is a weak sign of linear instability, the phase speed of these computational modes (c) is kept bounded by the N-SI scheme to the general stability criterion $c\,\Delta t/k_g = c\,\Delta t/2\Delta x \leq 1$ (Haltiner, 1971). This shows that the N-SI scheme alone has the capability of controlling the numerical noise generated in presence of steep topography, but still needs the Robert-Asselin (RA) frequency filter as a fundamental component of the leap-frog scheme to obtain a robust SISL algorithm.

As explained by Durran (2010), for the pure leap-frog scheme solution to remain numerically stable it is a sufficient stability condition to be bounded to the Courant-Friedrichs-Lewy (CFL) criterion $c\,\Delta t/\Delta x \leq 1$. If this is not fulfilled, there will always be some waves that experience spurious amplification. Even if these computational modes were not initially present, the

round-off errors during calculations could derive into amplified spurious oscillations. Consequently, the linearly dependent physical and computational modes of the leap-frog solutions grow with a period of $4\Delta t$ (Durran 2010). Therefore the need of employing a second-order RA time-filter, which preferentially restricts the high frequency waves and impacts the poorly resolved $2\Delta t$ component of the solution. The conjunction of the 3-TL SI scheme and the leap-frog scheme with RA time-filter ensures a stable SISL solver for non-linear advection oscillatory problems (Asselin 1972, Robert 1981).

Nonetheless, it has been noticed by Durran (2010) and Williams (2011) that the RA time-filter degrades the global truncation error from second-order to first-order accuracy, which is certainly a minor problem but quite important in the context of the 3-TL SI stability investigation. To recover higher accuracy for the new SISL scheme, the Robert-Asselin-Williams (RAW) time-filter based on Williams (2011) was implemented in MC2 since it conserves the total energy of the solution and reduced significantly the truncation errors while filtering non-linear unresolved spurious waves. Williams proved that the RAW frequency filter ensures numerical stability and a higher performance for the model, although in practice it still exhibits first-order accuracy. The application of this additional enhancement to the model will be illustrated in the following sub-sections.

Finally, regarding the steep slope limitations of oblique σ-coordinates, Giebel (2006) remarked that simulations over high-impact orography using MC2 with the O-SI scheme were strongly restricted by terrain slopes. Hence the need to filter the topographic signal in order to obtain a gently-sloping smoothed surface, which usually do not exceed a maximum slope of 0.2 ($\vartheta \approx 11.3°$) as seen in Benoit et al. (2002), Pinard et al. (2005) and Pinard (2009). Without the pre-processing of small-scale steep slopes the model will definitely yield very noisy results and even blow up. Real fine-scale simulations with the O-SI scheme have been possible only when employing the off-centering operator that hides the model's slope limitation. The N-SI scheme seems to be a plausible solution to overcome this steep slope constraint and obtain more accurate results for mesoscale modelling.

2.5.2 Atmosphere-at-rest Simulations with Different Parametric Combinations

A second series of initially resting-atmosphere tests is now presented to gain insight on the effects of varying one or more control parameters. Apart from the terrain slope, the N-SI scheme is tested with different time-steps (Δt), grid resolution (Δx, Δz), surface temperature ratio (α_{surf}) and Brunt-Väisälä frequency (N). Table 2.2 lists the values of the tested parameters, one at a time to isolate their individual effect on the model's response. These experiments use the same bottom, lateral and top boundary conditions, and grid specifications ($L_x = 10$ km, $L_z = 5$ km, 100×100 points) as detailed in section 2.4.1, using the steepest mountain with maximum slope of $\vartheta = 71.6°$ for all parametric combinations.

Table 2.2 Different parametric combinations of terrain slope (ϑ), time-step (Δt), grid resolution (Δx, Δz), surface temperature ratio (α_{surf}), and Brunt-Väisälä frequency (N) for atmosphere-at-rest experiments with the N-SI scheme.

Control parameter	Tested values	Fixed values				
		ϑ	Δt	(Δx, Δz)	α_{surf}	N (*)
Maximum terrain slope	Flat (0), 45°, 63.4°, 71.6°	-	1 s	(100 m, 50 m)	0.2	Isothermal
Time-step (Δt)	1 s, 10 s, 15 s, 20 s	71.6°	-	(100 m, 50 m)	0.2	Isothermal
Grid resolution (Δx, Δz)	(25 m, 12.5 m), (50 m, 25 m), (75 m, 37.5 m), (100 m, 50 m)	71.6°	1 s	-	0.2	Isothermal
Surface temperature ratio (α_{surf})	-0.3, 0.05, 0.2, 0.5	71.6°	1 s	(100 m, 50 m)	-	Isothermal
Brunt-Väisälä frequency (N)	0 s^{-1}, 0.01 s^{-1}, 0.02 s^{-1}, 0.03 s^{-1}, (*) isothermal $N = 0.0187$ s^{-1}	71.6°	1 s	(100 m, 50 m)	0.2	-

In Figure 2.4a we observe that for fixed horizontal and vertical resolutions of $\Delta x = 100$ m and $\Delta z = 50$ m, a small time-step (e.g., $\Delta t = 1$ s) seems to be the best alternative to keep a stable model. Henceforth, a time-interval of $\Delta t = 1$ s will be used for the subsequent combinations. Notably, with a larger time-step such as $\Delta t = 10$ s the solution is still bounded to the nominal CFL condition, but it should be cautiously tuned with the grid resolution to ensure linear stability when employing the unfiltered leap-frog scheme (cf. section 2.4.1).

Employing a larger time-step such as $\Delta t = 20$ s with a fine-scale mesh generates an asymptotically growing computational mode that drives the unstable solver to an inevitable crash. Even though the SISL scheme allows the use of large time-steps to reduce the calculation overhead (Simmons 1978, Robert 1982, Staniforth and Côté 1991), the fundamental stability relationship between the spatial resolution, time interval and wave phase-speed is restrictive for fine-scale meshes when no frequency filter is employed.

Then, to evaluate the model's sensitivity to mesh spacing, four combinations of horizontal and vertical resolutions are tested, keeping the same domain size ($L_x = 10$ km, $L_z = 5$ km), aspect ratio ($A_R = \Delta x / \Delta z = 2$) and a fixed time-step of $\Delta t = 1$ s. In Fig.4b we observe how refining the grid cells affects the numerical stability for these settings. As the resolution increases the model becomes noisier, more unstable and prone to blow-up. This instability can be prevented by tuning the mesh resolution so the linear stability condition is respected. Thus, horizontal and vertical grid-spacing of $\Delta x = 100$ m and $\Delta z = 50$ m, respectively, seems appropriate to achieve a stable long-term integration for the given conditions.

In this isothermal context, the variation of the surface temperature with respect to the basic reference sounding (T_*) is sufficient to produce buoyancy perturbations throughout the domain, which potentially causes numerical instability and spurious forcing due to the non-linear relationship of temperature and pressure-gradient imbalances. These initial temperature fluctuations can be controlled through the surface temperature ratio $\alpha_{surf} = \left(T_{surf} - T_*\right) / T_*$. Test results for the same α_{surf} used in Table 2.1 are illustrated in Figure 2.4c, for which the values

of reference and surface temperatures are $T_* = 250$ K and $T_{surf} = 175$ K (262.5 K, 300 K or 375 K), respectively. Results in Figure 2.4c shows that as the absolute value of the temperature perturbation $|\alpha_{surf}|$ increases the model becomes unstable and rather noisy. In fact, without any explicit diffusion mechanism, all these cases present some degree of numerical instability. This demonstrates the close relationship between numerical stability and temperature perturbations, which become more evident in a non-isothermal context.

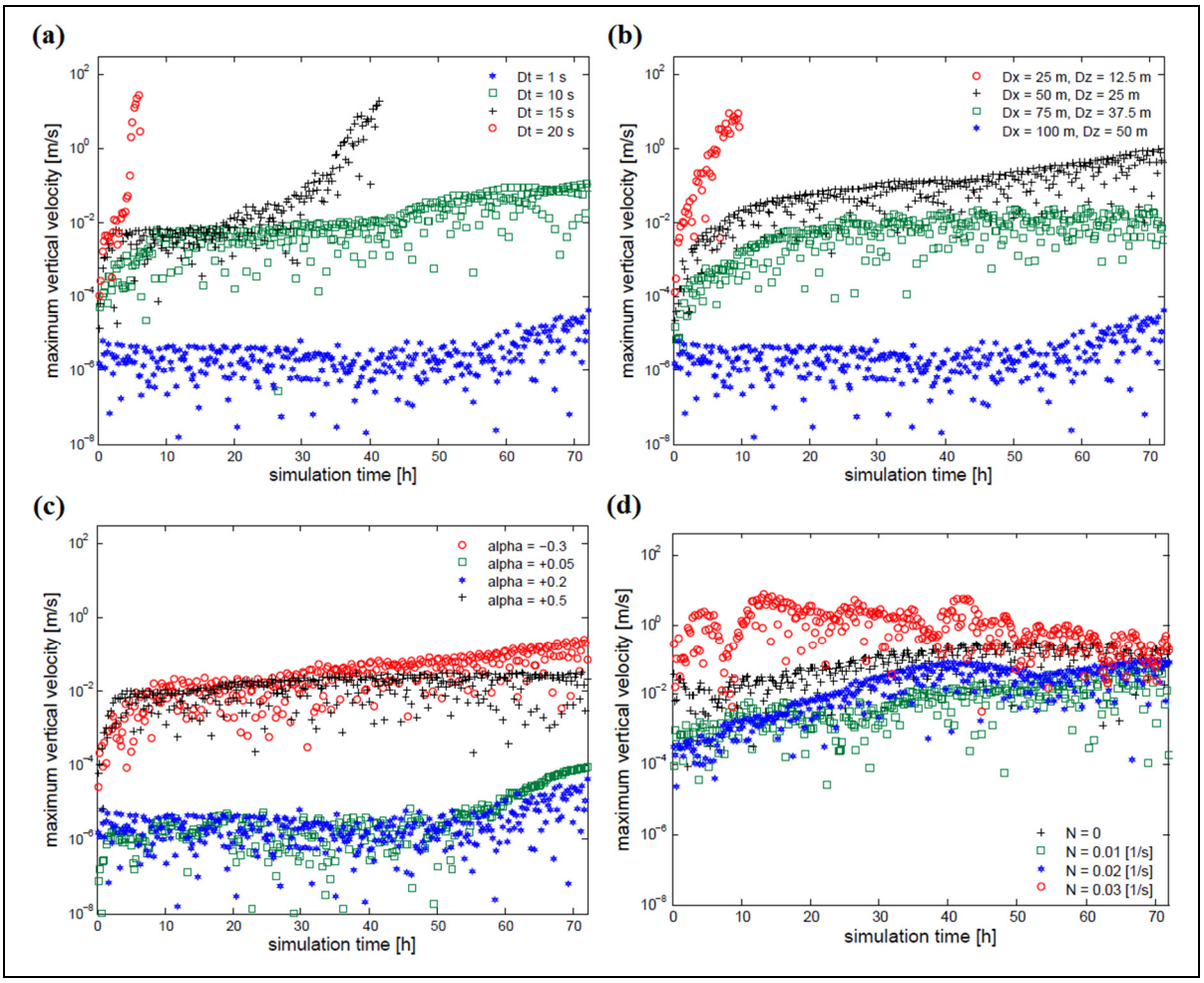

Figure 2.4 Evolution of the maximum vertical velocity $|w|_{\max}$ with the N-SI scheme when varying (a) time-step, (b) grid resolution, (c) surface temperature and (d) stratification.

The outcomes obtained for neutral, slightly stable, stable and strongly stable atmospheres with buoyancy frequencies of $N = 0$ s^{-1}, 0.01 s^{-1}, 0.02 s^{-1} and 0.03 s^{-1}, respectively, are presented in

Figure 2.4d. It is evident that as the Brunt-Väisälä frequency deviates farther from the isothermal natural frequency (i.e., $N = 0.0187\ s^{-1}$) the temperature perturbations become larger, therefore, generating high-speed computational modes. We can infer that stronger thermal stratifications for cold atmospheres will challenge the N-SI numerical stability due to large temperature deviations with respect to reference and mean values. Thus, for mesoscale modelling in cold-climate mountainous sites, such as the Alps (Benoit et al., 2002a) or the northern Rocky Mountains (Pinard et al., 2009), it is of particular interest that the SISL method performs efficiently.

In general, the N-SI scheme performs well for relatively small temperature perturbations in isothermal and quasi-isothermal stratified atmospheres. However, due to the inherent linear and non-linear instability of the pure multi-step leapfrog scheme, prone to excite fast computational modes, the RAW time-filter is also needed to preserve the SISL's robustness and second-order accuracy. To demonstrate the significant improvement obtained with the RAW time-filter, we selected the most challenging cases previously discussed, for which the pure N-SI scheme was not effective. These selected cases are done employing the RAW filter with the traditional Asselin coefficient of $\delta = 0.05$ and a new RAW smoothing coefficient of $\delta_{RAW} = 0.5$, specifically recommended in Williams (2011) for the SI discretization schemes. Results for the N-SI scheme combined with the RAW time-filter are presented in Figure 2.5.

Firstly, Figures 2.5a and 2.5b respectively illustrate how the model's response is kept bounded when the RAW filter is applied to the failed cases of a large time-step $\Delta t = 20$ s and high resolution $\Delta x = 25$ m & $\Delta z = 12.5$ m. Moreover, Figure 2.5c and 2.5d exemplify the application of the RAW filter to control the numerical noise and non-linear instability caused by strong temperature perturbations or due to a strong thermal stratification. Gladly, this combined solution yields excellent results with weak spurious circulations that remain bounded to an order of 10^{-5} m s^{-1}. Accordingly, the RAW time-filter is found to be necessary for more accurate and numerically stable simulations, enabling MC2 with N-SI scheme to achieve long integrations of stratified atmospheric flow over high impact terrain as will be discussed in the following sub-section.

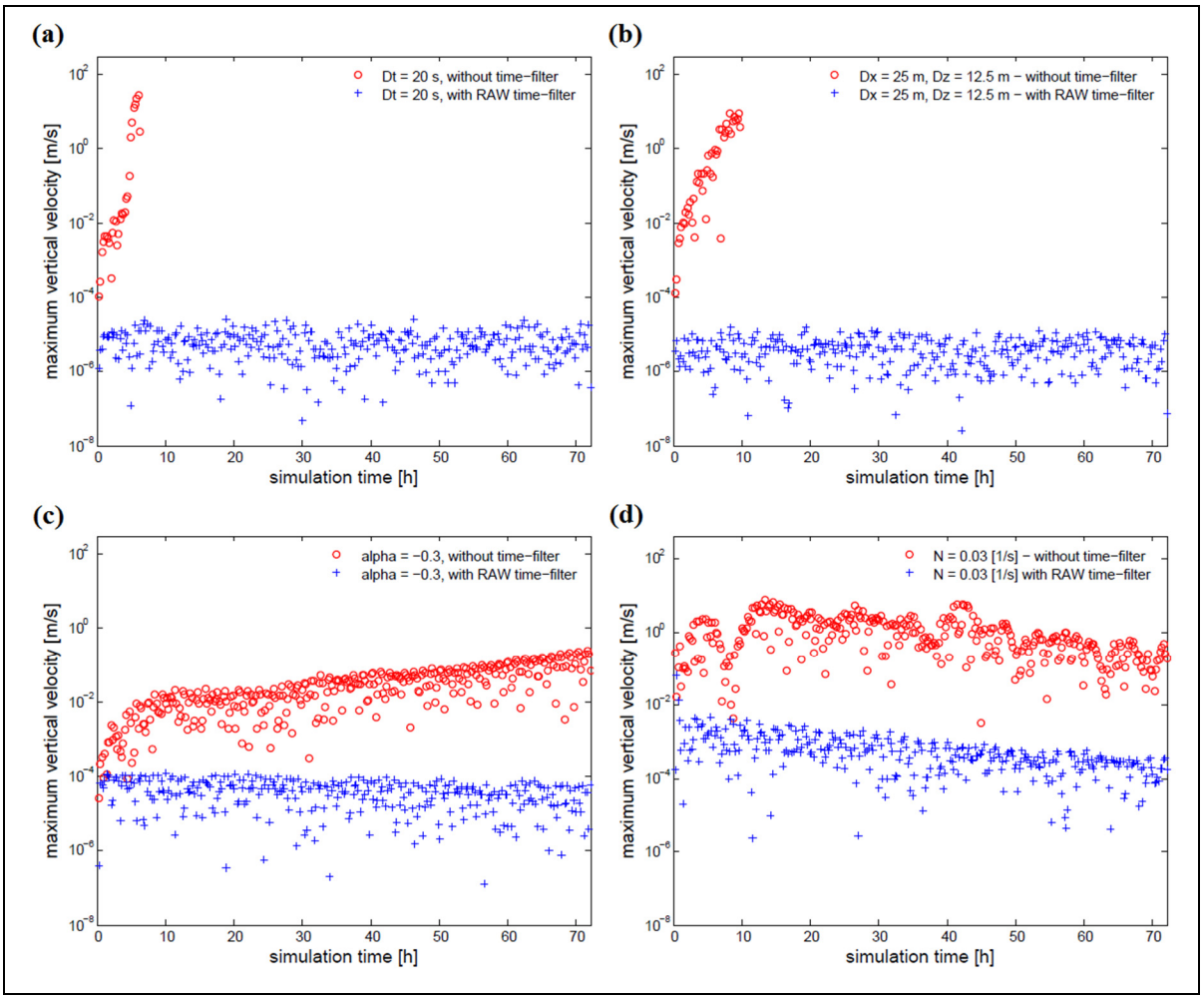

Figure 2.5 As in Figure 2.4, but using the combined N-SI scheme and RAW time-filter for the previous unstable resting-atmosphere tests.

2.5.3 Atmosphere-at-rest Multi-layer Simulations over Steep Parallel Ridges

To examine and validate the proposed solution with a more challenging topographic configuration, the classical Schär mountain is used for a set of 2D multi-layer non-isothermal atmosphere-at-rest experiments. For this set of tests, the following cosinusoidal signal of parallel ridges superposed on a Gaussian profile is employed:

$$h(x) = h_m \exp\left[-\left(\frac{x}{a}\right)^2\right] \cos^2\left(\frac{\pi x}{\lambda}\right), \tag{2.17}$$

where h_m represents the maximum terrain height, a the width of the large-scale terrain features and λ the width of the small-scale terrain features. This terrain profile is basically a superposition of corrugated fine-scale features over gently sloping mesoscale topography.

As previously mentioned in the introduction, MC2 employs the BTF σ-coordinate based on the standard Gal-Chen and Somerville transformation $Z = z_t\,(z - z_s)/(z_t - z_s)$, which was reported to yield noisy results over steep complex terrain. For this reason, the smooth level vertical (SLEVE) coordinate, introduced by Schär et al. (2002) and Leuenberger et al. (2010), was adopted to reduce the remaining numerical noise and maintain the model's computational stability for steep complex terrain. Girard et al. (2005) validated the enhancement with the SLEVE coordinate running a 2D non-hydrostatic mountain wave simulation over the Schär mountain and a 3D simulation over a complex region in the Alps. The latter case was aimed to reproduce the IOP-2b field experiment of the Meteorological Alpine Program (MAP), which was successfully simulated with a reasonable reduction of terrain-induced noise.

Presumably, the combination of the N-SI scheme, RAW time-filter and SLEVE coordinate will allow the reduction of any remnant numerical noise. To prove this hypothesis we reproduce the atmosphere-at-rest canonical test suggested by Klemp (2011) and Zängl (2012), who respectively reported similar solutions for the numerical noise problem based on a correction of the HPG force calculation when employing the oblique σ-coordinate. This idealized case is launched with a non-isothermal multilayer resting-atmosphere and the Schär mountain profile (17), with the same settings originally defined in Schär et al. (2002) ($h_m = 1$ km, $a = 5$ km and $\lambda = 4$ km). Then, in congruence with the test performed by Klemp (2011), the decay scale heights for the SLEVE coordinate are fixed to $s_1 = 4$ km and $s_2 = 1$ km, which yields a minimum coordinate invertibility condition of $\gamma_{\min} \approx 0.38$ for our grid configuration.

The time-step is kept as $\Delta t = 1$ s for a uniform structured grid $L_x = 200$ km long and $L_z = 20$ km high, set with horizontal and vertical mesh-sizes of $\Delta x = 500$ m and $\Delta z = 100$ m, respectively. The choice of mesh resolution is particularly important when using σ-coordinates

since the model's stability and noise control depends mostly on the vertical grid increment, which Steppeler et al. (2002) recommend to be greater than or equal to the terrain height increment per grid cell ($\Delta z \geq \delta h$), and in this particular case has a mean value of $\delta h = 80$ m. For the same case, Klemp (2011) reported results only for a coarse vertical resolution, i.e. $\Delta z =$ 500 m, which ensured a stable simulation with his settings since the steep slopes were under-resolved. However, for mesoscale models the lowest main level is set at 10 m a.g.l. or lower, and the height difference between neighboring grid points Δh may be two orders of magnitude larger than this near-surface thickness Δz_1. Although not explored in this study, currently, the accuracy and numerical stability of the back-trajectory calculation of the new SISL method is being assessed to define the implications of large ratios of $\Delta h/\Delta z$ for strong orographic flows. This important aspect will be reported in a future paper.

The temperature profile presented in equation (2.15) is employed for thermal initialization, yielding a multi-layer non-isothermal basic state with a buoyancy frequency of $N = 0.01$ s^{-1} throughout the domain, except for a 1 km thick strongly stratified inversion layer with a gradient of $N = 0.02$ s^{-1} located between 2 and 3 km above the flat terrain surface. A surface temperature of 300 K is chosen for this case, as suggested Klemp (2011). The results obtained after 6 h for different combinations of SI schemes and terrain-following coordinates are presented in Figure 2.6. It is worth noting that Figure 2.6a is scaled one order of magnitude higher than Figures 2.6b to 2.6d in order to underline the O-SI and N-SI differences.

Combining the OSI scheme and BTF σ-coordinate without any physical parameterization, explicit diffusion, off-centering or time-filtering operators, yields very strong pressure and temperature perturbations, clearly distinguished in Figures 2.6a and 2.6e with the deformed potential temperature isentropes and high-speed spurious motions of an order of 10 m s^{-1}. Then, combining the N-SI scheme and BTF σ-coordinate achieves a numerical noise reduction of at least two orders of magnitude under the same conditions (Figures 2.6b and 2.6e). This remarkable improvement is already comparable with the results reported by Klemp (2011, Figure 2.1f) and Zängl (2012, Figure 2.4a), with less active motions in the inversion layer.

This was expected to happen, since the linearity of the hydrostatic relation is recovered with N-SI scheme and the initial pressure and temperature imbalances are controlled with the implicit treatment of the left-hand side terms in the discretized EE system. As an immediate consequence of the N-SI scheme, the vertically propagating artificial motions are significantly weaker than the previous results. Although some terrain-induced noise persists, the hydrostatic imbalances caused by the deformed BTF σ-coordinate are dealt with the N-SI scheme provided an adequate choice of model settings.

Then, replacing the BTF coordinate with the SLEVE coordinate, combined with the N-SI scheme, does not change significantly the flow fields and time evolution of $|w|_{\max}$ (Figures 2.6c, 2.6e and 2.6f, respectively), but the model sustains a low noise level and smoother potential temperature isentropes aloft the underling surface. Indeed, this effect was improved when combining the N-SI scheme, RAW time-filter and SLEVE coordinate (Figures 2.6d and 2.6f), which demonstrates that artificial motions close to steep slopes tend to disappear with this final combination. The present assessment certainly proves that the N-SI scheme combined with the energy conserving RAW time-filter and the scale-dependent SLEVE coordinate significantly enhances MC2's numerical stability, accuracy and noise control for mesoscale modelling over complex topography.

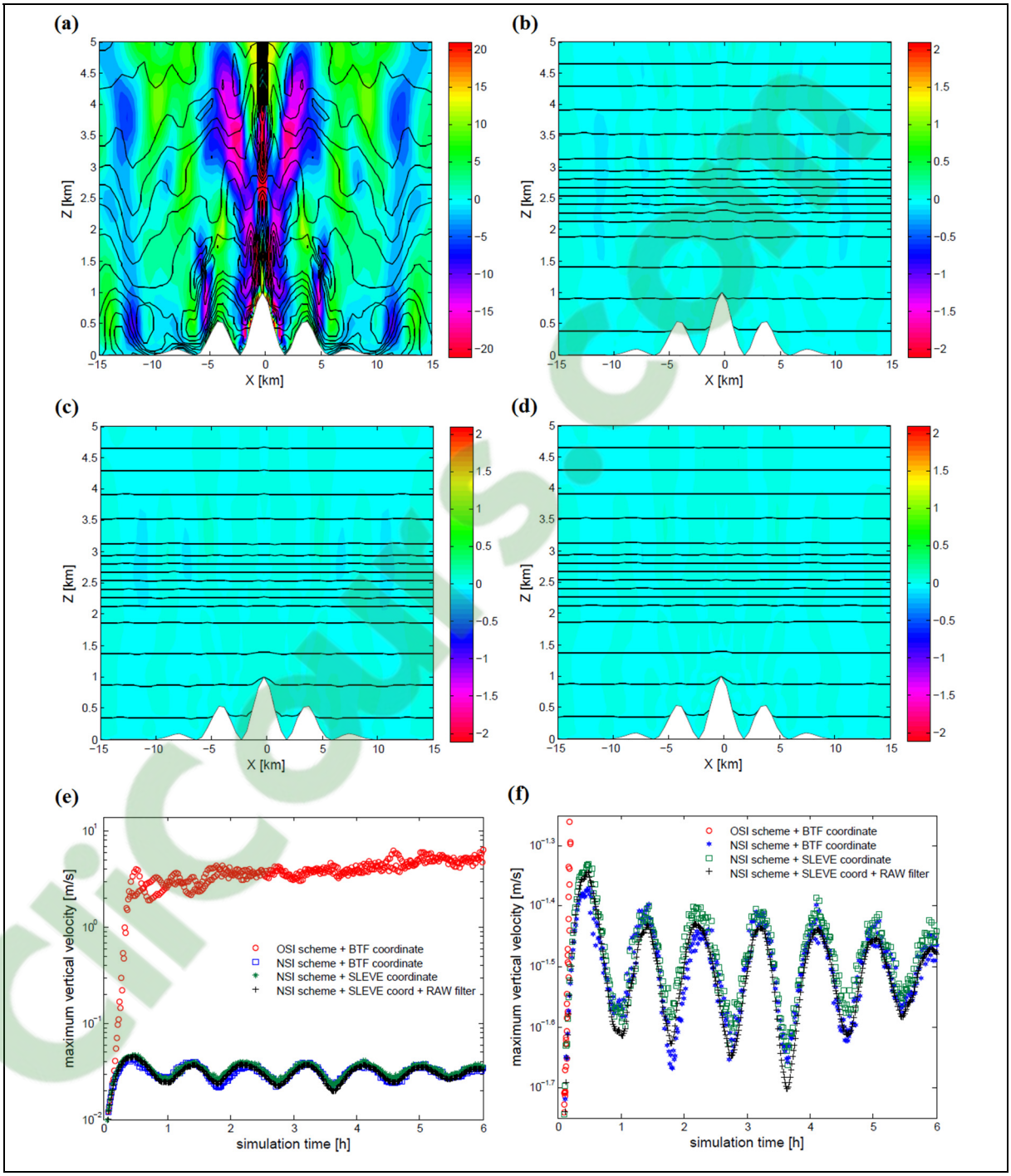

Figure 2.6 Vertical velocity cross-sections at $t = 6$ h for a non-isothermal resting-atmosphere over the classic Schär mountain tested with the combined (a) O-SI scheme + BTF coordinate, (b) N-SI scheme + BTF coordinate, (c) N-SI scheme + SLEVE coordinate and (d) N-SI scheme + SLEVE coordinate + RAW time-filter. Panel (e) shows the time evolution of $|w|_{\max}$, and panel (f) corresponds to a zoom in of $|w|_{\max}$.

2.6 Summary

An extended stability analysis of the 3-TL SI scheme applied to the compressible non-hydrostatic EE system with height-based σ-coordinates has been examined for flat and complex topography. This extended stability analysis confirmed Bénard's et al. (2004, 2005) observations on the intrinsic numerical instability and sensitivity to the choice of prognostic variables for the original constant-coefficient 3-TL SI scheme. Indeed, the O-SI scheme in presence of temperature perturbations and steep terrain slopes, without any time decentering and/or filtering, develops an asymptotically growing computational mode, high-frequency numerical noise and strong spurious flows. This numerical instability degrades the capability of the SISL algorithm to achieve long-term integrations, and the resulting artificial motions rapidly contaminate the model's physical mode.

This numerical stability and noise problem can be considerably reduced with a careful reformulation of the SI time discretization scheme, based on a linearization of the EE system around mean values of temperature and pressure and the adequate choice of prognostic variables that ensure the model's response is kept bounded to the fundamental stability condition. In particular, an appropriate redefinition of the buoyancy force yields a restructuration of the explicitly treated residuals on the right-hand side of the EE system, which link the pressure-gradient and temperature perturbations. Namely, the coefficients of non-linear terms, responsible for the numerical instability in the classical SI scheme, are modified in such a way that the linearity of the hydrostatic perturbation relation is recovered and the scheme enters in a stable domain. In a practical sense, tests done with steep topography and various model settings demonstrate the robustness of the N-SI scheme, which is able to complete long integrations generating very weak numerical noise.

Nonetheless, when the N-SI scheme is employed for very stiff problems, without any other explicit damping mechanisms, it does not entirely remove the computational mode, indicating that the proposed method needs to be combined with a smooth height σ-coordinate and more effective frequency filtering. For this purpose, the SLEVE terrain-following coordinate is

employed to reduce the initial pressure-gradient imbalances and distorted model levels above high-resolution orography. Additionally, the improved Robert-Asselin-Williams energy conserving time-filter has been introduced to ensure a better performance of the leap-frog scheme. This combination was validated with a multi-layer strongly stratified atmosphere in presence of steep isolated and multiple parallel ridges. The outcomes reproduce the benchmark results of Klemp (2011) and Zängl (2012), which demonstrate the effectiveness of the proposed solution to achieve a significant noise reduction of nearly three orders of magnitude under complex conditions.

The enhanced MC2 mesoscale model that employs this consistent SISL method yields more stable and accurate results for stratified flow simulations over high-resolution steep terrain without overestimating the wind due to numerically generated spurious flows. MC2 is also expected to become the dynamical kernel of the next-generation fine-scale Wind Energy Simulation Toolkit (WEST), which will be soon available for wind resource assessment applications. Hence, we recommend the examination of the N-SI scheme in the context of modern turbulence parameterization and SL trajectory calculations over steep slopes, in order to assess the model's performance for atmospheric boundary layer simulations.

CHAPTER 3

ENHANCED MESOSCALE MODELLING OF THE STRATIFIED SURFACE LAYER OVER STEEP TERRAIN FOR WIND RESOURCE ASSESSMENT

Alex Flores-Maradiaga [1,2], Philippe Pham [2], Robert Benoit [2] and Christian Masson [2]

[1] Department of Mechanical Engineering, Federico Santa María Technical University, 1680, Ave. España, Box 110-V, Office C-430, Valparaíso, Chile
[2] Département de Génie Mécanique, École de Technologie Supérieure, 1100, Notre-Dame Ouest, Montréal, Québec, Canada, H3C 1K3
Article submitted in January 2018 to *Boundary Layer Meteorology*. Currently in revision.

Abstract

The Mesoscale Compressible Community (MC2) model, devoted for weather forecasting and used in the Wind Energy Simulation Toolkit (WEST), performs well for simulations over flat, gentle and moderate terrain slopes but is subject to numerical instability and strong spurious flows in presence of steep topography. To remove its inherent computational mode and reduce the wind overestimation due to terrain-induced numerical noise, a new semi-implicit (N-SI) scheme was implemented to discretize and linearize the non-hydrostatic Euler equations with respect the mean values of pressure and temperature instead of arbitrary reference state values, redefining as well the buoyancy to use it as the thermodynamic prognostic variable. Additionally, the climate-state classification of the statistical-dynamical downscaling (SDD) method is upgraded by including the Brunt-Väisälä frequency that accounts for the atmospheric thermal stratification effect on wind flow over topography. The present study provides a real orographic flow validation of these numerical enhancements in MC2, assessing their individual and combined contribution for an improved initialization and calculation of the surface wind in presence of high-impact terrain. By statistically comparing the wind simulations with met-mast data, obtained within the Whitehorse area of the Canadian Rocky Mountains, it is confirmed the numerical enhancements may reduce over 40% of the wind overestimation, thus, attaining more accurate results that ensure reliable wind resource assessments over complex terrain.

3.1 Background and Context

The fast growing wind industry requires highly accurate atmospheric boundary layer (ABL) simulations over complex topographic formations for wind farm planning at the lowest possible cost. To obtain a reliable wind model with multiscale capabilities, the NEAT laboratory at the University of Quebec has upgraded the Canadian mesoscale compressible community (MC2) model, thoroughly discussed by Robert et al. (1985), Tanguay et al. (1990), Thomas et al. (1998), Girard et al. (2005) and Gasset et al. (2014). MC2 is employed as the multiscale kernel of the open-source Wind Energy Simulation Toolkit (WEST), based on the statistical-dynamical downscaling (SDD) method presented and validated in Yu et al. (2006), Pinard et al. (2005, 2009), Gasset et al. (2012), Waewsak et al. (2015), Landry et al. (2016) and Niyomtham et al. (2017).

The MC2 model solves the non-hydrostatic fully compressible Euler equations (EE), and includes state-of-the-art Unsteady Reynolds Averaged Navier-Stokes (URANS) and Large-Eddy Simulation (LES) capabilities, which allow solving highly complex time evolving atmospheric flow dynamics over topography. In this Chapter, URANS is employed to capture the time-evolving features of the orographic flow over steep slopes. MC2 is also equipped with advanced sub-grid scale schemes, sounding initialization, data assimilation schemes, high-order interpolation schemes, variable vertical grid staggering and dynamic downscaling (Gasset, 2014). Preliminary studies demonstrate the latter version of MC2 yields more accurate results than its former versions for thermally stratified wind over flat and gentle terrain slopes (Girard et al. 2005, Gasset et al. 2014). However, similar to other mesoscale models that employ terrain-following height-based σ-coordinates (e.g. Gal-Chen and Somerville, 1975), MC2 sometimes generates surface wind overestimations and locally distorts the wind directions over steep terrain (Bonaventura 2000, Benoit et al. 2002a, Klemp et al. 2003, Girard et al. 2005, Pinard et al. 2005, Pinard et al. 2009).

A comparable multiscale software, dedicated mostly for flat (or offshore) and gentle-slope terrain wind plant control evaluations, is the NREL Simulator for On/offshore Wind Farm

Applications (SOWFA) by Churchfield et al. (2013), Fleming et al. (2013) and Fleming et al. (2014). The SOWFA limited area model employs LES capabilities, designed to operate as a multiscale wind solver. Although SOWFA has successfully introduced an innovative methodology with high-fidelity simulations to gain insight of wind farm aero-structural dynamics over gentle slopes, it also has difficulties with ABL modelling over mountainous terrain. Churchfield et al. (2013) recognized that the main constraints in their stratified surface wind simulations over steep topography are the correct surface stress calculations and low-level jet overestimation. They clearly remarked that using local Monin-Obukhov similarity for the surface layer over complex terrain does not necessarily make sense, and should not be expected to hold for steep slopes since the log-law scaling is primarily applicable over flat terrain. Additionally, they underlined the importance of initializing appropriately the thermal stratification for the lower atmosphere, as it affects the wind shear and velocity variances mostly for strongly stable airflow over terrain.

Several studies (e.g. Ross and Vosper 2003, Bergström and Juuso 2006, Pinard et al. 2009 and Blocken et al. 2015), highlight how strongly stable wind simulations over natural topography pose a difficulty for accurate mesoscale modelling, since secondary airflow is usually channeled within deep valleys and the mountain top jets separate downstream in the lee-sides. Gerling et al. (1986) explained that as cold wind increases aloft two mountainous formations, the low-level jet intensifies towards the middle and across the valley. Wind models may not capture these combined phenomena, facing some limitations to accurately replicate the flow field in the lower atmosphere. For example, Pinard et al. (2009) demonstrated that MC2 simulations of strongly stable wind over steep mountainous sites spuriously yields a stronger surface stream displaced further downstream relative to the flow aloft, which they relate to an inappropriate wind-climate classification that disregards thermal stratification in the initialization routine for the lower atmosphere.

As part of the diagnostics of MC2 and WEST, Pinard et al. (2009) underlined that the original wind-climate classification employed for the SDD method of WEST flow solver lacks a stratification parameter that accounts for thermal induced forcing in the lower atmosphere

highly influenced by topography. Pham (2012) successfully implemented most of Pinard et al. (2009) suggestions to upgrade MC2 for WEST, reporting a slender improvement by taking the Pinard (2007) reanalysis data at heights above mountain tops instead of sea-level and introducing the Froude number in the SDD routines to link the strength of thermal stratification with geostrophic wind direction and speed. However, additional testing of orographic flows revealed that the Froude number misrepresents temperature profiling since it varies simultaneously with the wind speed. Hence, in this work the Brunt-Väisälä buoyancy frequency (N) is proposed to attain the desired thermal effect.

Another important aspect of models that employ terrain-following σ-coordinates is that the pressure-gradient force may be miscalculated near steep slopes, mostly due to the computational grid-cell deformation. As shown in Klemp (2011), Zängl (2012) and Blocken et al. (2015), this terrain-induced spurious forcing is enhanced when an instable discretization scheme is applied, causing numerical noise and the overestimation of the surface wind speed at the mountain crests and lee-sides. This aspect is quite preoccupying for multiscale wind modelling, since wind farm engineering and financial decision-making depends heavily on the resource assessment results. Pinard et al. (2009) and Gasset et al. (2012) studies suggest that terrain-induced spurious forcing along with inappropriate initialization procedures significantly degrade the model's accuracy for real orographic flow realizations in highly complex sites.

As demonstrated in Chapter 2 of this work, the computational mode generated by the classical semi-implicit (SI) time discretization scheme -employed on MC2's equations- grows asymptotically with each integration time interval, producing intense spurious flows close to steep terrain slopes that propagate throughout the modelling domain. This unphysical numerical mode is inherent to the three time-level original semi-implicit (O-SI) scheme that discretizes MC2's equations, formulated in height-based coordinates, with respect to an arbitrary reference state for temperature (T_*) and pressure ($q_* = \ln p_*$). Bénard et al. (2004) underline that this type of numerical instability arises from the inadequate choice of prognostic

variables, and the explicit treatment of non-linear terms that relate the pressure and temperature perturbations with the flow divergence.

The latter problem is corrected with a new semi-implicit (N-SI) scheme presented in Chapter 2, which discretizes the model equations about the mean values of temperature (T_0) and pressure ($q_0 = \ln p_0$) and redefines the buoyancy -prognostic thermodynamic variable for MC2-, yielding a profound restructuration of the non-linear residuals to ensure numerical stability and more accurate results. The combined enhancement obtained from the N-SI scheme and the new SDD wind-climate classification is expected to improve mostly the surface layer modelling and reduce the initialization errors for vertical momentum transport. It should enable an efficient and more accurate integration with high-order numerical algorithms, such as the semi-implicit semi-Lagrangian (SISL) solver first introduced by Robert et al. (1985) and Tanguay et al. (1990). The model is also supplemented with a second-order accurate Robert-Asselin-Williams (RAW) time-filter (Williams, 2011) to conserve better the system's total energy, and the SLEVE coordinate (Schär et al., 2002) to smooth terrain conforming σ-surfaces in order to reduce hydrostatic imbalances aloft steep slopes. The proposed enhancements are general enough to be applicable in any other multiscale model with similar numerical schemes.

Hence, the objective of the present study is the validation with real orographic flow of the combined enhancements obtained from the N-SI time discretization scheme and the introduction of the Brunt-Väisälä buoyancy frequency in the new wind-climate classification. This testing and validation process is based on the comparison of modeled versus observed wind variables with a series of met-masts distributed over the steep mountain slopes in the Whitehorse area of the Canadian Yukon Territory. To present this work, firstly, a general description of the model equations and numerical problems is introduced in Section 3.2. Then, the methodology and numerical implementation of the proposed solutions is detailed in Section 3.3, followed by a thorough analysis of the validation tests in Section 3.4. Finally, Section 3.5 summarizes the achievements and general findings of this study, as well as the possibilities for future work.

3.2 Model Description and Main Issues

The equation system and numerical schemes of MC2 were modified several times in the past decades, aiming for a more efficient and robust dynamical kernel able to perform high-resolution atmospheric simulations without increasing the computational overhead. The two supported versions of MC2 still in use are v4.9.6 and v4.9.8, which differ mainly in the choice of thermodynamic variables solved with the SISL algorithm. Both versions solve the same physical quantities but in a different manner. Nevertheless, the latter version has proven to be more reliable, numerically stable and less noisy, reason why it is preferred for most applications. Detailed descriptions of MC2 v4.9.6 and v4.9.8 are provided by Thomas et al. (1998) and Girard et al. (2005), respectively.

Both model versions have been devoted to weather forecasting, mountain wave studies and wind resource assessment. For example, both were employed for the MAP project and their outcomes compared against field observations over the Swiss Alps. Firstly, MC2 v4.9.6 was employed in real-time forecasting mode by Benoit et al. (2002a) and, then, MC2 v4.9.8 by Girard et al. (2005) for selected case studies. Both successfully simulated gravity wave phenomena over high impact orography in cold climate conditions, even though the latter version returned more accurate results. However, both versions still present unresolved noise problems that emerge in presence of steep terrain, which must be corrected to obtain a robust mesoscale method.

MC2 v4.9.6 is still employed for WEST but its results present spurious numerical noise and wind speed overestimation in mountainous sites, such as the Rocky Mountains in Western Canada (Pinard et al. 2005, Pinard et al. 2009 and Pham 2012). This problem adversely affects the wind potential evaluations, which are generally overestimated for onshore projects in steep topography. As the standard procedure of the WEST package, the results obtained with MC2 are directly fed to MS-Micro (i.e., the linearized microscale model based on a first-order steady state scheme introduced by Walmsley et al. (1986,1992)), which yields the final solution on a finer mesh after a downscaling iterative process. In the present study, only the results of the

mesoscale component are analyzed since the fundamental enhancements are introduced for MC2. As demonstrated in previous works (cf. Gasset et al. 2012, Waewsak et al. 2015, Landry et al. 2016, Niyomtham et al. 2017), the WEST statistical dynamic-downscaling method is quite efficient to map the average wind speed, wind energy density and other fundamental indicators for resource assessment.

Among the differences between both model releases, perhaps, the most important is the way the Euler equations are casted. In the former version v4.9.6 the formulation is based on the fully compressible non-hydrostatic system involving the velocity and the three main thermodynamic variables (temperature *T*, pressure $q = \ln(p)$ and density ρ), closed with the diagnostic equation of state (Thomas et al. 1998). The equation system is usually expressed in terms of the thermodynamic variable deviations (ψ') with respect to a hydrostatic basic state (ψ_*), as follows:

$$\frac{d\mathbf{v}}{dt} + f\,\mathbf{k}\times\mathbf{v} + RT_*\nabla q' - g\left(\frac{T'}{T_*}\right)\mathbf{k} = \mathbf{f} - RT'\nabla q', \tag{3.1a}$$

$$\frac{d}{dt}\left(T' - \frac{RT_*}{c_p}q'\right) + \frac{T_*}{g}N_*^2 w = \left(1 + \frac{RT'}{c_v T}\right)\frac{Q}{c_p} - \frac{RT'}{c_v}\nabla\cdot\mathbf{v}, \tag{3.1b}$$

$$\frac{c_v}{c_p}\frac{dq'}{dt} + \nabla\cdot\mathbf{v} - \frac{g}{c_*^2}w = \frac{Q}{c_p T}. \tag{3.1c}$$

Variables and constants have the standard meaning, as those presented in Girard et al. (2005), where $d/dt = \partial/\partial t + \mathbf{v}\cdot\nabla$ represents the material derivative, $\mathbf{v} = (u, v, w)$ is the velocity, f the Coriolis parameter, $\mathbf{f} = (\mathrm{f}_u, \mathrm{f}_v, \mathrm{f}_w)$ is the non-conservative forcing and Q the heat sources. The prognostic variables are supplemented with the reference speed of sound $c_*^2 = (c_p/c_v)(RT_*)$ and buoyancy frequency $N_*^2 = g(\beta_A + \gamma_A)$, for which $\beta_A = \partial \ln T_*/\partial z$ and $\gamma_A = g/c_p T_*$. In this study, the reference temperature T_* is set as a constant (i.e., isothermal atmospheric condition), which simplifies the equation system by reducing the reference

buoyancy frequency to $N_*^2 = g^2 / c_p T_* = g\gamma_*$. System (3.1) governs all usual dynamical processes of the atmosphere; for instance it includes both synoptic scale pressure gradients and more localized gradients. If desired, one could impose an idealized initial 3D pressure field representative of particular geostrophic winds and its vertical gradient, i.e. thermal wind.

Contrary to the previous version, as presented in Girard et al. (2005), MC2 v4.9.8 has a governing equation system reformulated in terms of the generalized prognostic variables for the buoyancy $b = gT'/T_*$ and pressure $P = RT_*(\ln p')$. This is a more meaningful generalization of the perturbation variables instead of just considering the deviation from arbitrary values of temperature and pressure (Girard et al., 2005). Thus, version v4.9.8 solves the following three-dimensional EE system:

$$\frac{d\mathbf{v}}{dt} + f\,\mathbf{k}\times\mathbf{v} + \left[\nabla - \gamma_*\mathbf{k}\right]P + \mathbf{k}(b - \gamma_A P) = \mathbf{f} - \frac{b}{g}\left(\nabla - \beta_A\mathbf{k}\right)P, \tag{3.2a}$$

$$\frac{d}{dt}(b - \gamma_* P) + N_*^2 w = \gamma_A Q - b\left[\beta_A w + \frac{R}{c_v}\nabla\cdot\mathbf{v}\right], \tag{3.2b}$$

$$\frac{d}{dt}\left(\frac{P}{c_*^2}\right) + \nabla\cdot\mathbf{v} - \frac{g}{c_*^2}w = \frac{Q}{c_p T}. \tag{3.2c}$$

Both model versions use the O-SI time discretization scheme, which inherently generates the computational mode and terrain-induced noise during wind simulations over steep slopes. Thus, regardless of the model version, the numerical schemes of MC2 definitely need to be enhanced in order to obtain a numerically stable and more accurate mesoscale modelling.

The terrain-induced noise generated by MC2 was clearly identified in the studies performed by Benoit et al. (2002a), Girard et al. (2005), Pinard et al. (2009) and Gasset el al. (2012), who alerted of the propagation of spurious motions that develop during flow simulations over steep terrain. In Bénard et al. (2005), and Chapter 2 of this study, it was demonstrated how the O-SI scheme is numerically unstable and noisy in presence of steep slopes due to the inappropriate

choice of prognostic variables and reference state conditions to linearize the EE system. Nonetheless, the model could perform well with the help of stabilizing mechanisms such as time decentering and frequency filtering, which smooth the solution to weaken the effect of high frequency oscillations combined with the computational mode that grows asymptotically until the model halts.

Bénard et al. (2004, 2005) recognized in their stability analysis of the semi-implicit (SI) scheme that the application of relatively mild time filter is customarily used and necessary to maintain stable leapfrog integrations, even for large temperature perturbations provided the time-step is not excessively large. Traditionally, this parameter is fixed to ensure the model's accuracy and stable performance; thus, for this study the time filter is kept as supplementary stabilizing mechanism with a value of $\delta = 0.05$ (cf. Asselin 1972, Williams 2011).

According to the assessment by Pinard et al. (2005, 2009) and Pham (2012), based on strongly stratified orographic flow simulations over the Yukon Rocky Mountains in Western Canada, MC2 generates a spurious speed-up down the mountain lee-sides that causes an overestimation of the surface streams in this region. More precisely their studies remark this fictitious speed-up is caused, firstly, by the steep slope limitation of height-based terrain-following coordinates used in MC2 and, secondly, by the fact that the modelled climatological conditions disregard the local buoyancy frequency and static stability observed for the surface layer temperature profiles. Consequently, the model overestimates the surface wind speeds and, occasionally, shifts wind directions in presence of finescale steep terrain. Namely, the simulated airflow does not behave naturally within deep valleys and around mountain features. Additionally, Pinard et al. (2009) underline that other possible causes of errors are the mesoscale and microscale model coupling, the disparity of different numerical schemes used by each component of WEST, and the inappropriate setup of the initial and boundary conditions.

3.3 Model Enhancement

Among the most important modifications, the buoyancy frequency was implemented in the SDD algorithm as the new classification (NC) criterion for wind-climate states, which accounts for the air compressibility effect of atmospheric thermal stratification needed to represent the full spectrum of meteorological situations. The Brunt-Väisälä frequency (N) is added to the conventional criteria (i.e., wind speed, wind direction and wind shear) employed for the original classification (OC), to improve the vertical momentum transport calculation over mountainous orography. The latter enhancement has an important effect in the SDD initialization method since the climate states are classified based on the combined geostrophic wind vector and the strength of local thermal stratifications.

The other modification implemented to counteract the terrain-induced noise and numerical instability is the N-SI time discretization scheme, coupled with the RAW filter (Williams, 2011) and SLEVE vertical coordinate (Schär et al., 2002). Even though these two last utilities were not used by Pinard et al. (2009) for their case study in the Whitehorse area, the tests of Chapter 2 have proven this combination is able to significantly reduce the numerical noise and spurious flows in presence of steep slopes, ensuring better stability and accuracy, with a more robust dynamic kernel able to sustain long-term integrations without the non-linear stability limitations of the O-SI scheme. Hence, it is necessary to include these additional enhancements as the new standard settings in WEST for mesoscale modelling of stratified wind over steep complex terrain.

The subsequent sections presents a thorough explanation of the numerical enhancements and the validation tests of their individual and combined implementation, aimed to reduce the model's numerical noise and yield more accurate results for wind resource assessment.

3.3.1 The New Wind Climate-state Classification for the SDD Method

Following the methodology introduced in Frank and Landberg (1997) and Frank et al. (2001), the SDD method of WEST uses long-term global atmospheric reanalysis data such as the 40-

year database of Kalnay et al. (1996) or the 50-year database of Pinard (2007), and processes it through a classification scheme to obtain basic large-scale parametric sets that describe reference climatological conditions (i.e., climate-states) to initialize the model. The original classification (OC) of wind climate-states is performed according to the associated *x*–*y* components of geostrophic wind direction and speed at 0 m above sea level (ASL) and the wind vertical shear calculated between 0 and 1500 m ASL (Yu et al. 2006, Pinard 2007). These weather situations are sorted in equally sized bins for speed and direction so that different mesoscale domains always have the same predefined climate-states with different frequencies of occurrence, such that the outcomes from several model regions can be merged together effortlessly.

The main issue with the OC used in the SDD initialization is a misrepresentation of the vertical momentum transfer when the atmospheric thermal stratification is disregarded for wind climate-state classification. Pinard et al. (2005, 2009) also remarked that the initial temperature profile does not correspond to the one measured with radiosondes (i.e. telemetry instruments carried by a weather ballon to measure various atmospheric variables) and, thus, a new criterion should be added to the classification scheme to distinguish between different thermal stratifications for a better representation of these observed temperature profiles. The new criterion that reproduces this physical phenomenon is the Brunt-Väisälä frequency (N), since it directly addresses the temperature variation with height and is involved in the vertical displacement calculation of oscillating air parcels as function of thermal stability.

The inclusion of the buoyancy frequency, as a new classification (NC) parameter, adds a fourth dimension in the multivariable classification that increases the amount of possible weather situations represented with a unique set of geostrophic wind speeds, direction sectors, vertical shears and Brunt-Väisälä frequencies. The data used for both the OC and NC schemes is estimated logarithmically at 30 m AGL from measurements obtained mainly from multiple 10 m AGL wind-stations (Pinard, 2007). Taking as an example the case study analyzed in Pinard et al. (2009), the NC scheme applied to the Whitehorse area sorts the Brunt-Väisälä frequencies into four non-equally sized bins (between 0 s^{-1} and 0.04 s^{-1}), each related to a particular type

of thermal stratification ranging from neutral to strongly stable cases, respectively. Figure 3.1 presents the observed distribution of static stabilities in this mountainous region, based on radiosonde data, where the frequency of occurrence of a stable stratification condition is dominant in that cold-climate site. It is worth noting that for this case none unstable stratification was measured, hence, it is not included in Figure 3.1.

Still, in addition to this fourth sorting criterion, correction factors derived from the Whitehorse radiosonde station data are needed because the reanalysis method (Fujiwara et al., 2017) underestimates the frequencies of occurrence of strongly stratified cases. Hence, these correction factors are used to modify the weighting coefficient of each climate-state employed for the final ensemble average based on its individual buoyancy frequency (Pinard, 2007).

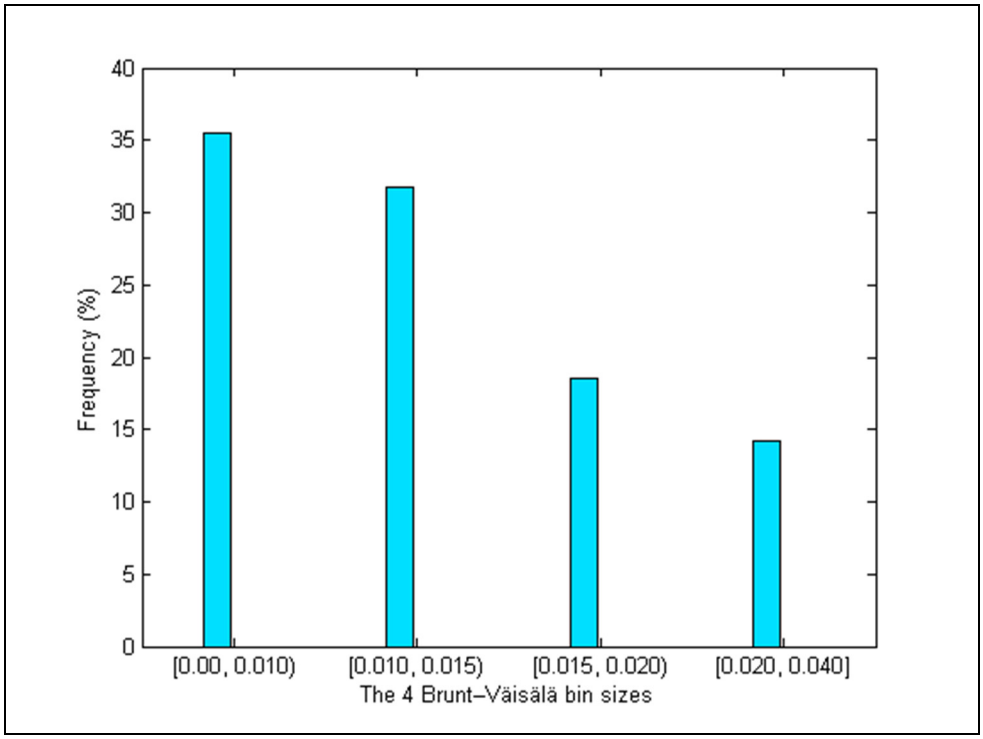

Figure 3.1 Frequency of (a) neutral [0 - 0.01[s^{-1}, (b) slightly stable [0.01 - 0.015[s^{-1}, (c) stable [0.015 - 0.02[s^{-1} and (d) strongly stable [0.02 - 0.04] s^{-1} thermal stratification in the Whitehorse area.

3.3.2 The New Semi-Implicit (N-SI) Scheme for Numerical Noise Reduction

The N-SI scheme is introduced with a redefinition of the buoyancy as $\hat{b} = gT'/T$, keeping the generalized pressure unchanged as $P = RT_*(\ln p')$. This change of variables requires a slight reformulation of system (3.2) to recover the linearity of the hydrostatic relation. After the SISL restructuration, the resulting semi-discrete system becomes:

$$\frac{\delta \mathbf{v}}{2\Delta t} + f\mathbf{k}\times\mathbf{v} + \overline{(\alpha+1)(\nabla P + \mathbf{k}\hat{b})} - (\gamma_* + \gamma_A)\mathbf{k}P = \mathbf{f} + \frac{\hat{b}}{g}\beta_A \mathbf{k}P\,, \tag{3.3a}$$

$$\frac{\delta}{2\Delta t}\left[(\alpha+1)\hat{b} - \gamma_* P\right] + \overline{N_0^2 w} = \gamma_A Q + \left(N_0^2 - N_*^2\right)w\,, \tag{3.3b}$$

$$\frac{\delta}{2\Delta t}\left[\frac{P}{c_*^2}\right] + \overline{\nabla\cdot\mathbf{v} - \frac{g}{c_0^2}w} = \frac{Q}{c_p T} - \left[\frac{g}{c_0^2} - \frac{g}{c_*^2}\right]w\,. \tag{3.3c}$$

where ${N_0}^2 = {N_*}^2/(1+\alpha)$ and ${c_0}^2 = {c_*}^2(1+\alpha)$. Here $\alpha = (T - T_*)/T_*$ represents the non-dimensional temperature perturbation and scales the buoyancy oscillations with respect to a hydrostatically balanced atmosphere. The over-bars $\overline{[\ ]}$ in system (3.3) denote the semi-implicitly treated terms averaged over three time-levels, which ensures the numerical stability of MC2. With the N-SI scheme the linearization of the model equations is applied with respect to mean values of the thermodynamic variables, which allows a more stable treatment of nonlinear terms relating the pressure gradient and temperature perturbations. Additionally, the latter formulation enforces the hydrostatic balance in the vertical momentum transport equation, preventing the initial pressure-gradient imbalances that usually generate numerical noise in presence of steep slopes. A complete description and thorough analysis of these modifications was provided previously in Chapter 2.

It is worth remaking that the buoyancy frequency is used for both the wind-climate classification and the N-SI discretization, but its purpose is different in each scheme. Its use in the new wind-climate classification incorporates static stability to the SDD initialization

algorithm, whereas in the N-SI scheme it is employed to reformulate the EE in order to enforce the hydrostatic balance for the pressure-gradient and temperature perturbation non-linear terms. Consequently, in the context of high resolution mesoscale modelling over mountainous regions, the buoyancy forcing is a determining factor that influences energy and momentum transport of turbulent wind flow and internal gravity waves induced by prominent orographic features. Taking into account the air compressibility during initialization and prognostic calculations is fundamental for a proper wind potential evaluation.

3.4 Validation and Discussion

To demonstrate that the enhancements implemented in MC2 effectively reduce the wind-speed overestimation, we employ the WEST methodology to simulate the wind over the cold-climate mountainous Whitehorse area (Figure 3.2a) in the Yukon Territory of Western Canada. This area is bordered and influenced by the Wrangell St. Elias Mountains, Western Costal Mountains, Mackenzie Mountains and Canadian Rocky Mountains. The landscape is covered with prominent ice-capped peaks, deep valleys, rivers and lakes, where the majority of terrain features range between 1000 and 3000 m ASL, among which Mount Logan stands out with a maximum height of 5959 m ASL. In the present study, the main part of the discussion is dedicated to wind simulations over the Whitehorse valley, located at the center of the depicted orography (Figure 3.2b), where the local climate conditions and seasonal wind flow variations are highly influenced by the mountainous forcings and strong thermal stratification. The diagonal line in Figure 3.2a represents the vertical cross section over Whitehorse valley.

In the 50-year climatological study reported by Pinard et al. (2005, 2007) for this particular region, the WEST method was used by coupling MC2 with MS-Micro to obtain a detailed mapping of the surface layer. Their study predicted wind speeds 20 to 40% higher than those measured by 16 wind stations at 10 m and 30 m above ground level (AGL), distributed as shown in Figure 3.3 (or Figure 2 of Pinard et al., 2005) and described in Table 3.1. To use a consistent dataset at 30 m AGL to study the flow patterns in the Whitehorse valley, Pinard (2007) extrapolated the 10 m met-mast data to 30 m AGL employing multipliers obtained from

the logarithmic law profile. For this particular work, the 5 year averages from 2001-2005 are employed, based on the observations discussed in Pinard (2007) that justify this choice in the significant climate change observed in the last 15 years in that site.

Primarily relevant is the fact that the 5 km resolution mesoscale terrain used for MC2 is substantially smoothed, causing wind speed and direction errors with poor correlation with respect to on-site measurements. As underlined by Pinard et al. (2005), some sites of interest for wind energy development in this area have steep slopes that exceed 0.25 (i.e., $\vartheta \approx 15°$), a clear limitation for the linear model MS-Micro for which smoothing of the topographic relief is required. Generally, slopes less than 0.1 should be used to obtain accurate results with MS-Micro and similar linear models. This numerically smoothed terrain, along with the ice-field weak roughness length, decreases the orographic forcing allowing strong overestimated winds over hills and into the valleys.

Additionally, there is a clear discrepancy of the real local static stability with the one prescribed by the classic SDD algorithm of WEST, since both MC2 and MS-Micro are initialized with a quasi-neutral atmosphere using a adiabatic temperature profile (Pinard et al., 2009). Hence, the characteristic strongly stable and shallow atmospheric boundary layer of this cold-climate region is poorly represented. The neutral atmosphere assumption is likely to cause higher wind speeds and weaker wind shear, thus, causing stronger vertical momentum transfer close to the ground (Pinard et al., 2005).

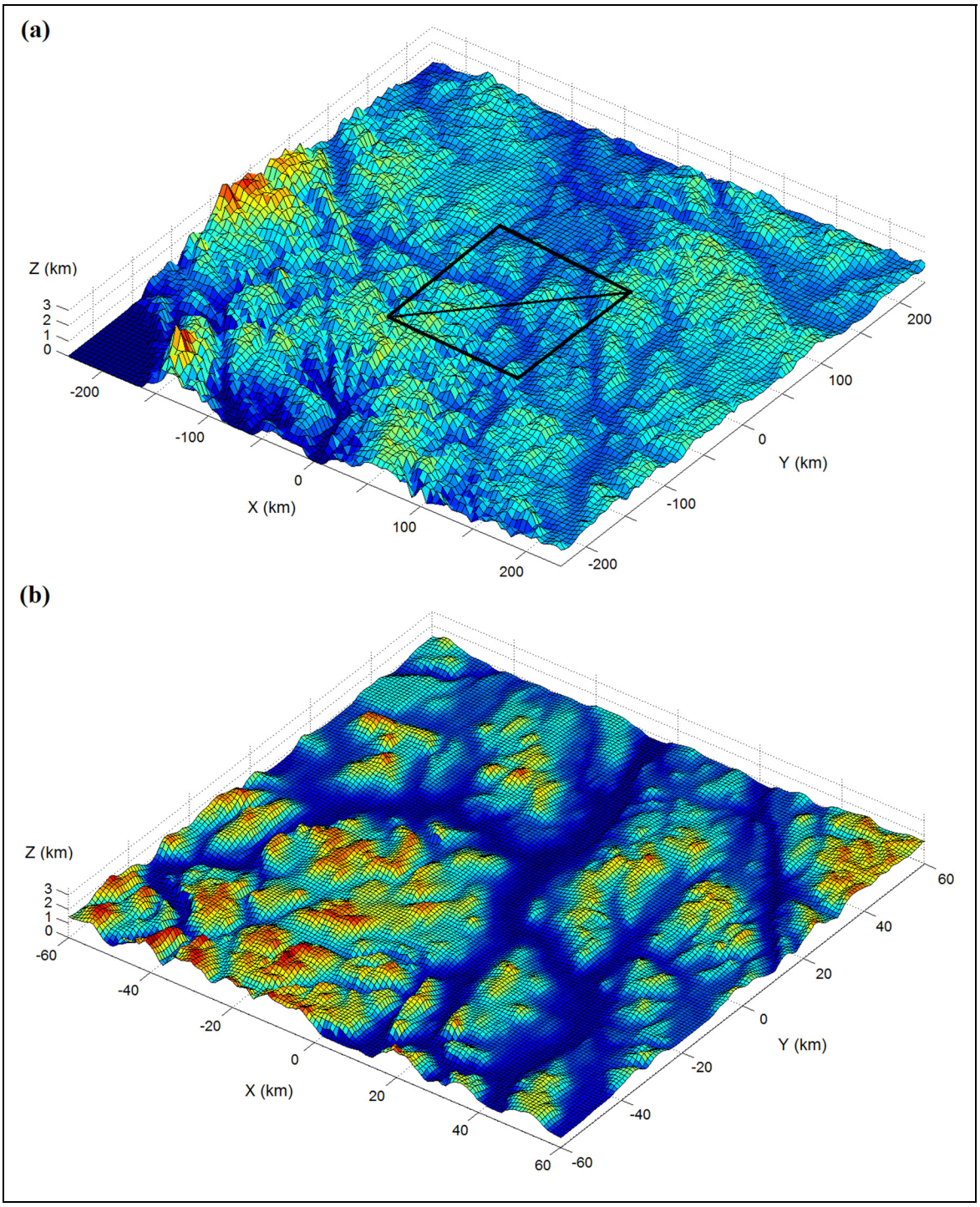

Figure 3.2 Three-dimensional illustrations of the (a) Whitehorse area at 5 km resolution and (b) Whitehorse valley at 1 km resolution.

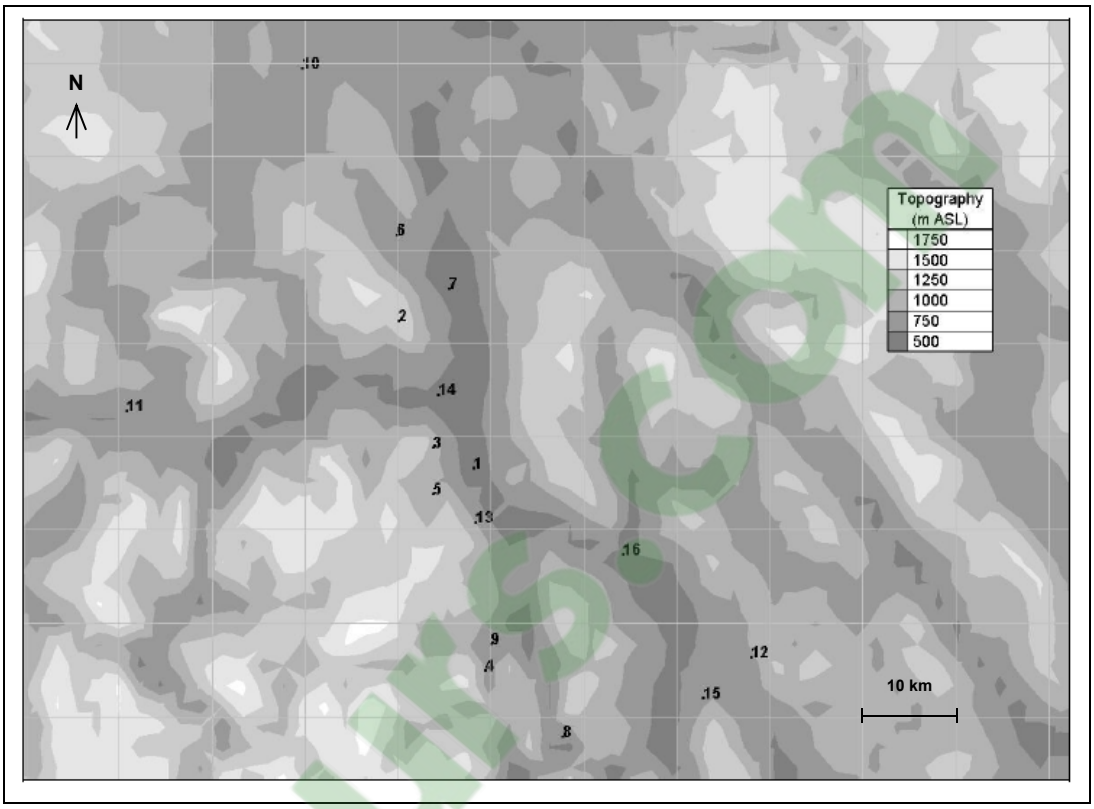

Figure 3.3 Wind stations distributed within the Whitehorse valley, at Yukon Territory of Western Canada, measuring meteorological conditions at 30 m AGL.

Depending on the local static stability used for MC2, the turbulent surface layer directly interacts with the surrounding mountain slopes generating stationary mountain-valley systems with lee-side windstorms, down-valley mountain breezes and mid-valley jet channeling. Under the natural cold-climate conditions of Yukon Territory the SDD method should initialize the simulations with a stronger thermal stratification in the surface layer, which requires the buoyancy frequency as a classification criterion for local wind-climate states.

This high-resolution simulation entails special attention on the selection of model settings, boundary conditions and the initialization scheme. In order to relate to the study by Pinard et al. (2009), we employ the same values for grid size, domain layering, time interval and integration period. The grid's horizontal resolution is $\Delta x = \Delta y = 5$ km, with square lateral length of 500 km and height of 20 km, vertically stretched with 12 layers in the first 1500 m

above ground level (i.e., $100\times100\times100$ grid-points). The prescribed time-step is $\Delta t = 60$ s and the total simulation time is 16 hrs, which ensures quasi-steady convergence after 12 hrs.

Table 3.1 Description of the wind stations distributed within the Whitehorse valley.

#	Wind Station	Lat. [deg. °]	Long. [deg. °]	Elevation [mASL]	Mean wind [ms^{-1}]	Uncertainty [%]
1	Whitehorse	60.710	-135.067	706	4.6	6
2	Flat Mtn	60.994	-135.370	1930	8.4	40
3	Haeckel Hill	60.749	-135.231	1430	6.9	8
4	Annie	60.319	-135.020	876	3	12
5	Fish	60.659	-135.230	1175	4.1	9
6	Fox Lake	61.160	-135.380	793	2.7	12
7	Laberge	61.057	-135.170	645	4.5	12
8	Watson	60.190	-134.720	702	4.1	11
9	Wheaten	60.370	-135.000	783	2.2	13
10	Braeburn	61.481	-135.770	725	3.1	9
11	Champagne	60.811	-136.448	732	2.9	9
12	Jakes	60.339	-133.980	814	2.5	13
13	Mt Sima	60.604	-135.060	939	5.1	12
14	Nursery	60.851	-135.210	674	3.5	13
15	Jubilee Mtn	60.262	-134.170	1280	4.5	12
16	Marsh Lake	60.542	-134.480	656	3	12

The geophysical file provides the model with all the topographic, surface roughness and land-use characteristics, and the surface temperature distribution is taken from Pinard (2007) reanalysis data set. Additionally, an explicit fourth-order horizontal diffusion constant is set to $K_m = 0.01$ m^{2}s^{-1}, along with RAW time-filter coefficients of $\delta = 0.05$ and $\delta_{RAW} = 0.5$, respectively, as suggested in Williams (2011) nd Chapter 2 of this work. The column-type URANS scheme is used for turbulence parameterization with the conventional physical tendencies, constant lateral boundary conditions and a Shuman (1957) wave absorbing sponge at the top 10 layers to avoid gravity wave reflection that could bias the results. Other validation cases with LES imbedded in MC2 are presented in Chapter 3.

3.4.1 Validation of the Model Enhancements

Firstly, to test that the new classification (NC) captures effectively the desired stratification effect, we choose a subset of climate-states sharing the same wind speed (7 m s^{-1}), direction sector (225 degrees) and positive shear (favorable pressure gradient) with four different Brunt-Väisälä frequency classes. Figure 3.4 illustrates a comparison of the vertical velocity cross-sections of the airflow across the Whitehorse valley for these climatological conditions. The vertical velocity standard deviation drops progressively from ± 0.9 ms^{-1} (Figure 3.4a) to ± 0.15 ms^{-1} (Figure 3.4d), as the Brunt-Väisälä frequency increases for each case. Clearly, the vertical momentum transfer has been reduced with stronger stratification, demonstrating that the new classification criterion is able to capture the buoyancy effect of different static stabilities. The NC also ensures that the physical phenomena observed by Pinard et al. (2005) is realistically reproduced, with a more accurate calculation of the ensemble averages for the full set of climate-state simulations.

On the other hand, the performance of N-SI scheme is verified over these terrain features with an atmosphere-at-rest test, initialized with a non-rotational hydrostatically balanced atmosphere, without physical parameterization of moisture, precipitation, radiation, tracers and turbulence. The numerical diffusion and time decentering operators are turned off to isolate and highlight the effect of the new time discretization without any explicit diffusion mechanisms. This simplified case is initialized with a zero horizontal velocity input, zero horizontal pressure gradient, horizontally homogenous thermodynamic sounding of 250 K and lateral *x-y* periodicity. At the surface a free-slip condition is selected and at the top of the domain a sponge layer is prescribed based on equation 5 of Shuman (1957), typically set to restrict the spurious reflection of gravity waves in MC2.

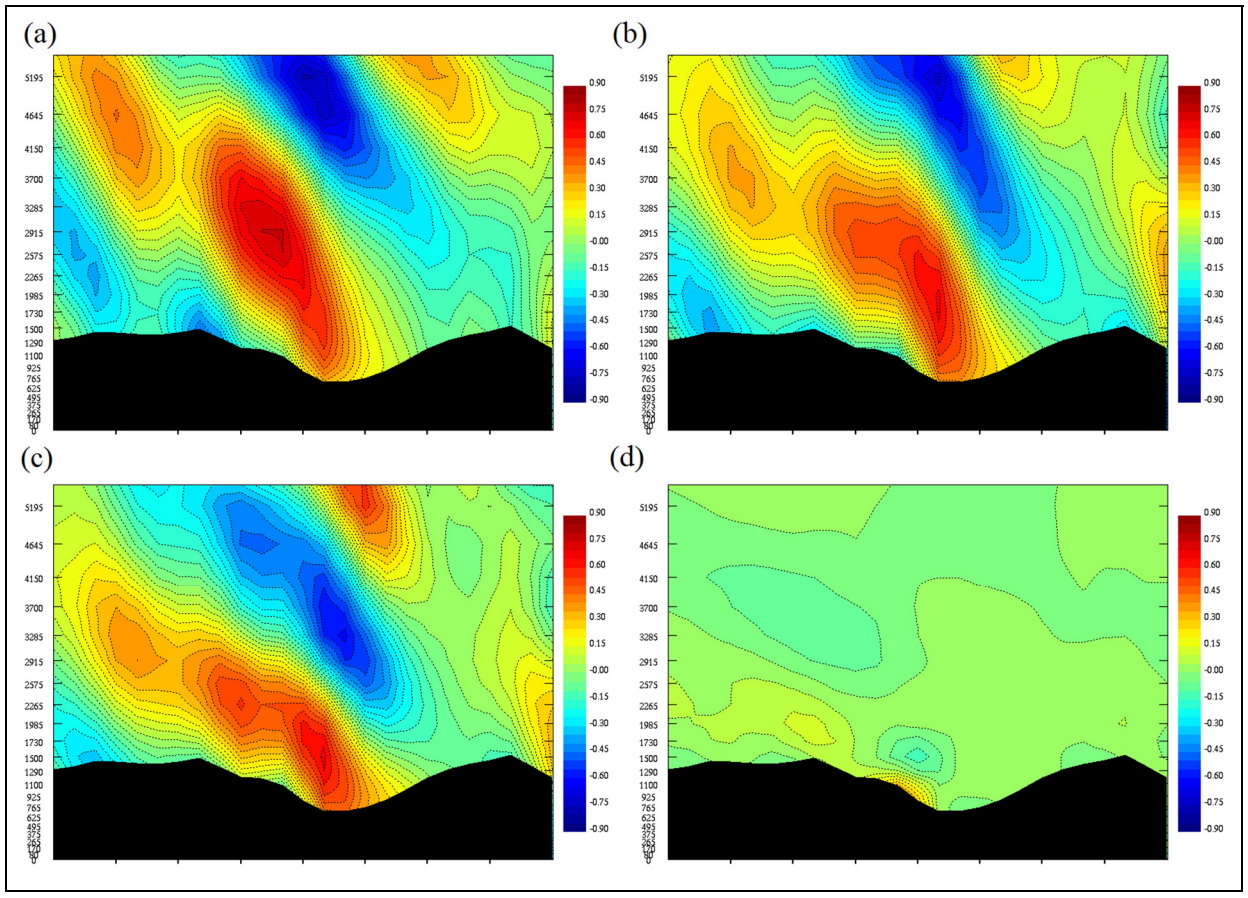

Figure 3.4 Vertical velocity cross-sections of four climate-states with the same mean wind speed of 7 ms^{-1}, wind direction of 225 degrees and positive shear, classified with different Brunt-Väisälä frequencies of (a) 0.0091 s^{-1}, (b) 0.0137 s^{-1}, (c) 0.0174 s^{-1} and (d) 0.022 s^{-1}, respectively.

For the thermal initialization, as employed in Klemp (2011), a three layer non-isothermal atmosphere is set with a constant thermal stratification of N = 0.01 s^{-1} throughout the domain, and a 1 km thick strongly stratified inversion layer of N = 0.02 s^{-1} located between 2000 and 3000 m AGL. This three-dimensional multi-layer test examines the N-SI scheme in a realistic mountainous site with a strongly stratified inversion layer, where numerical noise transforms into spurious flows enhanced by the steep complex terrain. This test aims to assess the propagating gravity oscillations under stringent conditions, with a strongly stable atmosphere initially at rest with underlying multiscale ridges. The numerical noise generated in the stream-wise and span-wise directions by MC2 during a 16 hours simulation is presented in Figure 3.5,

comparing both the O-SI and N-SI schemes. For this case, the comparison is made only between the former and latter SI schemes since the reference studies (Pinard et al. 2005, 2009) did not present any numerical noise assessment based on atmosphere-at-rest simulations.

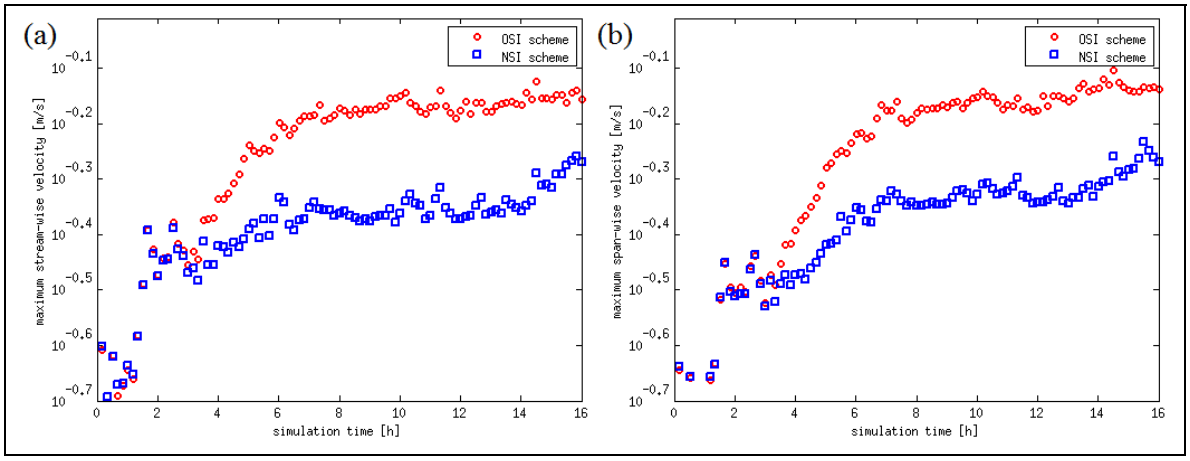

Figure 3.5 Time evolution of the numerical noise for (a) stream-wise and (b) span-wise surface wind speeds (ms^{-1}) at the Whitehorse # 1 wind station.

As expected, the wind speed starts with a similar magnitude for both SI schemes and grows asymptotically as the integration progresses. However, the maximum horizontal velocities obtained with the N-SI scheme display an approximate reduction of 30% with respect to the O-SI results. This noise reduction, achieved by the N-SI scheme alone without any other stabilizing mechanism, certainly enhances MC2's accuracy and numerical stability by weakening its spurious computational mode. Essentially, the combination of the wind-climate NC and N-SI discretization scheme, implemented in the latest model version MC2 v4.9.9, is expected to yield a significant noise reduction and correct the surface wind overestimation for mesoscale modelling. This hypothesis will be demonstrated in the following section with the simulation of a full set of climate-states for real orographic flow over the Whitehorse Valley.

3.4.2 Numerical Simulation of Strongly Stratified Wind over the Whitehorse Valley

In order to compare adequately the real orographic flow outcomes, the numerical simulations are performed prescribing the same model settings and boundary conditions as Pinard et al. (2009). The main difference with respect to Pinard et al. (2009) is that, instead of modelling a single macro-state (i.e., an ideal assembly of initial conditions that mimics the long-term climatological conditions), we choose to run the full set of wind climate-states and average the final results to obtain more realistic and significant ensemble statistics. The mesoscale outcomes analyzed here are compared point-wise to a series of 5 years observations, measured with the 16 met-masts distributed throughout the Whitehorse valley (cf. Figure 3.3 and Table 3.1), to determine the mean absolute error of the modelled wind speed.

The original wind-climate classification defines a suite of 224 cases as function of the geostrophic wind speed (14 classes), direction (8 classes) and vertical shear (2 classes). The new classification takes these classes and sorts them with respect to four thermal stratification bins, as illustrated in Figure 3.1, yielding 896 cases. The full set of simulations is initialized with the SDD algorithm that automatically defines the number of situations to model, depending on the chosen wind climate-state classification, all computed in parallel with a 64 processors cluster (i.e. 8×8 Intel Xeon cores, 2 socket CFG, 1.5 TB memory, 6 channel DDR4, 2x UPI links at 9.6 GT/s, 16 DP flops per cycle) for a 16 hours realization.

In Section 3.2 we explained that both MC2 versions (v4.9.6 and v4.9.8) employ the O-SI scheme. Thus, we first analyze the performance of the OC+O-SI combination for both model versions, based on the comparison of modelled versus observed data at 16 wind-stations, pin-pointed with white squares in Figure 3.6. The error bars in figure panels 3.6b and 3.6d (as well as in Figures 3.7b, 3.7d and 3.7f) represent the intervals containing the estimate for the 50 years long-term average wind speeds for each station based on the short-term 5 year average. The closer the mean values are to the modelled–observed diagonal line, the higher the accuracy and correlation of the scheme combination. Also, mean values above (or under) this diagonal line indicate that the modelled wind speed for those stations is overestimated (or underestimated, respectively).

Table 3.2 presents the postprocess statistics summerized for the whole set of scheme combinations. These statistics refer to the station to station average wind magnitudes, minimum and maximum winds, cross-station standard deviation, dataset combined correlation and mean absolute error (MAE). The OC+O-SI combination, employed for MC2 v4.9.6, is considered hereon as the baseline for all other comparisons.

Table 3.2 Statistics of the mesoscale simulations of surface wind in Whitehorse valley.

Schemes	Average (ms^{-1})	Minimum (ms^{-1})	Maximum (ms^{-1})	σ_U (ms^{-1})	Correlation model-obs.	Mean Abs. Error (ms^{-1})	MAE reduction
OC+OSI	4.3392	2.7493	6.7301	1.1107	0.7485	0.9687	-
NC+OSI	4.2709	2.8268	6.4874	1.0671	0.7669	0.9238	4.64 %
OC+NSI	3.7669	2.1601	7.0317	0.6811	0.9175	0.5584	42.35 %
NC+NSI	3.8106	2.0973	7.2712	0.6589	0.9299	0.5291	45.38 %

The wind speed distributions (Figures 3.6a and 3.6c), and the corresponding comparisons of modelled versus observed wind speeds (Figures 3.6b and 3.6d), reflect how the reformulation of the former MC2 v4.9.6 equation system (3.1) with a more significant set of prognostic variables as done for MC2 v4.9.8 system (3.2) reduces the spurious speed-up over mountainous terrain. The latter version achieves a reduction of the MAE by 0.39 ms^{-1} (41%) with respect to the baseline combination, which confirms the effectiveness of the corrected vertical displacements with σ-coordinate by Girard et al. (2005). Most of the mean wind speeds obtained with the OC+O-SI of MC2 v4.9.8 approach better the modelled-observed diagonal than the baseline combination, even though there still are some clear deviations. To solve this persistent deficiency, the wind-climate NC for SDD method and the N-SI scheme implemented in MC2 v4.9.9 (i.e., the most recent modified version) are tested for the same wind simulations over the Whitehorse area.

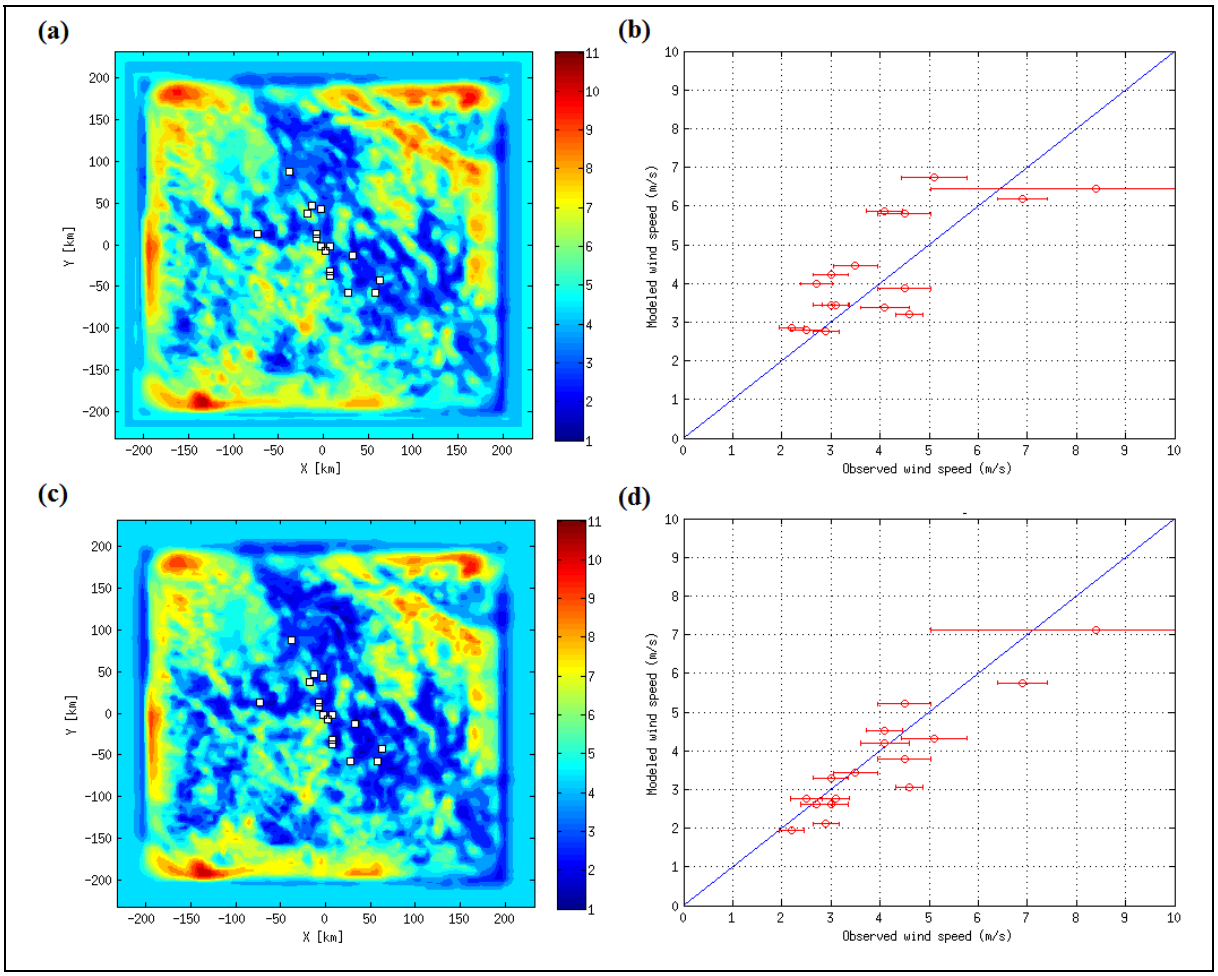

Figure 3.6 Wind speed (ms^{-1}) distribution (left panels) and comparison of modeled versus observed wind speeds (right panels) over the Whitehorse area, obtained with the OC+OSI combination implemented in (a)-(b) MC2 v4.9.6 and (c)-(d) MC2 v4.9.8, respectively.

The three permutations NC+O-SI, OC+N-SI and NC+N-SI implemented in MC2 v4.9.9 are compared in Figure 3.7 to the baseline combination (i.e., Figure 3.6a and 3.6b). Table 3.2 provides a comprehensive summary of the first and second central moments obtained from the ensemble statistics of each scheme combination. An inspection of the wind speeds modelled with the NC+O-SI (Figures 3.7a and 3.7b) reveals that changing only the climate-state classification slightly improves the velocity module, with a 0.045 ms^{-1} reduction of the MAE respect to the baseline schemes. This represents an improvement of 4.6 % obtained only by using a better SDD initialization algorithm.

A more significant readjustment is obtained with the OC+N-SI combination (Figures 3.7c and 3.7d), which corresponds to the correction of the spurious acceleration when changing the O-SI by the N-SI scheme. In this case, we achieve a reduction of the wind MAE by 0.41 ms^{-1}, which translates into a 42.4 % improvement with respect to the baseline combination, revealing a clear reduction of the surface winds over the main mountain features. Finally, the two novel schemes together as NC+N-SI (Figures 3.7e and 3.7f) yield the best flow field readjustment, attaining a 0.44 ms^{-1} reduction of the wind MAE, i.e. 45.4 % improvement, that ensures a higher accuracy for wind resource assessment.

Table 3.2 also shows a progressive reduction of the mean wind speed with each scheme combination, revealing that the model enhancements yield an approximate 0.5 ms^{-1} correction on the overestimated winds obtained with the baseline model. Although, the breach between minimum and maximum wind speeds increases with each scheme combination, we attained a distinct reduction of the wind speed dispersion and a notable improvement in the modelled versus observed data correlation.

The progressive improvement of the average wind speed, standard deviation and mean average error reflects the individual and combined contribution of both solutions. Thus, the NC+N-SI combination is expected to yield the desired correction for the surface wind overestimation in the WEST method, with a better initialization of the local climatological conditions and more stable SISL solver for simulations over steep terrain.

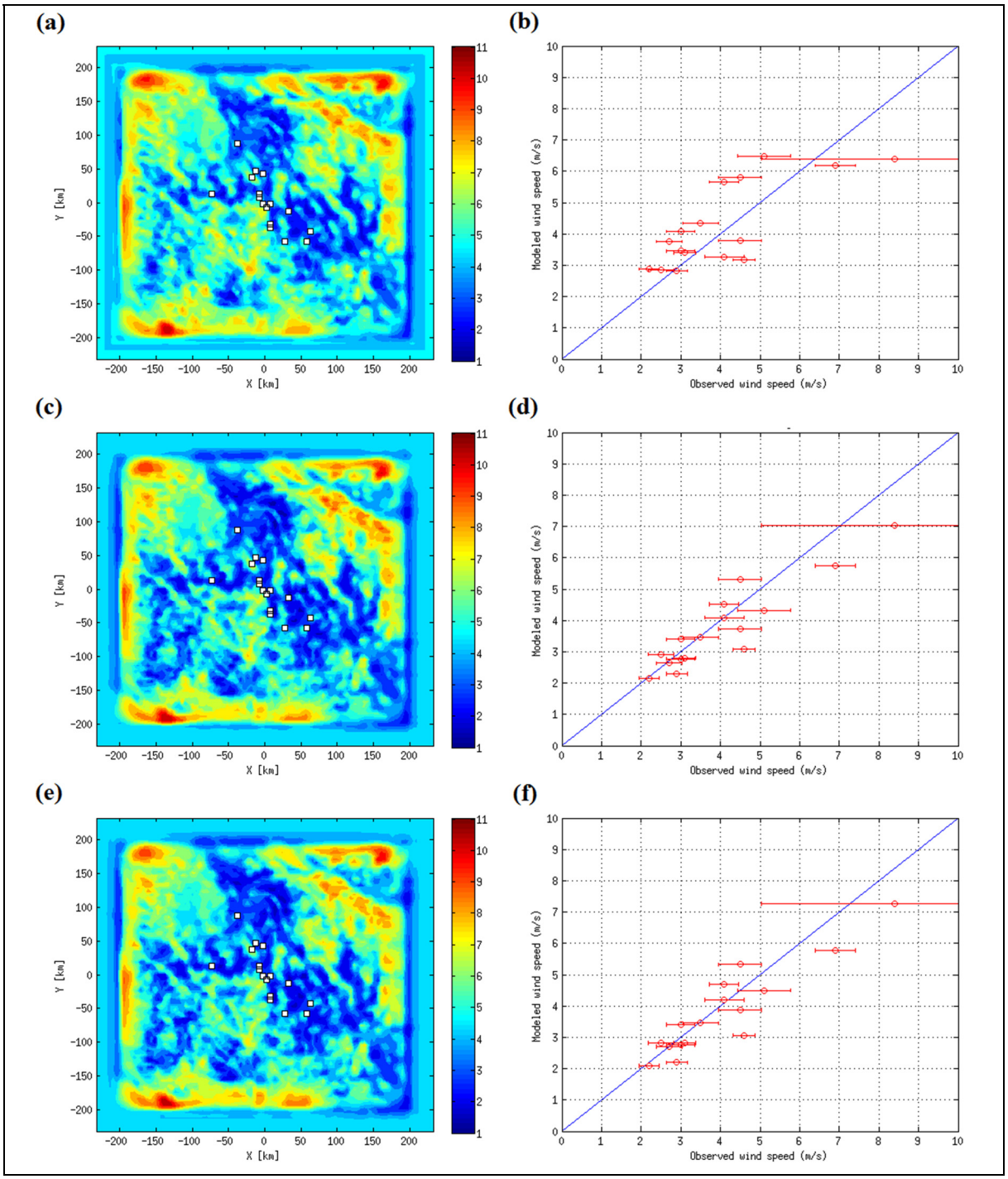

Figure 3.7 Wind speed (ms^{-1}) distribution (left panels) and comparison of modeled versus observed wind speeds (right panels) over the Whitehorse area, obtained with the (a)-(b) NC+OSI, (c)-(d) OC+NSI and (e)-(f) NC+NSI combinations implemented in MC2 v.4.9.9.

Replicating correctly the surface flow pattern over prominent mountain and valley features is a key challenge to achieve an effective improvement in multiscale wind resource assessment. Fortunately, the NC+N-SI scheme combination imbedded in the SDD method yields a correction of the surface flow field misrepresented with OC+O-SI. Figure 3.8 depicts the mean wind field realizations over the Whitehorse valley, that is supposed to flow east-northward based on the observed and reanalysis data. Clearly, the OC+O-SI baseline combination (Figure 3.8a) fails to obtain appropriate wind speeds and directions. In fact, it reveals that this baseline permutation significantly overestimates the wind magnitudes when the air masses interact with steep terrain slopes. Although the OC+O-SI combination is able to replicate the deep valley flow channeling, the adverse influence of the miscalculated wind aloft yields a wrong vector orientation with recirculation and flow inversion in the valleys.

Indeed, the cold airflow in this site should be oriented primarily east-wise, with nearly half of the magnitude, as it is evident in the NC+N-SI realization (Figure 3.8b). The former scheme combination also achieves the expected mountain-valley systems, with low-level jets over the hilltops and cross channeling within the valleys. Hence, the proposed enhancements for the MC2 model and SDD algorithm will, most likely, correct the long-standing difficulties faced by WEST and similar wind resource assessment toolkits for ABL simulations over steep complex terrain.

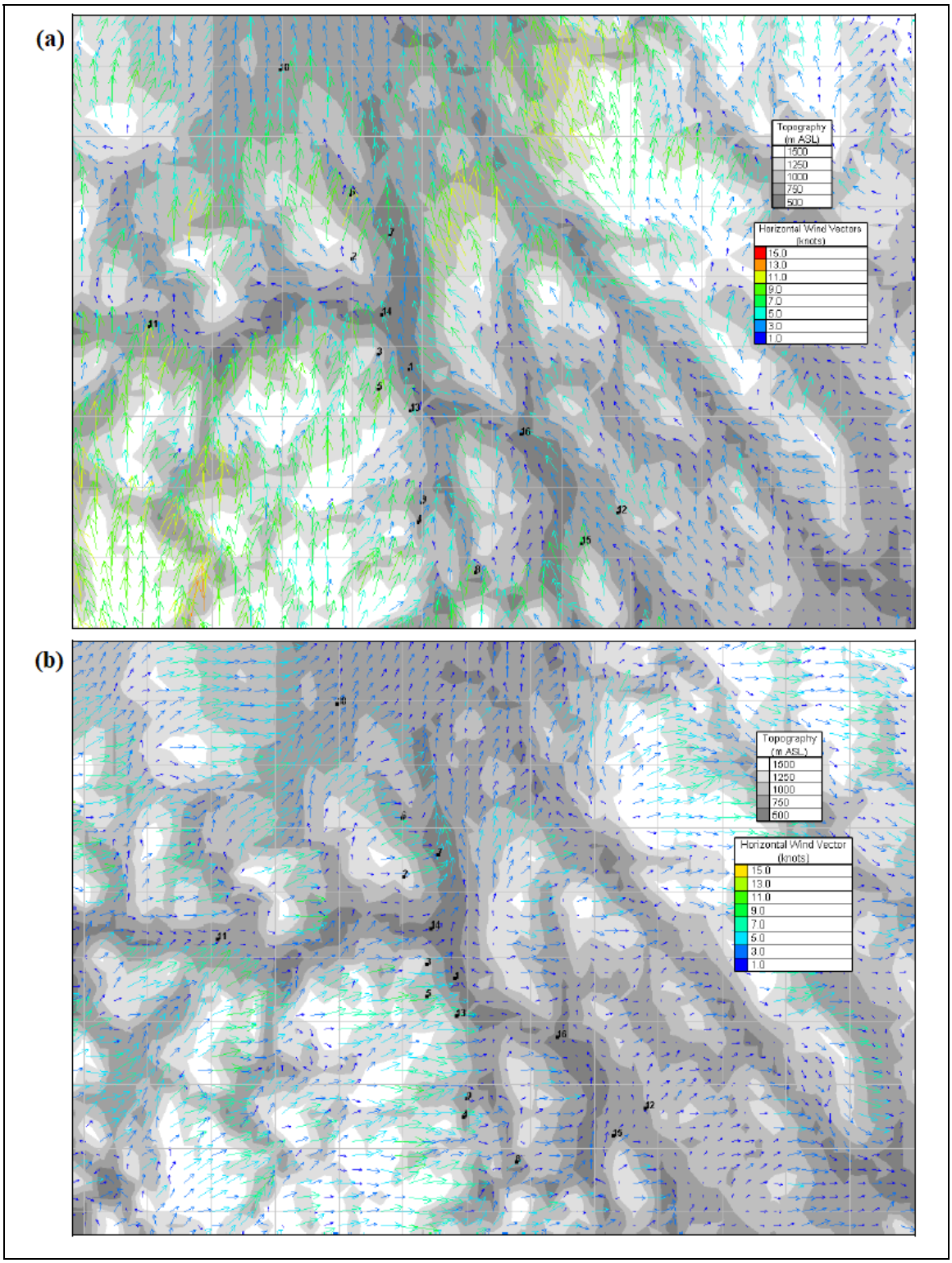

Figure 3.8 Mean wind flow patterns at 30 m AGL in the Whitehorse valley, obtained with the (a) OC+OSI and (b) NC+NSI combinations implemented in MC2 v.4.9.9.

3.5 Summary

During the last three decades the MC2 mesoscale model has been used for weather forecasts and wind resource assessment, obtaining good results and stable integrations over flat terrain and gentle slopes. However, it was noticed that the Wind Energy Simulation Toolkit (WEST), which employs MC2 as its dynamical core, generates intensive numerical noise and yields overestimated surface wind speeds for simulations over steep topography. At the same time, the previous SDD initialization scheme in WEST disregards the thermal stratification for wind climate-states classification, which ultimately yields a misrepresentation of the vertical transport processes causing a spurious downward speed-up on the mountain lee-sides.

To overcome these numerical problems, the method has been upgraded with a new semi-implicit discretization scheme for MC2 aimed to reduce the numerical noise that amplifies its inherent computational mode, originated from the model's non-linear instability. Preliminary tests demonstrate that the N-SI scheme reduces approximately a 30% of the numerical noise and ensures stable integrations with MC2, even for steep terrain cases. Additionally, the SDD initialization has been upgraded by including the Brunt-Väisälä frequency as a new criterion for the wind climate-states classification, which better accounts for the thermal stratification that affects the vertical momentum transfer of oscillating air parcels. This new classification (based on the wind speed, direction, shear and Brunt-Väisälä frequency) simulates correctly the vertical displacements as function of the atmospheric static stability, achieving a 4.6% reduction of the mean average error of surface wind speeds plus a readjustment of the surface flow field that better correspond the one expected over steep topography.

When these two solutions are combined and tested over high-impact terrain in the cold-climate Whitehorse area, of the Yukon Territory in Western Canada, a 45% reduction of the wind mean average error is obtained that represents a significant noise reduction and excellent readjustment of the velocity field on steep topography. Thus, the foremost achievement of the combined solutions introduced in MC2 and the SDD algorithm is the reduction of the spurious

wind speed-up and a better representation of the vertical energy and momentum transport for strongly stratified wind simulations over escarped mountainous formations.

In general, the upgrading process of MC2's semi-implicit scheme along with the SDD new climate-state classification scheme constitute major improvements for the WEST method, equipped with a more stable dynamic kernel capable of accurately modelling the wind in highly complex sites. As the next upgrading steps, we recommend a thorough study of turbulence modelling employing this enhanced version with the large-eddy simulation method and dynamic downscaling, to provide a better representation of the unstationary processes of the atmospheric boundary layer. The final version of MC2-LES (the coupled methodology of MC2 mesoscale and large-eddy simulations) is foreseen to become the standard dynamical kernel of the next-generation WEST method for advanced wind resource assessment over steep terrain.

CHAPTER 4

WIND MODELLING OVER STEEP TERRAIN WITH LARGE EDDY SIMULATION EMBEDDED IN A MESOSCALE ATMOSPHERIC MODEL

Alex Flores-Maradiaga [1,3], Nicolas Gasset [2], Robert Benoit [3] and Christian Masson [3]

[1] Department of Mechanical Engineering, Federico Santa María Technical University, 1680, Ave. España, Box 110-V, Office C-430, Valparaíso, Chile
[2] Recherche en Prévision Numérique, Meteorological Service of Canada, Environment Canada, 2121, Route Transcanadienne, Dorval, Québec, Canada, H9P 1J3
[3] Département de Génie Mécanique, École de Technologie Supérieure, 1100, Notre-Dame Ouest, Montréal, Québec, Canada, H3C 1K3
Article submitted in January 2018 to *Boundary Layer Meteorology*. Currently in revision.

Abstract

Lately, important advancements have been achieved in numerical methods of multiscale models used for high resolution wind simulations over steep topography. As a contribution to this effort, an enhanced numerical method was devised in the non-hydrostatic mesoscale compressible community (MC2) model of the Meteorological Service of Canada, adapting a new semi-implicit scheme with its large-eddy simulation (LES) capability for mountainous terrain. The model can be run both in a meso-microscale downscaling mode or simply with its microscale LES mode. Its implementation has been verified by simulating the neutrally stratified atmospheric boundary layer (ABL) over flat terrain, a moderate slope Gaussian ridge and the steep RUSHIL H3 symmetric ridge with maximum slope of 0.2 and 0.3, respectively. The test results indicate that the enhanced MC2-LES model reproduces efficiently the expected flow patterns, separation and recirculation zone over steep terrain, and yields accurate results comparable to those reported from experimental data or by other researchers who use numerical models with more sophisticated turbulence closure schemes. This novel method resolves multiscale structures with more stable and accurate results than the former model version, particularly, in presence of high impact topography. The resulting model can be used for wind resource assessment at meso- and micro-scales, reducing significantly the wind speed and turbulent stresses overestimation in mountainous areas.

4.1 Background and Context

The atmospheric boundary layer (ABL) is governed by complex physical phenomena acting at scales that range from synoptic to microscales, requiring a considerable effort in the development of accurate and numerically stable prediction methods. Wind flow over steep terrain particularly generates unsteady interactions between the thermally stratified turbulent ABL and the Earth's surface that reveal certain limitations of the models using conventional numerical methods. The resulting wind patterns of these phenomena are complicated multiscale non-linear relationships of turbulent transport, which challenge the current computational fluid dynamics (CFD) techniques employed for weather forecasting, wind resource assessment and wind farm aerodynamics.

Comparisons of CFD simulations with wind tunnel and field experiments have demonstrated that predicting the mean structure of wind flow over topography is achieved with relative success independent of the turbulence closure employed (Kim and Patel 2000, Castro et al. 2002, Weigel et al. 2006, Yu Fat et al. 2007, Silva-Lopes et al. 2007, Ayotte 2008 and Breton et al. 2017). However, these studies also show that turbulence modelling is greatly altered by different features of the solver and, mainly, simulations should account for the surface layer anisotropy and reduce the numerical errors that arise from strong hydrostatic imbalances due to grid deformations over steep slopes. The flow separation, recirculation and reattachment between the crests, lee-sides and troughs of mountain ridges, cliffs and valleys are also some of the major concerns in the ABL modelling research (Allen and Brown 2002, Lundquist et al. 2010, Castagna et al. 2014, Liu et al. 2016).

Usually, in the surface vicinity the numerical errors are significant when LES outputs are compared to some of the expected surface similarities based on constant energy and momentum fluxes and/or local isotropy. Several studies have shown that the classical low-order turbulence closures struggle to fit the velocity, temperature and momentum flux profiles to the Monin-Obukhov similarities even for flat terrain (Mason and Thomson 1992, Andren et al. 1994, Kosović 1997, Porté-Agel et al. 2000, Chow et al. 2005, Drobinsky et al. 2007,

Senocak et al. 2007, Stoll and Porté-Agel 2008, Brasseur and Wei 2010). Even though higher-order sub-grid scale (SGS) schemes reduce these numerical errors in the order of 20% without the need to increase grid resolution, the eddy-viscosity closures are still in use since they lessen the computational overhead and complexity for an efficient implementation (Kosović and Curry 2000, Redelsperger et al. 2001, Kirkil et al. 2012, Gasset et al. 2014, Brenton et al. 2017).

When the thermally stratified wind is modelled in presence of steep topography, a careful selection of numerical methods is necessary to reproduce the unsteady flow separation phenomena due to the strong wind shear and turbulence, which may be polluted with spuriously generated flow and numerical instability by ineffective discretization and parameterization schemes (Bénard et al. 2005, Durran 2010, Lundquist et al. 2012, Dietze et al. 2013). Ayotte (2008), Sumner et al. (2010) and Breton et al. (2017) reviewed some of the latest improvements tailored in diverse CFD models, underlining that modern microscale solvers generate significant errors when simulating wind flow over maximum terrain slopes greater than 0.2.

Coincidentally, in order to harvest the maximum amount of energy, the onshore wind farms tend to be installed over steep cliffs or ridges where the ABL separation affects the surface drag and vertical transport processes. Namely, wind turbine heights fit in the surface layer (i.e., 10 to 20% of the ABL height) and are affected by the dominant shear stresses. The correct positioning of wind turbines then requires a precise wind prediction method, within the framework of industrial standards for the design of mechanical components and structures that resist material fatigue due to variable wind forcing. This issue is of great interest for modern computational wind engineering (CWE) since CFD models must be able to solve unsteady microscale turbulence near the surface without requiring highly refined meshes in the wind farm sites.

Over the last few decades the microscale CFD techniques, such as Reynolds-Averaged Navier-Stokes (RANS) simulation and Large Eddy Simulation (LES), along with local equilibrium

assumptions and high-performance computational power capabilities have set the basis for high-resolution ABL modelling (Mason and Thomson 1992, Chow et al. 2005, Brasseur and Wei 2010, Sumner et al. 2010, Cabezón 2013, Bengtsson 2015, Breton et al. 2017). These have evolved into more advanced methods that combine meso- and microscale models to reproduce large-scale circulations, influenced by meteorological conditions, as well as small-scale physical processes subjected to local surface and canopy features. Considerable interest now exists on these combined multiscale methods, with embedded or built-in LES schemes in non-hydrostatic mesoscale models for surface bounded flows over complex terrain (Brown et al. 2001, Weigel et al. 2006, Chow and Street 2009, Bechmann and Sørensen 2010, Sumner and Masson 2012, Marjanović 2015, Liu et al. 2016). The multiscale context of these of methods relates to the so-called "terra incognita" described by Wyngaard (2004), which is the range of scales that cover the energy transport process from macroscales (synoptic and mesoscale structures) to microscales (small, energy dissipating eddies).

The evident advantages of multiscale modelling have led this method to become one of the mainstream trends in CWE, with interesting developments such as the NREL Simulator for On/offshore Wind Farm Applications (SOWFA) that has successfully validated over flat terrain a high-fidelity simulation method to gain insight of wind farm aero-structural dynamics (Churchfield et al. 2012, Fleming et al. 2013, Churchfield et al. 2014). Although modern multiscale models allow more flexibility in the choice of numerical schemes and have broadened the range of resolvable scales, some sources of error persist in wall modelling, terrain smoothing, data assimilation techniques and model coupling for high resolution simulations. Multiscale methods are mostly restricted by proper boundary conditions and surface layer modelling over steep slopes, which require robust and stable algorithms capable of solving transient phenomena in presence of high impact complex terrain (e.g. Chow and Street 2009, Gasset et al. 2012).

Hence, the objective of this paper is to describe and validate the numerical enhancements implemented in a robust multiscale solver, capable of simulating orographically generated turbulence and flow separation over steep slopes. This enhanced solver embeds a LES method

with an eddy-vicosity SGS parameterization in the Canadian non-hydrostatic mesoscale compressible community (MC2) model. A thorough description of the latest supported version of MC2 (i.e., v4.9.8) can be found in Thomas et al. (1998), Girard et al. (2005), Pinard et al. (2005) and Pinard et al. (2009), and the details of the first successful LES implementation in MC2 are presented by Gasset et al. (2014) and Gasset (2014), who validated the MC2-LES v4.9.8 method over flat terrain. Additionally, this multiscale model has been upgraded with the new semi-implicit (N-SI) discretization scheme as discussed in Chapter 2, and validated with real orographic flow in Chapter 3. This enables MC2-LES perform ABL simulations over steep slopes while retaining the convenient terrain-following coordinates (Gal-Chen and Somerville 1975, Schär et al. 2002) and the Robert-Asselin-Williams (RAW) energy-conserving frequency filter by Williams (2011). Hereafter, this upgraded version will be referred to as the MC2-LES v4.9.9 model.

The basic governing equations and the latest improvements are briefly described in section 4.2, providing an overview of the SGS parameterization employed for this study and the additional metric terms introduced in the strain rate tensor calculation to adapt the LES algorithm for terrain-conforming grids. Section 4.3 is dedicated to present the modelling results of the neutral ABL flow over flat terrain, aimed to define the SGS scheme constant, grid aspect ratio sensitivity and to compare the former and new SI time discretization schemes within the MC2-LES method for turbulence modelling. Then, canonical validation tests over an isolated moderate-to-steep sloping Gaussian ridge (maximum slope of 0.2 or $\vartheta \sim 11.3°$) and the steep RUSHIL H3 (maximum slope of 0.33 or $\vartheta \sim 18.5°$) case are discussed, analysing and comparing their resulting mean flow structure and turbulence features against other multiscale model outputs and experimental observations. Finally, section 4.4 presents some concluding remarks and future work recommendations, providing ideas to further improve this multiscale methodology.

4.2 Model Equations and Numerical Enhancements

The MC2 kernel solves the governing equations for the state variables (**Ψ**) by separating the material derivatives ($d\boldsymbol{\Psi}/dt$) and linear terms (**L**, treated implicitly) from the non-linear terms (**R**, treated explicitly), external forcing and source terms (**F**), expressed in matrix form as:

$$\frac{d\boldsymbol{\Psi}}{dt} + \mathbf{L} = \mathbf{R} + \mathbf{F} \,. \tag{4.1}$$

The semi-implicit semi-Lagrangian (SISL) discretization is applied on the first three terms of matrix system (4.1) to calculate the fluid particle's trajectory over three time-levels and, then, the external forcing and source terms are added in a fractional-step procedure. Thus, the fundamental improvement introduced in system (4.1) is the restructuration of the linear **L** and non-linear **R** terms, in order to remove the computational mode and terrain-induced noise in the new formulation. As explained in Gasset et al. (2014), the momentum and heat turbulent fluxes are included in the **F** terms after the governing equations are filtered. These turbulent fluxes need to be modeled using a particular SGS scheme in order to close the equation system.

The former equation system of MC2 v4.9.8 (Girard et al., 2005), discretized with the original semi-implicit (O-SI) scheme, solves the following momentum, energy and continuity equations (closed with the diagnostic ideal gas equation $p = \rho RT$) for the prognostic state variables **Ψ** = (**v**, P and b):

$$\frac{d\mathbf{v}}{dt} + f\,\mathbf{k}\times\mathbf{v} + \left[\nabla - \gamma_*\mathbf{k}\right]P + \mathbf{k}(b - \gamma_A P) = \mathbf{f} - \frac{b}{g}\left(\nabla - \beta_A\mathbf{k}\right)P \,, \tag{4.2a}$$

$$\frac{d}{dt}(b - \gamma_* P) + N_*^2 w = \gamma_A Q - b\left[\beta_A w + \frac{R}{c_v}\nabla\cdot\mathbf{v}\right], \tag{4.2b}$$

$$\frac{d}{dt}\left(\frac{P}{c_*^2}\right) + \nabla\cdot\mathbf{v} - \frac{g}{c_*^2}w = \frac{Q}{c_p T} \,. \tag{4.2c}$$

where $d/dt = \partial/\partial t + \mathbf{v}\cdot\nabla$ represents the material derivative, $\mathbf{v} = (u, v, w)$ the velocity vector, $\mathbf{k}$ the vertical direction unit vector, f the Coriolis parameter, $P = RT_* \ln(p')$ the generalized pressure, $p' = p - p_*$ the pressure perturbation, $b = g\left(T'/T_*\right)$ the buoyancy, $T' = T - T_*$ the temperature perturbation, $\mathbf{f} = \left(\mathrm{f}_u, \mathrm{f}_v, \mathrm{f}_w\right)$ the non-conservative forces, Q the heat sources, $c_*^2 = \left(c_p/c_\upsilon\right)\left(RT_*\right)$ the speed of sound and $N_*^2 = g\left(\beta_A + \gamma_A\right)$ the natural oscillation frequency, with two constants $\beta_A = \partial \ln T_*/\partial z$ and $\gamma_A = g/c_p T_*$.

By applying an eigenmode analysis to system (4.2), it is possible to identify how the O-SI scheme inherently generates a spurious computational mode that, for simulations over steep slopes, induces strong numerical noise and instability. A new semi-implicit (N-SI) time discretization scheme is proposed to yield a reformulated equation system with a numerically stable structure of the non-linear terms related to the buoyancy and pressure gradient, as follows:

$$\frac{d\mathbf{v}}{dt} + f\mathbf{k}\times\mathbf{v} + \overline{(\alpha+1)(\nabla P + \mathbf{k}\hat{b})}^{t} - \left(\gamma_* + \gamma_A\right)\mathbf{k}P = \mathbf{f} + \frac{\hat{b}}{g}\beta_A \mathbf{k}P, \tag{4.3a}$$

$$\frac{d}{dt}\left[(\alpha+1)\hat{b} - \gamma_* P\right] + \overline{\frac{N_*^2 w}{(\alpha+1)}}^{t} = \gamma_A Q - \alpha N_*^2 w, \tag{4.3b}$$

$$\frac{d}{dt}\left[\frac{P}{c_*^2}\right] + \overline{\nabla\cdot\mathbf{v} - \frac{g}{(\alpha+1)c_*^2}w}^{t} = \frac{Q}{c_p T} + \alpha\frac{g}{c_*^2}w. \tag{4.3c}$$

where the overbar $\overline{[\ ]}^{t}$ denotes the implicit time averaging operator for terms solved over three time levels, $\alpha = (T - T_*)/T_*$ is the temperature perturbation ratio and $\hat{b} = gT'/T$ is the new buoyancy definition. Equation system (4.3) constitutes the enhanced kernel of MC2 v4.9.9, which contains explicitly treated terms properly modified to recover the linearity in the hydrostatic relationship and to remove the spurious computational mode, thus, ensuring the

model's numerical stability in the presence of steep topography. A comprehensive discussion of this numerical enhancement is provided in Chapter 3.

As many atmospheric models, MC2 employs a curvilinear terrain-following coordinate system defined in terms of a height-based monotonic transformation, such as the Gal-Chen height (Gal-Chen and Somerville, 1975):

$$Z(X,Y,z)=\left[\frac{z-h(X,Y)}{z_T-h(X,Y)}\right]z_T \ , \tag{4.4}$$

where z is the local Cartesian height, $h(X,Y)$ is the topographic height and z_T is the height of model's top lid. Hence, the model's kernel (4.3) is transformed with the metric tensor transformation based on equation (4.4). A thorough explanation of this procedure is also provided in Girard et al. (2005).

Based on the Boussinesq hypothesis and using Einstein's notation, the turbulent stresses and heat fluxes can be expressed in terms of the eddy- and heat-mixing coefficients $(\mu_t=\rho K_M;\mathrm{Pr}_t=K_M/K_T)$, the resolved strain rate $S_{ij}=1/2\left[\partial\bar{u}_i/\partial x_j+\partial\bar{u}_j/\partial x_i\right]$, the sub-filter turbulent kinetic energy $\bar{\rho}k=1/2\overline{\rho u_l' u_l'}$ and the gradient of the resolved potential temperature ($\partial\tilde{\theta}/\partial x_i$), such that (Gasset et al., 2014):

$$-\overline{\rho u_i' u_j'}=\tau_{ij}=2\mu_t S_{ij}-2/3\left(\mu_t S_{ll}-\bar{\rho}k\right), \tag{4.5a}$$

$$-\overline{\rho u_i'\theta'}=\mu_t/\mathrm{Pr}_t\left[\partial\tilde{\theta}/\partial x_i\right] , \tag{4.5b}$$

Here the tilde ($\tilde{\psi}$) represents the application of the implicit filter on the prognostic variables when the solution is projected onto the numerical grid. This tilde is employed on the spatially filtered model variables, while the averaging overbar is applied for Favre filtering other quantities such as momentum and heat fluxes.

As explained by Gasset et al. (2014), the volumetric part of the Reynolds stress tensor τ_{ij} [i.e., $2/3(\mu_t S_{ll} - \overline{\rho}k)$] is added to the pressure and included along with the **R** terms to be solved explicitly. In the standard MC2-LES method, the **R** and **F** terms of matrix system (4.1) are respectively subdivided into $\mathbf{R} = R_{dyn} + R_{turb}$ and $\mathbf{F} = F_{dyn} + F_{turb}$, where terms directly solved with the dynamic kernel are identified with the subindex '*dyn*' and terms modelled with a parameterization scheme are identified with the subindex '*turb*'). For this implementation, the R_{dyn} contains the non-linear dynamic terms, F_{dyn} the non-conservative forces and heat sources, R_{turb} the volumetric part of τ_{ij} and F_{turb} the deviatoric part of τ_{ij} and turbulent heat diffusion terms.

The computation on terrain-conforming grids of the deviatoric part of the Reynolds stress tensor (i.e., $2\mu_t S_{ij}$ included in F_{turb}) requires its transformation based on equation (4.4). After including the metric terms $G_0 \equiv \partial z/\partial Z$, $G_1 \equiv \partial z/\partial X$ and $G_2 \equiv \partial z/\partial Y$ that recover the terrain's curvature, the horizontal turbulent diffusion tendencies $\left(F^H_{turb}\right)$ become:

$$F^H_{turb} = \begin{Bmatrix} F^H_{turb-U} \\ F^H_{turb-V} \\ F^H_{turb-w} \\ F^H_{turb-T} \\ 0 \end{Bmatrix} = \begin{Bmatrix} \frac{1}{\overline{\rho}}\left[\frac{\partial A_{UV}}{\partial Y_Z} + \frac{G_2}{G_0}\frac{\partial A_{UV}}{\partial Z} + \frac{1}{G_0}\frac{\partial B_U}{\partial Z}\right] \\ \frac{1}{\overline{\rho}}\left[\frac{\partial A_{UV}}{\partial X_Z} + \frac{G_1}{G_0}\frac{\partial A_{UV}}{\partial Z} + \frac{1}{G_0}\frac{\partial B_V}{\partial Z}\right] \\ \frac{1}{\overline{\rho}}\left[\frac{\partial A_w}{\partial X_Z} + \frac{G_1}{G_0}\frac{\partial A_w}{\partial Z} + \frac{\partial B_w}{\partial Y_Z} + \frac{G_2}{G_0}\frac{\partial B_w}{\partial Z}\right] \\ \frac{g\pi}{\overline{\rho}T_*}\left[\frac{\partial A_T}{\partial X_Z} + \frac{G_1}{G_0}\frac{\partial A_T}{\partial Z} + \frac{\partial B_T}{\partial Y_Z} + \frac{G_2}{G_0}\frac{\partial B_T}{\partial Z}\right] \\ 0 \end{Bmatrix}, \quad (4.6)$$

where $\pi = T/\theta = \left(p/p_0\right)^{R/c_p}$ is the isentropic Exner relation, with R and c_p as the dry-air gas constant and specific heat at constant pressure, respectively. The state variable turbulent fluxes

in equation (4.6), denoted here as (A_Ψ, B_Ψ), are then related with the eddy-mixing coefficients and map scale factor (m^2) in a gradient form such that, for example:

$$A_{UV} = \rho K_M m^2 \left[\frac{\partial \tilde{v}}{\partial X_Z} + \frac{G_1}{G_0}\frac{\partial \tilde{v}}{\partial Z} + \frac{\partial \tilde{u}}{\partial Y_Z} + \frac{G_2}{G_0}\frac{\partial \tilde{u}}{\partial Z} \right], \tag{4.7a}$$

$$B_U = \rho K_M \left[\frac{\partial \tilde{w}}{\partial X_Z} + \frac{G_1}{G_0}\frac{\partial \tilde{w}}{\partial Z} \right]. \tag{4.7b}$$

Appendix IV of this work presents further details on the full transformation of the Reynolds stress tensor with the corresponding metric coefficients and its implementation in the MC2-LES code. The classical Smagorinsky (SMAG) and the Deardorff (TKE) SGS schemes (Smagorinsky 1963 and Deardorff 1971, respectively) have been also implemented in MC2-LES as constant-coefficient parametrizations with stability functions based on the Richardson's number ($Ri = N^2 / \overline{S}^2$), where $N^2 = \left(g/\tilde{\theta}\right)\left(\partial\tilde{\theta}/\partial z\right)$ is the square of Brunt-Väisälä frequency of an air parcel's oscillation and $\overline{S} = 2\left(S_{ij} - \delta_{ij}/2\, S_{ll}\right)$ is the corresponding strain rate tensor modulus for compressible flow simulations. However, only the SMAG turbulence closure scheme will be presented since both models yield very close results. As mentioned in Gasset et al. (2014), the SMAG closure is formulated with:

$$K_M = \lambda f_m \overline{S}, \quad K_T = \lambda f_h \overline{S}, \tag{4.8a}$$

$$\lambda = \left[\frac{1}{C_s \Delta} + \frac{1}{\kappa\left(z + z_0\right)^2} \right]^{-1/2}, \tag{4.8b}$$

$$f_m = \begin{cases} \left(1 - 16Ri\right)^{1/2}, & Ri < 0 \\ \left(1 - \dfrac{Ri}{Ri_c}\right)^4, & 0 \le Ri \le Ri_c \end{cases}, \tag{4.8c}$$

$$f_h = \begin{cases} \dfrac{\left(1-40Ri\right)^{1/2}}{\mathrm{Pr}_t}, & Ri < 0 \\ \dfrac{\left(1-1.2Ri\right)}{\mathrm{Pr}_t}\left(1-\dfrac{Ri}{Ri_c}\right)^4, & 0 \le Ri \le Ri_c \end{cases}, \tag{4.8d}$$

where λ is the characteristic length scale, f_m and f_h are the stability functions for momentum and heat transport, respectively, C_S is the Smagorinsky coefficient, $\Delta = \left(\Delta x \Delta y \Delta z\right)^{1/3}$ is the filter length scale, $\kappa = 0.4$ is the von Kármán constant, z_0 is the aerodynamic roughness length and Ri_c is the critical Richardson number. Although the shortcomings of the constant coefficient Smagorinsky-based scheme are well known (e.g. excessive energy dissipation, inappropriate law-of-the-wall scaling, disregard of the energy backscatter) it still constitutes an important and necessary step towards better LES based wind modelling (Zhiyin, 2015). A complete explanation on the SGS scheme implementation for MC2-LES is provided by Gasset et al. (2014) and Gasset (2014).

Hence, the combination of the N-SI discretization scheme, RAW time filter and proper metric terms for SLEVE terrain-following coordinates, shall enable a robust multiscale MC2-LES method with reduced numerical noise and stable leap-frog integrations. This enhanced implementation also avoids a major model overhaul, such as changing from terrain-following coordinates to the immersed boundary method (IBM) used in WRF (cf. Lundquist et al. 2010, Lundquist et al. 2012, Arthur et al. 2016).

4.3 Validation and Discussion

To verify the quality of the results for multiscale modelling, three test cases are presented in this section, all performed with both the former and enhanced model versions to outline how the proposed numerical modifications help overcome the longstanding steep-slope limitation of mesoscale models using terrain-following coordinates. Firstly, a neutrally stratified ABL is simulated over flat terrain to reproduce the rotational Ekman layer, discussed by researchers

who employed different LES approaches (Andren et al. 1994, Kosović and Curry 2000, Brasseur and Wei 2010, Kirkil et al. 2012). This canonical case allows the verification of several parameters to ensure that the upgraded version of MC2-LES achieves the expected benchmark results. Then, the model is tested with a neutral ABL over a moderate slope symmetric Gaussian ridge (maximum slope of 0.2) and its results are compared with those reported in Kirkil et al. (2012), who used the state-of-the-art version of WRF-LES model.

Finally, the canonical RUSHIL H3 case is simulated to assess the performance of the proposed method for neutrally stratified wind flow simulations over a steeper ridge (maximum slope of 0.3). Based on the experimental observations and due to the steepness of the RUSHIL H3 surface, it is expected to obtain flow separation, recirculation and reattachment downstream past the hillcrest. Reproducing correctly these nonlinear phenomena is of great interest since it has major implications on the surface flow field (e.g., Chapter 3), and it has been one of the most challenging demands for LES wind modelling over complex terrain for the past two decades. Details on the model's setup for the RUSHIL H3 benchmark case will be provided in a subsequent section.

For the tests over flat terrain and Gaussian ridge, the flow is driven by a large scale pressure gradient with a Coriolis parameter of $f = 10^{-4}\,\mathrm{s}^{-1}$ to maintain a balance with a geostrophic wind of $(U_G, V_G) = (10.0, 0.0)\,\mathrm{m\,s}^{-1}$. The $f-$plane approximation is applied to use a single Coriolis parameter for the whole domain. Following the common practice for mesoscale models, these simulations are initialized with a sounding based on the wind speed, wind direction, pressure gradient and thermal stratification provided by a global atmospheric model. Also, the analytical Ekman layer velocity profile is initially perturbed with random fluctuations ranging between $\pm 0.1\,\mathrm{m\,s}^{-1}$ to generate sufficient instabilities for a fully developed turbulent flow field. The simulations are carried out during $t\,f/2\pi = 5$ time cycles (equivalent to 300,000 s with $\Delta \mathrm{t} = 4\,\mathrm{s}$) on a $4032\mathrm{m} \times 2016\mathrm{m} \times 1008\mathrm{m}$ C-type grid (depicted in Figure 4.1), with spatial resolution of $\Delta x = \Delta y = 32\,\mathrm{m}$ and $\Delta z = 4\,\mathrm{m}$. With these settings, MC2-LES meets

the basic stability criterion of a Courant-Friedrich-Levy (CFL) number for the horizontal scales of nearly a unit ($CFL_H \sim 1$).

The Arakawa's C-type staggered grid is usually employed in atmospheric models because it eases the calculations of the fluid particle's trajectory and velocity through the grid cells (Haltiner and Williams, 1980), which is particularly useful for semi-Lagrangian solvers, such as MC2 and similar models. As explained in Gasset et al. (2014), depending on the transport quantity calculation, the horizontal velocity components are taken at the cell faces and the pressure $q = \ln(p)$ at the center points (both on the 'momentum levels') to calculate their respective gradients. The vertical velocity, temperature and buoyancy, as well as the TKE, are located at the center of the lower and upper cell faces (i.e. 'thermodynamic levels'). The Coriolis parameter, map scale factor ($S = m^2$) and mixing coefficients (K_M, K_T) are stored at the cell corners.

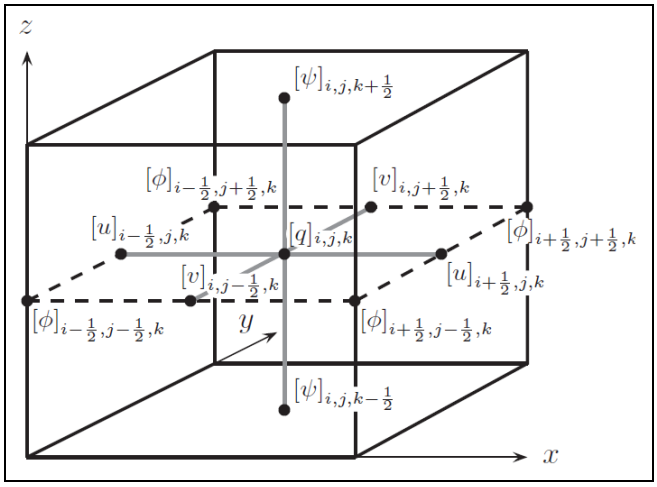

Figure 4.1 Spatial distribution of model variables and constants in the Arakawa C-type grid, for which $\phi = f, S, K_M, K_T$ and $\psi = w, T, b, TKE$.

These tests are performed with periodic lateral boundary conditions (BC), a wave-damping sponge for the last ten upper layers (based on equation 5 of Shuman, 1957) to prevent spurious

gravity wave reflection, and the local surface stresses ($\overline{uw_s}\big|_{i,j}, \overline{vw_s}\big|_{i,j}$) are assigned by the following logarithmic drag law at each horizontal grid point (i, j):

$$\overline{uw_s}\big|_{i,j} = C_d \tilde{u}_{i,j}\sqrt{\langle\tilde{u}\rangle^2 + \langle\tilde{v}\rangle^2},\ \overline{vw_s}\big|_{i,j} = C_d \tilde{v}_{i,j}\sqrt{\langle\tilde{u}\rangle^2 + \langle\tilde{v}\rangle^2},, \tag{4.9a}$$

$$C_d = \left[\frac{1}{\kappa}\ln\left(\frac{z_1 + z_0}{z_0}\right)\right]^{-2}. \tag{4.9b}$$

Here < > represents the planar averaging operation and C_d the constant drag coefficient, both computed at the height of the first momentum level (i.e., $z_1 = \Delta z/2$) with a fixed roughness length of $z_0 = 0.1\,\text{m}$ over the whole domain surface. The surface heat flux is based on the scheme proposed by Mailhot and Benoit (1982), which depends on the surface temperature (here set to 300 K). It is worth mentioning that, contrary to the velocity field, the temperature field is not initially perturbed with random fluctuations and the neutral stratification is achieved by decoupling the temperature and pressure when assigning an ideal large value to the dry-air heat capacity of the Exner function.

4.3.1 Neutral ABL Simulations over Flat Terrain for Model Calibration

In this subsection, the first- and second-order statistics obtained for the classical Ekman layer (EL) test over flat terrain will be discussed and compared with those reported in the literature. Based on these primary results, we will proceed to calibrate the model by selecting appropriate values for the SGS scheme coefficient, grid resolution and aspect ratio to ensure quality simulations over topography. As mentioned earlier, for all three cases we provide a comparison of MC2-LES's performance with both O-SI and N-SI schemes.

As a first verification, following Andren et al. (1994) and Chow et al. (2005), Figure 4.2 displays the time evolution of non-stationarity parameters for the plane-averaged horizontal

velocity components ($\langle\bar{u}\rangle, \langle\bar{v}\rangle$) departing from the geostrophic wind of $(U_G, V_G) = (10, 0)$, computed from the surface to the stress-free ABL height ($H = 1008$ m) such that:

$$C_u = -\frac{f}{\overline{uw}_s}\int_0^H \left(\langle\bar{v}\rangle - V_G\right) dz \ , \tag{4.10a}$$

$$C_v = \frac{f}{\overline{vw}_s}\int_0^H \left(\langle\bar{u}\rangle - U_G\right) dz \ . \tag{4.10b}$$

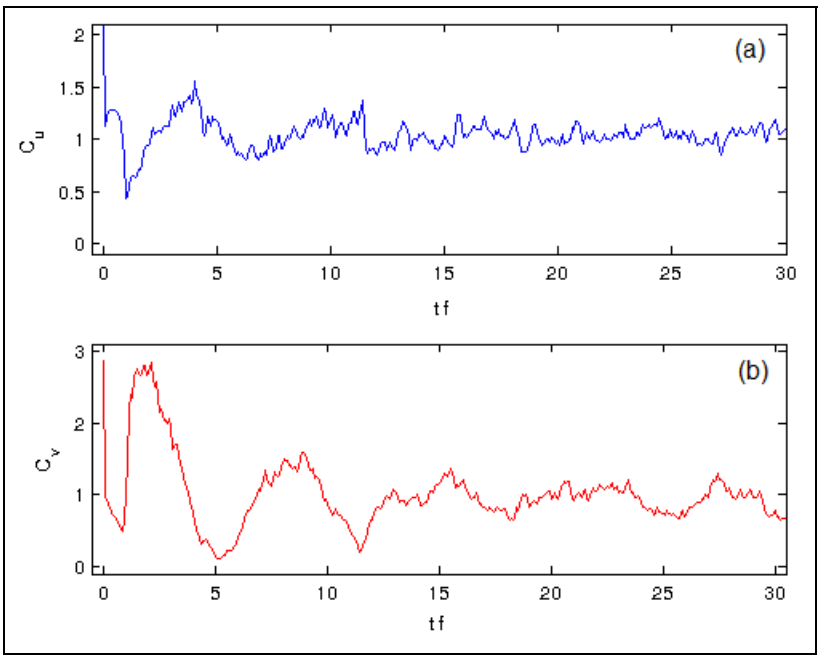

Figure 4.2 Evolution of the non-stationarity parameters for the (a) stream-wise and (b) span-wise velocity components of the EL over flat terrain, as function of the eddy time cycles.

These sensitivity plots exhibit that the model's spin-up inertial oscillations are attenuated sufficiently enough after $t\,f = 15$ time cycles, thus, achieving statistical steadiness thereafter when both parameters approximate the unity. The rational of scaling the velocity deficit with the surface shear stresses to achieve the unity equilibrium is inspired on the general concept of the velocity defect law for the outer layer, which is directly connected to and balances the inner layers (i.e. surface and overlap layers). Namely, equations 4.10 express the proportional

influence between the macroscale geostrophic driving force (outer layer) and the surface turbulent drag forcing (inner layers) on the model's inertial adjustment.

Even though the model keeps a gentle balance after $t\,f = 15$, with an approximate period of $2\pi/f$, statistics are obtained for the last 10 time cycles to ensure the effective steady-state conditions of the turbulent flow. Based on reliability theory (Grosh 1989, Rausand and Høyland 2004, Deodatis et al. 2014, Ercole et al. 2017) and mimicking Andren et al. (1994) procedure, a long-term transient simulation initialized with a randomly perturbed velocity profile (i.e., using fluctuations of an order of $\pm 0.1\,\mathrm{m\,s^{-1}}$) is consistent enough and equivalent to the average of multiple short-term realizations. Gasset (2014) showed how MC2-LES long simulations of the ABL over flat terrain encompass the statistical characteristics of several short runs.

A fundamental parameter for turbulence modelling is the SGS scheme coefficient (i.e., the Smagorinsky constant c_S for this model), which is varied by 0.025 in a range between 0.125 and 0.225, obtaining first- and second-order statistics for each value of c_S to decide which controls better the energy dissipation and numerical noise. As it can be observed in Figure 4.3a, for the flat terrain case the mean values of stream-wise and span-wise velocity components have the expected behavior and compare well with the literature (Andren et al. 1994, Kosović 1997, Chow et al. 2005). Since this ABL flow is predominantly oriented in the longitudinal direction, the stream-wise velocity component contributes more to balance the large-scale pressure gradient in the entrainment zone. On the contrary, the transverse velocity component exhibits the rotational effect of the Coriolis force on the wind. However, from Figure 4.3a, no significant differences are yet noticed in the mean velocity profiles as the c_S is varied.

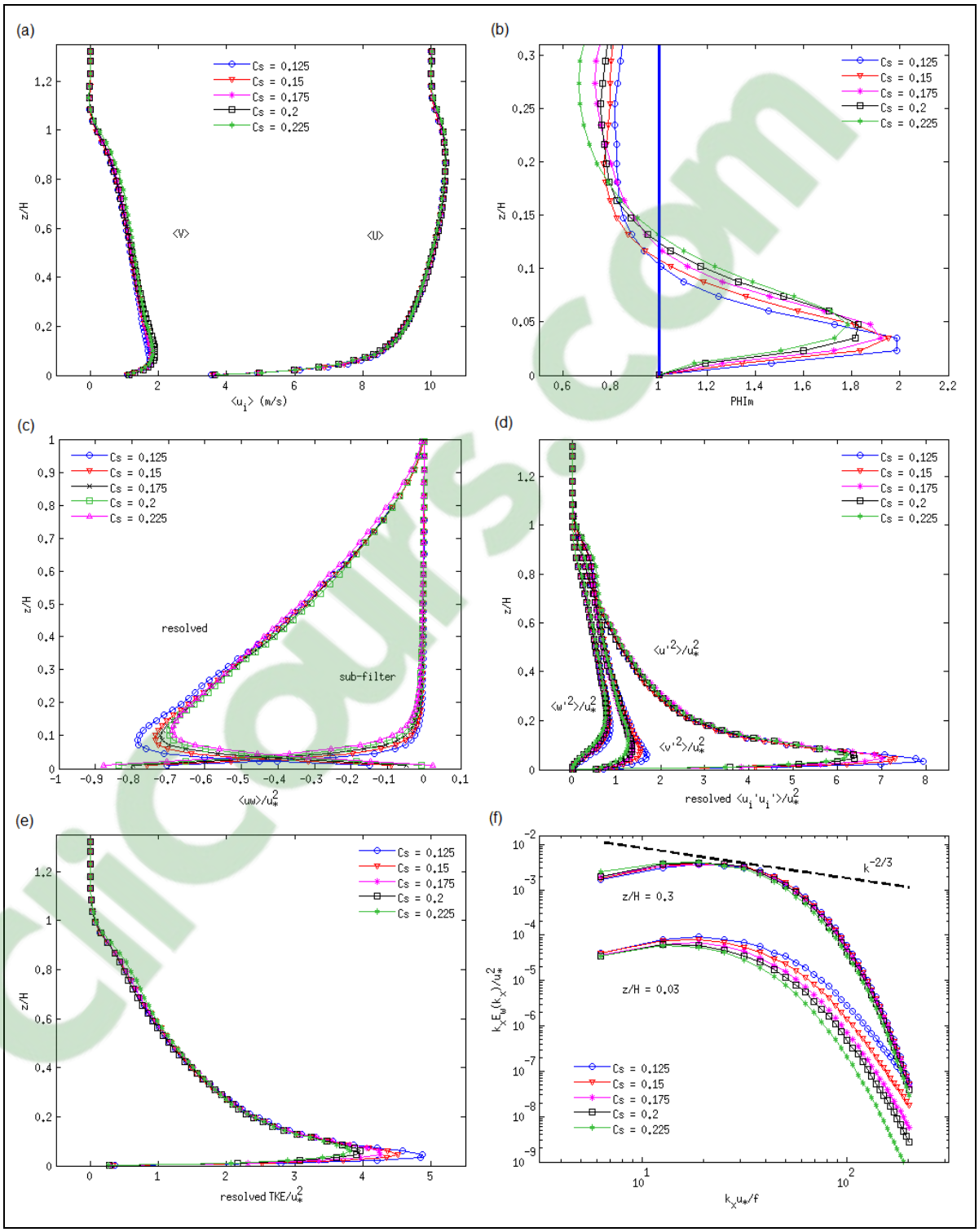

Figure 4.3 Space and time averaged (a) u and v velocity components, (b) wind non-dimensional gradient, (c) resolved and SGS τ_{13} stresses, (d) resolved velocity variances, (e) resolved TKE and (f) energy spectra in the flow's interior and surface layer over flat terrain.

Figure 4.3b illustrates how higher values of c_S reduce the wind shear within the surface layer (i.e., $z/H \leq 0.1$) and, consequently, reduce the numerically generated friction, which is one of the main reasons for the overshoot on the non-dimensional gradient of the mean horizontal wind field $\Phi_M = (\kappa z/u_*)\left[\left(\partial\langle\overline{\tilde{u}}\rangle/\partial z\right)^2 + \left(\partial\langle\overline{\tilde{v}}\rangle/\partial z\right)^2\right]^{1/2}$ (Drobinsky et al. 2007, and Brasseur and Wei, 2010). Even though with higher values of c_S the magnitude of Φ_M is reduced up to 10% (i.e., Φ_M should approximate to a unit based on the Monin-Obukhov similarity), this dissipation is transported throughout the bulk flow, hence, degrading the well-resolved scales (Brasseur and Wei, 2010).

On the contrary, profiles of both resolved and sub-grid scale parts of the τ_{13} stress (Figure 4.3c) reveal that smaller values of c_S help solve more flow structures close to the surface, thus, relying less on the SGS turbulence parameterization as desired for the MC2-LES method. These outcomes as well as the normalized velocity variances (Figure 4.3d) compare well to those reported in the literature (Andren et al. 1994, Kosović 1997, Chow et al. 2005), also confirming that smaller values of c_S feature stronger momentum fluxes within the surface layer. However, smaller values of c_S may yield noisier results reflected in higher energy accumulation close to the surface, as shown in the TKE vertical profiles (Figure 4.3e) and energy spectra (Figure 4.3f).

The decision of which value of c_S is more appropriate should rely on a balanced energy transfer between the surface layer (governed by finescale structure energy dissipation) and the flow's interior (where large eddies usually govern the energy transport). Independent of the enhanced numerical methods employed, it is preferable to avoid over-dissipation of TKE for high wavenumbers, while keeping good control of any spurious flows and noise in the surface layer. Thus, a mid-range value of $c_S = 0.175$ seems advisable for neutral ABL cases, keeping a moderate level of energy dissipation and a well-balanced energy transfer between the production and destruction scales. Unless otherwise indicated, this value for the SGS coefficient will be used on the subsequent suite of tests for both flat and complex terrain.

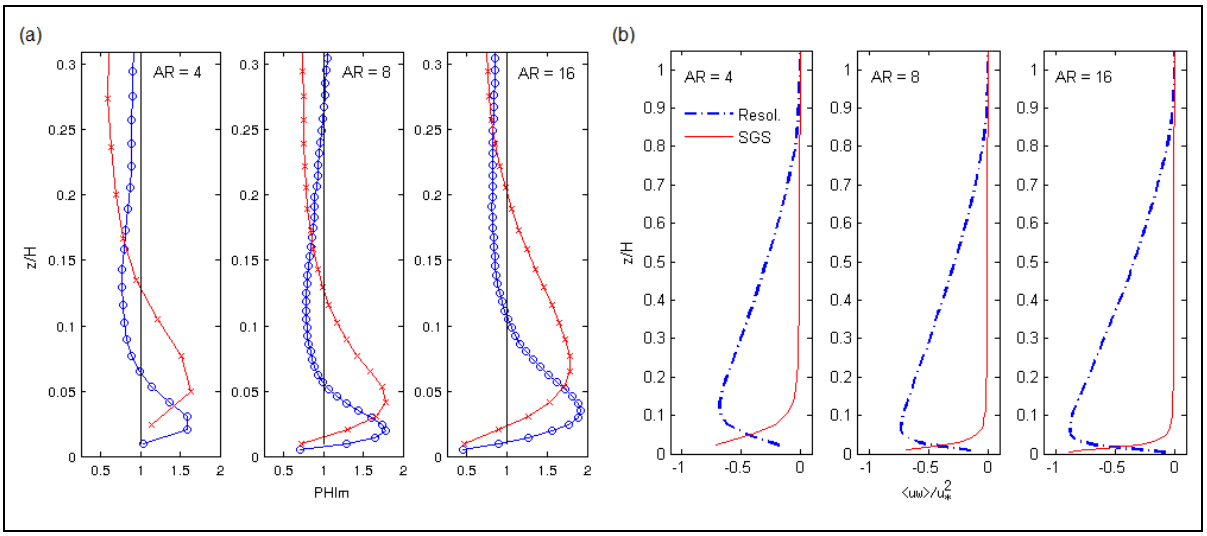

Figure 4.4 Evolution of the non-stationarity parameters for the (a) stream-wise and (b) span-wise velocity components of the EL over flat terrain, as function of the time cycles.

Figure 4.4 illustrates the influence of grid configuration with $4032\times2016\times1008$ points, comparing six combinations obtained with coarse $(\Delta x=\Delta y=36\,\text{m},72\,\text{m},144\,\text{m}$ and $\Delta z=9\,\text{m})$ and fine meshes $(\Delta x=\Delta y=16\,\text{m},32\,\text{m},64\,\text{m}$ and $\Delta z=4\text{m})$, for the aspect ratios $AR=\Delta x/\Delta z=4,8$ and 16. For all combinations, the CFL_H ranged between 0.6 and 1.25, hence, complying with the unity stability criterion ($\text{CFL}_\text{H}\sim1$). From the aspect ratio point of view, as observed in Figure 4.4a, with an anisotropic ratio of $AR=16$ or greater the Φ_M overshoot increases near the wall, indicating that there is some spurious energy backscatter (Porté-Agel et al. 2000, Stoll and Porté-Agel 2008). Unfortunately, when the horizontal mesh size is refined towards more isotropic grid cells, i.e. $AR=4$ or less, the Φ_M overshoot expands upwards exceeding the surface layer height, a condition which has been proven to generate spurious energy dissipation (Porté-Agel et al. 2000, Redelsperger et al. 2001, Senocak et al. 2007, Brasseur and Wei 2010). Therefore, $AR=8$ seems to be appropriate with an optimal balance between the energy transfer and dissipation processes to minimize errors for subsequent simulations.

Furthermore, Figure 4.4a compares the effect of the grid resolution on the model's response, based on Φ_M as the analysis parameter. Clearly, the magnitude of the velocity gradient's

overshoot is very close between both coarse and fine resolutions. Consequently, the velocity profiles can be expected to be similar and proportional by a scale factor. However, as Brasseur and Wei (2010) recommend, it is convenient and important to keep the Φ_M overshoot as close to the ground as possible to reduce the numerically induced friction and its influence on the resolved scales. Here, the finer mesh yields better results since it doubles the amount of grid points in the vertical direction close to the ground.

On the other hand, Figure 4.4b presents the resolved and SGS parts of the τ_{13} stress obtained only with the fine mesh configurations, showing that mid-range and high aspect ratios help better resolve the turbulent structures in the surface layer and depend less on the SGS parameterization scheme. The lower aspect ratio range seem to leave unresolved part of the flow structures within the surface layer. Regardless, the anisotropic 'pancake-like' grid configuration with $AR = 16$ or greater is not desirable for the Smagorinsky SGS scheme employed for the present LES implementation, since it pertains to the constant coefficient eddy-viscosity models based on 3D homogeneous and isotropic turbulence. Scotti and Meneveau (1997) remarked that with high AR pancake-like grids the triadic interactions at small scales close to the surface are available only to a limited amount of modes, which is not natural for the typical 3D turbulence. Additionally, the pancake-like mesh configuration yields extremely deformed grid cells that cause spurious pressure-gradient imbalances for simulations over steep slopes with terrain-following coordinates (Mahrer 1984, Klemp 2003, Zängl 2012). Since the grid with $AR = 8$ yields very good outcomes too, and considering the previous observations for both aspect ratio and resolution, a fine mesh of $\Delta x = \Delta y = 32$ m and $\Delta z = 4$ m, appears to be a worthy choice for the modelling settings.

The Ekman layer case is repeated with the previously selected settings, using the two semi-implicit time discretization schemes (i.e., O-SI and N-SI), thoroughly discussed in Chapter 2, to assess their influence on the turbulent flow modelling. MC2-LES v4.9.8 is the former version, casted and validated by Gasset et al. (2014), which only has the O-SI scheme and a baseline LES implementation with no complex terrain capabilities. MC2-LES v4.9.9 is the

most recent version that has both the O-SI and N-SI schemes, along with several numerical enhancements including the respective metric tensor terms to perform LES over complex terrain. An intermediate combination of the new model version MC2-LES v4.9.9 with the former O-SI scheme is also devised and tested, with the sole purpose of verifying if the latest implementation correctly replicates the flat-terrain canonical results, available in the literature and achieved by the former with the same discretization scheme.

Figure 4.5 presents the first and second order moments of the neutral Ekman layer simulations over flat terrain, obtained with the three model combinations. It confirms that the latter implementation is indeed capable of faithfully replicating the benchmark results (comparable to Andren et al. 1994, Kosovic 1997, Chow et al. 2005, Kirkil et al. 2012). Nevertheless, no significant distinctions are observed in the mean velocity profiles or momentum fluxes, except for MC2-LES v4.9.8 with O-SI that yields slightly weaker stream-wise momentum fluxes and variances (Figures 4.5b and 4.5c). It is worth noting that the SGS parameterization takes over the main contribution of the shear stresses within the surface layer (Figures 4.5b). Although the stream-wise velocity variance is as expected, the span-wise and vertical velocity variances are underestimated (Andren et al., 1994). These aspects indicate that the energy content and non-linear features of the EL flow may be slightly misrepresented.

In the context of this flat-terrain case, the energy spectra in Figure 4.5d also illustrate how the implementations with the O-SI scheme tend to dissipate slightly more TKE than the N-SI scheme for structures located at higher wavenumbers. Allegedly, this excessive dissipation is related to the spurious numerical friction that arises with the inadequate treatment of non-linear terms in the model equations. Regardless, either SI discretization scheme seem not to affect the overall performance of the sub-filter parameterization over flat terrain, maintaining a very similar repartition of resolved and modeled parts of the turbulent structures. The flat-terrain turbulent flow properties are evidently conserved with the N-SI scheme and the latter implementation of MC2-LES v4.9.9, which anticipates that accurate solutions of other canonical tests over irregular surfaces can be achieved and compared to the literature.

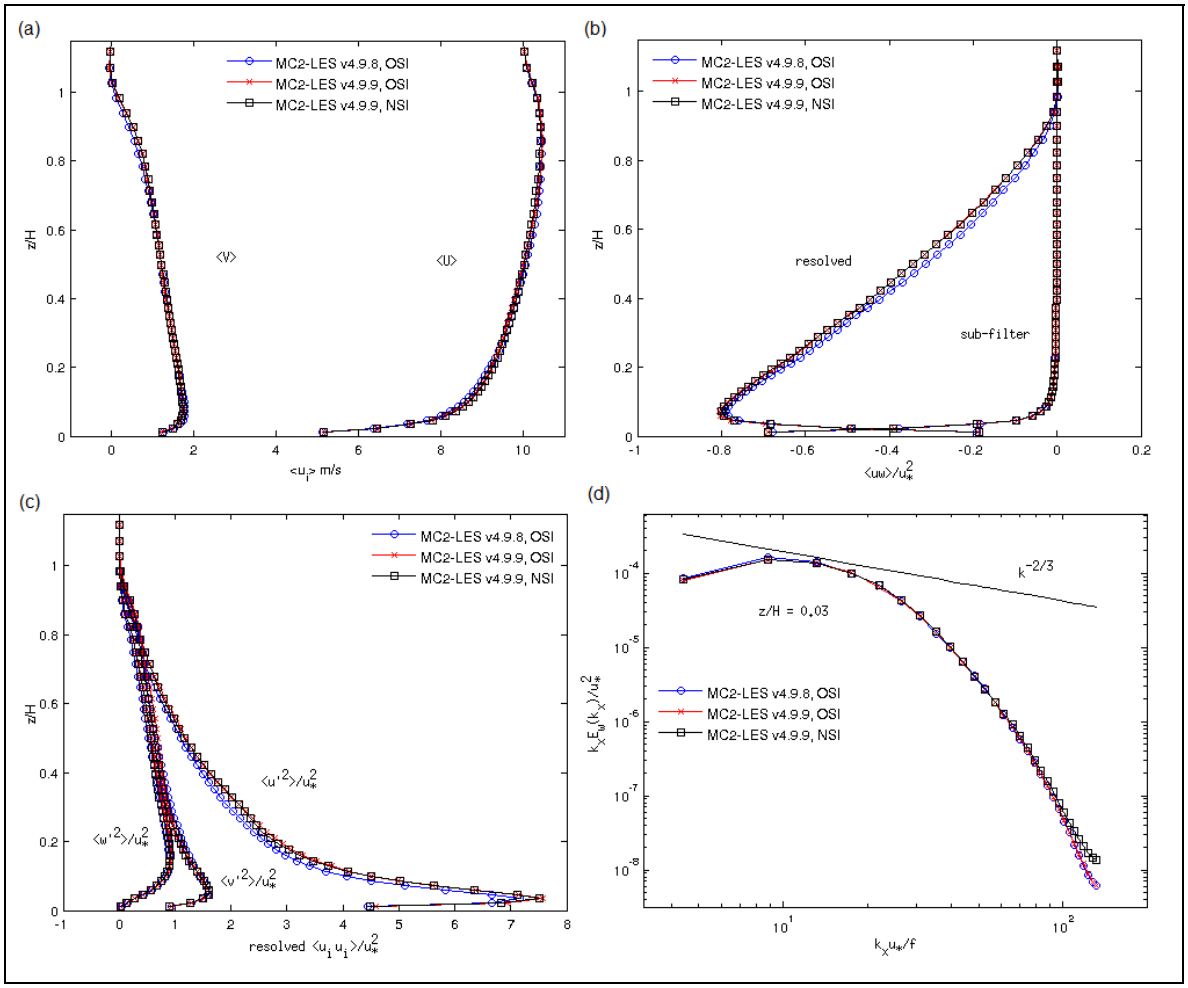

Figure 4.5 Ensemble averaged (a) streamwise and spanwise velocity components, (b) resolved and SGS normalized τ_{13} stresses, (c) resolved velocity variances and (d) surface layer energy spectra.

4.3.2 Neutral ABL Simulations over an Isolated Gaussian Ridge

A symetric Gaussian ridge is chosen as the topographic obstacle, inspired on Taylor (1977) and following the tests presented by Mirocha et al. (2010), Lundquist et al. (2012) and Kirkil et al. (2012). The mathematical expression of this topographic profile (c.f. Figure 4.6a), taking h_m as the maximum terrain height and a as the mountain half-length, is given by:

$$h(x) = h_m \exp\left[-\left(\frac{x}{a}\right)^2\right]. \tag{4.11}$$

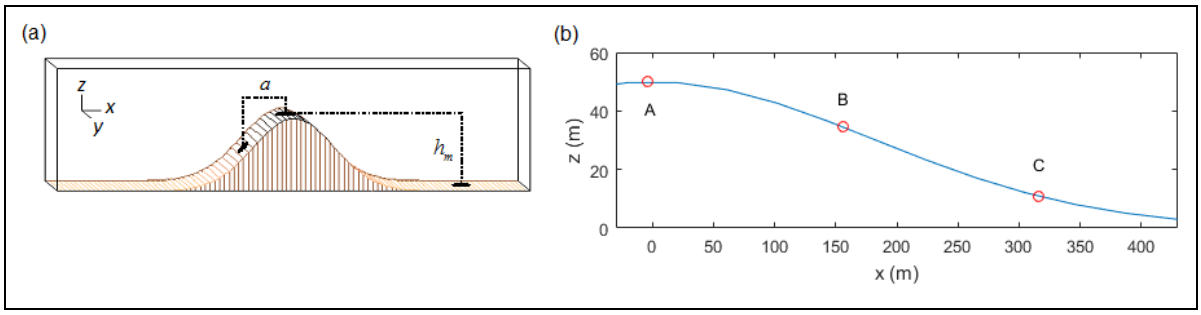

Figure 4.6 (a) Schematic view of the Gaussian ridge geometry and (b) locations of the [A] hill crest, [B] downslope lee-side and [C] base valley over the Gaussian ridge.

A neutrally stratified ABL simulation over this transverse Gaussian ridge is performed with MC2-LES using the same surface model, streamwise and spanwise periodic boundary conditions, as well as the same model settings assigned in the previous flat terrain case (i.e., roughness length of $z_0 = 0.1\,\mathrm{m}$, geostrophic wind of $(U_G, V_G) = (10.0, 0.0)\,\mathrm{m\,s^{-1}}$, Coriolis parameter of $f = 10^{-4}\,\mathrm{s^{-1}}$, time interval of $\Delta t = 4\,\mathrm{s}$, integration time of 300,000 s, domain size of $4032\mathrm{m} \times 2016\mathrm{m} \times 1008\mathrm{m}$, mesh resolution of $\Delta x = \Delta y = 32\,\mathrm{m}$ and $\Delta z = 4\,\mathrm{m}$ and aspect ratio of $AR = 8$). The topographic surface, with $h_m = 50\,\mathrm{m}$, $a = 256\,\mathrm{m}$ and maximum slope of 0.2 ($\vartheta \sim 11.3°$), is set to grow progressively until it reaches the maximum terrain height over 250 time-steps. It was observed that imposing it abruptly from the initial time-step triggers strong inertial oscillations and numerical instability. The terrain's maximum slope of 0.2 corresponds to the one employed by Kirkil et al. (2012), not to be confused with their ratio of 0.3 for the change in height with respect to the horizontal distance between model grid points.

The simulation is initialized with the resulting fully developed turbulent flow obtained from the previous Ekman layer over flat terrain. The results of this case are compared with the outcomes of Kirkil et al. (2012) for windflow over a 2D ridge, at the same positions on the (a) hill-top or crest, (b) downslope lee-side and (c) downslope valley, as shown in Figure 4.6b.

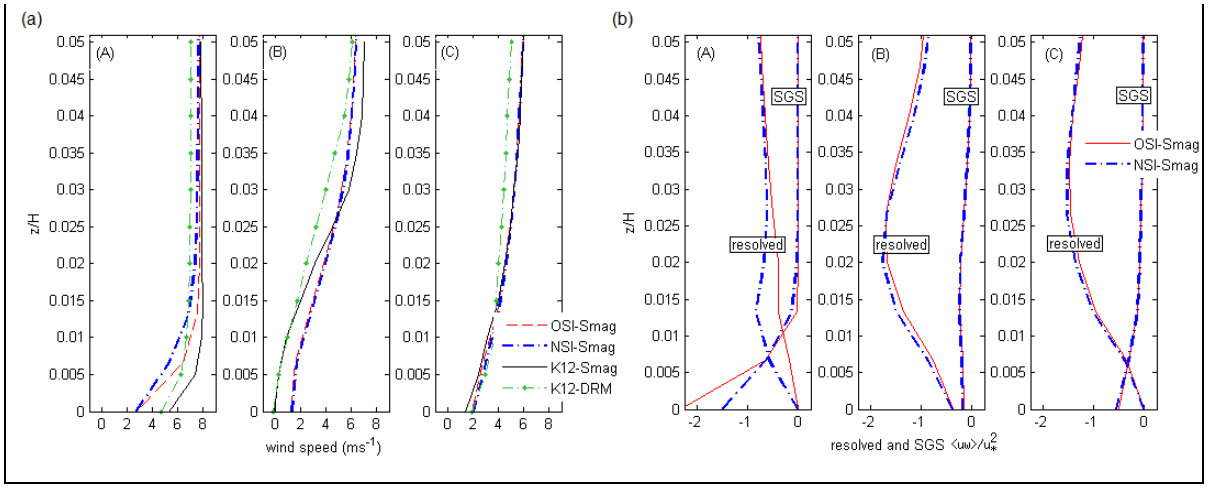

Figure 4.7 Time and span-wise averaged (a) wind speed and (b) resolved and SGS parts of the τ_{13} stress within the surface layer at the [A] hill crest, [B] downslope lee-side and [C] base valley along the Gaussian ridge.

Figure 4.7a presents the time and span-wise averaged velocity profile at each corresponding position within the surface layer. The interaction of this neutrally stratified ABL flow with a moderately sloping symmetric ridge evolves from a flow acceleration at the crest, to a deceleration and/or flow inversion in the lee-side due the adverse pressure gradient and, finally, to a mild acceleration in the downstream base valley, with the progressive reestablishment of the mean velocity profile. A sudden change from a favorable to an unfavorable pressure gradient, combined with the obstacle's slope and a neutral (or slightly stable) thermal stratification, causes flow reversal, separation and recirculation in the leeward valley (Stull, 1998). However, the flow reversal and separation phenomenon is not present for this turbulent ABL because the ridge is not steep enough (Brown et al., 2001).

As illustrated in Figure 4.7a, the wind speeds obtained with MC2-LES compare favourly with those reported by Kirkil et al. (2012) (denoted here with K12), who used both the standard Smagorinsky scheme (SMAG) and the dynamic reconstruction model (DRM) with backscatter TKE. As declared in K12, the DRM is more sophisticated but computationally demanding, and mainly devised to predict the TKE production and inertial range scaling of the power spectra. In spite of this, MC2-LES appears to underestimate the surface wind over the hillcrest and marginally overestimates it in the downstream lee-side. These differences may arise due to the

backscatter kinetic energy contributed by the WRF SGS schemes that yield a more active surface layer with an excess speed-up at the hilltop and a stronger flow reversal downstream. Nevertheless, the N-SI scheme yields a better-adjusted wind profile to the one of K12-DRM at the hillcrest, as compared to the O-SI and/or K12-SMAG schemes. Also, at the downward valley the MC2-LES profiles recover the expected wind gradient and speed. Hence, from a general scope, comparable results can be achieved with MC2-LES, that requires lower computational effort and ensures numerical stability with the N-SI scheme.

Unfortunately, Kirkil et al. (2012) do not present stress profiles; hence, in this case we only compare in Figure 4.7b the resolved and SGS parts of the τ_{13} stresses obtained with MC2-LES for both SI schemes. As illustrated, the τ_{13} stresses compare very closely except at the summit, where the surface wind speed is stronger with the O-SI scheme. Apparently, the combination of the N-SI discretization and SMAG schemes allows MC2-LES to better resolve the turbulent structures nearer to the ground, depending less on the SGS parameterization at this critical position. Even though the rest of the N-SI τ_{13} stress profiles appear to be almost the same as the ones obtained with the O-SI combination in the downstream lee-side and base valley, we noted that the model with N-SI scheme is able to perform stably without time decentering needed for the O-SI scheme in this case (namely, fixing an off-centering of $\delta = 0.1$). It is also worth noting that the resolved and SGS parts of the τ_{13} stress at the downslope lee-side do not cross within the surface layer, which is unusual as compared to the hilltop and valley stations but predictable based on the flow's non-linear nature at this position. As Allen and Brown (2002) point out, for laminar boundary layers the flow displacement near the hill causes a pressure field alteration that in turn drives the flow in a recirculating loop. On the contrary, for turbulent boundary layers the separation point and recirculation bubble is a complex phenomenom, which cannot be solely explained in terms of the terrain-induced displacement. The ABL separation not necessarily occurs at the point of zero wall stress and/or may not be located at the surface. Turbulent boundary layer experiments over rough hills (Athanasiadou and Castro 2001, Brown et al. 2001, Allen and Brown 2002) have proven that in the lee-side

and recirculation zone the velocity profiles do not follow the log law, which makes SGS modelling more challenging.

Lastly, Figure 4.8 presents the surface wind field, time averaged over the last ten time cycles (i.e., $t\,f = 10$), obtained with both SI schemes at 10 m AGL. As it is to be expected based on the previous discussion, certain similarities can be recognized between these surface layers. Analogous to the results presented in K12, both scheme combinations yield the streamwise-oriented skewed wind streaks, seemingly generated by the rotational Coriolis effect, and the flow acceleration is induced over the terrain-impacted area, approximately within the range $-a \le x \le a/2$. For both SI schemes, Figure 4.8 depicts flow reversal structures past the lee of the ridge, although with the O-SI scheme the wind field appears to be slightly more stretched over the symmetric transverse ridge upslope and lee-side, overshooting in the range $x \ge a$.

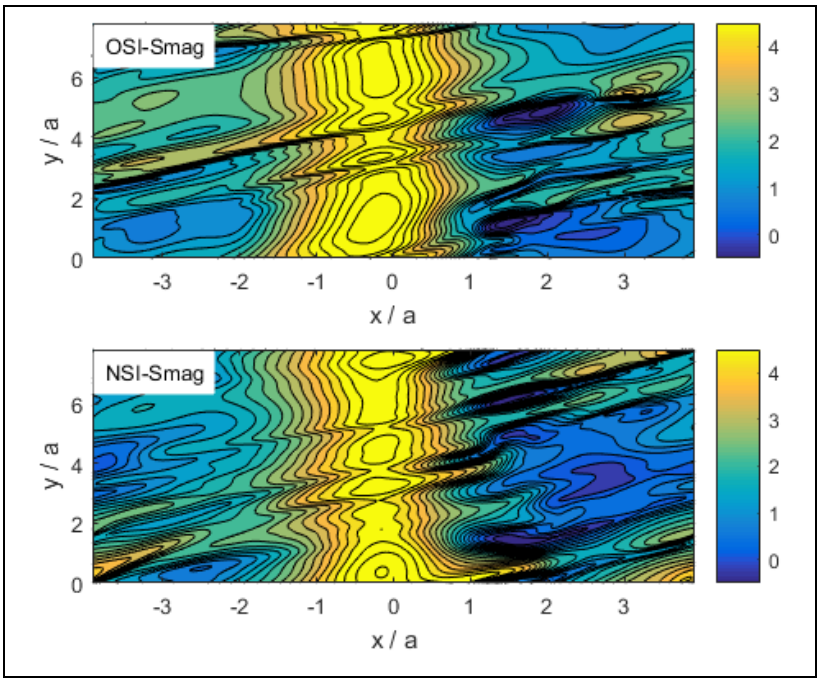

Figure 4.8 Time averaged wind fields (ms^{-1}) at 10 m a.g.l. over the symmetric Gaussian ridge with both SI schemes combined with the Smagorinsky turbulence closure.

This excessive streakiness is likely to be related to spurious motions inherently generated when employing the O-SI scheme for flow simulations over non-uniform terrain, as highlighted in

Chapters 2 and 3. On the other hand, with the N-SI scheme the expected flow lee-side deceleration and smaller streaks in the range $a/2 \le x \le 2a$ may be associated to reduced numerical noise and better resolved turbulent structures close to the ground. This effect is confirmed Gong et al. (1996) and in the following subsection with the RUSHIL test case.

4.3.3 Neutral ABL Simulations over the RUSHIL H3 Ridge

The "Russian Hill" (RUSHIL) experiments, conducted by the U.S. Environmental Protection Agency (EPA) along with a team of Russian researchers, were originally reported by Khrushudyan et al. (1981) and further postprocessed by Trombetti et al. (1991) and Castro (2004). These neutrally stratified flow experiments are widely employed for turbulent wind modelling comparisons and benchmark validations over isolated hills (e.g., Ying et al. 1994, Castro and Apsley 1997, Allen and Brown 2002, Castro 2004, Šíp and Beneš 2016). These canonical tests were originally performed within a rough surface wind tunnel to simulate flow and pollutant dispersion in the irrotational neutrally stratified ABL over three 2-D symmetric ridges of different curvatures, with hill aspect ratios of a/h_m = 3, 5 and 8 (being a the half-width and h_m the mountain height) denoted H3, H5 and H8, respectively. The present study focuses on the steepest hill H3 (i.e., maximum slope of 0.33 or $\vartheta \sim 18.5°$), to analyze its flow separation and compare the MC2-LES outcomes to the experimental data and the LES results reported by Allen and Brown (2002) (referred here as AB02). The RUSHIL bell-shaped ridge is formed with the following parametric set of equations:

$$\left.\begin{aligned} x &= \frac{1}{2}\xi\left[1+\frac{a^2}{\xi^2+m^2\left(a^2-\xi^2\right)}\right] \\ h &= \frac{1}{2}m\left(a^2-\xi^2\right)^{1/2}\left[1-\frac{a^2}{\xi^2+m^2\left(a^2-\xi^2\right)}\right] \end{aligned}\right\} \quad |\xi| < a, \qquad (4.12)$$

$$x = \xi \quad h = 0 \quad |\xi| \ge a,$$

where $m = n + \left(n^2 + 1\right)^{1/2}$ and $n = h_m / a$ is the maximum hill slope. As defined in AB02, the mountain height and half-width are $h_m = 0.117\,\mathrm{m}$ and $a = 0.351\,\mathrm{m}$, respectively. The surface roughness is fixed uniformly to $z_0 = 1.57 \times 10^{-4}\,\mathrm{m}$, with a friction velocity of approximately $u_* = 0.16\,\mathrm{m\,s^{-1}}$ from the log-law fitting to an upstream reference velocity of $U_{ref} = 4\,\mathrm{m\,s^{-1}}$. Following AB02, this irrotational flow has no Coriolis force and is driven by an imposed pressure gradient of $P_{0x} = -0.034\,\mathrm{Pa \cdot m^{-1}}$ that ensures the effective surface stress, consistent with the experimental measurements of Khrushudyan et al. (1981).

These model settings respect the dimensional similarity parameters employed in AB02, such as the mountain width to roughness length ratio $2a/z_0 \approx 4500$, the roughness Reynolds number $\mathrm{Re}_* = u_* z_0 / \nu \approx 1.88$ and the filter size to roughness length ratio $\Delta / z_0 \approx 58$. The numerical domain is 2 m long, 1 m wide and 1.3 m tall (i.e., $5.7a \times 2.85a \times 3.7a$) with $200 \times 100 \times 200$ points on an Arakawa C-type grid. The RUSHIL H3 simulations are carried out during 1250 s with $\Delta t = 0.025\,\mathrm{s}$, maintaining an average $\mathrm{CFL_H} \sim 1.25$, and statistics are time-averaged over the last 625 s (equivalent to 100 eddy turn-over times $t_* = z_i / u_*$, where $z_i \approx 1\,\mathrm{m}$ is the boundary layer depth) and spatially averaged over the span-wise direction of the symmetric hill. The previous boundary conditions (BC) are kept unchanged with lateral periodicity, a wave-damping lid for the last ten upper layers (cf. Shuman, 1957) and a surface drag log-law given by equation (4.9).

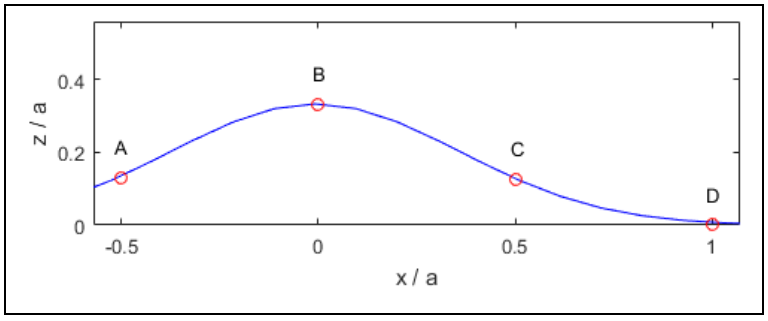

Figure 4.9 Schematic view of the RUSHIL H3 ridge with the locations of the [A] upslope, [B] hill crest, [C] downslope lee-side and [D] base valley control stations, as in Allen and Brown (2002).

Before running the simulation over RUSHIL H3 ridge, a fully turbulent channel flow over flat terrain is performed during 900 s with the selected settings, and its results are then employed to initialize the H3 simulation. To compare with the H3 experimental data (Trombetti et al. 1991, Castro 2004) and the AB02 results, four positions along the hill are chosen herein referred as the upslope $(x=-a/2)$, crest $(x=0)$, downslope $(x=a/2)$ and base $(x=a)$ points (cf. Figure 4.9).

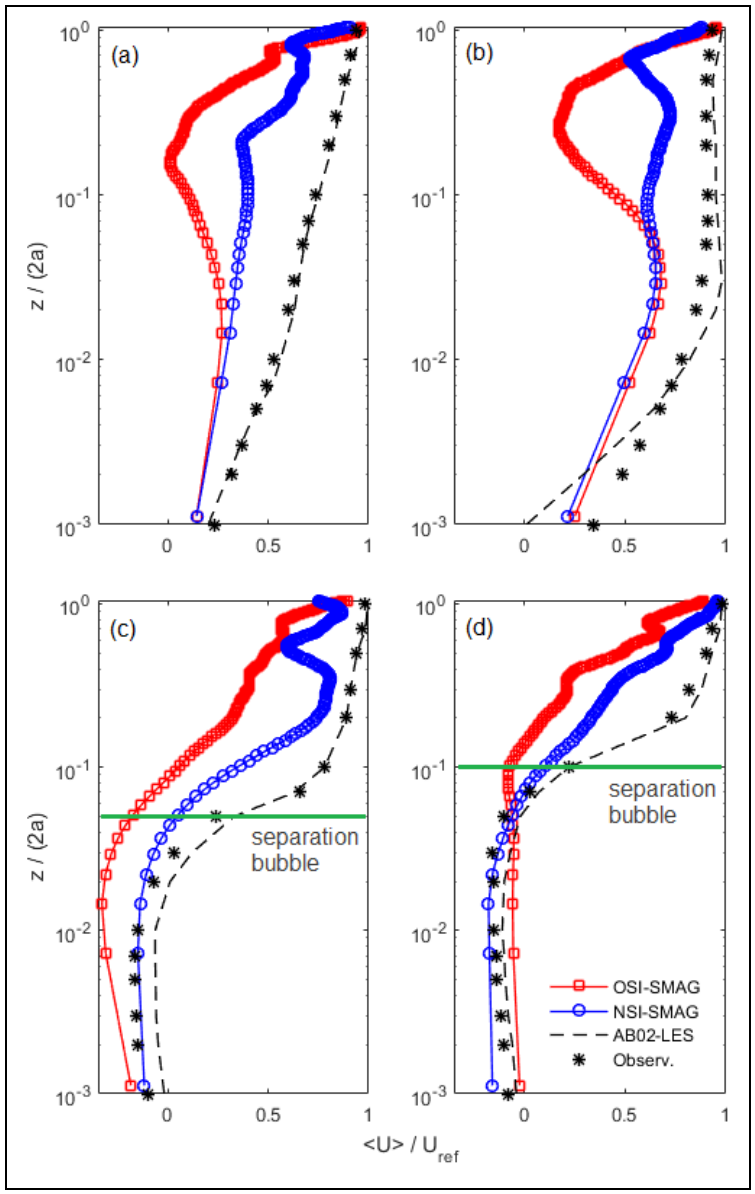

Figure 4.10 Time and span-wise averaged wind speed at the (a) upslope, (b) hill crest, (c) downslope and (d) base points of the H3 ridge. As in AB02, the ordinate is compared to the hill's full-width $2a$.

In Figure 4.10, the normalized mean stream-wise velocity profiles reveal that MC2-LES realizations with both SI schemes follow consistently the H3 experimental observations, mostly within the surface layer over the crest, downslope and base points (Figures 4.10b, 4.10c and 4.10d, respectively) where the N-SI scheme yields better wind estimates than the O-SI scheme. Close to the surface, these first order statistics are in good agreement for both SI schemes but, within the separation bubble and at higher altitudes above ground level, MC2-LES noticeably over- and/or under-predicts the wind, an issue slightly improved with the N-SI scheme implementation. The wiggles of the velocity profiles aloft $z/2a \geq 0.5$ result from the momentum balance compensated at the uppermost levels with the wave-damping layer at the domain's lid.

The AB02 model has overall better wind profile accuracy, that can be attributed to their more sophisticated Smagorinsky SGS scheme with stochastic energy backscatter (Mason and Thomson, 1992), which is not as diffusive as the classical Smagorinsky scheme. It is noteworthy that in the downslope and base valley stations (Figure 4.10c and 4.10d), where the flow's behavior is predominantly non-linear within the separation bubble, MC2-LES is able to capture well the reverse flow with the standard SMAG and N-SI schemes, effectively matching the RUSHIL H3 experimental observations in the ABL separation and recirculation zone.

Figure 4.11a compares the MC2-LES mean vertical flow fields obtained with both SI schemes at the transverse centerline after the hill's summit and lee-side. These plots illustrate how the model overshoots the wind speed with the former O-SI scheme, anticipates the ABL separation point and extends its recirculating bubble without properly achieving the flow's reattachment. On the contrary, the N-SI scheme reduces the wind overshoot and yields a well-defined recirculation zone, approximating the flow's separation and reattachment points at $x_S \approx 0.3a$ and $x_R \approx 1.4a$, respectively, measured from the crest position. Coinciding with the AB02 outcomes, the reattachment distance obtained with N-SI ranges between 65 to 70% of the expected position $x_R \approx 2a$, observed in RUSHIL H3 experiment. In addition, Figure 4.11b presents the surface wind patterns at the first grid layer, demonstrating that MC2-LES with N-

SI effectively reduces the spurious flow overshoot and achieves a better-defined reattachment zone than with the O-SI scheme.

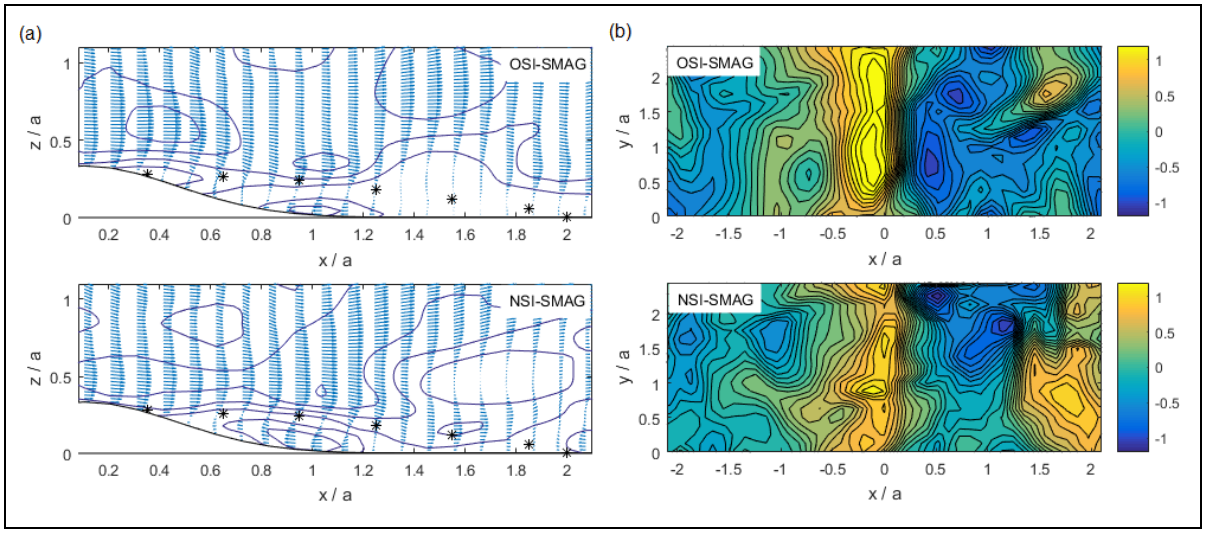

Figure 4.11 Time-averaged (a) vertical flow field contours and vector depiction at the transverse centerline, with $*$ representing the observed H3 separation streamline, and (b) horizontal winds $\overline{u}/U_{ref}$ at $z \approx 7\times10^{-3}$ m a.g.l., the first internal momentum level.

Figure 4.12 presents the normalized profiles of the τ_{13} Reynolds stress, which also exhibit the improvement achieved by MC2-LES with the N-SI scheme. Although the model combinations with both SI schemes follow appropriately the tendencies of experimental data, the N-SI implementation yields slightly better results near the surface at the upslope and crest positions (Figures 4.12a and 4.12b), and reduces the τ_{13} stress overestimation aloft on the downslope and base positions (Figures 4.12c and 4.12d) with respect to the AB02 results.

Regardless of the uncertainty in experimental observations, the weak variation of these Reynolds stresses above the hill is reasonable (Castro, 2004) and demonstrates how the numerical modifications improve the MC2-LES outcomes within the highly non-linear leeward separation bubble. It is worth remarking that the AB02 model captures –but overestimates– the strong changes in momentum fluxes present in the interface between the separation bubble and the ABL flow aloft. They justify this excess in a possible fault of the

RUSHIL experimental data, and they support the compliance of their results to the expected behaviour since their model grossly resolves the Reynolds stress.

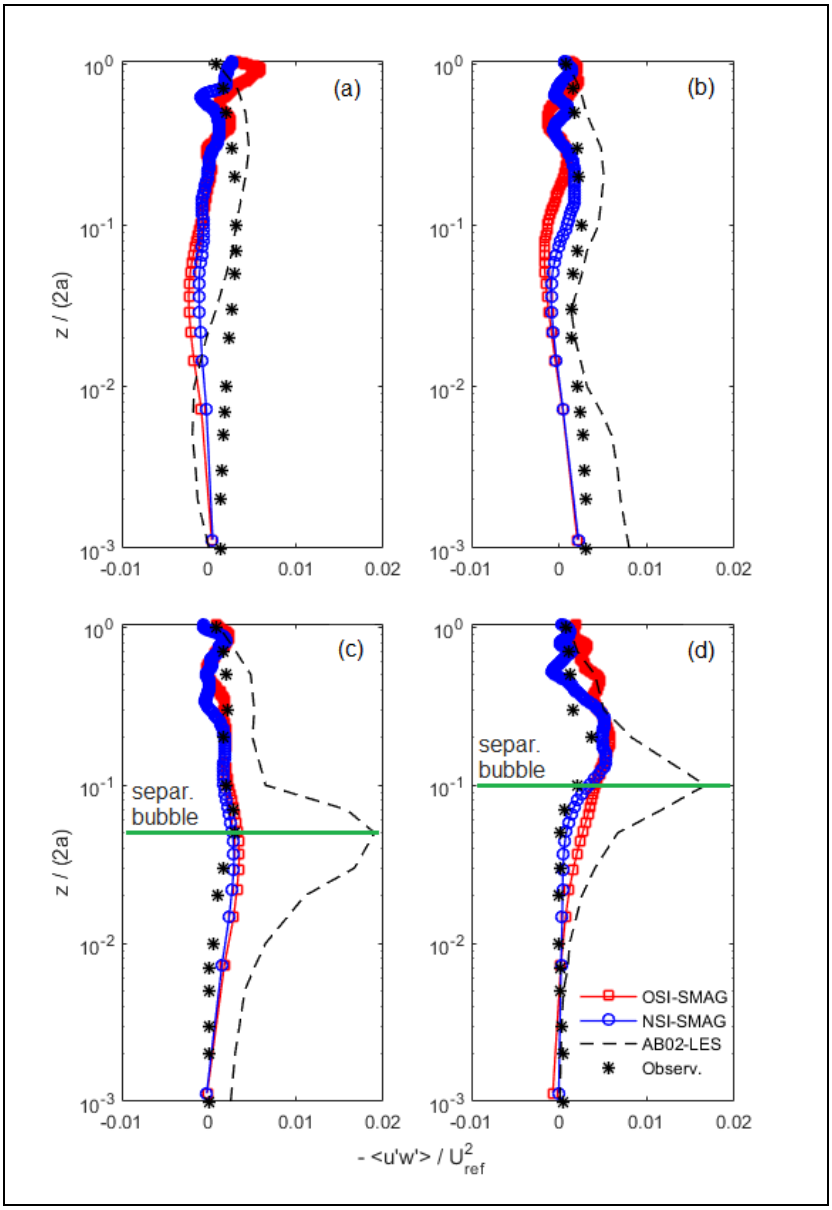

Figure 4.12 Time and spanwise averaged normalized τ_{13} stress at the (a) upslope, (b) hill crest, (c) downslope and (d) base positions of the H3 ridge.

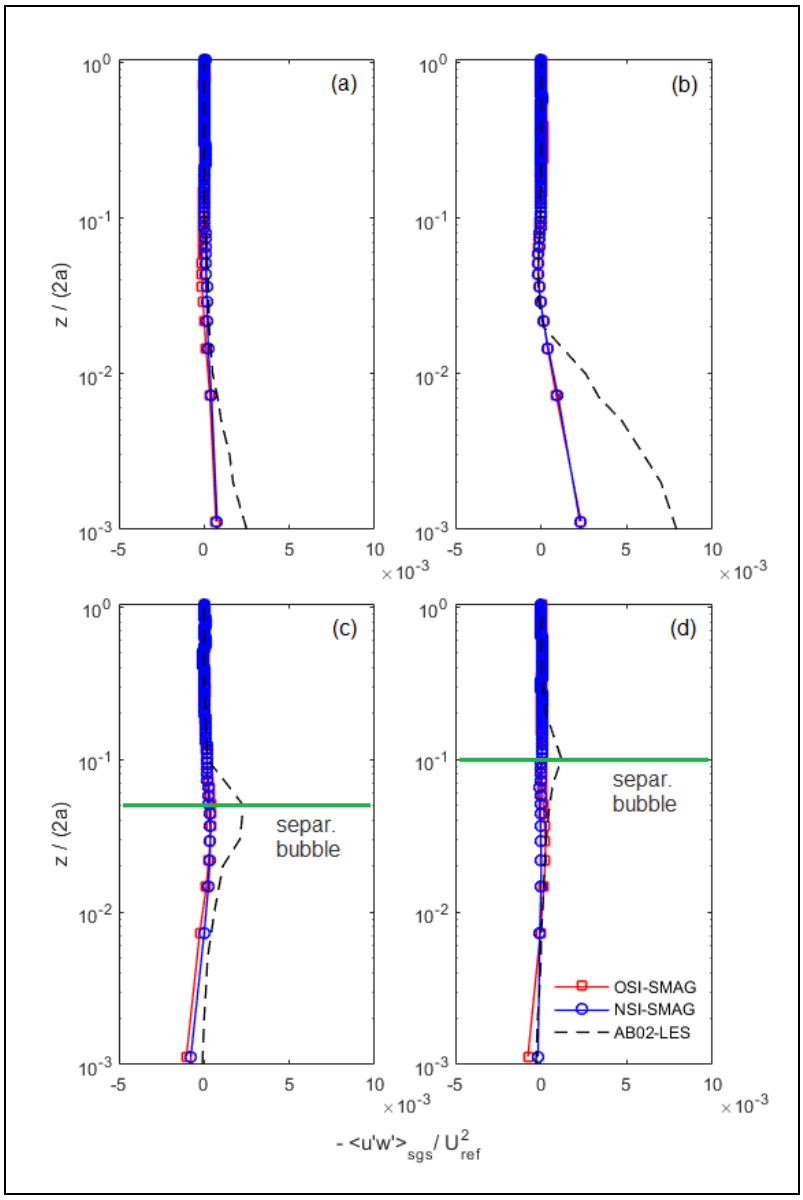

Figure 4.13 Time and spanwise averaged normalized SGS τ_{13} stress at the (a) upslope side, (b) hill crest, (c) downslope and (d) base positions of the H3 ridge.

The sub-filter part of the τ_{13} Reynolds stress shown in Figure 4.13 endorses the good performance of MC2-LES as compared to the AB02 results, which becomes more apparent at the hilltop and above the downslope recirculation zone (Figures 4.13b and 4.13c, respectively), where MC2-LES is able to resolve better the surface small structures. Although in this case

there is no distinct improvement of MC2-LES with N-SI scheme over the O-SI model combination, these SGS τ_{13} stress profiles confirm that the N-SI implementation maintains the turbulence closure contribution to a minimum close to the surface.

Undoubtedly, based on these second order statistics, the modified MC2-LES multiscale method with N-SI scheme has an overall improved performance and is capable of replicating the expected flow dynamics by reducing the wind speed overshoot and stress perturbation overprediction above the separation bubble. The main advantages of the N-SI implementation for MC2-LES flow modelling over steep terrain is the numerical robustness it adds without the necessity of additional subterfuges to control the spurious computational noise and instability.

4.4 Summary

The present study focuses on showing how the numerical modifications implemented in the MC2-LES model aid overcome characteristic deficiencies of multiscale wind simulations over complex terrain, mostly related to computational instability and spurious noise. Amongst these enhancements, a new time discretization scheme was put in place after a stability analysis, thoroughly discussed in Chapter 2, was applied on the model equations to identify and remove the terrain-induced sources of numerical error and instability. Additionally, the LES method embedded in MC2 was upgraded for wind modelling over complex terrain by adapting its Reynolds stress tensor with the model's metric terms for terrain-following coordinates. These changes are necessary for multiscale atmospheric models that solve compressible turbulent flow over high-resolution topography.

The present chapter only focusses on neutrally stratified flow, and reserves the sensitivity analysis of other thermal stratifications for future work. The statistical analysis (in terms of the time and spatially averaged velocity components, non-dimensional wind gradient, momentum fluxes, velocity variances and energy spectra) of the suite of ABL simulations performed and reported here indicates that over flat terrain there is good agreement with the similarity solution, but no significant improvements are achieved with the modified multiscale method.

However, in presence of mountainous terrain it effectively reduces the numerical errors and instability compared to the former model version. With the proposed model enhancements the neutral ABL flow past both a moderately sloping and a steep symmetric ridge generates the expected acceleration at the summit, reproduces well the flow patterns on the downwind lee-side and valley, solves better the small structures close to the surface and maintains the numerical stability for long-term integrations. The MC2-LES results obtained with the N-SI scheme over steep topography demonstrates the model's capacity to accurately replicate the flow separation and recirculation, as observed in the RUSHIL H3 experiment, even though the reattachment point is underestimated by approximately 30% yielding a shallower separation bubble.

The proposed enhancements reduce the need of excessive mesh refinement, modestly improves the model's accuracy and ensures its numerical stability in presence of steep terrain. Although modest and still needing more evaluation, these improvements contribute to the advancement of computational wind engineering and a step towards more precise wind resource assessment over complex topography. In future studies this multiscale method will be tested with orographic flow over real complex terrain, other static stabilities and dynamic models, and validated with atmospheric field data.

CONCLUSIONS

In order to continue the process of refinement of the MC2 model, and consequently the WEST application, the necessary issues to be solved are the SI scheme's numerical instability and spuriously generated noise, the thermal stratification disregard in the original wind-climate classification for the statistical dynamic downscaling initialization scheme, and the adaptation of the Reynolds stress tensor with metric transformations to correct terrain forcing for the 3D turbulence diffusion calculations. Although modest but conceptually noteworthy, this work contributes on the achievement of solutions to these issues and a higher quality mesoscale modelling in presence of steep terrain for more accurate wind resource assessment.

A literature review has been presented on the theoretical background and modelling aspects relevant for the analysis of high-resolution wind simulations over steep terrain. It provides a moderately complete state of progress in ABL flow modelling over topography, ranging from microscales to mesoscales, in addition to a view of the capabilities and limitations of existing methods and, most importantly, an identification of suitable solutions. Progress in each particular aspect of the problem conjunction is introduced in each chapter, providing the reader with comprehensive specificities on the approach followed by other researchers that oriented the methodology adopted for this research.

The work demonstrates unambiguously that the constant-coefficient, three time-level original SI scheme (O-SI) in presence of temperature perturbations and steep terrain slopes, without any time decentering and/or filtering, develops an asymptotically growing computational mode, high-frequency numerical noise and strong spurious flows. The widely used O-SI scheme is preconditioned by a constant-in-time linear operator, which usually consists in the linearization of the original system around a stationary reference state. The extended eigenmode analysis of the compressible non-hydrostatic EE system, with height-based σ-coordinates, manifested that by introducing an alternative definition of the buoyancy and linearizing with respect to the variables' mean values, contrary to arbitrary reference values,

the model recovers its numerical stability and reduces its spurious noise in two or three orders of magnitude for simulations over flat and steep topography.

Namely, an appropriate redefinition of the buoyancy force yields a restructuration of the explicitly treated residuals on the right-hand side of the EE system, which link the pressure-gradient and temperature perturbations and are responsible for the numerical instability in the O-SI scheme. The coefficients of these residuals are modified in such a way that the linearity of the hydrostatic perturbation relation is recovered and the scheme enters in a stable domain. An extensive suite of atmosphere-at-rest tests, performed with steep topography and various model settings, prove that the new semi-implicit (N-SI) scheme fixed-point configuration enables MC2 to complete long integrations with negligible numerical noise.

Regardless of the N-SI scheme effectiveness, it does not entirely remove the computational mode, which requires this solution to be combined with a smooth height σ-coordinate and more effective frequency filtering. Hence, the SLEVE terrain-following coordinate is employed to reduce the initial pressure-gradient imbalances and distorted model levels above high-resolution orography. Additionally, the improved Robert-Asselin-Williams energy conserving time-filter has been introduced to ensure a better performance of the leap-frog scheme. This combination was validated with a multi-layer strongly stratified atmosphere in presence of steep isolated and multiple parallel ridges. The outcomes reproduce the benchmark results reported by other researchers, which confirms the effectiveness of the proposed solution to achieve a significant noise reduction under complex conditions.

Moreover, stably stratified orographic flow simulations performed over the mountainous Whitehorse area, in the Canadian Yukon Territory, prove that MC2 is now capable of maintaining stable integrations and that it yields more accurate results in presence of steep complex terrain when employing the N-SI scheme. This real case study also allowed the validation of the upgraded statistical-dynamical downscaling (SDD) initialization scheme, which now includes the Brunt-Väisälä frequency as an additional criterion for the wind

climate-states new classification (NC), thus, better accounting for the thermal stratification that affects the vertical momentum transfer of wind flow over orography.

The comparison of the mean average error (MAE) of modelling outcomes with on-site met mast measurements indicates that the N-SI and NC schemes yield an individual improvement of 30% and 5%, respectively, for stable and strongly stable wind simulations. The combination of these enhancements, along with the SLEVE coordinate and RAW time filter, yields a 45% reduction of the numerical noise and enables the appropriate readjustment of the flow field over steep slopes. Consequently, the foremost achievement of the combined solutions introduced in MC2 and the SDD algorithm is the reduction of the spurious wind speed-up, an accurate calculation of the vertical momentum transport, and a better representation of the wind patterns for shear-driven ABL simulations over escarped mountainous formations.

The built-in LES method of MC2 is also upgraded by adapting its Reynolds stress tensor with the metric tensor transformations for terrain-following coordinates, which allows the recognition of topographic slopes projected on the model grid, and the correct computing of horizontal and vertical gradients for the 3D turbulence diffusion scheme. This metric adaptation is necessary for any multiscale turbulent flow simulation over high-resolution topography, although it is only the completion of the LES implementation in MC2. The statistical analysis of a suite of neutrally stratified, shear-driven wind simulations indicates that over flat terrain there is a relatively good agreement with the similarity solution, but no significant improvements are achieved with the upgraded MC2-LES model with N-SI scheme compared to the previous method. However, in presence of complex terrain slopes it effectively reduces the numerical errors and instability as compared to the former model version.

Neutrally stratified wind simulations over, both, moderately sloping and steep symmetric ridges prove that the upgraded MC2-LES model generates the expected acceleration at the summit, improves the flow patterns on the downwind lee-side and valley, solves better the small structures close to the surface and maintains the numerical stability for long-term integrations. The vertical profiles of wind speed and τ_{13} stress illustrate how the wind behaves

differently with increasing terrain slopes, sometimes generating a separation and recirculation bubble whose length is function of the wind speed, thermal stratification and obstacle's width. As observed in the RUSHIL H3 simulation, MC2-LES is now capable of adequately replicating the flow separation and recirculation, even though the reattachment point is underestimated (by 25 to 30%), thus, yielding a shallower separation bubble. The surface wind plots illustrate how the model with the former O-SI scheme overshoots the wind speed, anticipates the ABL separation point and extends its recirculating bubble without properly achieving the flow's reattachment. The N-SI scheme, on the contrary, effectively aids MC2 in realizing an adjusted flow pattern to the surrounding obstacles with the expected downhill reattachment, and reducing the dependence on the sub-grid scale parameterization.

Fortunately, these enhancements all together reduce the need of excessive mesh refinement and keep the second-order accuracy of MC2-LES. Although modest, these improvements seem to contribute to computational wind engineering and could be considered step forward towards more precise wind resource assessment over complex topography. This novel version of MC2-LES can easily become the standard dynamical kernel of the next-generation WEST method for advanced wind resource assessment over steep terrain.

As part of future work, a thorough study of atmospheric turbulence modelling employing this enhanced version of MC2-LES, upgrading the SGS scheme with a dynamic Smagorinsky scheme and energy backscatter formulation is recommended to provide a better representation of the transient processes in the ABL, as shown by Kirkil et al. (2012). This multiscale approach should also be tested with orographic flow over real complex terrain, and validated against dynamic reconstruction models and experimental data. The effect of incorporating the vertical velocity component in the surface stress calculation, the appropriate nesting of boundary conditions for a LES mesoscale model, as well as the high-resolution data assimilation schemes should be evaluated for complex terrain, which could enable MC2 (and WEST) to become a robust prediction system for operational decision-making of wind farms.

APPENDIX I

Surface Stress Calculation with the Oblique Coordinate System for Complex Terrain

The equations of MC2 are formulated in terms of an oblique (non-orthogonal) coordinate system. So far, though, this fact has been neglected in the calculation of the surface stress. As the slope of the topography increases with model resolution, this neglect may become significant for some applications. Nonetheless, there is a simple and easy way to correct this issue. In the horizontal momentum equations of MC2 there are turbulent forcing terms ($\mathbf{F}_{turb}^{H}$) which are presently approximated by:

$$\mathbf{F}_{turb}^{H} \approx \frac{1}{\rho}\frac{\partial \boldsymbol{\tau}}{\partial z} \equiv \frac{1}{\rho}\frac{\partial}{\partial z}\left(\rho K_M \frac{\partial \mathbf{V}_h}{\partial z}\right). \tag{I.1}$$

Here $\boldsymbol{\tau}$ is the stress vector and at the surface it is specified using the drag law formulation:

$$\boldsymbol{\tau}_s = \rho c_d \left|\mathbf{V}_s\right| \mathbf{V}_s , \tag{I.2}$$

where $\mathbf{V}_s$ is $\mathbf{V}_h$ close to the model surface. In the oblique coordinate system, $\mathbf{V}_h$ is not horizontal but tangent to the model coordinate levels. Therefore, $\mathbf{V}_s$ must be tangent to the model lower surface, which can be visualized using non-unitary basic vectors as:

$$\mathbf{V}_s = u_s\left(\mathbf{i} + \frac{\partial z_s}{\partial x}\mathbf{k}\right) + v_s\left(\mathbf{j} + \frac{\partial z_s}{\partial y}\mathbf{k}\right). \tag{I.3}$$

Over flat terrain u_s and v_s are truly horizontal, but in mountainous terrain the module of the basis vectors are greater than one such that (Clark, 1977):

$$\left|\mathbf{V}_s\right|^2 = \left(u_s\right)^2 + \left(v_s\right)^2 + \left(u_s \frac{\partial z_s}{\partial x} + v_s \frac{\partial z_s}{\partial y}\right)^2 . \tag{I.4}$$

Since $u_s\left(\partial z_s/\partial x\right) + v_s\left(\partial z_s/\partial y\right) = \mathbf{V}_s \cdot \nabla z_s = w_s$, the equivalent surface velocity vector module becomes:

$$\left|\mathbf{V}_s\right|^2 = \left(u_s\right)^2 + \left(v_s\right)^2 + \left(w_s\right)^2 . \tag{I.5}$$

Hence, for orographic flow simulations the surface stress calculation should include the vertical velocity to quantify correctly the terrain forcing and turbulence diffusion.

APPENDIX II

Extended Stability Analysis of the 3-TL O-SI Scheme Applied to the EE System in Height Based σ-coordinate

Additional to the variables defined for system (2.3), new ones can be introduced as $\alpha = (T_0 - T_*)/T_*$, $N_0{}^2 = N_*{}^2/(1+\alpha)$, $c_0{}^2 = c_*{}^2(1+\alpha)$, $b_1 = gT''/T_*$ and $P_1 = RT_*q''$, such that the substitution of $b = b_1 + g\alpha$ and $P = P_1 + gz\alpha/(1+\alpha)$ in the semi-discrete system obtained after applying the SISL scheme yields:

$$\frac{\delta u}{2\Delta t} + \frac{\partial \overline{P_1}}{\partial x} = -\frac{1}{g}(b_1 + g\alpha)\frac{\partial P_1}{\partial x}, \tag{II.1a}$$

$$\frac{\delta w}{2\Delta t} + \frac{\partial \overline{P_1}}{\partial z} + \frac{g\alpha}{1+\alpha} - (\overline{b_1} + g\alpha) = -\frac{1}{g}(b_1 + g\alpha)\left[\frac{\partial P_1}{\partial z} + \frac{g\alpha}{1+\alpha}\right], \tag{II.1b}$$

$$\frac{\delta}{2\Delta t}(b_1 - \gamma_* P_1) - \gamma_* w\frac{g\alpha}{1+\alpha} + N_*{}^2\overline{w} = -\frac{R}{c_v}(b_1 + g\alpha)D, \tag{II.1c}$$

$$\frac{1}{c_*{}^2}\left[\frac{\delta P_1}{2\Delta t} + w\frac{g\alpha}{1+\alpha} - g\overline{w}\right] + \overline{D} = 0. \tag{II.1d}$$

It is worth noting that the second term resulting from the expansion of the substantial derivative $dP/dt = dP_1/dt + gw\alpha/(1+\alpha)$ is an explicit term. After simplifying and linearizing about the mean state the resulting equation system, identified as (2.8) in section 2-b, becomes:

$$\frac{\delta u}{2\Delta t} + \frac{\partial \overline{P_1}}{\partial x} = -\alpha\frac{\partial P_1}{\partial x}, \tag{II.2a}$$

$$\frac{\delta w}{2\Delta t} + \frac{\partial \overline{P_1}}{\partial z} - \overline{b_1} = -\alpha\frac{\partial P_1}{\partial z} - b_1\frac{g\alpha}{1+\alpha}, \tag{II.2b}$$

$$\frac{\delta}{2\Delta t}(b_1 - \gamma_* P_1) + N_*{}^2\overline{w} = -\alpha g\frac{R}{c_v}D + N_*{}^2 w\frac{\alpha}{1+\alpha}, \tag{II.2c}$$

$$\frac{1}{c_*^{\,2}}\left[\frac{\delta P_1}{2\Delta t}-g\overline{w}\right]+\overline{D}=-\frac{g}{c_*^{\,2}}w\frac{\alpha}{1+\alpha}. \qquad \text{(II.2d)}$$

The left-hand-side of (2.19) is identical to that of system (2.5), but its right-hand side contains many non-vanishing terms proportional to α. Then, applying the same type of eigenmode solution on the new system (2.19) yields the following:

$$\Lambda^{-}u+(1+\alpha)ik\Lambda_1^{+}P_1=0\,, \qquad \text{(II.3a)}$$

$$\Lambda^{-}w+(1+\alpha)n\Lambda_1^{+}P_1-\Lambda_2^{+}\frac{b_1}{1+\alpha}=0\,, \qquad \text{(II.3b)}$$

$$\Lambda^{-}(b_1-\gamma_*P_1)+N_0^{\,2}\Lambda_2^{+}w+g\frac{R}{c_v}\alpha\lambda D=0\,, \qquad \text{(II.3c)}$$

$$\frac{\Lambda^{-}}{c_*^{\,2}}P_1-\frac{g}{c_0^{\,2}}\Lambda_2^{+}w+\Lambda^{+}D=0\,. \qquad \text{(II.3d)}$$

Having $\Lambda_1^{+}=(\Lambda^{+}+\alpha\lambda)/(1+\alpha)$ and $\Lambda_2^{+}=\Lambda^{+}(1+\alpha)-\alpha\lambda$, as well as $N_0^{\,2}=N_*^{\,2}/(1+\alpha)$ and $c_0^{\,2}=c_*^{\,2}(1+\alpha)$, the resulting dispersion relation is:

$$\frac{(\Lambda^{-})^4}{c_0^{\,2}}+(\Lambda^{-})^2\Lambda_1^{+}\left[(k^2+nn^{*})\Lambda^{+}+\frac{n\alpha}{H_0}(\Lambda_2^{+}-\Lambda^{+})\right]+N_0^{\,2}k^2(\Lambda_1^{+})^2(\Lambda_2^{+})^2=0\,, \qquad \text{(II.4a)}$$

$$\begin{aligned}\frac{\sin^4\gamma}{\Delta t^4 c_0^{\,2}}-\frac{\sin^2\gamma}{\Delta t^2}(\cos\gamma+\alpha)&\left[(k^2+nn^{*})\cos\gamma+\frac{n\alpha}{H_0}(\cos\gamma-1)\right]\\ &+\;N_0^{\,2}k^2(\cos\gamma+\alpha)^2\left[\cos\gamma-\frac{\alpha}{1+\alpha}\right]^2=0\end{aligned}\,. \qquad \text{(II.4b)}$$

In the asymptotic limit of large time-steps ($\Delta t\to\infty$), considering only an external mode with $\nu=0$ and $k\neq 0$ the dispersion relation reduces to:

$$(\cos\gamma+\alpha)^2\left[\cos\gamma-\frac{\alpha}{1+\alpha}\right]^2=0\,, \tag{II.5}$$

for which the stability criterion is $-\frac{1}{2}\le\alpha\le 1$. For an external mode with $\nu=0$ and $k=0$ (1D version in the vertical direction) the dispersion relation turns out to be:

$$(1-\cos^2\gamma)(\cos\gamma+\alpha)\left[\cos\gamma-\frac{2\alpha}{1+\alpha}\right]=0\,, \tag{II.6}$$

with a stability condition of $-\frac{1}{4}\le\alpha\le 1$. Finally, for an internal mode with $\nu\neq 0$ and $k=0$ the dispersion relation is:

$$(\cos\gamma+\alpha)\left[\cos\gamma-\frac{2\alpha}{1+2\alpha-2i\nu H_0}\right]=0\,, \tag{II.7}$$

which yields complex eigenvalues as soon as $\alpha\neq 0$. Thus, the resulting SI scheme is always unstable for any temperature perturbation.

APPENDIX III

Extended Stability Analysis of the 3-TL N-SI Scheme Applied to the EE System in Height Based σ-coordinate

A hydrostatic version of the model is easily obtained by eliminating the vertical acceleration term dw/dt from system (2.3). A particularity of this modified version is the fact that, once written in terms of perturbations, the resulting hydrostatic relation is non-linear. Accordingly, after time discretization, the hydrostatic constraint can only be satisfied weakly across three time-levels. Thus, a strong constraint can be applied if the vertical momentum equation is written in terms of ρ' and p' as:

$$\frac{dw}{dt}+\frac{1}{\rho}\left[\frac{\partial p'}{\partial z}-g\rho'\right]=0, \tag{III.1}$$

even though, there is need to split the term across time-levels in the non-hydrostatic case:

$$\frac{\delta w}{2\Delta t}+\frac{1}{\rho_*}\overline{\left[\frac{\partial p'}{\partial z}-g\rho'\right]}=\frac{\rho'}{p_*}\left[\frac{\partial p'}{\partial z}-g\rho'\right] \tag{III.2}$$

or its equivalent (as explained in Section 2.3), such that:

$$\frac{\delta w}{2\Delta t}+\overline{\frac{\partial P}{\partial z}-\hat{b}}=-\alpha\left[\frac{\partial P}{\partial z}-\hat{b}\right]. \tag{III.3}$$

which requires a redefinition of the buoyancy prognostic variable as $\hat{b}=gT'/T=g\alpha/(\alpha+1)$. Applying an extended stability analysis, similar to the one presented in Appendix II, to the formulation with equations (2.27) leads to an unstable scheme whenever the divergence term

D in the thermodynamic equation remains treated explicitly. In fact, so is the case with the following equivalent implicit form:

$$\frac{\delta w}{2\Delta t} + \overline{(\alpha+1)\left[\frac{\partial P}{\partial z} - \hat{b}\right]} = 0\,, \tag{III.4}$$

where $\alpha + 1 = T/T_*$. This can be easily verified by rewriting system (2.20) in a more general form:

$$\Lambda^- u + (1+\alpha) ik \Lambda_1^+ P_1 = 0\,, \tag{III.5a}$$

$$\Lambda^- w + (1+\alpha) n \Lambda_1^+ P_1 - \Lambda_2^+ \frac{b_1}{1+\alpha} = 0\,, \tag{III.5b}$$

$$\Lambda^-(b_1 - \gamma_* P_1) + {N_0}^2 \Lambda_4^+ w + g\frac{R}{c_v}\alpha\Lambda_3(iku + nw) = 0\,, \tag{III.5c}$$

$$\frac{\Lambda^-}{{c_*}^2} P_1 - \frac{g}{{c_0}^2}\Lambda_5^+ w + \Lambda^+(iku + nw) = 0\,. \tag{III.5d}$$

Here $\Lambda_i^+ = \Lambda^+ + \alpha\Lambda_i/(1+\alpha)$ for (i = 1, 3), $\Lambda_i^+ = \Lambda^+(1+\alpha) - \alpha\Lambda_i$ for (i = 4, 5) and $\Lambda_i = (\Lambda^+, \lambda)$, leaving Λ_2^+ undetermined to end up with a more general dispersion relation:

$$\begin{aligned} &\frac{(\Lambda^-)^4}{{c_0}^2} + (\Lambda^-)^2 \frac{N_0^2}{{c_0}^2}\Lambda_2^+\left[\frac{\Lambda_4^+ - \Lambda_5^+}{1+\alpha}\right] + (\Lambda^-)^2 n\left[\begin{array}{l} \dfrac{N_0^2}{g}\left(\Lambda_2^+\Lambda_3^+ - \Lambda^+\Lambda_1^+\right) \\ + \dfrac{g}{{c_0}^2}\left(\Lambda_1^+\Lambda_5^+ - \Lambda^+\Lambda_1^+\right) \end{array}\right] \\ &+ \ (\Lambda^-)^2\Lambda^+\Lambda_1^+\left(k^2 + nn^*\right) + N_0^2 k^2 \Lambda_1^+\Lambda_2^+\left[\left(\frac{\Lambda_4^+ - \Lambda_5^+}{1+\alpha}\right)\Lambda^+ + \Lambda_4^+\Lambda_5^+\right] = 0 \end{aligned}\,. \tag{III.6}$$

Hence, the stability absolutely requires that $\Lambda_5^+ = \Lambda^+$, which emphasizes the importance of accurately representing the sound velocity in this implicit scheme. Also, it is possible to set

$\Lambda_4^+ = \Lambda_5^+$, which yields a better implicit representation of the buoyancy frequency and a simpler dispersion relation, reducing equation (2.30) to:

$$\frac{(\Lambda^-)^4}{c_0^{\,2}} + (\Lambda^-)^2 \Lambda^+ \Lambda_1^+ \left(k^2 + nn^*\right) - (\Lambda^-)^2 n \frac{N_0^2}{g}\left(\Lambda^+\Lambda_1^+ - \Lambda_2^+\Lambda_3^+\right) + N_0^2 k^2 \Lambda^+ \Lambda_1^+ \Lambda_2^+ \Lambda_3^+ = 0 \qquad \text{(III.7)}$$

There remain some choices to eliminate the complex coefficient term and get a stable scheme. Setting $\Lambda_2^+ = \Lambda^+$ corresponds to the first solution, which requires equating $\Lambda_3^+ = \Lambda_1^+$. However, the pressure-gradient term cannot be treated fully implicitly without treating implicitly the divergence term in the thermodynamic equation. As a second option, the pressure gradient and buoyancy terms may be treated on an equal footing, either partially implicit (2.11c) or totally implicit (2.11b), resulting in $\Lambda_2^+ = \Lambda_1^+$. However, an implicit treatment of the non-linear divergence term is then an absolute requirement to force $\Lambda_3^+ = \Lambda^+$ and finally eliminate the complex coefficient source of instability. Thus, after taking into consideration all these aspects for the N-SI scheme, the resulting semi-discrete EE system and its corresponding dispersion relation are:

$$\frac{\delta u}{2\Delta t} + \overline{(\alpha+1)\frac{\partial P}{\partial x}} = 0, \qquad \text{(III.8a)}$$

$$\frac{\delta w}{2\Delta t} + \overline{(\alpha+1)\left[\frac{\partial P}{\partial z} - \hat{b}\right]} = 0, \qquad \text{(III.8b)}$$

$$(\alpha+1)\frac{\delta \hat{b}}{2\Delta t} - \gamma_* \frac{\delta P}{2\Delta t} + \overline{N_0^2 w} = \left(N_0^2 - N_*^2\right) w, \qquad \text{(III.8c)}$$

$$\frac{1}{c_*^2}\frac{\delta P}{2\Delta t} + \overline{D - \frac{g}{c_0^2} w} = -\left[\frac{g}{c_0^2} - \frac{g}{c_*^2}\right] w, \qquad \text{(III.8d)}$$

$$\frac{(\Lambda^-)^4}{{c_0}^2} + (\Lambda^-)^2 \frac{\Lambda_1^+}{1+\alpha} \Lambda^+ \left(k^2 + nn^*\right) + (\Lambda^+)^2 \left(\frac{\Lambda_1^+}{1+\alpha}\right) N_0^2 k^2 = 0\,, \qquad \text{(III.8e)}$$

which achieves numerical stability in the extended range $-1 \le \alpha \le 1$, as demonstrated by Bénard et al. (B04), with the appropriate choice of prognostic variables for the EE system.

APPENDIX IV

Metric Terms for MC2-LES Turbulent Diffusion Formulae

The external forcing and heat sources in the standard turbulence scheme of MC2-LES Gasset (2014) are subdivided into horizontal and vertical terms $F_{turb} = F^{H}_{turb} + F^{V}_{turb}$, formulated in terms of the filtered velocity components $(\tilde{u}, \tilde{v}, \tilde{w})$, potential temperature $(\tilde{\theta})$, pressure $(\tilde{\pi})$, density $(\bar{\rho})$ and diffusion coefficients $(\overline{K_M}, \overline{K_T})$ such that (hereon dropping the Favre and Reynolds filtering notations):

$$F^{H}_{turb} = \begin{Bmatrix} \frac{1}{\rho}\left[\frac{\partial}{\partial y}\rho K_M\left(\frac{\partial v}{\partial x}+\frac{\partial u}{\partial y}\right)+\frac{\partial}{\partial z}\rho K_M\left(\frac{\partial w}{\partial x}\right)\right] \\ \frac{1}{\rho}\left[\frac{\partial}{\partial x}\rho K_M\left(\frac{\partial v}{\partial x}+\frac{\partial u}{\partial y}\right)+\frac{\partial}{\partial z}\rho K_M\left(\frac{\partial w}{\partial y}\right)\right] \\ \frac{1}{\rho}\left[\frac{\partial}{\partial x}\rho K_M\left(\frac{\partial w}{\partial x}+\frac{\partial u}{\partial z}\right)+\frac{\partial}{\partial y}\rho K_M\left(\frac{\partial w}{\partial y}+\frac{\partial v}{\partial z}\right)\right] \\ \frac{g\pi}{\rho T_*}\left[\frac{\partial}{\partial x}\rho K_T\left(\frac{\partial \theta}{\partial x}\right)+\frac{\partial}{\partial y}\rho K_T\left(\frac{\partial \theta}{\partial y}\right)\right] \\ 0 \end{Bmatrix}, \tag{IV.1}$$

$$F^{V}_{turb} = \begin{Bmatrix} \frac{1}{\rho}\left[\frac{\partial}{\partial z}\rho K_M\left(\frac{\partial u}{\partial z}\right)\right] \\ \frac{1}{\rho}\left[\frac{\partial}{\partial z}\rho K_M\left(\frac{\partial v}{\partial z}\right)\right] \\ 0 \\ \frac{g\pi}{\rho T_*}\left[\frac{\partial}{\partial z}\rho K_T\left(\frac{\partial \theta}{\partial z}\right)\right] \\ 0 \end{Bmatrix}. \tag{IV.2}$$

The horizontal terms F_{turb}^{H} are pre-computed in the model's kernel (i.e., dynamics) and, then, passed to the physical parameterization routines (i.e., physics), whereas the vertical terms F_{turb}^{V} are directly calculated in the physics library. For the standard version of MC2-LES, metric transformations are considered only for the horizontal terms since the vertical terms are already appropriately transformed for terrain-conforming grids within the physics package [25, 29, 43]. Thus, only the horizontal terms are going to be discussed hereafter. Considering the map scale factor ($m, S = m^2$) for the horizontal dimensions $(\partial X = m\partial x, \partial Y = m\partial y)$ and image velocities $(SU, SV) = (\partial X/\partial t, \partial Y/\partial t)$, system (A1) transforms into:

$$F_{turb}^{H} = \begin{Bmatrix} \frac{1}{\rho}\left[\frac{\partial}{\partial Y_z}\rho K_M S\left(\frac{\partial V}{\partial X_z}+\frac{\partial U}{\partial Y_z}\right)+\frac{\partial}{\partial z}\rho K_M\left(\frac{\partial w}{\partial X_z}\right)\right] \\ \frac{1}{\rho}\left[\frac{\partial}{\partial X_z}\rho K_M S\left(\frac{\partial V}{\partial X_z}+\frac{\partial U}{\partial Y_z}\right)+\frac{\partial}{\partial z}\rho K_M\left(\frac{\partial w}{\partial Y_z}\right)\right] \\ \frac{1}{\rho}\left[\frac{\partial}{\partial X_z}\rho K_M\left(\frac{\partial w}{\partial X_z}+S\frac{\partial U}{\partial z}\right)+\frac{\partial}{\partial Y_z}\rho K_M\left(\frac{\partial w}{\partial Y_z}+S\frac{\partial V}{\partial z}\right)\right] \\ \frac{g\pi}{\rho T_*}\left[\frac{\partial}{\partial X_z}\rho K_T\left(\frac{\partial \theta}{\partial X_z}\right)+\frac{\partial}{\partial Y_z}\rho K_T\left(\frac{\partial \theta}{\partial Y_z}\right)\right] \\ 0 \end{Bmatrix}. \qquad \text{(IV.3)}$$

Here, the independent variables with a z subindex (X_z, Y_z) indicate the proyection onto a regular Cartesian coordinate grid. To simplify this formulation, and following the procedure presented in [25, 43], the horizontal deviatory terms of the strain rate tensor are expressed as:

$$F_{turb}^{H}=\begin{Bmatrix}\frac{1}{\rho}\left[\frac{\partial A_U}{\partial Y_z}+\frac{\partial B_U}{\partial z}\right]\\ \frac{1}{\rho}\left[\frac{\partial A_V}{\partial X_z}+\frac{\partial B_V}{\partial z}\right]\\ \frac{1}{\rho}\left[\frac{\partial A_w}{\partial X_z}+\frac{\partial B_w}{\partial Y_z}\right]\\ \frac{g\pi}{\rho T_*}\left[\frac{\partial A_T}{\partial X_z}+\frac{\partial B_T}{\partial Y_z}\right]\\ 0\end{Bmatrix}. \qquad \text{(IV.4)}$$

Based on the Gal-Chen and Somerville (1975) transformations for the Cartesian height coordinate (z) in terms of the terrain-following oblique vertical coordinate $Z=z_T[z-h(X,Y)]/[z_T-h(X,Y)]$, model's height ($z_T$) and topography $h(X,Y)$, the partial derivatives of any variable $\Psi=(U,V,w,\theta)$ or group of variables (A_Ψ,B_Ψ) extended using the chain rule of derivation become:

$$\frac{\partial \Psi}{\partial X_z}=\frac{\partial \Psi}{\partial X_Z}+\frac{\partial Z}{\partial X_Z}\frac{\partial \Psi}{\partial Z}=\frac{\partial \Psi}{\partial X_Z}+\frac{G_1}{G_0}\frac{\partial \Psi}{\partial Z}, \qquad \text{(III.5a)}$$

$$\frac{\partial \Psi}{\partial Y_z}=\frac{\partial \Psi}{\partial Y_Z}+\frac{\partial Z}{\partial Y_Z}\frac{\partial \Psi}{\partial Z}=\frac{\partial \Psi}{\partial Y_Z}+\frac{G_2}{G_0}\frac{\partial \Psi}{\partial Z}, \qquad \text{(III.5b)}$$

$$\frac{\partial \Psi}{\partial z}=\frac{\partial Z}{\partial z}\frac{\partial \Psi}{\partial Z}=\frac{1}{G_0}\frac{\partial \Psi}{\partial Z}. \qquad \text{(III.5c)}$$

Reformulating system (A4) in terms of oblique coordinates with these metric transformations yields:

$$F^H_{turb} = \begin{Bmatrix} F^H_{turb-U} \\ F^H_{turb-V} \\ F^H_{turb-w} \\ F^H_{turb-T} \\ 0 \end{Bmatrix} = \begin{Bmatrix} \frac{1}{\rho}\left[\frac{\partial A_U}{\partial Y_Z} + \frac{G_2}{G_0}\frac{\partial A_U}{\partial Z} + \frac{1}{G_0}\frac{\partial B_U}{\partial Z}\right] \\ \frac{1}{\rho}\left[\frac{\partial A_V}{\partial X_Z} + \frac{G_1}{G_0}\frac{\partial A_V}{\partial Z} + \frac{1}{G_0}\frac{\partial B_V}{\partial Z}\right] \\ \frac{1}{\rho}\left[\frac{\partial A_w}{\partial X_Z} + \frac{G_1}{G_0}\frac{\partial A_w}{\partial Z} + \frac{\partial B_w}{\partial Y_Z} + \frac{G_2}{G_0}\frac{\partial B_w}{\partial Z}\right] \\ \frac{g\pi}{\rho T_*}\left[\frac{\partial A_T}{\partial X_Z} + \frac{G_1}{G_0}\frac{\partial A_T}{\partial Z} + \frac{\partial B_T}{\partial Y_Z} + \frac{G_2}{G_0}\frac{\partial B_T}{\partial Z}\right] \\ 0 \end{Bmatrix}, \quad \text{(IV.6)}$$

where the horizontal turbulent fluxes, with the corresponding metric transformations, are:

$$A_U = \rho K_M S\left[\frac{\partial V}{\partial X_Z} + \frac{G_1}{G_0}\frac{\partial V}{\partial Z} + \frac{\partial U}{\partial Y_Z} + \frac{G_2}{G_0}\frac{\partial U}{\partial Z}\right], \quad \text{(III.7a)}$$

$$B_U = \rho K_M\left[\frac{\partial w}{\partial X_Z} + \frac{G_1}{G_0}\frac{\partial w}{\partial Z}\right], \quad \text{(III.7b)}$$

$$A_V = \rho K_M S\left[\frac{\partial V}{\partial X_Z} + \frac{G_1}{G_0}\frac{\partial V}{\partial Z} + \frac{\partial U}{\partial Y_Z} + \frac{G_2}{G_0}\frac{\partial U}{\partial Z}\right], \quad \text{(III.7c)}$$

$$B_V = \rho K_M\left[\frac{\partial w}{\partial Y_Z} + \frac{G_2}{G_0}\frac{\partial w}{\partial Z}\right], \quad \text{(III.7d)}$$

$$A_w = \rho K_M\left[\frac{\partial w}{\partial X_Z} + \frac{G_1}{G_0}\frac{\partial w}{\partial Z} + \frac{S}{G_0}\frac{\partial U}{\partial Z}\right], \quad \text{(III.7e)}$$

$$B_w = \rho K_M\left[\frac{\partial w}{\partial Y_Z} + \frac{G_2}{G_0}\frac{\partial w}{\partial Z} + \frac{S}{G_0}\frac{\partial V}{\partial Z}\right], \quad \text{(III.7f)}$$

$$A_T = \rho K_T\left[\frac{\partial \theta}{\partial X_Z} + \frac{G_1}{G_0}\frac{\partial \theta}{\partial Z}\right], \quad \text{(III.7g)}$$

$$B_T = \rho K_T\left[\frac{\partial \theta}{\partial Y_Z} + \frac{G_2}{G_0}\frac{\partial \theta}{\partial Z}\right]. \quad \text{(III.7h)}$$

Then, velocity tendencies are discretized based on the rules presented in Girard et al. (2005), which require the correct interpolation of all variables according to their positioning on the staggered grid with projected indices (c.f. Fig. 1). Using the projected form of the metric terms ($[G_0]_{i,j,k}$;$[G_1]_{i-\frac{1}{2},j,k-\frac{1}{2}}$;$[G_2]_{i,j-\frac{1}{2},k-\frac{1}{2}}$), density ($[\rho]_{i,j,k-\frac{1}{2}}$), the mixing coefficients ($[K_M]_{i,j,k-\frac{1}{2}}$;$[K_T]_{i,j,k-\frac{1}{2}}$) and the Exner function ($[\pi]_{i,j,k-\frac{1}{2}}$), the horizontal tendencies are expressed as follows:

$$\left[F^H_{turb-U}\right]_{i-\frac{1}{2},j,k} = \left[\frac{1}{\overline{\rho}^{XZ_w}}\left(\frac{\delta_Y A_U}{\Delta Y_{Z_m}} + \frac{1}{\overline{G_0}^X}\left(\overline{\overline{G_2}^X \delta_{Z_m} A_U}^{YZ_w} + \delta_{Z_w} B_U\right)\right)\right]_{i-\frac{1}{2},j,k}, \tag{III.8a}$$

$$\left[F^H_{turb-V}\right]_{i,j-\frac{1}{2},k} = \left[\frac{1}{\overline{\rho}^{YZ_w}}\left(\frac{\delta_X A_V}{\Delta X_{Z_m}} + \frac{1}{\overline{G_0}^Y}\left(\overline{\overline{G_1}^Y \delta_{Z_m} A_V}^{XZ_w} + \delta_{Z_w} B_V\right)\right)\right]_{i,j-\frac{1}{2},k}, \tag{III.8b}$$

$$\left[F^H_{turb-w}\right]_{i,j,k-\frac{1}{2}} = \left[\frac{1}{\rho}\left(\frac{\delta_X A_w}{\Delta X_{Z_w}} + \frac{\delta_Y B_w}{\Delta Y_{Z_w}} + \frac{1}{\overline{G_0}^{Z_m}}\left(\overline{G_1 \delta_{Z_m} \overline{A_w}^{Z_w}}^X + \overline{G_2 \delta_{Z_m} \overline{B_w}^{Z_w}}^Y\right)\right)\right]_{i,j,k-\frac{1}{2}} \tag{III.8c}$$

$$\left[F^H_{turb-T}\right]_{i,j,k-\frac{1}{2}} = \left[\frac{g\pi}{\rho T_*}\left(\frac{\delta_X A_T}{\Delta X_{Z_T}} + \frac{\delta_Y B_T}{\Delta Y_{Z_T}} + \frac{1}{\overline{G_0}^{Z_m}}\left(\overline{G_1 \delta_{Z_m} \overline{A_T}^{Z_T}}^X + \overline{G_2 \delta_{Z_m} \overline{B_T}^{Z_T}}^Y\right)\right)\right]_{i,j,k-\frac{1}{2}} \tag{III.8d}$$

Applying the same type of discretization on the horizontal turbulent fluxes these become:

$$[A_U]_{i-\frac{1}{2},j-\frac{1}{2},k} = \left[\overline{\rho}^{XYZ_w}\overline{K_M}^{XYZ_w} S\left(\frac{\delta_X V}{\Delta X_{Z_m}} + \frac{\delta_Y U}{\Delta Y_{Z_m}} + \frac{1}{\overline{G_0}^{XY}}\left(\overline{\overline{G_1}^Y \delta_{Z_m} \overline{V}^X}^{Z_w} + \overline{\overline{G_2}^X \delta_{Z_m} \overline{U}^Y}^{Z_w}\right)\right)\right]_{i-\frac{1}{2},j-\frac{1}{2},j} \tag{III.9a}$$

$$[B_U]_{i-\frac{1}{2},j,k-\frac{1}{2}} = \left[\overline{\rho}^X \overline{K_M}^X \left(\frac{\delta_X w}{\Delta X_{Z_w}} + G_1 \overline{\frac{1}{G_0} \delta_{Z_w} w}^{XZ_m}\right)\right]_{i-\frac{1}{2},j,k-\frac{1}{2}}, \tag{III.9b}$$

$$\left[A_V\right]_{i-\frac{1}{2},j-\frac{1}{2},k} = \left[\overline{\rho}^{XYZ_w}\,\overline{K_M}^{XYZ_w} S\left(\frac{\delta_X V}{\Delta X_{Z_m}} + \frac{\delta_Y U}{\Delta Y_{Z_m}} + \frac{1}{\overline{G_0}^{XY}}\left(\overline{\overline{G_1}^{Y}\,\delta_{Z_m}\overline{V}^{X}}^{Z_w} + \overline{\overline{G_2}^{X}\,\delta_{Z_m}\overline{U}^{Y}}^{Z_w}\right)\right)\right]_{i-\frac{1}{2},j-\frac{1}{2},k} \quad \text{(III.9c)}$$

$$\left[B_V\right]_{i,j-\frac{1}{2},k-\frac{1}{2}} = \left[\overline{\rho}^{Y}\,\overline{K_M}^{Y}\left(\frac{\delta_Y w}{\Delta Y_{Z_w}} + G_2\overline{\frac{1}{G_0}\delta_{Z_w} w}^{YZ_m}\right)\right]_{i,j-\frac{1}{2},k-\frac{1}{2}}, \quad \text{(III.9d)}$$

$$\left[A_w\right]_{i-\frac{1}{2},j,k-\frac{1}{2}} = \left[\overline{\rho}^{X}\,\overline{K_M}^{X}\left(\frac{\delta_X w}{\Delta X_{Z_w}} + G_1\overline{\frac{1}{G_0}\delta_{Z_w} w}^{XZ_m} + \frac{\overline{\overline{S}^{Y}}^{Z_m}}{\overline{G_0}^{X}}\,\delta_{Z_m} U\right)\right]_{i-\frac{1}{2},j,k-\frac{1}{2}}, \quad \text{(III.9e)}$$

$$\left[B_w\right]_{i,j-\frac{1}{2},k-\frac{1}{2}} = \left[\overline{\rho}^{Y}\,\overline{K_M}^{Y}\left(\frac{\delta_Y w}{\Delta Y_{Z_w}} + G_2\overline{\frac{1}{G_0}\delta_{Z_w} w}^{YZ_m} + \frac{\overline{\overline{S}^{X}}^{Z_m}}{\overline{G_0}^{Y}}\,\delta_{Z_m} V\right)\right]_{i,j-\frac{1}{2},k-\frac{1}{2}}, \quad \text{(III.9f)}$$

$$\left[A_T\right]_{i-\frac{1}{2},j,k-\frac{1}{2}} = \left[\overline{\rho}^{X}\,\overline{K_T}^{XZ_T}\left(\frac{\delta_X \theta}{\Delta X_{Z_T}} + G_1\overline{\frac{1}{G_0}\delta_{Z_T}\theta}^{XZ_m}\right)\right]_{i-\frac{1}{2},j,k-\frac{1}{2}}, \quad \text{(III.9g)}$$

$$\left[B_T\right]_{i,j-\frac{1}{2},k-\frac{1}{2}} = \left[\overline{\rho}^{Y}\,\overline{K_T}^{YZ_T}\left(\frac{\delta_Y \theta}{\Delta Y_{Z_T}} + G_2\overline{\frac{1}{G_0}\delta_{Z_T}\theta}^{YZ_m}\right)\right]_{i,j-\frac{1}{2},k-\frac{1}{2}}. \quad \text{(III.9h)}$$

All these formulae are then expressed in full indices in order to be coded in the numerical model routines. Thus, the velocity and temperature tendencies with absolute indices turn into:

$\bullet \left[F^{H}_{turb-U}\right]_{i-\frac{1}{2},j,k}$:

$$\left[\overline{\rho}^{XZ_w}\right]_{i-\frac{1}{2},j,k} = \frac{\left(\rho_{i,j,k}+\rho_{i-1,j,k}\right)+\left(\rho_{i,j,k-1}+\rho_{i-1,j,k-1}\right)}{4}; \left[\frac{\delta_Y A_U}{\Delta Y_{Z_m}}\right]_{i-\frac{1}{2},j,k} = \frac{A_{Ui,j,k}-A_{Ui-1,j,k}}{\Delta Y};$$

$$\frac{1}{\overline{G_0}^{X}}\left(\overline{\overline{G_2}^{X}\delta_{Z_m}A_U}^{YZ_w}\right)\Bigg]_{i-\frac{1}{2},j,k} = \frac{1}{G^{u}_{0\,i,j,k}}\frac{1}{8}\begin{bmatrix}\left(G_{2i,j,k+1}+G_{2i-1,j,k+1}\right)\left(A_{Ui,j,k+1}-A_{Ui,j,k}\right)+\\ \left(G_{2i,j-1,k}+G_{2i-1,j-1,k}\right)\left(A_{Ui,j-1,k+1}-A_{Ui,j-1,k}\right)+\\ \left(G_{2i,j,k}+G_{2i-1,j,k}\right)\left(A_{Ui,j,k}-A_{Ui,j,k-1}\right)+\\ \left(G_{2i,j-1,k-1}+G_{2i-1,j-1,k-1}\right)\left(A_{Ui,j-1,k}-A_{Ui,j-1,k-1}\right)\end{bmatrix}; \quad \text{(III.10a)}$$

$$\frac{1}{\overline{G_0}^{X}}\left(\delta_{Z_w}B_U\right)\Bigg]_{i-\frac{1}{2},j,k} = \frac{1}{G^{u}_{0\,i,j,k}}\left(B_{Ui,j,k}-B_{Ui,j,k-1}\right);$$

$\bullet \left[F^{H}_{turb-V}\right]_{i,j-\frac{1}{2},k}$:

$$\left[\overline{\rho}^{YZ_w}\right]_{i,j-\frac{1}{2},k} = \frac{\left(\rho_{i,j,k}+\rho_{i,j-1,k}\right)+\left(\rho_{i,j,k-1}+\rho_{i,j-1,k-1}\right)}{4}; \left[\frac{\delta_X A_V}{\Delta X_{Z_m}}\right]_{i,j-\frac{1}{2},k} = \frac{A_{Vi,j,k}-A_{Vi,j-1,}}{\Delta X}$$

$$\left[\frac{1}{\overline{G_0}^{Y}}\left(\overline{\overline{G_1}^{Y}\delta_{Z_m}A_V}^{XZ_w}\right)\right]_{i,j-\frac{1}{2},k} = \frac{1}{G^{v}_{0\,i,j,k}}\frac{1}{8}\begin{bmatrix}\left(G_{1i,j,k+1}+G_{1i,j-1,k+1}\right)\left(A_{Vi,j,k+1}-A_{Vi,j,k}\right)+\\ \left(G_{1i-1,j,k}+G_{2i-1,j-1,k}\right)\left(A_{Vi-1,j,k+1}-A_{Vi-1,j,k}\right)+\\ \left(G_{1i,j,k}+G_{1i,j-1,k}\right)\left(A_{Vi,j,k}-A_{Vi,j,k-1}\right)+\\ \left(G_{1i-1,j,k-1}+G_{1i-1,j-1,k-1}\right)\left(A_{Vi-1,j,k}-A_{Vi-1,j,k-1}\right)\end{bmatrix} \quad \text{(III.10b)}$$

$$\left[\frac{1}{\overline{G_0}^{Y}}\left(\delta_{Z_w}B_V\right)\right]_{i,j-\frac{1}{2},k} = \frac{1}{G^{v}_{0\,i,j,k}}\left(B_{Vi,j,k}-B_{Vi,j,k-1}\right);$$

$\bullet \left[F^{H}_{turb-w} \right]_{i,j,k-\frac{1}{2}}$:

$$[\rho]_{i,j,k-\frac{1}{2}} = \rho_{i,j,k}; \left[\frac{\delta_X A_w}{\Delta X_{Z_w}} \right]_{i,j,k-\frac{1}{2}} = \frac{A_{wi,j,k} - A_{wi-1,j,k}}{\Delta X}; \left[\frac{\delta_Y B_w}{\Delta Y_{Z_w}} \right]_{i,j,k-\frac{1}{2}} = \frac{B_{wi,j,k} - B_{wi,j-1,k}}{\Delta Y}$$

$$\left[\frac{1}{\overline{\overline{G_0}^{Z_m}}} \left(\overline{G_1 \delta_{Z_m} \overline{A_w}^{Z_w}}^{X} \right) \right]_{i,j,k-\frac{1}{2}} = \frac{1}{G^w_{0\,i,j,k}} \frac{1}{4} \left[\begin{array}{l} G_{1i,j,k} \left(A_{wi,j,k+1} - A_{wi,j,k-1} \right) + \\ G_{1i-1,j,k} \left(A_{wi-1,j,k+1} - A_{wi-1,j,k-1} \right) \end{array} \right]; \qquad \text{(III.10c)}$$

$$\left[\frac{1}{\overline{\overline{G_0}^{Z_m}}} \left(\overline{G_2 \delta_{Z_m} \overline{B_w}^{Z_w}}^{Y} \right) \right]_{i,j,k-\frac{1}{2}} = \frac{1}{G^w_{0\,i,j,k}} \frac{1}{4} \left[\begin{array}{l} G_{2i,j,k} \left(B_{wi,j,k+1} - B_{wi,j,k-1} \right) + \\ G_{2i,j-1,k} \left(B_{wi,j-1,k+1} - B_{wi,j-1,k-1} \right) \end{array} \right];$$

$\bullet \left[F^{H}_{turb-T} \right]_{i,j,k-\frac{1}{2}}$:

$$\left[\frac{g\pi}{\rho T_*} \right]_{i,j,k-\frac{1}{2}} = \frac{g}{T_*} \frac{\pi_{i,j,k}}{\rho_{i,j,k}}; \left[\frac{\delta_X A_T}{\Delta X_{Z_T}} \right]_{i,j,k-\frac{1}{2}} = \frac{A_{Ti,j,k} - A_{Ti-1,j,k}}{\Delta X}; \left[\frac{\delta_Y B_T}{\Delta Y_{Z_T}} \right]_{i,j,k-\frac{1}{2}} = \frac{B_{Ti,j,k} - B_{Ti,j-1,}}{\Delta Y}$$

$$\left[\frac{1}{\overline{\overline{G_0}^{Z_m}}} \left(\overline{G_1 \delta_{Z_m} \overline{A_T}^{Z_T}}^{X} \right) \right]_{i,j,k-\frac{1}{2}} = \frac{1}{G^w_{0\,i,j,k}} \frac{1}{4} \left[\begin{array}{l} G_{1i,j,k} \left(A_{Ti,j,k+1} - A_{Ti,j,k-1} \right) + \\ G_{1i-1,j,k} \left(A_{Ti-1,j,k+1} - A_{Ti-1,j,k-1} \right) \end{array} \right]; \qquad \text{(III.10d)}$$

$$\left[\frac{1}{\overline{\overline{G_0}^{Z_m}}} \left(\overline{G_2 \delta_{Z_m} \overline{B_T}^{Z_T}}^{Y} \right) \right]_{i,j,k-\frac{1}{2}} = \frac{1}{G^w_{0\,i,j,k}} \frac{1}{4} \left[\begin{array}{l} G_{2i,j,k} \left(B_{Ti,j,k+1} - B_{Ti,j,k-1} \right) + \\ G_{2i,j-1,k} \left(B_{Ti,j-1,k+1} - B_{Ti,j-1,k-1} \right) \end{array} \right];$$

as well as the turbulent momentum and heat fluxes, expressed with absolute indices, become:

$\bullet \left[A_U\right]_{i-\frac{1}{2},j-\frac{1}{2},k}$:

$$\left[\overline{\rho}^{XYZ_w}\,\overline{K_M}^{XYZ_w}\right]_{i-\frac{1}{2},j-\frac{1}{2},k}=\frac{1}{8}\begin{bmatrix}\left(\rho_{i,j,k}+\rho_{i-1,j,k}\right)+\\ \left(\rho_{i,j-1,k}+\rho_{i-1,j-1,k}\right)+\\ \left(\rho_{i,j,k-1}+\rho_{i-1,j,k-1}\right)+\\ \left(\rho_{i,j-1,k-1}+\rho_{i-1,j-1,k-1}\right)\end{bmatrix}\times\frac{1}{8}\begin{bmatrix}\left(K_{Mi,j,k}+K_{Mi-1,j,k}\right)+\\ \left(K_{Mi,j-1,k}+K_{Mi-1,j-1,k}\right)+\\ \left(K_{Mi,j,k-1}+K_{Mi-1,j,k-1}\right)+\\ \left(K_{Mi,j-1,k-1}+K_{Mi-1,j-1,k-1}\right)\end{bmatrix};$$

$$\left[S\right]_{i-\frac{1}{2},j-\frac{1}{2},k}=S_{i,j,k};\left[\overline{G_0}^{XY}\right]_{i-\frac{1}{2},j-\frac{1}{2},k}=\frac{1}{2}\left(G^u_{0\,i,j,k}+G^u_{0\,i,j-1,k}\right);$$

$$\left[\frac{\delta_X V}{\Delta X_{Z_m}}\right]_{i-\frac{1}{2},j-\frac{1}{2},k}=\frac{V_{i,j,k}-V_{i-1,j,k}}{\Delta X};\left[\frac{\delta_Y U}{\Delta Y_{Z_m}}\right]_{i-\frac{1}{2},j-\frac{1}{2},k}=\frac{U_{i,j,k}-U_{i,j-1,k}}{\Delta Y};\qquad\text{(III.11a)}$$

$$\left[\overline{\overline{G_1}^{Y}\,\delta_{Z_m}\overline{V}^{X}}^{Z_w}\right]_{i-\frac{1}{2},j-\frac{1}{2},k}=\frac{1}{8}\begin{Bmatrix}\left(G_{1i,j,k+1}+G_{1i,j-1,k+1}\right)\left[\left(V_{i,j,k+1}+V_{i-1,j,k+1}\right)-\left(V_{i,j,k}+V_{i-1,j,k}\right)\right]\\ +\left(G_{1i,j,k}+G_{1i,j-1,k}\right)\left[\left(V_{i,j,k}+V_{i-1,j,k}\right)-\left(V_{i,j,k-1}+V_{i-1,j,k-1}\right)\right]\end{Bmatrix};$$

$$\left[\overline{\overline{G_2}^{X}\,\delta_{Z_m}\overline{U}^{Y}}^{Z_w}\right]_{i-\frac{1}{2},j-\frac{1}{2},k}=\frac{1}{8}\begin{Bmatrix}\left(G_{2i,j,k+1}+G_{2i-1,j,k+1}\right)\left[\left(U_{i,j,k+1}+U_{i,j-1,k+1}\right)-\left(U_{i,j,k}+U_{i,j-1,k}\right)\right]\\ +\left(G_{2i,j,k}+G_{2i-1,j,k}\right)\left[\left(U_{i,j,k}+U_{i,j-1,k}\right)-\left(U_{i,j,k-1}+U_{i,j-1,k-1}\right)\right]\end{Bmatrix}$$

$\bullet \left[B_U\right]_{i-\frac{1}{2},j,k-\frac{1}{2}}$:

$$\left[\overline{\rho}^{X}\,\overline{K_M}^{X}\right]_{i-\frac{1}{2},j,k-\frac{1}{2}}=\frac{\left(\rho_{i,j,k}+\rho_{i-1,j,k}\right)}{2}\frac{\left(K_{Mi,j,k}+K_{Mi-1,j,k}\right)}{2};\left[\frac{\delta_X w}{\Delta X_{Z_w}}\right]_{i-\frac{1}{2},j,k-\frac{1}{2}}=\frac{w_{i,j,k}-w_{i-1,j,}}{\Delta X}$$

$$\left[G_1\overline{\frac{1}{G_0}\delta_{Z_w}w}^{XZ_m}\right]_{i-\frac{1}{2},j,k-\frac{1}{2}}=\frac{G_{1i,j,k}}{4}\begin{bmatrix}\frac{\left(w_{i,j,k+1}-w_{i,j,k}\right)}{G^u_{0\,i,j,k+1}}+\frac{\left(w_{i-1,j,k+1}-w_{i-1,j,k}\right)}{G^u_{0\,i-1,j,k+1}}+\\ \frac{\left(w_{i,j,k}-w_{i,j,k-1}\right)}{G^u_{0\,i,j,k}}+\frac{\left(w_{i-1,j,k}-w_{i-1,j,k-1}\right)}{G^u_{0\,i-1,j,k}}\end{bmatrix};\qquad\text{(III.11b)}$$

$\bullet\left[A_V\right]_{i-\frac{1}{2},j-\frac{1}{2},k}$:

$$\left[\overline{\rho}^{XYZ_w}\overline{K_M}^{XYZ_w}\right]_{i-\frac{1}{2},j-\frac{1}{2},k}=\frac{1}{8}\begin{bmatrix}\left(\rho_{i,j,k}+\rho_{i-1,j,k}\right)+\\ \left(\rho_{i,j-1,k}+\rho_{i-1,j-1,k}\right)+\\ \left(\rho_{i,j,k-1}+\rho_{i-1,j,k-1}\right)+\\ \left(\rho_{i,j-1,k-1}+\rho_{i-1,j-1,k-1}\right)\end{bmatrix}\times\frac{1}{8}\begin{bmatrix}\left(K_{Mi,j,k}+K_{Mi-1,j,k}\right)+\\ \left(K_{Mi,j-1,k}+K_{Mi-1,j-1,k}\right)+\\ \left(K_{Mi,j,k-1}+K_{Mi-1,j,k-1}\right)+\\ \left(K_{Mi,j-1,k-1}+K_{Mi-1,j-1,k-1}\right)\end{bmatrix};$$

$$\left[S\right]_{i-\frac{1}{2},j-\frac{1}{2},k}=S_{i,j,k};\left[\overline{G_0}^{XY}\right]_{i-\frac{1}{2},j-\frac{1}{2},k}=\frac{1}{2}\left(G^u_{0\,i,j,k}+G^u_{0\,i,j-1,k}\right);$$

$$\left[\frac{\delta_X V}{\Delta X_{Z_m}}\right]_{i-\frac{1}{2},j-\frac{1}{2},k}=\frac{V_{i,j,k}-V_{i-1,j,k}}{\Delta X};\left[\frac{\delta_Y U}{\Delta Y_{Z_m}}\right]_{i-\frac{1}{2},j-\frac{1}{2},k}=\frac{U_{i,j,k}-U_{i,j-1,k}}{\Delta Y};\qquad\text{(III.11c)}$$

$$\left[\overline{\overline{G_1}^{Y}\delta_{Z_m}\overline{V}^{X}}^{Z_w}\right]_{i-\frac{1}{2},j-\frac{1}{2},k}=\frac{1}{8}\begin{Bmatrix}\left(G_{1i,j,k+1}+G_{1i,j-1,k+1}\right)\left[\left(V_{i,j,k+1}+V_{i-1,j,k+1}\right)-\left(V_{i,j,k}+V_{i-1,j,k}\right)\right]\\ +\left(G_{1i,j,k}+G_{1i,j-1,k}\right)\left[\left(V_{i,j,k}+V_{i-1,j,k}\right)-\left(V_{i,j,k-1}+V_{i-1,j,k-1}\right)\right]\end{Bmatrix};$$

$$\left[\overline{\overline{G_2}^{X}\delta_{Z_m}\overline{U}^{Y}}^{Z_w}\right]_{i-\frac{1}{2},j-\frac{1}{2},k}=\frac{1}{8}\begin{Bmatrix}\left(G_{2i,j,k+1}+G_{2i-1,j,k+1}\right)\left[\left(U_{i,j,k+1}+U_{i,j-1,k+1}\right)-\left(U_{i,j,k}+U_{i,j-1,k}\right)\right]\\ +\left(G_{2i,j,k}+G_{2i-1,j,k}\right)\left[\left(U_{i,j,k}+U_{i,j-1,k}\right)-\left(U_{i,j,k-1}+U_{i,j-1,k-1}\right)\right]\end{Bmatrix}$$

$\bullet\left[B_V\right]_{i,j-\frac{1}{2},k-\frac{1}{2}}$:

$$\left[\overline{\rho}^{Y}\overline{K_M}^{Y}\right]_{i,j-\frac{1}{2},k-\frac{1}{2}}=\frac{\left(\rho_{i,j,k}+\rho_{i,j-1,k}\right)}{2}\frac{\left(K_{Mi,j,k}+K_{Mi,j-1,k}\right)}{2};\left[\frac{\delta_Y w}{\Delta Y_{Z_w}}\right]_{i,j-\frac{1}{2},k-\frac{1}{2}}=\frac{w_{i,j,k}-w_{i,j-1,k}}{\Delta Y};$$

$$\left[G_2\overline{\frac{1}{G_0}\delta_{Z_w}w}^{YZ_m}\right]_{i,j-\frac{1}{2},k-\frac{1}{2}}=\frac{G_{2i,j,k}}{4}\begin{bmatrix}\frac{\left(w_{i,j,k+1}-w_{i,j,k}\right)}{G^v_{0\,i,j,k+1}}+\frac{\left(w_{i,j-1,k+1}-w_{i,j-1,k}\right)}{G^v_{0\,i,j-1,k+1}}+\\ \frac{\left(w_{i,j,k}-w_{i,j,k-1}\right)}{G^v_{0\,i,j,k}}+\frac{\left(w_{i,j-1,k}-w_{i,j-1,k-1}\right)}{G^v_{0\,i,j-1,k}}\end{bmatrix};\qquad\text{(III.11d)}$$

• $\left[A_w\right]_{i-\frac{1}{2},j,k-\frac{1}{2}}$:

$$\left[\overline{\rho}^{X}\overline{K_M}^{X}\right]_{i-\frac{1}{2},j,k-\frac{1}{2}}=\frac{\left(\rho_{i,j,k}+\rho_{i-1,j,k}\right)}{2}\frac{\left(K_{Mi,j,k}+K_{Mi-1,j,k}\right)}{2};\left[\frac{\delta_X w}{\Delta X_{Z_w}}\right]_{i-\frac{1}{2},j,k-\frac{1}{2}}=\frac{w_{i,j,k}-w_{i-}}{\Delta X}$$

$$\left[G_1\overline{\frac{1}{G_0}\delta_{Z_w}w}^{XZ_m}\right]_{i-\frac{1}{2},j,k-\frac{1}{2}}=\frac{G_{1i,j,k}}{4}\left[\begin{array}{l}\frac{\left(w_{i,j,k+1}-w_{i,j,k}\right)}{G^u_{0\,i,j,k+1}}+\frac{\left(w_{i-1,j,k+1}-w_{i-1,j,k}\right)}{G^u_{0\,i-1,j,k+1}}+\\ \frac{\left(w_{i,j,k}-w_{i,j,k-1}\right)}{G^u_{0\,i,j,k}}+\frac{\left(w_{i-1,j,k}-w_{i-1,j,k-1}\right)}{G^u_{0\,i-1,j,k}}\end{array}\right];\qquad \text{(III.11e)}$$

$$\left[\frac{\overline{\overline{S}^{Y}}^{Z_m}}{\overline{G_0}^{X}}\delta_{Z_m}U\right]_{i-\frac{1}{2},j,k-\frac{1}{2}}=\frac{1}{4}\left[\frac{\left(S_{i,j,k}+S_{i,j-1,k}\right)}{G^u_{0\,i,j,k}}+\frac{\left(S_{i,j,k-1}+S_{i,j-1,k-1}\right)}{G^u_{0\,i,j,k-1}}\right]\left(U_{i,j,k}-U_{i,j,k-1}\right);$$

• $\left[B_w\right]_{i,j-\frac{1}{2},k-\frac{1}{2}}$:

$$\left[\overline{\rho}^{Y}\overline{K_M}^{Y}\right]_{i,j-\frac{1}{2},k-\frac{1}{2}}=\frac{\left(\rho_{i,j,k}+\rho_{i,j-1,k}\right)}{2}\frac{\left(K_{Mi,j,k}+K_{Mi,j-1,k}\right)}{2};\left[\frac{\delta_Y w}{\Delta Y_{Z_w}}\right]_{i,j-\frac{1}{2},k-\frac{1}{2}}=\frac{w_{i,j,k}-w_{i,j-1,}}{\Delta Y}$$

$$\left[G_2\overline{\frac{1}{G_0}\delta_{Z_w}w}^{YZ_m}\right]_{i,j-\frac{1}{2},k-\frac{1}{2}}=\frac{G_{2i,j,k}}{4}\left[\begin{array}{l}\frac{\left(w_{i,j,k+1}-w_{i,j,k}\right)}{G^v_{0\,i,j,k+1}}+\frac{\left(w_{i,j-1,k+1}-w_{i,j-1,k}\right)}{G^v_{0\,i,j-1,k+1}}+\\ \frac{\left(w_{i,j,k}-w_{i,j,k-1}\right)}{G^v_{0\,i,j,k}}+\frac{\left(w_{i,j-1,k}-w_{i,j-1,k-1}\right)}{G^v_{0\,i,j-1,k}}\end{array}\right];\qquad \text{(III11f)}$$

$$\left[\frac{\overline{\overline{S}^{X}}^{Z_m}}{\overline{G_0}^{Y}}\delta_{Z_m}V\right]_{i,j-\frac{1}{2},k-\frac{1}{2}}=\frac{1}{4}\left[\frac{\left(S_{i,j,k}+S_{i-1,j,k}\right)}{G^v_{0\,i,j,k}}+\frac{\left(S_{i,j,k-1}+S_{i-1,j,k-1}\right)}{G^v_{0\,i,j,k-1}}\right]\left(V_{i,j,k}-V_{i,j,k-1}\right);$$

$\bullet \left[A_T\right]_{i-\frac{1}{2},j,k-\frac{1}{2}}$:

$$\left[\overline{\rho}^{X}\,\overline{K_T}^{XZ_T}\right]_{i-\frac{1}{2},j,k-\frac{1}{2}} = \frac{\left(\rho_{i,j,k}+\rho_{i-1,j,k}\right)}{2}\frac{1}{4}\left[\begin{array}{l}\left(K_{Ti,j,k}+K_{Ti-1,j,k}\right)+\\ \left(K_{Ti,j,k-1}+K_{Ti-1,j,k-1}\right)\end{array}\right];$$

$$\left[\frac{\delta_X\theta}{\Delta X_{Z_T}}\right]_{i-\frac{1}{2},j,k-\frac{1}{2}} = \frac{\theta_{i,j,k}-\theta_{i-1,j,k}}{\Delta X}; \qquad \text{(III.11g)}$$

$$\left[G_1\overline{\frac{1}{G_0}\delta_{Z_T}w}^{XZ_m}\right]_{i-\frac{1}{2},j,k-\frac{1}{2}} = \frac{G_{1i,j,k}}{4}\left[\begin{array}{l}\frac{\left(\theta_{i,j,k+1}-\theta_{i,j,k}\right)}{G^u_{0\,i,j,k+1}}+\frac{\left(\theta_{i-1,j,k+1}-\theta_{i-1,j,k}\right)}{G^u_{0\,i-1,j,k+1}}+\\ \frac{\left(\theta_{i,j,k}-\theta_{i,j,k-1}\right)}{G^u_{0\,i,j,k}}+\frac{\left(\theta_{i-1,j,k}-\theta_{i-1,j,k-1}\right)}{G^u_{0\,i-1,j,k}}\end{array}\right];$$

$\bullet \left[B_T\right]_{i,j-\frac{1}{2},k-\frac{1}{2}}$:

$$\left[\overline{\rho}^{Y}\,\overline{K_T}^{YZ_T}\right]_{i,j-\frac{1}{2},k-\frac{1}{2}} = \frac{\left(\rho_{i,j,k}+\rho_{i,j-1,k}\right)}{2}\frac{1}{4}\left[\begin{array}{l}\left(K_{Ti,j,k}+K_{Ti,j-1,k}\right)+\\ \left(K_{Ti,j,k-1}+K_{Ti,j-1,k-1}\right)\end{array}\right];$$

$$\left[\frac{\delta_Y\theta}{\Delta Y_{Z_T}}\right]_{i,j-\frac{1}{2},k-\frac{1}{2}} = \frac{\theta_{i,j,k}-\theta_{i,j-1,k}}{\Delta Y}; \qquad \text{(III.11h)}$$

$$\left[G_2\overline{\frac{1}{G_0}\delta_{Z_T}w}^{YZ_m}\right]_{i,j-\frac{1}{2},k-\frac{1}{2}} = \frac{G_{2i,j,k}}{4}\left[\begin{array}{l}\frac{\left(\theta_{i,j,k+1}-\theta_{i,j,k}\right)}{G^v_{0\,i,j,k+1}}+\frac{\left(\theta_{i,j-1,k+1}-\theta_{i,j-1,k}\right)}{G^v_{0\,i,j-1,k+1}}+\\ \frac{\left(\theta_{i,j,k}-\theta_{i,j,k-1}\right)}{G^v_{0\,i,j,k}}+\frac{\left(\theta_{i,j-1,k}-\theta_{i,j-1,k-1}\right)}{G^v_{0\,i,j-1,k}}\end{array}\right];$$

where the overbars represent the spatial interpolation applied on the given variable or derivative, considering either momentum levels $\left(Z_m\right)$, for horizontal velocity components and pressure, or energy-thermodynamic levels $\left(Z_T, Z_w\right)$ for temperature, TKE or vertical velocity. Special care has to be taken for interpolation on the bottom and top frontiers, where the momentum and thermodynamic variables are redistributed slightly different for other calculations, as explained and illustrated in Gasset et al. (2014, Fig. 1).

BIBLIOGRAPHY

"Annual Energy Outlook 2017, with projections to 2050", U.S. Energy Information Administration, Department of Energy, 64 p., 2017.

"BP Statistical Review of World Energy", British Petroleum, 52 p., 2017.

"Levelized Cost and Levelized Avoided Cost of New Generation Resources", U.S. Energy Information Administration, Department of Energy, 21 p., 2017.

"Small Wind World Report", World Wind Energy Association Bulletin, pp. 29, Issue 2, 2016.

"U.S. Wind Industry First Quarter 2017 Market Report", American Wind Energy Association, 16 p., 2017.

"Wind Energy 2050: on the shape of near 100% RE grid", World Wind Energy Association, Technical Committee Report, 84 p., 2015.

"Wind Energy Industry Records Strong Year", Wind Sight Magazine, spring 2017, Canadian Wind Energy Association, 30 p., 2017.

Allen, T. and Brown, A., 2002. Large-Eddy Simulation of Turbulent Separated Flow Over Rough Hills. Boundary-Layer Meteorology, Vol. 102, p. 177–198. DOI: 10.1023/A:1013155712154

Andren, A., Brown, A., Graf, J., Mason, P., Moeng, C., Nieuwstadt, F. and Schumann, U., 1994. LES for a Neutrally Stratified Boundary Layer: A Comparison of Four Computer Codes. Q. J. R. Meteorological Society, Vol. 120, p. 1457–1484.

Arfken, G., Weber, H. and Harris, F., 2013. Mathematical Methods for Physicists: A Comprehensive Guide. Academic Press, 7th Edition, Oxford, UK, 1208 p.

Arthur, R., Lundquist, K., Mirocha, J. and Chow, F. K., 2016. Topographic shading in WRF model with the immersed boundary method: implementation, validation and application to complex terrain. AGU Fall Meeting, San Francisco. Poster consulted at http://adsabs.harvard.edu/abs/2016AGUFM.A23B0213A.

Asselin, R. A., 1972. Frequency Filter for Time Integrations. Monthly Weather Review, Vol. 100, p. 487–490.

Athanasiadou, M. and Castro, I. P., 2001. Neutral Flow over a Series of Rough Hills: A Laboratory Experiment. Boundary-Layer Meteorology, Vol. 101 (1), p. 1-30. DOI: 10.1023/A:1019250801054

Ayotte, K., 2008. Computational Modelling for Wind Energy Assessment. Journal of Wind Engineering and Industrial Aerodynamics, Vol. 96, p. 1571-1590. DOI: 10.1016/j.jweia.2008.02.002

Bautista, M. 2015. Turbulence Modelling of the Atmospheric Boundary Layer over Complex Topography. PhD Thesis, École de Technologie Supérieure, University of Quebec.

Bechmann, A. and Sørensen, N., 2010. Hybrid RANS/LES method for wind flow over complex terrain. Wind Energy, Vol. 13, p. 36–50. DOI: 10.1002/we.346

Bechmann, A., Sørensen, N. N., Berg, J., Mann, J., and Réthoré, P.-E., 2011: The Bolund Experiment, Part II: Blind Comparison of Microscale Flow Models. Boundary-Layer Meteorology, vol. 141, p. 245–271. DOI:10.1007/s10546-011-9637-x.

Bénard, P., 2003. Stability of Semi-Implicit and Iterative Centered-Implicit Time Discretizations for Various Equation Systems used in NWP. Monthly Weather Review, Vol. 131, p. 2479–2491.

Bénard, P., Laprise, R., Vivoda, J. and Smolíková, P., 2004. Stability of Leapfrog Constant-Coefficients Semi-Implicit Schemes for the Fully Elastic System of Euler Equations: Flat-Terrain Case. Monthly Weather Review, Vol. 132, p. 1306–1318.

Bénard, P., Mašek, J. and Smolíková, P., 2005. Stability of Leapfrog Constant-Coefficients Semi-Implicit Schemes for the Fully Elastic System of Euler Equations: Case With Orography. Monthly Weather Review, Vol. 133, p. 1065–1075. DOI: 10.1175/MWR2907.1

Bengtsson, J., 2015. Turbulent Wind Flow Modelling in Complex Terrain, a Comparison between a Linear Model, a CFD Model and a NWP Model. Master Thesis, Chalmers University of Technology, Göteborg, Sweden, 27 p.

Benoit, R., Desgagné, M., Pellerin, P. and Chartier, Y., 1997. The Canadian MC2, a Semi-Lagrangian Semi-Implicit Wideband Atmospheric Model Suited for Finescale Process Studies and Simulation. Monthly Weather Review, Vol. 125, p. 2382–2415.

Benoit, R., C. Schär, P. Binder, S. Chamberland, H. C. Davies, M. Desgagné, C. Girard, C. Keil, N. Kouwen, D. Lüthi, D. Maric, E. Muller, P. Pellerin, J. Schmidli, F. Schubiger, C. Schwierz, M. Sprenger, A. Walser, S. Willemse, W. Yu and E. Zala, 2002a: The real-time ultrafinescale forecast support during the special observing period of the MAP, Bulletin of the American Meteorological Society, Vol. 83, p. 85-109.

Berg, J., Mann, J., Bechmann, A., Courtney, M. S. and Jørgensen, H. E., 2011. The Bolund Experiment, Part I: Flow Over a Steep, Three-Dimensional Hill. Boundary-Layer Meteorology, Vol. 141, p. 219–243; DOI:10.1007/s10546-011-9636-y.

Bergström, H. and Juuso, N., 2006. A study of valley winds using the MIUU mesoscale model. Wind Energy, Vol. 9, 109-129. DOI: 10.1002/we.188

Blackadar, A. K., 1997. Turbulence and Diffusion in the Atmosphere, Lectures in Environmental Sciences. Springer-Verlag, Berlin, Germany, 185 p.

Blocken, B., Hout, A., Dekker, J. and Weiler, O., 2015. CFD Simulations of Wind Flow over Natural Complex Terrain: Case Study with Validation by Field Measurements for Ria de Ferrol, Galicia, Spain. Journal of Wind Engineering and Industrial Aerodynamics, Vol. 147, p. 43-57. DOI: 10.1016/j.jweia.2015.09.007

Bonaventura, L., 2000. A Semi-Implicit Semi-Lagrangian Scheme Using the Height Coordinate for a Non-hydrostatic and Fully Elastic Model of Atmospheric Flows. Journal of Computational Physics, Vol. 158, p. 186–213.

Brasseur, J. and Wei, T., 2010. Designing Large-eddy Simulation of the Turbulent Boundary Layer to Capture Law-of-the-Wall Scaling. Physics of Fluids, Vol. 22 (2), 021303. DOI: 10.1063/1.3319073

Breton, J.-P., Sumner, J., Sørensen, J. N., Hansen, K. S., Sarmast, S. and Ivanell, S., 2017. A Survey of Modelling Methods for High-fidelity Wind Farm Simulations using Large Eddy Simulation. Phil. Trans. R. Soc. A. Vol. 375, 20160097. DOI: 10.1098/rsta.2016.0097

Brown, A.R., Hobson, J.M. and Wood, N., 2001. Large-eddy Simulation of Neutral Turbulent Flow over Rough Sinusoidal Ridges. Boundary-Layer Meteorology, Vol. 98, p. 411–441 (2001). DOI: 10.1023/A:1018703209408.

Burden, R. L. and Faires, J. D., 2005. Numerical Analysis, 8th edition. Boston, U.S., Thomson Brooks/Cole, 872 p.

Cabezón, D., 2013. Development of a Wake Model for Wind Farms Based on an Open Source CFD Solver: Strategies on Parabolization and Turbulence Modelling. PhD Thesis, Universidad Politécnica de Madrid, Madrid, Spain, 112 p.

Castagna, J., Yao, Y. and Yao, J., 2014. Direct Numerical Simulation of Turbulent Flow over an Axisymmetric Hill. Computers and Fluids, Vol. 95, p. 116-126. DOI: 10.1016/j.compfluid.2014.02.014

Castro, I. and Apsley, D., 1997. Flow and Dispersion Over Topography: A Comparison Between Numerical and Laboratory Data for Two-Dimensional Flows. Atmospheric Environment, Vol. 31 (6), p. 839-850. DOI: 10.1016/S1352-2310(96)00248-8

Castro, F., Palma, J. and Silva Lopes, A., 2002. Simulations of the Askervein flow. Part 1: Reynolds Averaged Navier-Stokes Equations (k-ε Turbulence Model). Boundary-Layer

Meteorology, Vol. 107, p. 501–530. DOI: 10.1023/A:1022818327584

Castro, I., 2004. ERCOFTAC QNET-CFD, Application Challenge 5-05. http://qnet-ercoftac.cfms.org.uk/w/index.php/AC_5-05. [accessed online on March 11, 2017]

Cavar, D., Réthoré, P.-E., Bechmann, A., Sørensen, N., Martínez, B., Zahle, F., Berg, J. and Kelly, M., 2016. Comparison of OpenFOAM and EllipSys3D for Neutral Atmospheric Flow over Complex Terrain. Wind Energy Science Discussions, Vol. 1, p. 55–70; DOI: 10.5194/wes-2016-3.

Caya, D. and Laprise, R., 1999. A Semi-implicit Semi-Lagrangian Regional Climate Model: The Canadian RCM. Monthly Weather Review, Vol. 127, p. 341–362.

Chen, F., Kusaka, H., Bornstein, R., Ching, J., Grimmond, C. S., 2010. The Integrated WRF/Urban Modelling System: Development, Evaluation, and Applications to Urban Environmental Problems. International Journal of Climatology, Vol. 31, p. 273–288, DOI:10.1002/joc.2158

Chow, F. K., Street, R., Xue, M. and Ferziger, J. H., 2005. Explicit Filtering and Reconstruction Turbulence Modeling for Large-eddy Simulation of Neutral Boundary Layer Flow. Journal of Atmospheric Sciences, Vol. 62, p. 2058–2077. DOI: 10.1175/JAS3456.1

Chow, F. K. and Street, R. L., 2009. Evaluation of Turbulence Closure Models for Large-Eddy Simulation over Complex Terrain: Flow over Askervein Hill. Journal of Applied Meteorology and Climatology, Vol. 48-5, p. 1050–1065. DOI: 10.1175/2008JAMC1862.1

Churchfield, M. J., G. Vijayakumar, J. G. Brasseur, and P. J. Moriarty, 2010: Wind Energy-Related Atmospheric Boundary Layer Large-Eddy Simulation Using OpenFOAM: Preprint. 19th Symp. on Boundary Layers and Turbulence, Keystone, CO, 26 p.

Churchfield, M., Lee, S., Michalakes, J. and Moriarty, P., 2012. A Numerical Study of the Effects of Atmospheric and Wake Turbulence on Wind Turbine Dynamics. Journal of Turbulence, Vol. 13, N14. DOI:10.1080/14685248.2012.668191

Churchfield, M., Lee, S. and Moriarty, P., 2014. Adding Complex Terrain and Stable Atmospheric Condition Capability to the Openfoam-Based Flow Solver of the Simulator for On/Offshore Wind Farm Applications (SOWFA). ITM Web Conference, Vol. 2, p. 02001. DOI:10.1051/itmconf/20140202001

Cushman-Roisin, B. and Beckers, J.-M., 2011. Introduction to Geophysical Fluid Dynamics, Physical and Numerical Aspects. Academic Press, Waltham, MA, 828 p.

Cuxart, J., P. Bougeault, and J.-L. Redelsperger, 2000: A Turbulence Scheme Allowing For Mesoscale and Large-Eddy Simulations. Quart. J. Roy. Meteor. Soc., Vol. 126, p. 1–30.

Dalpé, B. and Masson, C., 2008. Numerical Study of Fully Developed Turbulent Flow within and above a Dense Forest. Wind Energy, Vol. 11, p. 503–515; DOI: 10.1002/we.271.

Davidson, P., 2015. Turbulence: An Introduction for Scientists and Engineers. Oxford University Press, 2nd edition, London, UK, 688 p.

Deardorff, J. W., 1971. On the Magnitude of the Subgrid Scale Eddy Coefficient. Journal of Computational Physics, Vol. 7, p. 120-133. DOI: 10.1016/0021-9991(71)90053-2

Deardorff, J. W., 1971. On The Magnitude of the Subgrid Scale Eddy Coefficient. Journal of Computational Physics, Vol. 7, p. 120-133. DOI: 10.1016/0021-9991(71)90053-2

Dellwik, E. and Arnqvist, J., 2014. Mesoscale Modelling of a Forested Landscape. Journal of Physics: Conference Series. IOP Publishing, Vol. 524, p. 012121.

Deodatis, G., Ellingwood, B. and Frangopol, D., 2014. Safety, reliability, risk and life-cycle performance of structures and infrastructures. CRC Press, 1112 pp.

Dietze, E., Mellado, J. P., Stevens, B. and Schmidt, H., 2013. Study Of Low-Order Numerical Effects In The Two-Dimensional Cloud-Topped Mixing Layer. Theoretical and Computational Fluid Dynamics, Vol. 27, p. 239-251. DOI: 10.1007/s00162-012-0263-0

Ding, F., Pal Arya, S. & Lin, Y., 2001 (part I). Large-eddy Simulations of the Atmospheric Boundary Layer using a New Subgrid Scale Model. Slightly Unstable and Neutral Cases. Environmental Fluid Mechanics, Vol. 1, p. 29–47.

Drobinski, P., Carlotti, P., Redelsperger, J., Masson, V., Banta, R. and Newsom, R., 2007. Numerical and Experimental Investigation of the Neutral Atmospheric Surface Layer. Journal of Atmospheric Science, Vol. 64, p. 137-156. DOI: 10.1175/JAS3831.1

Durran, D. R., 2010. Numerical Methods for Fluid Dynamics, with Applications to Geophysics. Springer, 2nd edition, New York, NY, USA. 516 p.

Durran, D., 2010. Numerical methods for fluid dynamics, with applications to geophysics. Springer-Verlag, New York, 534 p. DOI: 10.1007/978-1-4419-6412-0

Eckermann, S., McCormack, J., Ma, J., Hogan, T. and Zawdie, K., 2014. Stratospheric Analysis and Forecast Errors Using Hybrid and Sigma Coordinates. Monthly Weather Review, Vol. 142, p. 476–485.

Ercole, L., Marcolongo, A. and Baroni, S., 2017. Accurate thermal conductivities form optimally short molecular dynamic simulations. Scientific Reports, 7, 15835. DOI: 10.1038/s41598-017-15843-2

Ferziger, J. H. and Perić, M., 2002. Computational Methods for Fluid Dynamics. Springer-

Verlag, Berlin, 3rd. Edition, 426 pp. DOI: 10.1007/978-3-642-56026-2

Fleming, P., M. Churchfield, A. Scholbrock, J. Michalakes, K. Johnson and P. Moriarty, 2013. "The SOWFA super-controller: a high-fidelity tool for evaluating wind plant control approaches. National Renewable Energy Laboratory, NREL/CP-5000-57175.

Flores-Maradiaga, A., Benoit, R., and Masson, C., 2016. Enhanced Method for Multiscale Wind Simulations over Complex Terrain for Wind Resource Assessment. Journal of Physics: Conference Series, Vol. 753, 082030. DOI: 10.1088/1742-6596/753/8/082030

Frank, H. P. and Landberg, L., 1997. Modelling the Wind Climate of Ireland. Boundary-Layer Meteorology, Vol. 85 (3), p. 359-378. DOI: 10.1023/A:1000552601288

Frank, H. P., Landberg, L., Rathmann, O., Mortensen, N. G. and Petersen, E. L., 2001. The Numerical Wind Atlas; The KAMM/WAsP method. Conference Proceedings of Windpower 2001, American Wind Energy Association (AWEA), Washington, DC (US), 3-7 Jun, 2001.

Fujiwara, M., Wright, J., Manney, G., Gray, L., 2017. Introduction of the SPARC Reanalysis Intercomparison Project (S-RIP) and Overview of the Reanalysis Systems. Atmospheric Chemistry and Physics, Vol. 17, p. 1417-1452.

Gal-Chen, T. and Somerville, R., 1975. On the Use of a Coordinate Transformation for the Solution of Navier-Stokes Equations. Journal of Computational Physics, Vol. 17, p. 209–228. DOI: 10.1016/0021-9991(75)90037-6

Gallus, W. and Klemp, J., 2000. Behavior of Flow over Step Orography. Monthly Weather Review, Vol. 128, p. 1153–1164.

Gasset, N., Laundry, M., Gagnon, Y. 2012. A Comparison of Wind Flow Models for Wind Resource Assessment in Wind Energy Applications. Energies, Vol. 5, p. 4288–4322. DOI: 10.3390/en5114288.

Gasset, N., 2014. Refinement of a Mesoscale Model for Large-Eddy Simulation. PhD Thesis, École de Technologie Supérieure, Université du Québec, Montréal, 581 pp. [http://espace.etsmtl.ca/1258/4/GASSET_Nicolas.pdf]

Gasset, N., Benoit, R., Masson, C., 2014. Implementing Large-eddy Simulation Capability in a Compressible Mesoscale Model. Monthly Weather Review, Vol. 142, p. 2733–2750. DOI: 10.1175/MWR-D-13-00257.1

Gerling, T. W., 1986. Structure of the Surface Wind Field from the Seasat SAR. Journal of Geophysical Research: Oceans, Vol. 91, p. 2308-2320. DOI: 10.1029/JC091iC02p02308

Germano, M., Piomelli, U., Moin, P. and Cabot, W., 1991. A dynamic subgrid-scale eddy

viscosity model. Physical Fluids, Vol. 3, p. 1760–1765.

Girard, C., Benoit, R. and Desgagné, M., 2005. Finescale topography and the MC2 dynamics kernel. Monthly Weather Review, 133, 1463–1477. DOI: 10.1175/MWR2931.1

Grosh, D. L., 1989. Primer of Reliability Theory. John Wiley and Sons, New York, 384 pp.

Gong, W., Taylor, P. A. and Dörnbrack, A., 1996. Turbulent Boundary-Layer Flow over Fixed Aerodynamically Rough Two-Dimensional Sinusoidal Waves. Journal of Fluid Mechanics, 312, p. 1-37, DOI: 10.1017/S0022112096001905

Haltiner, G. J. and Williams, R. T., 1980. Numerical Prediction and Dynamic Meteorology. John Wiley and Sons, 477 pp. DOI: 10.1017/S0022112084210938

Harris, L. M., and D. R. Durran, 2010: An Idealized Comparison of One-Way and Two-Way Grid Nesting. Monthly Weather Review, Vol. 138, p. 2174–2187, DOI:10.1175/2010MWR3080.1.

Héreil, P. and Laprise, R., 1996. Sensitivity of Internal Gravity Wave Solutions to the Time Step of a Semi-Implicit Semi-Lagrangian Nonhydrostatic Model. Monthly Weather Review, Vol. 124, p. 972–999.

Holton, J. R., 2012. An Introduction to Dynamic Meteorology, 5th edition. Elsevier Academic Press, Burlington, MA, USA, 552 p.

Iaccarino, G. and Verzicco, R., 2003. Immersed Boundary Technique for Turbulent Flow Simulations. Applied Mechanics, Vol. 56, p. 331–347.

Jimenez, A., Crespo, A., Migoya, E. and Garcia, J., 2007. Advances In Large-Eddy Simulation Of A Wind Turbine Wake. In Proceedings of The Science of Making Torque from Wind (2nd conference). Journal of Physics: Conference Series, Vol. 75.

Kalnay, E., Kanamitsu, M., Kistler, R., Collins, W., Deaven, D., Galvin, L. and Iredell, M., 1996. The NCEP/NCAR 40-year Reanalysis Project. Bulletin of the American Meteorological Society, Vol. 77, p. 437-471. DOI: 10.1175/1520-0477(1996)077<0437:TNYRP>2.0.CO;2

Khrushudyan, L. H., Snyder, W. H. and Nekrasov, I. V., 1981. Flow and Dispersion of Pollutants over Two-Dimensional Hills. U.S. Environment Protection Agency, Report No. EPA-6000/4-81-067.

Kim, H. and Patel, V., 2000. Test of Turbulence Models for Wind Flow over Terrain with Separation and Recirculation. Boundary-Layer Meteorology, Vol. 94, p. 5–21. DOI: 10.1023/A:1002450414410

Kirkil, G., Mirocha, J., Bou-Zeid, E., Chow, F. K. and Kosović, B., 2012. Implementation and

Evaluation of Dynamic Sub-Filter Scale Stress Models for Large-Eddy Simulation Using WRF. Monthly Weather Review, Vol. 140, p. 266–284. DOI: 10.1175/MWR-D-11-00037.1

Klemp, J., Shamarock, W. and Fuhrer, O., 2003. Numerical Consistency of Metric Terms in Terrain-following Coordinates. Monthly Weather Review, Vol. 131, p. 1229–1239.

Klemp, J., 2011. A Terrain-following Coordinate with Smoothed Coordinate Surfaces. Monthly Weather Review, Vol. 139, p. 2163–2169.

Kosović, B., 1997. Subgrid-scale modelling for the large-eddy simulation of high-Reynolds-number boundary layers. Journal of Fluid Mechanics, 336, 151-182. DOI: 10.1017/S0022112096004697

Kosović, B. and Curry, J., 2000. A Large-Eddy Simulation Study of a Quasi-Steady Stably Stratified Atmospheric Boundary Layer. Journal of Atmospheric Science, Vol. 57, p. 1052-1058. DOI: 10.1175/1520-0469(2000)057%3C1052:ALESSO%3E2.0.CO;2

Landberg, L., L. Myllerup, O. Rathmann, E. Petersen, B. Jørgensen, J. Badger, and N. Mortensen. 2003. Wind Resource Estimation - An Overview. Wind Energy, Vol. 6 (3), p. 261–271.

Laprise, R., Caya, D., Bergeron, G. and Giguère, M., 1997. The Formulation of André Robert's MC2 (Mesoscale Compressible Community) Model. Atmosphere–Ocean, Vol. 35, p. 195–220. DOI: 10.1080/07055900.1997.9687348

Launder, B. E. and Spalding, D. B., 1975. The Numerical Computation of Turbulent Flows. Computational Methods for Applied Mechanical Engineering, Vol. 3, p. 269-289.

Léonard, A., 1974. Energy Cascade in Large-eddy Simulations of Turbulent Fluid Flow. Advances in Geophysics, Vol. 18, p. 237.

Leuenberger, D., Schär, C., Fuhrer, O. and Girard, C., 2001. A New Terrain-Following Coordinate for High Resolution Atmospheric Models. Diploma thesis, ETH Zurich – School of Computational Science and Engineering.

Leuenberger, D., Koller, M., Fuhrer, O. and Schär, C., 2010. A generalization of the SLEVE vertical coordinate. Monthly Weather Review, Vol. 138, p. 3683–3689.

Lilly, D. K., 1992. A Proposed Modification of the Germano Subgrid Scale Closure Method. Physical Fluids, Vol. 4, p. 633-635.

Liu, Z., Ishihara, T., Tanaka, T. and He, X., 2016. LES of Turbulent Flow Fields Over A Smooth 3-D Hill And A Smooth 2-D Ridge. Journal of Wind Engineering and Industrial Aerodynamics, Vol. 153, p. 1-12. DOI: 10.1016/j.jweia.2016.03.001

Long, R. R., 1997. Homogeneous isotropic turbulence and its collapse in stratified and rotating fluids. Dynamics of Atmospheres and Oceans, Vol. 27, 471-483.

Lundquist, K., Chow, F. and Lundquist, J., 2010. An Immersed Boundary Method for the Weather Research and Forecast Model. Monthly Weather Review, Vol. 138, p. 796 – 817. DOI: 10.1175/2009MWR2990.1

Lundquist, K. A., Chow, F. K. and Lundquist, J. K., 2012. An Immersed Boundary Method Enabling Large-Eddy Simulations of Flow over Complex Terrain in the WRF Model. Monthly Weather Review, Vol. 140, p. 3936–3955. DOI:10.1175/MWR-D-11-00311.1

Mahrer, Y., 1984. An Improved Numerical Approximation of the Horizontal Gradients in a Terrain-Following Coordinate System. Monthly Weather Review, Vol. 112, p. 918–922.

Mailhot, J. and R. Benoit, 1982: A Finite-Element Model of the Atmospheric Boundary Layer Suitable for Use with Numerical Weather Prediction Models. Journal of Atmospheric Sciences, Vol. 39 (10), p. 2249–2266.

Manwell, J., McGowan, J. and Rogers, A., 2010. Wind Energy Explained: Theory, Design and Application. John Wiley & Sons, London, 704 p.

Marjanović, N, 2015. Simulation of the Atmospheric Boundary Layer for Wind Energy Applications. Ph.D. thesis, University of California, Berkeley, 108 p. [http://gradworks.umi.com/10/08/10086191.html]

Mason, P. and Thomson, D., 1992. Stochastic Backscatter in Large Eddy Simulations of Boundary Layers. Journal of Fluid Mechanics, Vol. 242, p. 51–78. DOI: 10.1017/S0022112092002271

Maurizi, A., 2000. Numerical Simulation of Turbulent Flows over 2-D Valleys Using Three Versions of the $K-\varepsilon$ Closure Model. Journal of Wind Engineering and Industrial Aerodynamics, Vol. 85, p. 59–73.

Meneveau, C. and Katz, J., 2000. Scale-invariance and Turbulence Models for Large-Eddy Simulation. Annual Review of Fluid Mechanics, Vol. 32, p. 1-32.

Mirocha, J., Lundquist, J. K. and Kosović, B., 2010. Implementation of a Nonlinear Subfilter Turbulence Stress Model for Large-Eddy Simulation in the Advanced Research WRF Model. Monthly Weather Review, Vol. 138, p. 4212–4228. DOI: 10.1175/2010MWR3286.1

Mirocha, J., Kirkil, G., Boud-Zeid, E., Chow, F. K. and Kosović, B., 2013. Transition and equilibration of neutral atmospheric boundary layer flow in one-way nested large-eddy simulations using the Weather Research and Forecasting model. Monthly Weather Review, Vol. 141, p. 918–940. DOI: 10.1175/MWR-D-11-00263.1

Moeng, C.-H., J. Dudhia, J. Klemp, and P. Sullivan, 2007: Examining Two-Way Grid Nesting for Large Eddy Simulation of the PBL Using the WRF Model. Monthly Weather Review, Vol. 135, p. 2295–2311.

Mohd-Yusof, J., 1997. Combined Immersed Boundary and B-Spline Methods for Simulations of Flows in Complex Geometries. Annual Research Briefs. Center for Turbulence Research, NASA – Ames/Stanford University.

Moin, P. and Mahesh, K., 1998. Direct Numerical Simulations: A Tool in Turbulence, Annual Review of Fluid Mechanics, Vol. 30, p. 539-578.

Murakami, S., 1997. Overview of the Turbulence Models Applied in CWE – 1997. Journal of Wind Engineering and Industrial Aerodynamics, Vol. 74, p. 1-24.

Palma, J., Castro, F., Ribeiro, L., Rodrigues, A., and Pinto, A., 2008. Linear and Nonlinear Models in Wind Resource Assessment and Wind Turbine Micro-Siting in Complex Terrain. Journal of Wind Engineering and Industrial Aerodynamics, Vol. 96 (12), p. 2308–2326.

Panton, R. L., 2013. Imcompressible Flow, 4th edition. John Wiley & Sons, London, 912 p. DOI: 10.1002/9781118713075

Pao, R. H., 1967. Fluid Dynamics. Charles Merrill Books Inc., Ohio, IL, USA, 497 p.

Peppier, R. A., 1988. A Review of Static Stability Indices and Related Thermodynamic Parameters. Illinois State Water Survey Division, Climate and Meteorology Section. SWS Miscellaneous Publication, 94 p.

Peskins, C., 2002. The Immersed Boundary Method. Acta Numerica, Cambridge University Press. DOI: 10.1017/S0962492902000077.

Pielke, R. A. and M. E. Nicholls, 1997: Use of meteorological models in computational wind engineering. Journal of Wind Engineering and Industrial Aerodynamics, Vol. 68, p. 363–372.

Pham, P., 2012. Improvement of the Initialization of the WEST Wind Resource Software for Mountainous Region in Cold Climates. Master of Engineering thesis, École de Technologie Superiéure, University of Quebec, p. 139.

Pinard, J. P., Benoit, R. and Yu, W., 2005. A WEST Wind Climate Simulation of the Mountainous Yukon. Atmosphere-Ocean, Vol. 43, p. 259–282.

Pinard, J. P., 2007. Wind Climate of the Whitehorse Area. Artic, Vol. 60 (3), p. 227-237.

Pinard, J. P., Benoit, R., Wilson, J. D., 2009. Mesoscale Wind Climate Modelling in Steep

Mountains. Atmosphere-Ocean, Vol. 47, p. 63–78. DOI:10.3137/AO922.2009

Pinty, J. P., Benoit, R., Richards, E. and Laprise, R., 1995. Simple Tests of a Semi-Implicit Semi-Lagrangian Model on 2D Mountain Wave Problems. Monthly Weather Review, vol. 123, p. 3042–3058.

Pope, S. B., 2000. Turbulent Flows. Cambridge University Press, London, UK, 802 p.

Porté-Agel, F., Meneveau, C. and Parlange, M., 2000. A Scale-Dependent Dynamic Model for Large Eddy Simulation: Application to a Neutral Atmospheric Boundary Layer. Journal of Fluid Mechanics, Vol. 415, p. 261–284.

Porté-Agel, F., Meneveau, C. and Parlange, M., 2000. A Scale-Dependent Dynamic Model for Large Eddy Simulation: Application to a Neutral Atmospheric Boundary Layer. Journal of Fluid Mechanics, Vol. 415, p. 261–284. DOI: 10.1017/S0022112000008776

Prandtl, L., 1925. Bericht Über die Ausgebildete Turbulenz. Z. Angew. Math. Mech., Vol. 5, p. 136-139.

Rausand, M. and Høyland, A., 2004. System Reliability Theory: models, statistical methods and applications. John Wiley and Sons, 2nd edition, New Jersey, 636 pp.

Redelsperger, J., Mahé, F. and Carlotti, P., 2001. A Simple and General Subgrid Model Suitable both for Surface Layer and Free-Stream Turbulence. Boundary-Layer Meteorology, Vol. 101, p. 375-408. DOI: 10.1023/A:1019206001292

Robert, A., 1966. The Integration of a Low Order Spectral Form of the Primitive Meteorological Equations. Journal of the Meteorological Society of Japan, Vol. 60, p. 319–324.

Robert, A., Lee, T. and Ritchie, H., 1985. A Semi-Lagrangian and Semi-Implicit Numerical Integration Scheme for Multilevel Atmospheric Models. Monthly Weather Review, Vol. 113, p. 388–394.

Ross, A. N. and Vosper, S. B., 2003. Numerical Simulations of Stably Stratified Flow through a Mountain Pass. Q. J. of the Royal Meteorological Society, Vol. 129, p. 97-115.

Schär, C., Leuenberger, D., Fuhrer, O. and Girard, C., 2002. A New Terrain-following Vertical Coordinate Formulation for Atmospheric Prediction Models. Monthly Weather Review, Vol. 130, p. 2459 – 2480.

Scotti, A. and Meneveau, C., 1997. Dynamic Smagorinsky Model on Anisotropic Grids. Physics of Fluids, Vol. 9, 1856. DOI: 10.1063/1.869306

Senocak, I., Ackerman, A., Kirkpatrick, M., Stevens, D. and Mansour, N., 2007. Study of Near-

Surface Models in Large Eddy Simulations of a Neutrally Stratified Atmospheric Boundary Layer. Boundary-Layer Meteorology, Vol. 124 (3), p. 405-424. DOI: 10.1007/s10546-007-9181-x

Senocak, I., Ackerman, A., Stevens, D. and Mansour, N., 2004, part II. Topography Modeling in Atmospheric Flows Using the Immersed Boundary Method. Annual Research Briefs. Center for Turbulence Research, NASA – Ames/Stanford University.

Shchepetkin, A. and McWilliams, J., 2003. A Method for Computing Horizontal Pressure-Gradient Force in an Oceanic Model with a Non-aligned Vertical Coordinate. Journal of Geophysical Research, Vol.108, 3090. DOI:10.1 029/2001JC001047.

Shuman, F., 1957. Numerical Methods in Weather Prediction: (II) Smoothing and Filtering. Monthly Weather Review, Vol. 85, p. 357-361. DOI: 10.1175/1520-0493(1957)085<0357:NMIWPI>2.0.CO;2

Shur, M. L., P. R. Spalart, M. Kh. Strelets, and A. K. Travin. 2008. A Hybrid RANS-LES Approach with Delayed-DES and Wall-Modelled LES Capabilities. International Journal of Heat and Fluid Flow, Vol. 29 (6), p. 1638–1649.

Silva Lopes, A., Palma, J. and Castro, F., 2007. Simulations of the Askervein flow. Part 2: Large eddy simulations. Boundary-Layer Meteorology, Vol. 125, p. 85-108. DOI: 10.1007/s10546-007-9195-4

Simmons, A. J., Hoskins, B. and Burridge, D., 1978. Stability of the Semi-Implicit Method of Time Integration. Monthly Weather Review, Vol. 106, p. 405–412.

Simmons, A. J., and Temperton, C., 1997. Stability of a Two-Time Level Semi-Implicit Integration Scheme for Gravity Wave Motion. Monthly Weather Review, Vol. 125, p. 600–615.

Šíp, V. and Beneš, L., 2016. RANS Solver for Microscale Pollution Dispersion Problems in Areas with Vegetation. https://arxiv.org/pdf/1609.03427.pdf [accessed online on March 11, 2017].

Smagorinsky, J., 1963. General Circulation Experiments with the Primitive Equations. Part 1: The Basic Experiment. Monthly Weather Review, Vol. 91, p. 99–164. DOI: 10.1175/1520-0493(1963)091<0099:GCEWTP>2.3.CO;2

Spalart, P. R., S. Deck, M. L. Shur, K. D. Squires, M. K. Strelets, and A. Travin. 2006. A New Version of Detached-Eddy Simulation, Resistant to Ambiguous Grid Densities. Theoretical and Computational Fluid Dynamics, Vol. 20 (3), p. 181-195.

Spalart, P., 2009. Detached Eddy Simulation. Annual Reviews of Fluid Mechanics, Vol. 41, p. 181-202.

Stensrud, D. J., 2007. Parameterization Schemes, Keys to Understanding Numerical Weather Prediction Models. Cambridge University Press, Cambridge, UK, 459 p.

Steppeler, J., Bitzer, H. W., Minotte, M. and Bonaventura, L., 2002. Nonhydrostatic Atmospheric Modeling Using a Z-Coordinate Representation. Monthly Weather Review, Vol. 130, p. 2143–2149.

Stoll, R. and Porté-Agel, F., 2008. Surface Heterogeneity Effects on Regional-Scale Fluxes in Stable Boundary Layers: Surface Temperature Transitions. Journal of Atmospheric Sciences, Vol. 66 (2), p. 412-431.

Strelets, M., 2001. Detached Eddy Simulation of Massively Separated Flows. American Institute of Aeronautics and Astronautics, AIAA, paper 2001-0879.

Stull, R. B., 1988. An Introduction to Boundary Layer Meteorology. Kluwer Academic Press, Dordrecht, Netherlands, 670 p.

Stull, R. B., 2000. Meteorology for Scientists and Engineers, 2nd edition. Brooks and Cole, CENGAGE Learning, Belmont, CA, USA, 502 p.

Sumner, J. and Masson, C., 2010. $K-\varepsilon$ Simulations of the Neutral ABL: Achieving Horizontal Homogeneity on Practical Grids. American Institute of Aeronautics and Astronautics 48th Aerospace Sciences Meeting, Vol. 48, p. 1–12.

Sumner, J., Sibuet, C. and Masson, C., 2010. CFD in Wind Energy: the Virtual, Multiscale Wind Tunnel. Energies, Vol. 3, p. 989-1013. DOI: 10.3390/en3050989.

Sumner, J. and Masson, C., 2012. Simulations of the neutral atmospheric boundary layer: analysis and correction of discretization errors on practical grids. Inter. J. for Numerical Methods in Fluids, Vol. 70, p. 724-774. DOI: 10.1002/fld.2709

Tanguay, M., Robert, A. and Laprise, R., 1990. A Semi-Implicit Semi-Lagrangian Fully Compressible Regional Forecast Model. Monthly Weather Review, Vol. 118, p. 1970–1980.

Taylor, P. A., 1977. Numerical Studies of Neutrally Stratified Planetary Boundary-Layer Flow above Gentle Topography. Boundary-Layer Meteorology, Vol. 12, p. 37–60.

Tennekes, H. and Lumley, J. L. 1972. A First Course in Turbulence. MIT Press, Boston, USA, 300 p.

Thomas, S., Girard, C., Benoit, R. and Pellerin, P., 1998. A New Adiabatic Kernel for the MC2 Model. Atmosphere–Ocean, Vol. 36, p. 241–270. DOI: 10.1080/07055900.1998.9649613

Tritton, D. J., 1988. Physical Fluid Dynamics. Oxford Science Publications, 2nd edition, Oxford, UK, 519 p.

Trombetti, F., Martano, P. and Tampieri, F., 1991. Data Sets for Studies of Flow and Dispersion in Complex Terrain: 1) The 'RUSHIL' Wind Tunnel Experiment (Flow Data). CNR Technical report No. 4 FISBAT-RT-91/1.

Walmsley, J. L., Taylor, P. A. and Keith, T., 1986. A Simple Model of Neutrally Stratified Boundary-Layer Flow over Complex Terrain with Surface Roughness Modulations (MS3DJH/3R). Boundary-Layer Meteorology, Vol. 36, p. 157–186.

Walmsley, J. L., Troen, I., Lalas, D. P. and Mason, P., 1990. Surface Layer Flow in Complex Terrain: Comparison of Models and Full Scale Observations. Boundary-Layer Meteorology, Vol. 52, p. 259–281.

Wang, X., 2017. A Simple Daily Cycle Temperature Boundary Condition for Ground Surfaces in CFD Predictions of Urban Wind Flows. Journal of Applied Meteorology and Climatology, Vol. 56, p. 2267-2283. DOI: 10.1175/JAMC-D-17-0095.1

Warner, T. T., 2011. Numerical Weather and Climate Prediction. Cambridge University Press, Cambridge, UK, 526 p.

Weigel, A., Chow, F. K., Rotach, M., Street, R. and Xue, M., 2006. High Resolution Large-Eddy Simulations of Flow in a Steep Alpine Valley. Part 2: Flow Structure and Heat Budget. Journal of Applied Meteorology and Climatology, Vol. 45, p. 87–107. DOI: 10.1175/JAM2323.1

Wilcox, D. C., 2006. Turbulence Modelling for CFD. DCW Industries, Cañada, CA, 3rd. Edition, 552 p.

Williams, P. D., 2011. The RAW Filter: an Improvement to the Robert-Asselin Filter in Semi-Implicit Integrations. Monthly Weather Review, Vol. 139, p. 1996–2007. DOI: 10.1175/2010MWR3601.1

Wyngaard, J. C., 2004. Toward Numerical Modeling in the « Terra Incognita ». Journal of Atmospheric Sciences, Vol. 61, p. 1816–1826.

Ying, R., Canuto, V. M. and Ypma, R. M., 1994. Numerical Simulation of Flow Data over Two-Dimensional Hills. Boundary Layer Meteorology, Vol. 70, p. 401-427.

Yu Fat, L., Mochida, A., Yoshino, H. and Murakami, S., 2007. Applicability of linear type revised $k-\varepsilon$ models to flow over topographic features. Journal of Wind Engineering and Industrial Aerodynamics, Vol. 95, p. 371-384. DOI: 10.1016/j.jweia.2006.09.004

Yu, C., Xiao, Z. and Li, X., 2017. Scale-adaptive Subgrid Scale Modelling for Large-eddy

Simulation of Turbulent Flows. Physics of Fluids, Vol. 29, 035101. DOI: http://dx.doi.org/10.1063/1.4977089.

Yu, W., Benoit, R., Girard, C., Glazer, A., Lemarquis, D., Salmon, J.R. and Pinard, T.P., 2006. Wind Energy Simulation Toolkit (WEST): A Wind Mapping System for Use by the Wind Energy Industry. Wind Engineering, Vol. 30, p. 15-33.

Zängl, G., 2003. A Generalized Sigma-coordinate System for MM5. Monthly Weather Review, Vol. 131, p. 2875–2884.

Zängl, G., 2012. Extending the Numerical Stability Limit of Terrain-Following Coordinate Models over Steep Slopes. Monthly Weather Review, Vol. 140, p. 3722–3733. DOI: 10.1175/MWR-D-12-00049.1

Zhiyin, Y., 2015. Large-Eddy Simulation: Past, Present and Future. Chinese Journal of Aeronautics, Vol. 28, p. 11-24.